

# Parquet theory in nuclear structure calculations

THESIS

Elise Bergli



## Acknowledgements

This thesis is primarily, of course, my own work. It has taken quite some time, not all of it pleasant, and I look forward to finally be doing something else. However, looking back, there are several people whom I would like to thank. Without them, I would not have been able to finish.

First of all, I thank my adviser Morten Hjorth-Jensen. You have provided more advise and encouragement than most advisers, being accessible and ready to answer questions at almost all times, regardless of time or place. I have really learned a lot from you these years. And I would also like to thank my co-adviser Eivind Osnes for pleasant discussions and having such an immense amount of literature available.

I would like to thank all my different office mates during these years: Victoria, Simen, Mateuz, Jon, Konrad, Maxim, Gustav and Øyvind. You have provided lots of interesting discussions and diversions on almost any subject imaginable. Sometimes we have even discussed physics... Most of you have also been able to provide insights and help me with numerous technical problems. Thanks also to Joakim, for all our lunch discussions and the last-minute proof-reading and comments.

And then there is as always my family, my most constant source of happiness. Thank you for simply being, my life would feel empty without you.



# Contents

<b>Contents</b>	<b>i</b>
<b>1 Introduction</b>	<b>1</b>
<b>2 <i>Ab initio</i> methods for nuclear structure calculations</b>	<b>7</b>
2.1 Many-body formalism and quasi particles . . . . .	8
2.2 The bare nucleon-nucleon (NN) interaction . . . . .	11
2.3 Effective interactions in finite model spaces . . . . .	13
2.4 <i>Ab Initio</i> approaches for light and medium-mass nuclei . . . . .	17
2.5 Effective interactions in the shell model . . . . .	20
2.6 Nuclear density functional theory . . . . .	21
<b>3 Many-Body theory and Green's functions</b>	<b>23</b>
3.1 The one-particle propagator . . . . .	23
3.2 The four-point Green's function . . . . .	26
3.3 Self energy . . . . .	30
3.4 The eigenvalue equation method . . . . .	34
<b>4 Parquet summation of diagrams</b>	<b>37</b>
4.1 Channels: Equivalent ways of building the interaction operator	38
4.2 Two-time propagators . . . . .	44
4.3 Self-consistent Parquet equations . . . . .	48
4.4 Approximate solution to the Dyson equation . . . . .	56
4.5 Summary of the different approximations . . . . .	58
<b>5 A simple model</b>	<b>63</b>
5.1 Description of the model . . . . .	63
5.2 Results for the pairing-only model . . . . .	65
5.3 Pair-breaking interaction . . . . .	81
5.4 Selected combinations of $g$ and $f$ . . . . .	106

5.5	Summary . . . . .	108
<b>6</b>	<b>Results for <math>^4\text{He}</math></b>	<b>111</b>
6.1	Results for unperturbed propagator structure (UPS) approximation . . . . .	112
6.2	Results for fixed-energy Dyson equation (FED) approximation	138
6.3	Summary of the $^4\text{He}$ results . . . . .	154
<b>7</b>	<b>Conclusions and future work</b>	<b>157</b>
	<b>Bibliography</b>	<b>163</b>

# 1 Introduction

Most real systems consist of several interacting bodies, and so many-body physics is an essential ingredient in any realistic description of the physical world. Quantum many-body theory concerns the fundamental properties of systems where the quantum nature of the constituents plays an important role. These include both small systems like nucleons, nuclei, atoms and small molecules, and large-scale systems as electrons in matter and nuclear matter in neutron stars. The problems encountered are notoriously complex and hard to solve, and many strategies exist to cope with different systems. The fundamental challenge common to all such problems is that describing the motion of all particles involved amounts to keeping track of far too much information for any straight-forward course of attack. Methods developed to handle this complex situation and transform it into something tractable are therefore mostly quite general and can be applied to a number of different systems, each providing different testing grounds for the general methods.

The physical systems chosen as subject for study in this thesis are low-energy nuclear systems, that is, nuclei and nuclear matter on an energy scale where the appropriate building blocks are the nucleons, the protons and neutrons. The range of possible combinations of nucleons spans from the single proton in a hydrogen nucleus to the couple of hundreds found in the heaviest nuclei, and then on to the (essentially) infinite number of particles in a neutron star. Nuclear systems are very challenging quantum many-body problems due both to the complexity of the strong force and to the number of particles involved, most nuclei being in the difficult mesoscopic range of too many particles to handle each separately and too few for statistical treatments.

The aim of *ab initio* methods in nuclear structure calculations is to describe the nucleus and nuclear matter from first principles only, with as little use of phenomenological determination as possible, ultimately building a coherent framework enabling calculations of low-energy nuclear structure and reaction ratios starting from the field theories of sub-nuclear particle physics and the standard model of Quantum Chromo Dynamic (QCD). If successful,

not only will we gain the satisfaction of being able to study nuclei and nuclear reactions from fundamental principles, but also the possibility of predicting key properties of short-lived nuclei present in stellar interiors and generated during supernova explosions, furthering our understanding of the ratios of different nuclei found in our part of the universe. On a more practical level, numerical computations across the range of exotic nuclei opens up for far easier determination of isotopes with specific characteristics that can be used in medicinal diagnostic and therapeutic treatments. Accurate computations could also be an ingredient in fine-tuning nuclear reactor designs to increase safety and efficiency.

The complexity of the computations increases very rapidly with increasing particle number. A layered approach is necessary, where only the relevant degrees of freedom for a given system are taken into account. Starting from QCD, the first step is to generate a theory where only nucleons exist, and all effects of the underlying strong force is taken into account by the effective force between the nucleons. This effective force acts between two nucleons in vacuum, and is called the bare interaction. Then we can start to put the nucleons together to form nuclei. Nuclei are quantum systems, and as such, there exists several general approaches which can be applied to these systems. One of the major obstacles is that the interaction between pairs of nucleons changes dramatically in the presence of other nucleons. The complexity of the computations increases and makes approaches to nuclear structure calculations based on the bare two-body interaction directly very impractical for heavier nuclei. A popular simplification is to generate a new effective interaction which takes the presence of the surrounding nucleons into account. This thesis concerns one possible framework, the summation of Parquet diagrams within Green's function theory, to obtain an effective interaction and use it to calculate properties of interest for finite nuclei.

The Green's functions (propagator) method is one of the standard theoretical descriptions of quantum mechanics, underlying the huge family of Feynman diagram methods employed in most high-energy physics. In the many-body context, two features of many-body systems provides the basis for applying propagator techniques. Firstly, almost all quantum systems of strongly interacting particles (where two particles exchange large amounts of energy each time they interact) can be described as a weakly interacting system of quasi particles (where the quasi particles exchange much smaller amounts of energy when they interact), given the right choice of definition of the quasi particles. Secondly, to find most of the important physical properties of a system, it is not necessary to know the behaviour of each particle exactly, rather it is enough to know the average behaviour of one or two typ-



ical particles. The quantities describing this average behaviour are the one- and two-body propagators. Once these are known, most physical properties of the system can be derived. The mathematical transparency, the generality and the close connection between the fundamental definitions and the physical observables makes Green's function based theories ideal for studies of general properties of many-body theories and the relations between different methods.

Within the field of nuclear structure calculations, this framework has long been widely used as a theoretical aid, but as most applications to realistic physical systems require self-consistent calculations, solutions in the form of closed expressions usually do not exist. The last 20 years, advances on calculating spectral functions and self-energies have been made [1, 2, 3, 4, 5, 6]. Several fundamental problems have still to be overcome, especially in connection with calculations on nuclei, as the structure of most interesting quantities to be calculated involves complex poles which are numerically difficult to handle and require large computational resources. On the other hand, the exact single particle propagator contains in principle all information on the state of the system, so the effort can be worthwhile [7].

For systems with many fermions, the antisymmetry of the wave function forces the particles to have different quantum numbers, that is, in the ground state (the state with lowest possible total energy), the available states will be filled with particles, starting from the states with lowest energy, up to a certain energy level called the Fermi level. A significant reduction of the complexity occurs if we assume only small excitations from the ground state. Thus most of the particles having low energies will never gain energy enough to jump above the Fermi level, and thus they need not be included in the calculation. For the cases where this is a good approximation, which include all nuclei except the lightest ones, we define the ground state as the so-called Fermi vacuum state, and record only the changes from this. The states with energy lower than the Fermi level are called holes, and removing particles from the ground state is then equivalent to creating holes.

Goeppert-Mayer [8] found that the remarkable regularities of the nuclear properties as a function of the proton and neutron numbers can be explained by assuming that each nucleon moves independently in a potential well set up by the mean interaction with all the other nucleons in the nucleus. The energy states of the Hamiltonian of this system are usually called orbitals. For some nuclei, called closed-shell nuclei, the single-particle picture is found to give an especially good description, with the neutrons or protons filling up all orbitals up to the Fermi level. The shell closures occur at the so-called magic numbers of neutrons or protons, and nuclei where both proton and neutron number are magic, are called doubly-closed or doubly-magic nuclei. The experimentally

available spectroscopic factors give a measure of what fraction of the full wave function can be factorized into a correlated state and an independent particle state.

The doubly-closed nuclei are especially suited for *ab initio* calculations, as their spherical symmetry can be exploited to reduce the number of necessary basis states. Recently, practically convergent results on the ground state of medium-mass closed nuclei like  $^{40}\text{Ca}$ ,  $^{48}\text{Ni}$  and  $^{48}\text{Ca}$  have been calculated by the coupled-cluster method [9, 10, 11]. This approach can be extended to a wider range of medium-mass nuclei by applying the so-called equation-of-motion method to the results of the closed-core result. Other methods commonly regarded as having potential possibility for extension to larger systems include the large-scale diagonalization methods (no-core shell model approaches)[12, 13], the unitary-model-approach [14], and (only applicable to doubly-closed nuclei) perturbative expansions [15, 16, 17]. The Parquet method is an alternative to these approaches, and it has been the aim of this thesis to investigate the practical possibilities and limitations of a numerical implementation.

For heavier nuclei, the shell structure provides the physical justification for introducing the simplification which makes calculations possible, namely that most of the nucleons are thought of as being inert in the closed core, and the active particles and holes are distributed among a select few valence orbitals on top of this core. By far the most used method is simply to set up the Hamiltonian for the valence orbitals, and perform a diagonalization of the resulting matrix, which in modern applications can contain of the order of  $10^9 - 10^{10}$  matrix elements [18]. Such a large-scale diagonalization calculation is commonly called a Shell Model calculation, and this has long been the standard solution method possible for calculations based on the assumption of a closed core. Another possibility is the so-called Shell Model Monte Carlo approach [19, 20].

The diagonalization Shell Model calculation needs an effective interaction which can incorporate the effect of the interaction between the active particles and the inert core as input. The Parquet method can, when extended to larger systems, provide a supplement to the traditional Lee-Suzuki transformation and  $\hat{Q}$ -box methods [21, 22, 23], and this possibility has given additional motivation for the work presented in this thesis.

The strong potential for *ab initio* calculations of medium-mass nuclei within the self-consistent Green's functions approach has been asserted by Barbieri *et al.* [6, 24], having recently calculated properties for selected nuclei up to  $^{56}\text{Ni}$  [25]. The Parquet method has a number of interesting features. It is possible to obtain better accuracy with a smaller numerical effort when com-

pared to large-scale diagonalization approaches, and the self-consistency requirement provides a path to ensure the conservation of basic macroscopic quantities. The main advantage, however, is the close connection with experimentally available data sets through the elementary basic blocks of the theory, namely the many-body propagators. These contain information on the energies of excitation processes and the amount of correlation in the system. The single-particle spectral function (and spectroscopic factor) can be experimentally extracted, for example in  $(e, e')$  knock-out reactions [26, 27], see also Refs. [28, 29, 30]. Extracting the spectroscopic factors from e.g. the coupled-cluster approach requires considerably more effort. Compared to the Faddeev random phase approach of Barbieri *et al.*, the Parquet method includes more particle-particle-hole-hole (pphh) correlations and is much easier to improve systematically.

The Parquet method of summing diagrams has been known for more than 50 years, having first been developed by Diatlov, Sudhakov and Ter-Martirosian [31] as an aid to describe meson-meson scattering in particle physics. These equations have since been used somewhat, most notably in one- and two-dimensional electron gas calculations [32, 33]. They have also been used for some critical-phenomena calculation [34, 35]. The most exhaustive theoretical investigations were carried out by Jackson, Landé and Smith [36, 37, 38, 39]. More recently, Yasuda has used the Parquet diagram method to construct approximations to the reduced density matrix of general quantum systems [40].

The effective interactions generated by this method include a large class of diagrams, and require no initial assumptions on the underlying interaction with respect to range and strength, as opposed to ladder type or ring type (standard random-phase approximation) interactions. The interaction is symmetric, that is, the particle-particle part of the interaction and the particle-hole part are treated on an equal footing, thus ensuring that all diagrams critical to a reasonable description of the many-body system are included. It is therefore applicable to systems where easier approaches fail, for example systems where it seems that both particle-particle type (calculated by ladder/ $G$ -matrix approximations) and particle-hole type (usually handled by random-phase approximation (RPA) methods) diagrams are equally important. Systems undergoing a phase transition is one such example, and there is clear evidence that both these parts of the interactions play a crucial role in nuclear systems [41]. By making a self-consistent calculation, the included diagram classes are summed to all orders. Only linked diagrams are included in the sum, which ensures that the method is size extensive, meaning that the total energy scales correctly with the number of particles [11]. Baym and

Kadanoff [42, 43] showed that the self-consistency requirement ensures the conservation of basic quantities like number, energy, momentum and angular momentum.

Furthermore, it is well established that at least three-body, possibly higher-body interactions are needed to obtain agreement between calculations and experiment for several quantities in nuclei, for example binding energies and spectra of light nuclei [44, 45], to solve the so-called  $A_y$  puzzle [46] and the binding energy in nuclear matter [47]. The formalism of the Parquet method can naturally be extended to include such higher-body terms [39].

The remainder of this thesis is sectioned into six more chapters. Chapter 2 provides general background material and motivation, and also some basic notation and concepts. A short introduction to the Green's function approach to many-body theory is given in chapter 3, before we present the Parquet summation method in chapter 4. In chapter 5 we discuss the results of applying the Parquet method to a simple model with a constant interaction, and in chapter 6 we move on to the more realistic system  $^4\text{He}$ . A short conclusion and plans for further work are given in chapter 7.

## 2 *Ab initio* methods for nuclear structure calculations

The aim of *ab initio* methods in nuclear structure calculations is to describe the nucleus and nuclear matter from first principles. Ideally, one would start with the particles which feel the strong interactions directly, i.e. quarks and gluons, and then use the rules of Quantum Chromo Dynamics (QCD). Due to the non-perturbative nature of the strong force, we do not know how to compute anything at the low energy scales involved in real, cold nuclei. Only if the nuclei are heated or compressed, as in a collider machine, is it possible to use perturbative expansions. Thus other approaches are necessary for calculations on nuclear structure and reactions. Based on observation, we know that the nucleonic degree of freedom, treating protons and neutrons as stable, unstructured particles is a good starting point, at least up to an energy of  $\sim 140$  MeV (the pion production threshold). However, then we run into the problem of determining the interaction between the nucleons, as this is a residual force originating from the interactions between the quarks which make up each particle. Furthermore, even if the interaction between free nucleons could be well determined, putting several nucleons together creates a strongly interacting system which is too complex to handle without further simplifications.

There are several methods that have been applied to nuclear structure problems, many of which are mostly or purely phenomenological, and we will not discuss these. Broadly speaking, the *ab initio* efforts fall into two classes, wave-function based methods and the propagator methods. The Green's functions method falls into this latter class. Approaches suited for calculations including all nucleons in the nucleus are presently restricted to light and in certain cases, medium-mass nuclei, while a closed-core approach in which several nucleons are regarded as inert works best for medium to heavy nuclei. For large nuclei, there is an ongoing effort to extend the range of *ab initio* calcu-

lations by applying Density Functional Theory based on an *ab initio*-derived density functional for nuclei. We will discuss certain aspects of these topics, with emphasis of the possible application of the Green's functions method within each subject.

This chapter is organized as follows. First, we introduce some necessary fundamental many-body notation in section 2.1. A short description of the various approaches for constructing the nucleon-nucleon force (the so-called bare NN interaction), being the common input to all the *ab initio* calculations, is provided in section 2.2. The repulsive short-range part of the bare interaction requires special attention, and the implications of this is discussed in the section on effective low-energy interaction is in section 2.3. Then we move on to describing the challenges and strategies of *ab initio* calculations of light and medium-mass nuclei in section 2.4. In section 2.5 the role of the effective interaction needed as input to standard Shell Model calculations is discussed.

## 2.1 Many-body formalism and quasi particles

In this section we introduce some fundamental concepts and notation of many-body theory. This provides the common, necessary background material for the discussion on different many-body approaches, and for the presentation of our chosen method, the Green's functions approach given in chapter 3.

### 2.1.1 Basic concepts and notation

Single-particle states are the basic building blocks of many-body nuclear theory. Nucleons are fermions, and each particle needs its own set of unique quantum numbers, both for infinite and finite cases. In the infinite case, the basis states are plane waves, and a single-particle state  $|\alpha\rangle$  has momentum  $\mathbf{k}_\alpha$ , spin projection  $s_\alpha$  and isospin projection  $\tau_\alpha$ . In the finite case, the quantum numbers of  $\alpha$  will depend on the chosen basis states. A set of basis states is assumed normalized and orthogonal.

The fermion wave function must be antisymmetric, that is, exchanging two particles must change the sign of the state. To ensure this, the two-body state is constructed as:

$$|\alpha\beta\rangle \equiv \frac{1}{\sqrt{2}}(|\alpha\rangle|\beta\rangle - |\beta\rangle|\alpha\rangle). \quad (2.1)$$

This state has the correct symmetry, and vanishes if  $\alpha = \beta$ , thus incorporating the Pauli principle. Only states where  $\alpha \leq \beta$  should be counted in the

completeness relation for the basis states, as exchanging the two states gives the same physical state.

For larger systems, the same antisymmetry considerations has to be made. To create an antisymmetrized  $N$ -particle state, we define the anti-symmetrizing operator

$$\mathcal{A} = \frac{1}{N!} \sum_P (-1)^P P, \quad (2.2)$$

where  $P$  is a permutation operator for  $N$  particles, the sum is over all  $N!$  possible permutations and the sign depends on whether the permutation is even or odd. Acting with the anti-symmetrizing operator upon the simple product state  $|\alpha_1\rangle \dots |\alpha_N\rangle$  generates wave functions that can be written as a single Slater determinant in the case of a system of non-interacting particles, and as a linear combination of such determinants in the case of interacting particles. To describe many-particle systems, we use an extension of the Hilbert space called a Fock space. Formally, this is defined as the Hilbert space made from the direct sum of tensor products of single-particle Hilbert spaces, so that the total space contains the vacuum state  $|0\rangle$ , the complete set of single-particle states  $\{|\alpha\rangle\}$ , the complete set of antisymmetric two-particle states  $\{|\alpha_1\alpha_2\rangle\}$  and so on for all particle numbers to infinity. This enables us to define operators between states with different particle numbers.

The concept of second-quantization makes the construction of many-body states easier. This is a compact way of keeping track of whether a single-particle state in the basis is occupied or not, by writing the state as

$$|\Psi^N\rangle = |n_1, n_2, \dots, n_N\rangle, \quad (2.3)$$

each  $n_i$  being either 0 or 1 depending on whether single particle state  $|\alpha\rangle$  is occupied or not. We define the creation and annihilation operators  $c_\alpha^\dagger$  and  $c_\alpha$  as operators that add or remove one particle with quantum numbers  $\alpha$  from a many-particle state, i.e.

$$c_\alpha^\dagger |\Psi^N\rangle = |\Psi^{N+1}\rangle = \mathcal{A}(|\alpha\rangle |\Psi^N\rangle), \quad (2.4)$$

and

$$c_\alpha |\Psi^N\rangle = c_\alpha \mathcal{A}(|\alpha\rangle |\Psi^{N-1}\rangle) = |\Psi^{N-1}\rangle. \quad (2.5)$$

Operating with  $c_\alpha^\dagger$  on a state already containing a state with quantum numbers  $\alpha$  produces zero, as does trying to operate with  $c_\alpha$  on a state which does not contain the state  $|\alpha\rangle$ . The vacuum state  $|\Psi^0\rangle$  is the state with no particles, and  $c_\alpha |\Psi^0\rangle = c_\alpha |0, \dots, 0\rangle = 0$ . In the Heisenberg picture the creator and

annihilator operators carries the time dependency, and are given as

$$c_\alpha^\dagger(t) = e^{i\hat{H}t} c_\alpha^\dagger e^{-i\hat{H}t}, \quad (2.6)$$

and

$$c_\alpha(t) = e^{i\hat{H}t} c_\alpha e^{-i\hat{H}t}. \quad (2.7)$$

Here  $H$  is the Hamilton operator. Within the second-quantization scheme, a generic Hamilton operator composed of a one-body term  $\hat{H}_0$  and an interaction term  $\hat{V}$  can be written as:

$$\hat{H} = \hat{H}_0 + \hat{V} = \sum_{\alpha\beta} \langle \alpha | H_0 | \alpha \rangle c_\alpha^\dagger c_\beta + \frac{1}{2} \sum_{\alpha\beta\gamma\delta} \langle \alpha\beta | V | \gamma\delta \rangle c_\alpha^\dagger c_\beta^\dagger c_\delta c_\gamma. \quad (2.8)$$

In the following, we will use the notation that  $|\Psi_0^N\rangle$  is the N-particle ground state of a set of eigenstates  $|\Psi_m^N\rangle$  such that  $H^N |\Psi_m^N\rangle = E_m^N |\Psi_m^N\rangle$  forms a complete orthonormal basis set with completeness relation

$$\sum_m |\Psi_m^N\rangle \langle \Psi_m^N| = 1. \quad (2.9)$$

### 2.1.2 Harmonic oscillator basis

The nuclear system is self-bound, that is, there is no externally imposed potential that keeps the nucleons together. The observed shell structure of the energy levels in the nucleus suggests that the action of all the nucleon-nucleon interactions adds up to a potential that can be modelled by a central field. A suitable physical model for this is the Woods-Saxon potential [48], but as the eigenfunctions cannot be given in closed form, the most used basis for calculations of finite nuclei is the harmonic oscillator basis. This basis has nice analytic properties while hopefully not requiring an unmanageable number of basis states to build up the true wave function, having incorporated the centrally bound structure into the basis.

The three-dimensional harmonic oscillator states are primarily characterized by the radial quantum number  $n$  and the angular momentum  $l$ . The energy of a given state is

$$\epsilon_N = \hbar\Omega(N + \frac{3}{2}), \quad (2.10)$$

where  $N = 2n + l$  and  $\Omega$  is the oscillator frequency determining the spacing between the energy levels. Ideally, all results should be independent of this parameter. In coordinate space, the eigenfunctions are Hermite polynomials.



Nucleons are particles with intrinsic spin  $s = \frac{1}{2}$ , which couples to the orbital momentum  $l$ . It is convenient to introduce the total angular momentum  $j$  with projection quantum number  $m$  to characterize the eigenstates. In addition, the isospin quantum number  $t_z$  is used to distinguish between the two species of nucleons, protons having  $t_z = -\frac{1}{2}$  and neutrons  $t_z = \frac{1}{2}$  (as we use isospin-dependent nuclear forces, we do not employ the full isospin formalism). Thus, the generic eigenstate  $|\alpha\rangle$  is an abbreviation for

$$|\alpha\rangle = |njmlst_z\rangle = \sum_{m_l m_s} \langle lm_l sm_s | jm \rangle |nt_z\rangle |lm_l\rangle \otimes |sm_s\rangle, \quad (2.11)$$

where the  $\langle lm_l sm_s | jm \rangle$  are Clebsch-Gordan coefficients.

Ideally, one would use a full (infinite) basis set in calculations of finite many-body systems, but implementations must necessarily be finite, and truncations have to be made. This introduces the concept of a model space, the set of basis states for the full Hilbert space chosen as basis set in the calculations. To find the best basis set and truncation for a given problem, combined with a method to include the effect of the excluded basis states is a difficult task. Numerous strategies have been tried for various systems, including the whole machinery of effective field theory in nuclear physics.

## 2.2 The bare nucleon-nucleon (NN) interaction

It is necessary to determine the interaction between the nucleons which is to be used as input to the nuclear structure calculations. The traditional first step is to first determine the force between two nucleons in free space, since this is an experimentally relatively accessible quantity. The force between nucleons is a residual force, created by the long-range leftovers from the strong interaction between the three quarks inside each nucleon. There are two main branches of methods for obtaining the so-called bare nucleon-nucleon interaction (i.e. in free space, not in a medium). The oldest is based on generating an interaction with a number of free parameters (typically around 40) and then fit these to experimental data, usually the phase shifts from nucleon-nucleon scattering experiments. The second approach was initiated by Weinberg [49], and is based on effective field theory, starting from a Lagrangian consistent with the symmetries of QCD.

### 2.2.1 Phase-shift fitted potentials

There are several modern nucleon-nucleon potentials based on fitting parameters to phase shifts, most notably the NijmI and NijmII,[50] the Argonne

$V_{18}$  [51] and the CD-Bonn [52] potentials. These potentials have a number of parameters which are fitted to scattering data analyzed by the Nijmegen group in the early 1990's, performing a multienergy partial-wave analysis for all NN scattering data below 350 MeV laboratory energy resulting in a database which by 1999 consisted of massive amounts of data for  $pp$  and  $np$  scattering [53, 52]. All the above potentials fit this database with  $\chi^2/\text{datum}$  values very close to 1 (less than 1.1 for all).

The Nijmegen potentials are based on one-boson-exchange (OBE) theory and parametrize each partial wave separately, with a total of 41 (NijmI) and 47 (NijmII) parameters. The NijmII is a local potential, while NijmI contains momentum-dependent terms which give rise to non-localities in the central force component. Both are soft-core potentials, that is, they regularize the strong repulsion between nucleons at short distances by the use of exponential form factors. The CD-Bonn potential is a charge-dependent OBE based potential which includes the effects of  $\pi$ ,  $\rho$  and  $\omega$  mesons plus two effective scalar-isoscalar  $\sigma$  bosons, having in total 43 free parameters. The Argonne  $V_{18}$  model is purely phenomenological, consisting of a sum of 18 operator terms,

$$V_{ij} = \sum_{p=1}^{18} V_p(r_{ij}) O_{ij}^p, \quad (2.12)$$

where the operators  $O^p$  are different combinations of the operators  $\mathbf{L}, \mathbf{S}, \sigma, \tau, \mathbf{r}$  and their components. As the Nijmegen potentials, it is regularized by exponential form factors at very short distances. The total numbers of free parameters is 40.

The differences between the above potentials at low energies are very small, the main difference being the D-state deuteron probability which differs between 4.85% and 5.76%. At higher energies and in the off-shell matrix elements, where they are no longer constrained by the scattering data, the differences becomes much larger, as seen for example in the calculation of the binding energy of nuclear matter [54, 55].

Recently, a new and somewhat different potential has been developed, the so-called JISP6 (J-matrix inverse scattering potential) [56, 57]. In this approach, a potential matrix is found for each partial wave separately. Very few a priori constraints are placed on the matrix elements, except for making the phenomenologically based assumption that the potential matrix in the uncoupled partial waves is tridiagonal. The off-shell matrix elements are then constrained by bound and resonant states in nuclei with  $A \leq 6$ .

### 2.2.2 Chiral potentials

The chiral potentials are derived from more fundamental principles than the above meson-exchange based potentials. For a review of the subject, see for example Ref. [58] and references therein. The main idea is to write down the most general Lagrangian for low-energy pions and nucleons consistent with the symmetries of QCD, of which the most important feature is the spontaneously broken chiral symmetry. This broken symmetry generates Nambu-Goldstone bosons, identified with the pions. The higher-energy degrees of freedom are taken into account in the coefficients of various terms in the pion-nucleon Lagrangian. This makes it possible to derive an NN interaction perturbatively, expanding in powers of the small parameter  $Q/\Lambda_\chi$ , where  $Q$  is a generic low-momentum parameter and  $\Lambda_\chi \approx 1$  GeV is the chiral symmetry breaking scale. Thus the potentials derived from this type of approach can be improved systematically, and contains controllable derivations of three- and higher-body terms. The current highest-order potentials are N<sup>3</sup>LO (next-to-next-to-next to leading order) potentials [59], which include some three-body diagrams, making treatment of the three-body terms necessary for any correct application of these potentials. Currently, there are several variants of chiral potentials, having between 25 and 30 free parameters and giving  $\chi^2/\text{datum}$  values comparable to, albeit a little higher than, the phase-shift potentials discussed in the previous section.

## 2.3 Effective interactions in finite model spaces

The bare NN interaction is very repulsive at short distances, colloquially known as being a hard core potential. Even if this is softer than a hard sphere approximation, it still causes significant convergence problems for all many-body theories using any of the variants of the bare interactions as input. The short-distance structure will be highly model-dependent since the short-range part of the NN interaction is determined by processes occurring at higher energies than the energy scale of the data used as basis for the phase-shift fitted potentials. Thus it is very desirable to reduce the effects of the short-range details of the interaction as much as possible, constructing an effective interaction which keeps the long-range behaviour of the bare interaction, but smooths out all higher-energy details. This new interaction will be applicable in a truncated space (model space) with less resolution in energy. The traditional approach for doing this is the energy-dependent Brueckner  $G$ -matrix [60, 61], while a more recent renormalization group (RG) derived interaction is the cutoff-dependent  $V_{\text{low}k}$  potential [62, 63].

### 2.3.1 $G$ -matrix

The original motivation for the  $G$ -matrix approach was to obtain a two-body interaction suitable for a perturbation expansion of the ground-state energy of nuclear matter. This also provided some theoretical foundation for the shell model. The central idea of the theory is that when two nucleons interact, we allow for any number of interactions to occur before the particles go on to meet other particles. This amounts to summing all diagrams with two particles as intermediate states, commonly called the ladder type diagrams, and use this sum in place of the interaction. The sum, called the  $G$ -matrix, is defined by the integral equation

$$G(\omega) = V + V \frac{Q_{2p}}{\omega - H_0} G(\omega), \quad (2.13)$$

where  $\omega$  is an energy variable known as the starting energy, and  $Q_{2p}$  is an operator projecting onto two-particle states. This projection operator becomes rather complicated when the  $G$ -matrix is generated to be used in perturbation expansions in finite nuclei, as the two-particle state must have at least one particle outside the chosen model space, which in turn depends on the nucleus in question. A two-partition scheme for solving for the  $G$ -matrix depending on choice of model space exists, see e.g. [13]. If the  $G$ -matrix is to be used as an input to a coupled-cluster or Parquet type of calculation, the objective is merely to sum the really high-energy contributions, and a 'free'  $G$ -matrix defined in a large model space will suffice.

There are some disadvantages to this approach, the main shortcomings being the energy dependence and, for direct applications to finite nuclei, the model space dependence introduced in the  $Q_{2p}$  operator. In addition, this is a one-step procedure which is difficult to improve on systematically to generate higher-body interactions, and there is no clear and direct connection back to the original potential.

### 2.3.2 $V_{lowk}$

A method for generating a well-behaved, energy-independent effective interaction is the so-called similarity renormalization group theory (SRG) approach [64]. The oldest and most tried variant is the  $V_{lowk}$  approach with a sharp momentum-cutoff [62, 63], equivalent to the Lee-Suzuki similarity transformation method [22]. Most published applications of the  $V_{lowk}$ -potential have used the latter algorithm, being more numerically stable. The conceptual framework, however, is simpler for the SRG-based method. Its origins lies in the central idea of effective field theory, namely that the physics at the

infrared region should be insensitive to the details of the short-range, high-energy details. The fact that as all the different bare NN interaction have a common low-energy long-range part which is unambiguously determined from data illustrate this point. Thus, rather than starting from a chiral Lagrangian, the initial interaction is an NN potential, which is then evolved through successive iterations into a potential where the effects of the model-dependent high-energy momentum modes are integrated out, and the common long-range tail is kept essentially unchanged. As expected, when such a calculation is performed, the differences between the bare NN interaction variants are largely removed, and all of them evolve into essentially the same  $V_{lowk}$  potential [63].

The calculation of  $V_{lowk}$  is based on the  $T$ -matrix equivalence relations defining a low-momentum scattering  $T$ -matrix  $T_{lowk}$  by

$$T_{lowk}(p', p, p^2) = V_{lowk}(p', p) + \mathcal{P} \int_0^\Lambda q^2 dq V_{lowk}(p', q) \frac{1}{p^2 - q^2} T_{lowk}(q, p, p^2), \quad (2.14)$$

where  $(p', p) \leq \Lambda$  and  $\mathcal{P}$  denotes the principal value integration. The low-momentum scattering matrix  $T_{lowk}$  must fulfil the condition

$$T(p', p, p^2) = T_{lowk}(p', p, p^2), \quad (p', p) \leq \Lambda, \quad (2.15)$$

with  $T(p', p, p^2)$  being the standard scattering  $T$ -matrix defined for all momenta  $p'$  and  $p$ . The above equations ensure that  $T_{lowk}$  preserves the low-momentum half-on-shell full  $T$ -matrix.

The Lee-Suzuki algorithm employed to calculate  $V_{lowk}$  was developed as a method for summing up the folded-diagram series in order to obtain an effective Shell Model interaction, as briefly discussed above. It is based on finding a similarity transformation operator  $X$  defined in the whole Hilbert space such that the transformed (effective) interaction

$$\mathcal{H} \equiv X^{-1} H X, \quad (2.16)$$

satisfies the decoupling condition

$$Q \mathcal{H} P = 0. \quad (2.17)$$

Here  $P$  and  $Q$  are the usual model space projectors, projecting into or out of the model space, respectively. The most common choice of similarity transformation operator is

$$X = e^\Omega, \quad (2.18)$$

where the wave operator  $\Omega$  satisfies the conditions

$$\Omega = Q\Omega P, \quad (2.19)$$

$$P\Omega P = Q\Omega Q = P\Omega Q. \quad (2.20)$$

The result of this is to construct an effective Hamiltonian defined in the smaller model space  $P$ , such that the eigenvalues of  $H_{\text{eff}}$  are the same as the eigenvalues of the original Hamiltonian within  $P$ .

The sharp cutoff introduced in this derivation has some disadvantages, as it can cause convergence problems at low energies. Recently, an algorithm for generating a  $V_{\text{low}k}$  potential with a smooth cutoff regulator has been proposed [65]. The first successful attempts to evolve the bare interaction using a SRG-based approach within a harmonic oscillator basis (generating three-body contributions in a controlled manner) has recently been reported [66].

### 2.3.3 Effective interactions and three-body forces

Recently, three-body forces have received quite a lot of attention. An increasing number of calculations show that such forces must be included to reproduce both properties of light nuclei and of nuclear matter [44, 67, 68, 69, 46, 70, 45, 66, 71, 72]. Higher-body interactions are a product of the truncation process when an effective interaction is generated as the high-energy degrees of freedom are assimilated into an effective interaction at lower energies. The standard example in nuclear physics is the  $\Delta$ -isobar resonance, in which two nucleons interact, one is excited into a  $\Delta$ , which subsequently interacts with a third nucleon and becomes a nucleon once more. Thus, with only nucleons as allowed degrees of freedom, the result of this event is an (attractive) effective force between three nucleons.

In the standard truncation schemes outlined above, higher-body effective interactions will appear in two layers, first when generating the bare NN interaction from QCD or phase shifts (including the effect of the  $\Delta$  resonance) and then again when performing either a  $G$ -matrix or an  $V_{\text{low}k}$  truncation. For the bare NN case, the existing attempts to generate three-body forces at the more phenomenological level of the phase-shift potential, the most commonly used three-body potentials are the Urbana/Illinois potentials [73, 74], which have two to five free parameters usually fitted to the triton binding energy.

The chiral potential method generate higher-body terms straightforwardly as more terms in the perturbation expansion are included, the first contributing three-body terms appearing at the NNLO level (thus being present in the current N<sup>3</sup>LO potential). The construction of the full class of contributing

three-body class is an ongoing project [75]. Recent efforts to ascertain the effects of missing many-body physics stemming from the truncations of the chiral interactions have shown that the neutron-rich oxygen isotopes are very sensitive to the strength of the three-body forces [71, 72].

Any theory which intends to use the best available bare interaction needs the capability to handle at least three-body forces.

## 2.4 *Ab Initio* approaches for light and medium-mass nuclei

For light nuclei, the degrees of freedom are moderate and several methods have been applied to these systems. For the lightest nuclei, there are methods which employ the bare NN interaction directly without relying on any additional truncation to handle the short-range correlations, the most versatile probably being the Green's function Monte Carlo methods [76, 19, 77] which can currently handle up to  $A \leq 12$ . Others in this group include Faddeev-Yakubovsky-methods for  $A=3-4$  [67], the correlated hyperspherical harmonics [78] and variational approaches [79, 80]. The rapid growth of the computational complexity of these methods make extensions to heavier nuclei in practice unattainable. Methods operating within the second quantization scheme rather than in coordinate space have the possibility of incorporating the effects of the short-range correlations into an effective interaction via a  $G$ -matrix or  $V_{lowk}$  scheme as described in section 2.3. Then smaller computational spaces are necessary, and methods which can employ such an effective interaction have better possibilities for extensions to larger systems. An added bonus is that as the computational resources increase, the large spaces needed for calculations with only the bare NN interaction become feasible, thus enabling a study of the effect of the truncation schemes. The topic of this dissertation, the Parquet method, fall into this class of methods, and we will give a short overview of some other approaches as natural candidates for comparison.

### 2.4.1 Large-scale diagonalization techniques

The family of approaches that rely on large-scale diagonalization techniques are commonly termed No-Core Shell Model (NCSM) or No-Core Full Configuration Interaction method. For a recent review, see for example [18]. The basic idea of these methods is simple, namely to chose a set of basis states and an interaction as input, and then solve the eigenvalue equation to obtain the eigenvalues and eigenstates. In the limit of an infinite basis, an exact solution

would be obtained, but real calculations necessitate cutoffs and truncation schemes. The difference between these methods and a common Shell Model calculation is that no inert core is assumed and all nucleons participate.

The common choice of basis is the harmonic oscillator basis, but several different choices of input interactions have been used. No-core shell model calculations have been performed with  $G$ -matrix input [81], with  $V_{lowk}$  input [70, 45], and with both sharp- and smooth-cutoff variants of free-space SRG-evolved potential [82]. The authors of Ref. [83] have performed calculations employing the bare NN interaction JISP6 as input, naming the approach No-Core Full Configuration Interaction method as no extra step to generate an effective interaction is taken in this case. The JISP6 results show quite good convergence, but the same calculations employing the bare  $N^3LO$  as input give less stable results.

All of these methods have dependencies on the harmonic oscillator energy  $\hbar\Omega$  and the size  $N_{\max}$  of the chosen space, which lessens with increasing  $N_{\max}$  as expected. The  $V_{lowk}$  and SRG results have an additional cutoff dependence.

### 2.4.2 Perturbation expansion

Ground-state energies of doubly-closed nuclei can be obtained by the well-known Goldstone perturbative expansion (see for example Refs. [84, 85]). The authors of Refs. [15, 16, 17] have solved the Hartree-Fock equations for doubly-closed nuclei on top of a  $V_{lowk}$  renormalization procedure to obtain an auxiliary potential and a new basis. This HF basis is then used in the summation of the Goldstone expansion to fourth order in the interaction. Although rather restricted as a many-body method, the Goldstone expansion is one of the cornerstones of many-body ground state energy calculations, and serves as a common point of reference for comparison between different methods.

### 2.4.3 Coupled cluster method

The coupled-cluster (CC) method was first developed within the field of nuclear structure calculations [86], but became almost exclusively used in computational chemistry until recently, when several successful calculations of light and closed-shell medium nuclei has been reported [9, 10]. For a review on the method in general and its application in quantum chemistry, see [11]. The central idea is to express the full correlated wave function  $|\Psi\rangle$  as a correlation operator  $T$  acting on a reference Slater determinant  $|\Phi_0\rangle$ :

$$|\Psi\rangle = e^T |\Phi_0\rangle. \quad (2.21)$$



The correlation operator is given by a sum of  $n$ -particle  $n$ -hole excitations for all  $n \in 1, N$ :

$$T = T_1 + T_2 + T_3 + \cdots + T_N \quad (2.22)$$

The  $T_i$  operators are expressed by creation and annihilation operators as

$$T_1 = \sum_{i,a} t_i^a c_a^\dagger c_i, \quad (2.23)$$

$$T_2 = \frac{1}{4} \sum_{ij,ab} t_{ij}^{ab} c_a^\dagger c_b^\dagger c_j c_i, \quad (2.24)$$

and so on. By convention, indices  $a, b, \dots$  denotes single-particle orbitals and  $i, j, \dots$  denote single-hole orbitals. Including only  $T_1$  gives a so-called singles CC calculation (CCS), including  $T_1$  and  $T_2$  gives a singles-and-doubles CC calculation (CCSD) and including  $T_1, T_2$  and  $T_3$  is called a singles-doubles-and-triples CC calculation (CCSDT). Usually, only a CCSD or an approximate CCSDT calculation (with acronym CCSD(T)) is performed in current nuclear structure calculations. By virtue of the exponential expansion used in calculation of the correlated wave function, also disconnected excitations like two separate single excitations are included to all possible orders.

The equations for the amplitudes  $t_{ij,\dots}^{ab,\dots}$  are found by left projection into a sufficient number of excitations:

$$\langle \Phi_{ij,\dots}^{ab,\dots} | e^{-T} H e^T | \Phi_0 \rangle = 0, \quad (2.25)$$

This gives rise to a set of non-linear, coupled equations which is solved self-consistently by iteration. The ground state energy is found from the Schrödinger equation:

$$E = \langle \Phi_0 | e^{-T} H e^T | \Phi_0 \rangle. \quad (2.26)$$

The main advantages of the coupled-cluster theory is the nice properties with respect to the computational effort as the system size increase compared to the diagonalization methods and that it scales correctly with increasing particle number (size extensive). The so-called equation-of-motion method is used to calculate excited states of closed-shell nuclei, and furthermore, the properties for nuclei in the vicinity of closed shell nuclei can be found by applying the so-called one-particle-attached and two-particle-attached schemes.

## 2.5 Effective interactions in the shell model

In the Shell Model, the underlying idea is that the nucleons outside the core (the valence nucleons) determine most of the properties of the nucleus. Thus the model space is restricted to include only the degrees of freedom relevant for the valence nucleons, and the solution is found by a large-scale diagonalization within this model space.

Even if most of the nucleons are considered as bound firmly in the core, their presence will modify the interactions between the valence nucleons outside. So, if a restricted space (model space) is to be used, the effects of the configurations left out of the model space has to be included in an effective interaction, which is then different from the "bare" interaction as measured between free nucleons. This effective interaction should also account for the Pauli exclusion principle, which forbids two interacting nucleons to scatter into already occupied orbitals. Furthermore, as the nucleus is a self-bound system, it makes sense to choose a basis with bound single-particle states, implying that a large part of the bare NN interaction is accounted for as an average field creating the bound system. Thus two other issues are closely related to the question on how to determine an effective residual interaction between the valence nucleons outside the core, namely the choice of basis and determining the energies of the valence orbitals. There are numerous approaches to these topics, and we will not go into any details here. For some recent reviews, see for example [87].

In the spirit of *ab initio* calculations, one may start from a realistic 'bare' force and use many-body techniques to construct an effective interaction for the given system, removing all dependencies on phenomenological input. Several steps are needed to obtain this. The input is the bare interaction and a basis. The common choice here is the harmonic oscillator basis, other options are a Hartree-Fock basis [88] or a Gamow basis [89, 90, 91, 10], the latter being a natural choice for weakly bound systems. Because of the strong repulsive short-range part of the nuclear interaction, it is often necessary to perform a preliminary step neutralizing the effects of this, in the form of generating a  $G$ -matrix or  $V_{lowk}$  interaction in a large space, as discussed in section 2.3.2.

The  $G$ -matrix approach is the oldest and most studied. The class of diagrams which is summed to all orders in this renormalized interactions are diagrams of the particle-particle type only, and the effects of other types of diagrams like the core-polarization diagram must be included by other means afterwards. As the Parquet summation method is a method to sum a much larger class of diagrams to all orders, of particle-particle, hole-hole and particle-hole types of diagrams, this method can be used to generate an

effective interaction for use in the Shell Model calculations.

## 2.6 Nuclear density functional theory

The heavier nuclei are regarded as having too many degrees of freedom to be handled by Shell-Model type calculations, and there is currently much effort directed towards generating a density functional for nuclei and nuclear matter [92]. To develop such a Density Functional Theory (DFT) is the logical approach to obtain *ab initio*-based calculations of heavy nuclei, as phenomenological descriptions of mean-field nature works well in this mass region. A nuclear DFT would have the possibility of systematic improvement, which the current phenomenological approaches lack. The Green's functions formalism could possibly be used a basis for such a functional.



# 3 Many-Body theory and Green's functions

In this chapter we set up the basic Green's function formalism describing a system of many non-relativistic nucleons interacting by means of a two-body interaction  $\hat{V}$ . We follow the standard convention of setting  $\hbar = c = 1$ . This chapter gives a short introduction to the main concepts we need in order to present the Parquet formalism in chapter 4. The Green's functions formalism is a standard framework within many-body quantum theory, and fuller accounts are found in most textbooks on the subject, see for example Refs. [84, 93, 94]. A comparatively recent presentation is given by the book of Dickhoff and Van Neck from 2004 [7], and a quite amusing account is given in Mattuck's book [85].

Here we shall be content with a short discussion of the one-body propagator in section 3.1, and the four-points Green's function and the interaction operator in section 3.2. Then we introduce the self energy and the Dyson equation in section 3.3, and finally, an account of the matrix inversion method for finding the one-body propagator is given in section 3.4.

## 3.1 The one-particle propagator

The one-particle Green's function is defined as:

$$\begin{aligned} g_{\alpha\beta}(\tau) &= g_{\alpha\beta}(t - t') = -i\langle\Psi_0^N|\mathcal{T}\{c_\alpha(t)c_\beta^\dagger(t')\}|\Psi_0^N\rangle \\ &= \begin{cases} -i\langle\Psi_0^N|c_\alpha(t)c_\beta^\dagger(t')|\Psi_0^N\rangle & t > t' \\ i\langle\Psi_0^N|c_\beta^\dagger(t')c_\alpha(t)|\Psi_0^N\rangle & t \leq t'. \end{cases} \end{aligned} \quad (3.1)$$

Here  $c(t)$  and  $c^\dagger(t)$  are the annihilation and creation operator in the Heisenberg representation as described in section 2.1.1,  $|\Psi_0^N\rangle$  is the N-particle ground state and  $\mathcal{T}$  is the time ordering operator. If we add a particle in state  $\beta$  at a given

time  $t'$ , the one-body propagator for  $t > t'$  gives the probability that we find the system still in its ground state if we remove a particle in state  $\alpha$  at time  $t$ . Similarly, for  $t \leq t'$  the one-body propagator gives the probability for recovering the ground state when a hole is created (a particle removed) at a time  $t$  and then annihilated at  $t'$ . Fourier transforming to obtain the so-called Lehmann representation, we see that the denominator is zero at energies corresponding to the excitation energies of the  $(N+1)$  and the  $(N-1)$  states with respect to the ground state  $|\Psi_0^N\rangle$  [1]:

$$\begin{aligned}
g_{\alpha\beta}(\omega) &= \frac{1}{2\pi} \int_{-\infty}^{\infty} d\tau e^{i\omega\tau} g_{\alpha\beta}(\tau) \\
&= \sum_n \frac{\langle \Psi_0^N | c_\alpha | \Psi_n^{N+1} \rangle \langle \Psi_n^{N+1} | c_\beta^\dagger | \Psi_0^N \rangle}{\omega - (E_n^{N+1} - E_0^N) + i\eta} + \sum_k \frac{\langle \Psi_0^N | c_\beta^\dagger | \Psi_k^{N-1} \rangle \langle \Psi_k^{N-1} | c_\alpha | \Psi_0^N \rangle}{\omega - (E_0^N - E_k^{N-1}) - i\eta} \\
&\equiv \sum_n \frac{z_{\alpha\beta}^{n+}}{\omega - \epsilon_n^+ + i\eta} + \sum_k \frac{z_{\alpha\beta}^{k-}}{\omega - \epsilon_k^- - i\eta},
\end{aligned} \tag{3.2}$$

where the last equation introduces the notation  $z_{\alpha\beta}^{n+}$  as abbreviation for  $\langle \Psi_0^N | c_\alpha | \Psi_n^{N+1} \rangle \langle \Psi_n^{N+1} | c_\beta^\dagger | \Psi_0^N \rangle$  and so on. The energies  $\epsilon_n^+$  and  $\epsilon_k^-$  are the energy differences  $E_n^{N+1} - E_0^N$  and  $E_0^N - E_k^{N-1}$  respectively.

The unperturbed (non-interacting, or free) one-particle propagator is given by:

$$g_{\alpha\beta}^0(\omega) = \delta_{\alpha,\beta} \left( \frac{\theta(\alpha - F)}{\omega - e_\alpha^0 + i\eta} + \frac{\theta(F - \alpha)}{\omega - e_\alpha^0 - i\eta} \right), \tag{3.3}$$

where  $F$  is the highest occupied state (at the Fermi level) in the system and  $e_\alpha$  is the unperturbed energy of the state  $|\alpha\rangle$ . In this case the energy differences between the energy of the state with  $N$  particles and the states with  $N \pm 1$  particles is just the energy of the single-particle state added or removed.

### 3.1.0.1 The spectral function

To study the effects of interactions between the single-particle states, the following representation of the diagonal elements of the single-particle propagator is useful:

$$g_{\alpha\alpha}(\omega) = \int_{-\infty}^{\infty} \frac{d\omega'}{2\pi} \frac{S(\alpha, \omega')}{\omega' - \omega}. \tag{3.4}$$

Here  $S(\alpha, \omega)$  is the spectral function, given by

$$S(\alpha, \omega) = -i \lim_{\eta \rightarrow 0^+} [g_{\alpha\alpha}(\omega + i\eta) - g_{\alpha\alpha}(\omega - i\eta)]. \tag{3.5}$$

The hole part of this is valid for energies  $\omega$  less than the lower Fermi energy  $\epsilon_F^- = E_0^N - E_0^{N-1}$ , and is given by

$$\begin{aligned} S_h(\alpha, \omega) &= \frac{1}{\pi} \text{Im} g_{\alpha\alpha}(\omega) \\ &= \sum_n |\langle \Psi_n^{N-1} | c_\alpha | \Psi_0^N \rangle|^2 \delta(\omega - (E_0^N - E_n^{N-1})). \end{aligned} \quad (3.6)$$

This quantity gives the probability at a given energy  $\omega$  of removing a particle (creating a hole) with quantum numbers  $\alpha$  while leaving the remaining  $N - 1$  particle system at an energy  $E_n^{N-1} = E_0^N - \omega$ . Similarly, the particle part  $S_p(\alpha, \omega)$  is valid for energies  $\omega > \epsilon_F^+ = E_0^{N+1} - E_0^N$ . It is given by

$$\begin{aligned} S_p(\alpha, \omega) &= -\frac{1}{\pi} \text{Im} g_{\alpha\alpha}(\omega) \\ &= \sum_m |\langle \Psi_m^{N+1} | c_\alpha^\dagger | \Psi_0^N \rangle|^2 \delta(\omega - (E_m^{N+1} - E_0^N)), \end{aligned} \quad (3.7)$$

and is the probability for adding a particle with quantum numbers  $\alpha$  to an  $N$ -particle system with energy  $\omega$ , resulting in an  $N + 1$ -system with energy  $E_m^{N+1} = E_0^N + \omega$ .

For a given single-particle state, we can define the occupation number  $n(\alpha)$  and the depletion number  $d(\alpha)$  as

$$n(\alpha) = \langle \Psi_0^N | c_\alpha^\dagger c_\alpha | \Psi_0^N \rangle = \int_{-\infty}^{\epsilon_F^-} d\omega \quad S_h(\alpha, \omega), \quad (3.8)$$

and

$$d(\alpha) = \langle \Psi_0^N | c_\alpha c_\alpha^\dagger | \Psi_0^N \rangle = \int_{\epsilon_F^+}^{\infty} d\omega \quad S_p(\alpha, \omega), \quad (3.9)$$

respectively. It can be shown that  $n(\alpha) + d(\alpha) = 1$ .

In a non-interacting system, choosing the set  $|\alpha\rangle$  determined by the single-particle Hamiltonian  $H_0$  as the basis gives the hole and particle spectral functions a particularly simple form, being delta functions with height 1 at the energies corresponding to the eigenvalues of the single-particle Hamiltonian.

In interacting systems, the spectral functions become smeared out. In principle, the number of poles in the propagator is infinite, giving a continuous distribution of probabilities for the energies of the  $N \pm 1$  particle systems. As long as the independent-particle picture remains relatively correct (that is, if the interactions between the particles are weak), the spectral functions will have sharp peaks at clearly defined energies, which we then identify as single-particle states.

The hole spectral function is relatively easy to compare to experimental data extracted from knock-out ( $e, e'p$ ) reactions in nuclei [26, 27]. In these experiments, an incident fast electron transfers a large amount of energy to a single proton inside the nucleus, sufficient to eject the proton, and the momentum profiles of this proton and the scattered electron are then measured. The most commonly extracted quantity is the so-called spectroscopic factor, defined as

$$S_\alpha = \int d\mathbf{p} |\langle \Psi_n^{N-1} | a_{\mathbf{p}} | \Psi_0^N \rangle|^2, \quad (3.10)$$

where  $a_{\mathbf{p}}$  is a momentum state annihilation operator. In an independent-particle system the spectroscopic factor is either 0 (unoccupied state) or 1 (occupied state). When the spectroscopic factor is less than 1, it can be thought of as measuring the amount of correlation present in the  $N$ -particle system, being the difference between the independent-particle spectroscopic factor of 1 and the measured value.

In our formalism, the spectroscopic factor is given by the height of the spectral function at the energy of the  $|\Psi_n^{N-1}\rangle$  state (this follows from the orthogonality of the basis  $\alpha$ ).

### 3.2 The four-point Green's function

From applying the equation of motion for a Heisenberg operator,  $dc_\alpha(t)/dt = -i[c_\alpha(t), \hat{H}]$  to equation (3.1), one obtains the first step in the Martin-Schwinger hierarchy [95], relating the  $N+1$ -particle propagator to the  $N$ -particle propagator. Thus, relating the two-particle propagator to the one-particle propagator [94]:

$$\begin{aligned} i \frac{\partial}{\partial t} g_{\alpha\beta}(t-t') &= \frac{\partial}{\partial t} \langle \Psi_0^N | \mathcal{T}[a_{\alpha_H}(t) a_{\beta_H}^\dagger(t')] | \Psi_0^N \rangle \\ &= \delta(t-t') \delta_{\alpha,\beta} + \epsilon_\alpha g_{\alpha\beta}(t-t') \\ &\quad + \frac{-i}{2} \sum_{\eta\gamma\sigma} \langle \alpha\eta | V | \gamma\sigma \rangle \langle \Psi_0^N | \mathcal{T}\{c_\eta^\dagger(t) c_\sigma(t) c_\gamma(t) c_\beta^\dagger(t')\} | \Psi_0^N \rangle. \end{aligned} \quad (3.11)$$

This generates a term containing the 4-point Green's function, defined by

$$\begin{aligned} K_{\alpha\beta,\gamma\delta}(t_\alpha, t_\beta; t_\gamma, t_\delta) &= -i \langle \Psi_0^N | \mathcal{T}\{c_\beta(t_\beta) c_\alpha(t_\alpha) c_\gamma^\dagger(t_\gamma) c_\delta^\dagger(t_\delta)\} | \Psi_0^N \rangle \\ &\equiv \langle \alpha\beta | K(t_\alpha, t_\beta; t_\gamma, t_\delta) | \gamma\delta \rangle. \end{aligned} \quad (3.12)$$



Since the 4-point Green's function is antisymmetric under exchange of indices,

$$\begin{aligned} K_{\alpha\beta,\gamma\delta}(t_\alpha, t_\beta; t_\gamma, t_\delta) &= -K_{\beta\alpha,\gamma\delta}(t_\beta, t_\alpha; t_\gamma, t_\delta) = \\ &= -K_{\alpha\beta,\delta\gamma}(t_\alpha, t_\beta; t_\delta, t_\gamma) = K_{\beta\alpha,\delta\gamma}(t_\beta, t_\alpha; t_\delta, t_\gamma) \end{aligned} \quad (3.13)$$

it is possible to define matrix elements of  $K$  between antisymmetric two-particle states as shown in the last equivalence in equation (3.12), provided the time arguments are exchanged at the same time.

Depending on the ordering of the time arguments, the 4-point Green's function describes the propagation of either two-particle (pp), two-hole (hh) or particle-hole (ph) excitations.

The Fourier transform of  $K$  is defined as

$$\begin{aligned} \langle\alpha\beta|K(\omega_\alpha, \omega_\beta, \omega_\gamma, \omega_\delta)|\gamma\delta\rangle &= \\ \int_{-\infty}^{+\infty} dt_\alpha dt_\beta dt_\gamma dt_\delta e^{i\omega_\alpha t_\alpha + i\omega_\beta t_\beta - i\omega_\gamma t_\gamma - i\omega_\delta t_\delta} \langle\alpha\beta|K(t_\alpha, t_\beta; t_\gamma, t_\delta)|\gamma\delta\rangle \end{aligned} \quad (3.14)$$

and the inverse relation as

$$\begin{aligned} \langle\alpha\beta|K(t_\alpha, t_\beta; t_\gamma, t_\delta)|\gamma\delta\rangle &= \\ \frac{1}{(2\pi)^4} \int_{-i\infty}^{+i\infty} d\omega_\alpha d\omega_\beta d\omega_\gamma d\omega_\delta e^{-i\omega_\alpha t_\alpha - i\omega_\beta t_\beta + i\omega_\gamma t_\gamma + i\omega_\delta t_\delta} \langle\alpha\beta|K(\omega_\alpha, \omega_\beta, \omega_\gamma, \omega_\delta)|\gamma\delta\rangle, \end{aligned} \quad (3.15)$$

When the Hamiltonian  $\hat{H}$  is time-independent,  $K$  does not depend on the sum of the time variables, i.e. it is independent of the variable  $t = \frac{1}{4}(t_\alpha + t_\beta + t_\gamma + t_\delta)$ .

### 3.2.1 Feynman diagrams

A very convenient way of expressing the equations of many-body theory is to use graphical representations of the various components, creating diagram equations. The exact rules for translating between diagram and algebraic expression varies somewhat depending on the underlying theory, but most have a number of essential elements in common. We will give a short summary of the rules employed in this thesis. The basic building blocks are interactions, represented by a horizontal line (dotted, wavy or thick-lined) connected by vertical particle/hole lines, as in the example diagrams shown in figure 3.1. The translation of the interaction lines are as matrix elements, the convention for numbering the incoming and outgoing states always being as shown in figure 3.2. Lines are associated with the full propagator, so the parti-

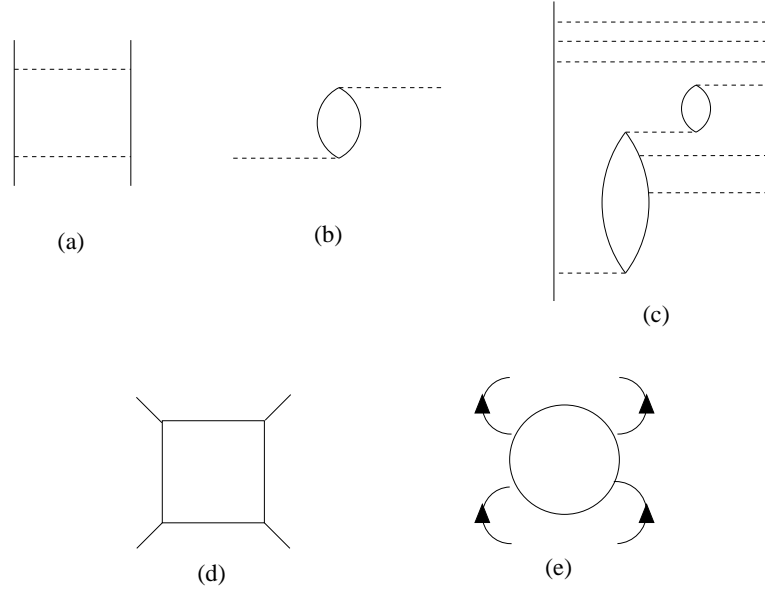


Figure 3.1: The basic ladder diagram (a) (which includes both propagation of two particles and of two holes) the basic ring diagram (b), an example diagram to eighth order in the interaction (c), a composite interaction (d) and a propagator (e), the arrows signifying which states are incoming and which are outgoing in the matrix element of the propagator .

$$\langle 12|V|34 \rangle = \begin{array}{c} 1 \qquad 2 \\ \diagdown \quad \diagup \\ \text{---} \text{---} \text{---} \\ \diagup \quad \diagdown \\ 3 \qquad 4 \end{array}$$

Figure 3.2: The convention for numbering the legs of an interaction.

cle/hole lines can be translated as either particle or hole propagators, each diagram giving rise to two Goldstone diagrams. A diagram with two parallel lines corresponds to two (skeleton) Goldstone diagrams, one with two particles and one with two holes propagating. A ring-like structure translates into a particle-hole pair. When combined, one of the two-particle/two-hole parallel lines might sometimes be part of a larger particle-hole bubble, and for aesthetic reasons no longer straight. No ambiguity should arise from this. Matrix elements of more complex operators than a simple interaction are represented as either rectangles (composite interactions) or circles (propagators), all conforming to the same numbering convention as the interaction matrix elements (figure 3.2). In some diagrams we will use arrows on the internal lines. These are intended as a graphical means of showing which states are incoming and

which are outgoing in the matrix elements of each operator, and thus have no separate physical translation.

### 3.2.2 The interaction operator

Using standard many-body perturbation techniques [93], we can obtain a diagrammatic expansion for the four-point propagator in equation (3.12). We see that there are two classes of contributions, one unconnected class in which two different particle lines propagate without any interaction between each other, and a second group where the particle lines are connected by interaction lines. In figure 3.3 we sketch in a schematic way the two classes.

The four-point interaction vertex  $\Gamma^{4\text{-pt}}$  is called the interaction operator, defined as all two-line irreducible diagrams with fully renormalized propagators. To lowest order,  $\Gamma^{4\text{-pt}}$  is identical to the two-body interaction  $V$ . To make the expressions a little more readable, we will henceforth use roman numerals on the incoming and outgoing states, and Greek letters for intermediate states. We can then express the diagram for  $K$  given in figure 3.3 in terms of the four-point interaction vertex  $\Gamma^{4\text{-pt}}$  as:

$$\begin{aligned} \langle 12|K(t_1, t_2; t_3, t_4)|34\rangle &= i[g_{13}(t_1 - t_3)g_{24}(t_2 - t_4) - g_{14}(t_1 - t_4)g_{23}(t_2 - t_3)] \\ &\quad - \int dt_\alpha \int dt_\beta \int dt_\gamma \int dt_\delta \sum_{\alpha\beta\gamma\delta} g_{1\alpha}(t_1 - t_\alpha)g_{2\beta}(t_2 - t_\beta) \\ &\quad \times \langle \alpha\beta|\Gamma^{4\text{-pt}}(t_\alpha, t_\beta; t_\gamma, t_\delta)|\gamma\delta\rangle g_{\gamma 3}(t_\gamma - t_3)g_{\delta 4}(t_\delta - t_4). \end{aligned} \quad (3.16)$$

We define the Fourier transform of the interaction operator as

$$\begin{aligned} \langle \alpha\beta|\Gamma^{4\text{-pt}}(\omega_\alpha, \omega_\beta, \omega_\gamma, \omega_\delta)|\gamma\delta\rangle &\equiv \\ \int dt_\alpha \int dt_\beta \int dt_\gamma \int dt_\delta e^{i\omega_\alpha t_\alpha} e^{i\omega_\beta t_\beta} e^{-i\omega_\gamma t_\gamma} e^{-i\omega_\delta t_\delta} &\langle \alpha\beta|\Gamma^{4\text{-pt}}(t_\alpha, t_\beta, t_\gamma, t_\delta)|\gamma\delta\rangle. \end{aligned} \quad (3.17)$$

If the bare interaction is time-independent, it does not depend on the energy, and consequently the interaction operator conserves energy and depends only on the incoming energies.

The Fourier transform of the four-point Green's function can be written as

$$\begin{aligned} \langle 12|K(\omega_1, \omega_\beta, \omega_3, \omega_4)|34\rangle &= 2\pi i\delta(\omega_1 + \omega_2 - \omega_3 - \omega_4) \\ &\quad \times [2\pi\delta(\omega_1 - \omega_3)g_{13}(\omega_1)g_{24}(\omega_2) - 2\pi\delta(\omega_1 - \omega_4)g_{14}(\omega_1)g_{23}(\omega_2)] \\ &\quad - \sum_{\alpha\beta\gamma\delta} g_{1\alpha}(\omega_1)g_{2\beta}(\omega_2)\langle \alpha\beta|\Gamma^{4\text{-pt}}(\omega_\alpha, \omega_\beta, \omega_\gamma, \omega_\delta)|\gamma\delta\rangle g_{\gamma 3}(\omega_3)g_{\delta 4}(\omega_4). \end{aligned} \quad (3.18)$$

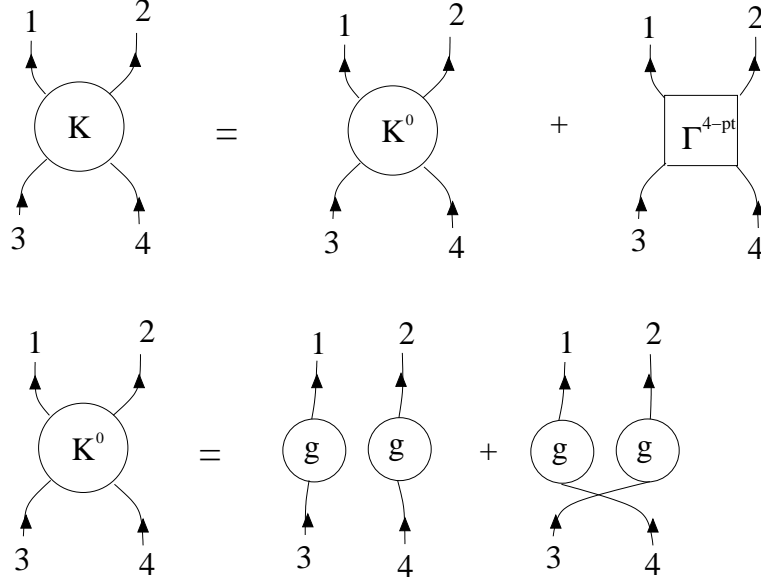


Figure 3.3: The four-point Green's function  $K$ , separated into a set of unconnected diagrams  $K^0$  and a set of connected diagrams. The unconnected diagrams can be summarized as consisting of two unconnected fully renormalized propagators and their exchange contributions, as shown in the lower equation. As stated in the rules described in section 3.2.1, a line indicates the result of a Wick contraction, depending on the time ordering this could be either a particle or a hole. The arrows on the lines are meant to clarify the relationship between the matrix elements and the pictorial description, and does not distinguish particles from holes, any of the lines could be of either type.

We call the first part of the four-point propagator (the first term in equation (3.16)) for the non-interacting or free four-point propagator. It consists of a product of two one-particle propagators. From the above expression we see that the Fourier transform of the non-interacting four-point propagator  $K^0$  is given by:

$$\begin{aligned} \langle 12 | K^0(\omega_1, \omega_2, \omega_3, \omega_4) | 34 \rangle &= 2\pi i \delta(\omega_1 + \omega_2 - \omega_3 - \omega_4) \\ &\times [2\pi \delta(\omega_1 - \omega_3) g_{13}(\omega_1) g_{24}(\omega_2) - 2\pi \delta(\omega_1 - \omega_4) g_{14}(\omega_1) g_{23}(\omega_2)]. \end{aligned} \quad (3.19)$$

### 3.3 Self energy

To find an expression for the one-particle propagator, we once again use standard many-body perturbation techniques [7, 84, 93]. This gives the Dyson equation, giving a decomposition of the propagator in terms of the irreducible

self energy  $\Sigma$  (also called the proper self energy or the mass operator):

$$g_{\alpha\beta}(\omega) = g_{\alpha\beta}^0(\omega) + \sum_{\gamma\delta} g_{\alpha\gamma}^0(\omega) \Sigma(\gamma, \delta; \omega) g_{\delta\beta}(\omega). \quad (3.20)$$

The self energy is the one-line irreducible diagrammatic insertions to the one-particle propagator, as shown in the diagrammatic representation of the Dyson equation in figure 3.4. By iterating on this we generate the exact one-particle propagator, provided the exact irreducible self-energy can be found. This is unfortunately in general not possible.

A small selection of the self energy diagrams is shown in figure 3.5. In terms of diagrams, a one-particle propagator including self-energy insertions is called a dressed propagator, often drawn as a double line. In the case of our Parquet diagrams, however, all propagators are dressed, and for the sake of simplicity, we have chosen to draw them as single lines nonetheless. Exceptions, as in the case of the self energy diagrams just referred to, are noted in the figure captions. We can find a useful relation between the self

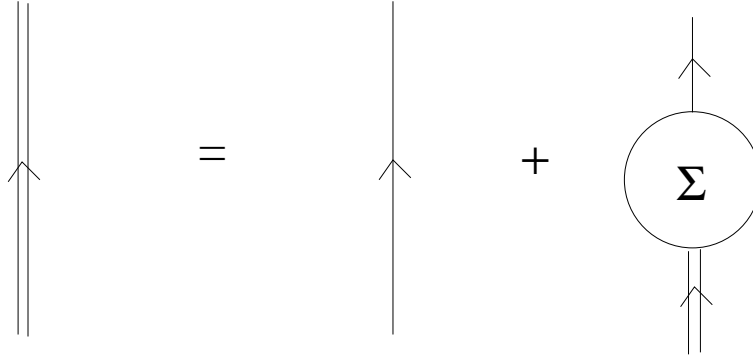


Figure 3.4: The diagrammatic representation of the Dyson equation. The single line represent the unperturbed propagator, the double line represents the full (dressed) propagator.

energy and the interaction operator  $\Gamma^{4\text{-pt}}$  from the equation of motion of the one-particle propagator given in equation (3.11). Inserting the expression in

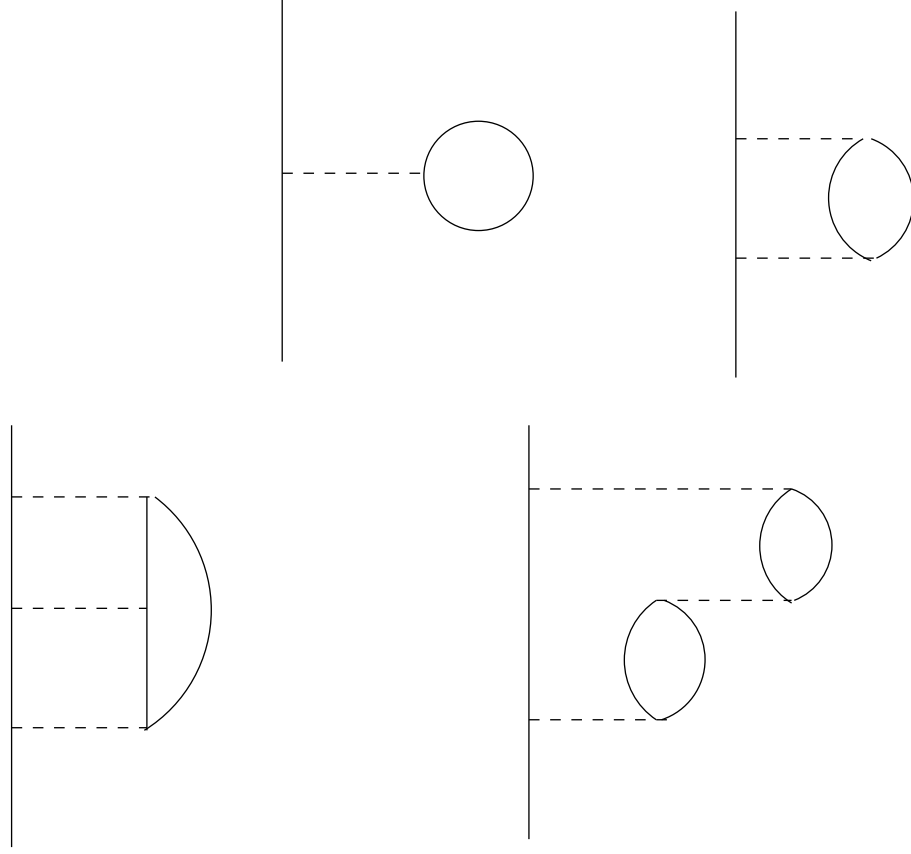


Figure 3.5: A few of the infinitely many self energy diagrams. The propagators are here the non-interacting propagators.

equation (3.16) for the 4-point propagator, we obtain:

$$\begin{aligned}
 i \frac{\partial}{\partial t} g_{12}(t-t') &= \delta(t-t') \delta_{12} + \epsilon_1 g_{12}(t-t') - i \sum_{\alpha\beta\gamma} \langle 1\alpha | V | \beta\gamma \rangle g_{\beta\alpha}(t-t^+) g_{\gamma 2}(t-t') \\
 &+ \frac{1}{2} \sum_{\alpha\beta\gamma} \sum_{\delta\xi\mu\nu} \int dt_\delta \int dt_\xi \int dt_\mu \int dt_\nu g_{\gamma\delta}(t-t_\delta) g_{\beta\xi}(t-t_\xi) g_{\nu\alpha}(t_\nu-t) \\
 &\times \langle \delta\xi | \Gamma^{4\text{-pt}}(t_\delta, t_\xi, t_\mu, t_\nu) | \mu\gamma \rangle g_{\mu 2}(t_\mu-t').
 \end{aligned} \tag{3.21}$$

Taking the Fourier transform of the above expression and performing some algebra, see Ref. [7], we arrive at an expression for the one-particle propagator

which is identical to the Dyson equation, provided we make the identification

$$\begin{aligned} \Sigma(1, 2; \omega) = & -i \int_{C\uparrow} \frac{d\omega_1}{2\pi} \sum_{\alpha\beta} \langle 1\alpha | V | 2\beta \rangle g_{\alpha\beta}(\omega_1) \\ & + \frac{1}{2} \int \frac{d\omega_1}{2\pi} \int \frac{d\omega_2}{2\pi} \sum_{\alpha\beta\gamma\delta\mu\nu} \langle 1\alpha | V | \beta\gamma \rangle g_{\beta\delta}(\omega_1) g_{\gamma\mu}(\omega_2) \\ & \times \langle \delta\mu | \Gamma^{4\text{-pt}}(\omega_1, \omega_2, \omega, \omega_1 + \omega_2 - \omega) | 2\nu \rangle g_{\nu\alpha}(\omega_1 + \omega_2 - \omega). \end{aligned} \quad (3.22)$$

Here the integral in the first expression is a contour integral along the real axis to be closed in the upper half plane, as indicated by the  $C \uparrow$  subscript. The expression for  $\Sigma$  is shown diagrammatically in figure 3.6. Equations (3.18) and

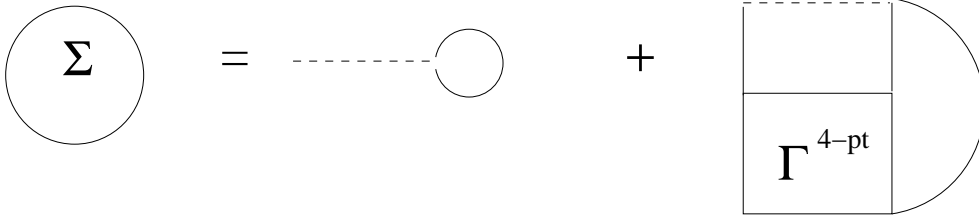


Figure 3.6: The self energy  $\Sigma$  expressed by the interaction operator  $\Gamma^{4\text{-pt}}$ . The propagators are dressed propagators.

(3.22) together with the Dyson equation (3.20) give the exact description of the one-particle propagator if the single particle propagators in the interaction operator are dressed, that is, the self energy insertions are included. This gives a set of non-linear equations, and any solution procedure needs to include some sort of self-consistency scheme, as will be further discussed in sections 4.3 and 4.4.

### 3.3.1 The Hartree-Fock approximation

The easiest approximation possible is to ignore the interaction operator  $\Gamma^{4\text{-pt}}$  altogether, and perform a self-consistent computation using only the first term in equation (3.22). This is the mean-field or Hartree-Fock (HF) approximation. At this level of approximation, the concept of quasi-particles is well-defined, that is, solving the Hartree-Fock equations for a given nucleus yields a spectrum of states each with specific energy and angular momentum. In more detail, the HF self energy is defined as

$$\Sigma_{HF}(\alpha, \beta) = -i \int_{C\uparrow} \frac{d\omega}{2\pi} \sum_{\gamma\delta} \langle \alpha\gamma | V | \beta\delta \rangle g_{\gamma,\delta}(\omega). \quad (3.23)$$

This is an energy-independent self-energy correction, which makes the Dyson equation a simple linear eigenvalue equation, equivalent to an independent-particle problem. The HF energies of the system is determined by solving the Dyson equation self-consistently (self-consistent since the one-body density matrix for each particle depends on the HF energies of the system). The Hartree-Fock approximation is discussed in all standard many-body textbooks, see for example the sources mentions in the beginning of this chapter for further information.

### 3.4 The eigenvalue equation method

We can write the Dyson equation, see again equation (3.20), as a matrix equation using the notation  $[g]$  as shorthand for the matrix with  $g_{\alpha\beta}$  with indices  $\alpha, \beta$ . Assuming the unperturbed propagator to be diagonal, with the inverse given as  $[g^0]^{-1} = \omega - [e]$ , the Dyson equation can be generically written as

$$[g(\omega)] = [\omega \cdot \mathbf{1} - ([e] + [\Sigma(\omega)])]^{-1}, \quad (3.24)$$

where  $e_\alpha$  represents the energies of the unperturbed Hamiltonian,  $[e]$  being a diagonal matrix with  $e_\alpha$  at the diagonal entries. From this we see that the poles of the propagator are the roots  $\omega_\lambda$  of the equation

$$([e] + [\Sigma(\omega_\lambda)])|\lambda\rangle = \omega_\lambda|\lambda\rangle. \quad (3.25)$$

Recalling the Lehmann representation of the propagator, see equation (3.2), we can identify these roots as the energies of the  $N \pm 1$  systems. The residue matrix  $[S_\lambda]$  of the propagator at the pole  $\omega_\lambda$  is given by [7]:

$$[S_\lambda] = \lim_{\omega \rightarrow \omega_\lambda} (\omega - \omega_\lambda)[g(\omega)] = \frac{1}{1 - \langle \tilde{\lambda} | [\Sigma'(\omega_\lambda)] | \lambda \rangle} |\lambda\rangle \langle \tilde{\lambda}| = s_\lambda |\lambda\rangle \langle \tilde{\lambda}|. \quad (3.26)$$

The eigenstate  $\langle \tilde{\lambda}|$  is the corresponding left eigenstate of the operator in equation (3.25). The left and right eigenstates are assumed to be normalized according to

$$\langle \tilde{\lambda} | \lambda \rangle = 1. \quad (3.27)$$

We assume that the propagator has only simple poles, the expression for the degenerate case is somewhat more involved. Now we can write the propagator as

$$[g(\omega)] = \sum_{\lambda} \frac{[S_\lambda]}{\omega - \omega_\lambda}. \quad (3.28)$$



The eigenvalue equation (3.25) is more complicated than an ordinary eigenvalue equation, as  $\Sigma$  depends on the energy and has to be calculated at the unknown eigenvalue. There is no longer only one solution, but a set of different  $\omega_\lambda$  which can be quite large (depending on the number of poles in  $\Sigma$ ). Physically, this means that adding or removing one particle from the ground state no longer leaves the system in one definite state, rather there are several possible states, each with its own amplitude. The sum over these are still unity. The independent-particle model is no longer appropriate, however, calculations show that at least for nuclear system, much of the single-particle strength is still concentrated in a single state for states close to the Fermi energy. States further away, either deep down in the nuclear well or high up, closer to the continuum, get smeared out and cannot properly be called single-particle states any more.

From the one-body propagator it is possible to find the energy of the ground state by using the so-called Migdal-Galitski-Koltun sum rule [7]:

$$\begin{aligned} E_0^A &= \langle \Psi_0^A | \hat{H} | \Psi_0^A \rangle \\ &= \frac{1}{2} \sum_{\alpha\beta} \langle \alpha | T | \beta \rangle \sum_{\lambda < \lambda_F} s_\lambda \langle \alpha | \lambda \rangle \langle \tilde{\lambda} | \beta \rangle + \frac{1}{2} \sum_{\alpha\beta} \sum_{\lambda < \lambda_F} s_\lambda \langle \alpha | \lambda \rangle \langle \tilde{\lambda} | \beta \rangle \omega_\lambda. \end{aligned} \quad (3.29)$$

In an infinite system this takes the form:

$$E_0^A = \frac{1}{2} \int_{-\infty}^{\epsilon_F^-} d\omega \sum_{\alpha\beta} (\langle \alpha | T | \beta \rangle + \omega \delta_{\alpha\beta}) \frac{1}{\pi} \text{Im} g_{\beta\alpha}(\omega). \quad (3.30)$$



## 4 Parquet summation of diagrams

The formalism presented in the previous chapter requires calculations of several infinite sums, and thus we need some procedure to handle these. The Parquet method offers an approximation to the interaction operator  $\Gamma^{4\text{-pt}}$  which includes a large, infinite subset of the full set of diagrams.

To proceed further, we observe that there are different possibilities for reducing this four-time operator down to a two-time operator. Depending on the physical system in question, reductions to a ladder-type or a ring-type operator has been used to include either pphh or ph correlations respectively. However, as argued by Jackson and Wettig, [37], neither of these approaches meet some basic requirements of a many-body theory to be certain of convergence. These authors have further argued that a necessary (but perhaps not sufficient) condition for any many-body summation of diagram to converge, is that both pp ladders and ph chains be summed to all orders.

A Green's function based approach like the Faddeev random-phase approximation of Barbieri and co-workers, see for example [1, 6], couples ladder diagrams and ring diagrams to all orders for the self-energy. The Parquet method offers a method of doing this in a fairly straightforward manner and includes more complicated pphh correlations.

In this chapter we first discuss the principle behind the Parquet theory, namely the different channels in which iterative expressions for the interaction operator can be found (section 4.1). Then we discuss the possible two-time reductions of the four-point propagators in section 4.2. In section 4.3 the Parquet equations are given in a form suitable for numerical implementations, discussed in section 4.4.

## 4.1 Channels: Equivalent ways of building the interaction operator

We can obtain iterative expressions for the interaction operator defined in section 3.2.2 by examining it order by order. To first order, it is just the bare interaction. Next order consists of two bare interactions connected by the non-interacting propagator  $K^0$ , third order is found by connecting a third interaction by another  $K^0$ , and so on. There are three equivalent ways of connecting the legs of the interactions, as shown in figure 4.3. We name the different possibilities according to the numbering discussed in section 3.2.1, for easy reference we repeat the figure 3.2 in figure 4.1. Thus, if we connect legs 1 and 2 we are in the [12] channel or particle-particle channel, while connecting legs 1 and 3 or legs 1 and 4 give the [13] channel or the [14] channel, respectively. These two latter channels are called the particle-hole channels. The [12], [13] and [14] channels are the equivalents of the Mandelstam variables  $s, t$  and  $u$  from relativistic quantum mechanics [93]. A diagram contributing



Figure 4.1: Convention for numbering the legs of an interaction.

to the interaction operator  $\Gamma^{4\text{-pt}}$  either can or cannot be split into two disconnected parts, one containing the legs 1 and 2 and the other the legs 3 and 4 by cutting two internal lines. If this splitting is impossible, the diagram is said to be simple in the [12] channel, if it is possible, the diagram is called non-simple. The particle-particle interaction  $\mathcal{V}^{12}$  is defined as the sum over all the [12]-simple diagrams. It is easily seen that the full interaction operator  $\Gamma^{4\text{-pt}}$  is obtained by iterating over  $\mathcal{V}^{12}$ , as shown in the first line of figure 4.3, where the dash-dot line represents an [12]-simple interaction. The equation for the vertex translates into the well-known Bethe-Salpeter equation:

$$\begin{aligned} \langle 12 | \Gamma^{4\text{-pt}}(\omega_1, \omega_\beta, \omega_3, \omega_4) | 34 \rangle &= \langle 12 | \mathcal{V}^{12}(\omega_1, \omega_2, \omega_3, \omega_4) | 34 \rangle \\ &+ \frac{1}{2} \int \frac{d\omega_\alpha}{2\pi} \int \frac{d\omega_\beta}{2\pi} \int \frac{d\omega_\gamma}{2\pi} \int \frac{d\omega_\delta}{2\pi} \sum_{\alpha\beta\gamma\delta} \langle 12 | \mathcal{V}^{12}(\omega_1, \omega_2, \omega_\alpha, \omega_\beta) | \alpha\beta \rangle \\ &\times \langle \alpha\beta | K^0(\omega_\alpha, \omega_\beta, \omega_\gamma, \omega_\delta) | \gamma\delta \rangle \langle \gamma\delta | \Gamma^{4\text{-pt}}(\omega_\gamma, \omega_\delta, \omega_3, \omega_4) | 34 \rangle. \end{aligned} \quad (4.1)$$

The factor  $\frac{1}{2}$  stems from the symmetry of the interaction with respect to the exchange of indices.

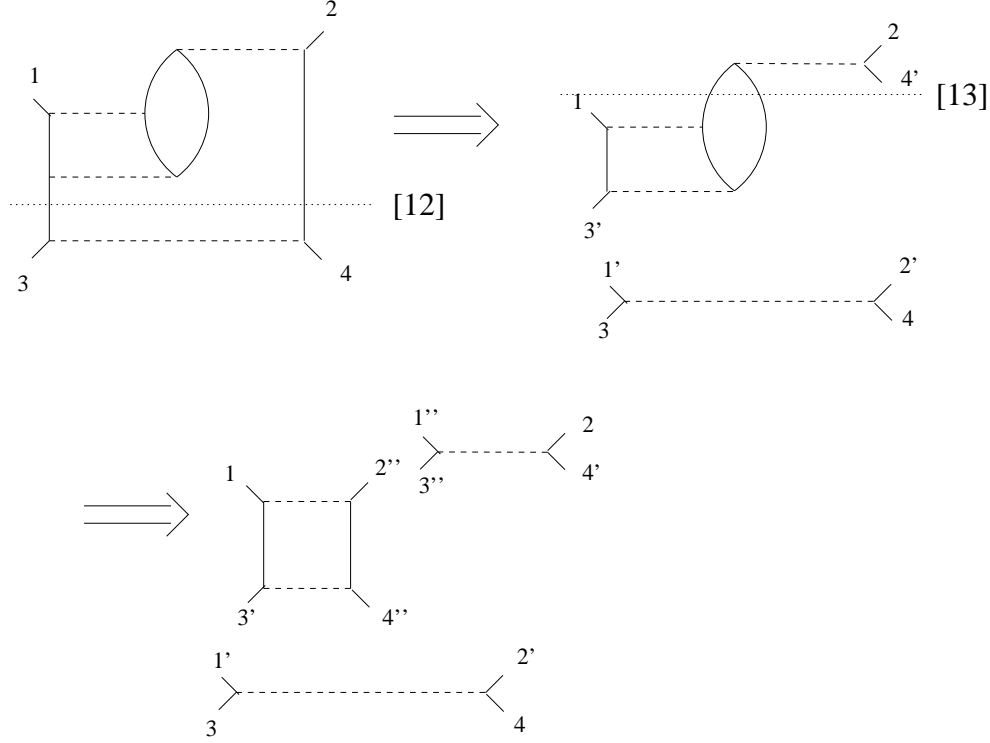


Figure 4.2: Example diagram broken down into components. The original diagram is non-simple in the [12] channel and can be split into two parts by cutting two internal lines in such a manner that one part contains legs 1 and 2 and the other legs 3 and 4. The results are both simple in the [12] channel. The upper part is non-simple in the [13] channel, and can be split into two parts, one containing legs 1 and 3', the other 2 and 4'. Both these are simple in the [12] channel. The final composite diagram is non-simple in the [12] channel.

Similarly, we define the particle-hole interaction  $\mathcal{V}^{13}$  as the sum over all diagrams which are simple in the [13] channel, that is, all diagrams that cannot be split into one part containing the external lines 1 and 3, and another containing the lines 2 and 4. The particle-hole interaction  $\mathcal{V}^{14}$  is defined as the sum over all [14]-simple diagrams (diagrams which cannot be split into one part containing the external lines 1 and 4, and another containing the lines 2 and 3). An example diagram and the splitting of different components is shown in figure 4.2.

Each of these will give the full interaction operator if we iterate as shown in figure 4.3, where the dash-dot-dot (large dot) line represents an [13]-simple ([14]-simple) interaction. The Bethe-Salpeter equations corresponding to these

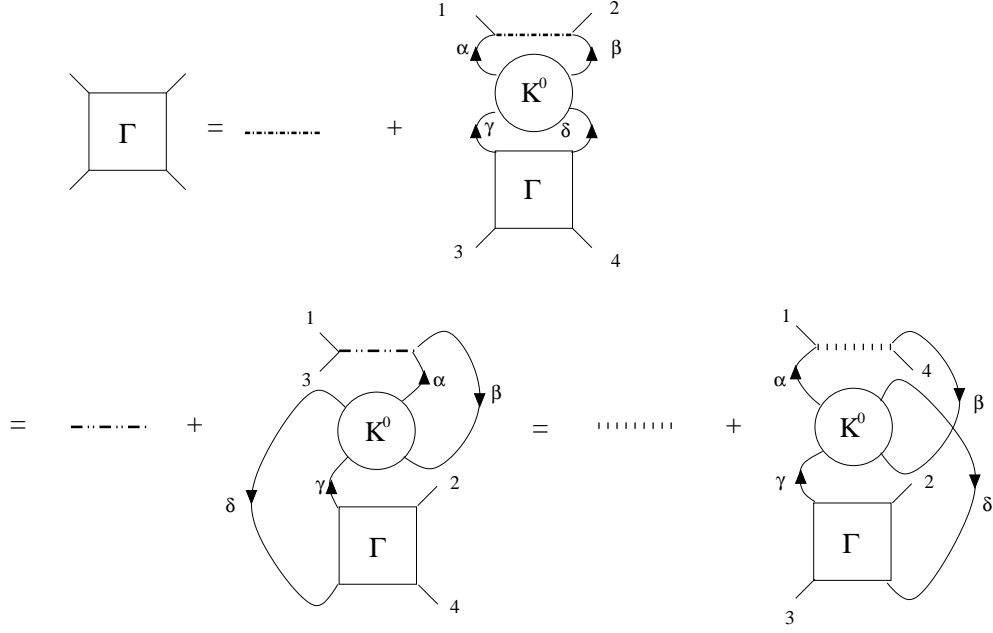


Figure 4.3: Iterative expressions for  $\Gamma^{4\text{-pt}}$  in the [12]-channel, the [13]-channel and the [14]-channel. The internal arrows determine which states are incoming and which are outgoing in the matrix elements of each operator.

diagrams are

$$\begin{aligned}
\langle 12 | \Gamma^{4\text{-pt}}(\omega_1, \omega_2, \omega_3, \omega_4) | 34 \rangle &= \langle 12 | \mathcal{V}^{13}(\omega_1, \omega_2, \omega_3, \omega_4) | 34 \rangle \\
&+ \int \frac{d\omega_\alpha}{2\pi} \int \frac{d\omega_\beta}{2\pi} \int \frac{d\omega_\gamma}{2\pi} \int \frac{d\omega_\delta}{2\pi} \sum_{\alpha\beta\gamma\delta} \langle 1\beta | \mathcal{V}^{13}(\omega_1, \omega_\beta, \omega_3, \omega_\alpha) | 3\alpha \rangle \\
&\times \langle \delta\alpha | K^0(\omega_\delta, \omega_\alpha, \omega_\gamma, \omega_\beta) | \gamma\beta \rangle \langle \gamma 2 | \Gamma^{4\text{-pt}}(\omega_\gamma, \omega_2, \omega_\delta, \omega_4) | \delta 4 \rangle. \quad (4.2)
\end{aligned}$$

and

$$\begin{aligned}
\langle 12 | \Gamma^{4\text{-pt}}(\omega_1, \omega_\beta, \omega_3, \omega_4) | 34 \rangle &= \langle 12 | \mathcal{V}^{14}(\omega_1, \omega_2, \omega_3, \omega_4) | 34 \rangle \\
&+ \int \frac{d\omega_\alpha}{2\pi} \int \frac{d\omega_\beta}{2\pi} \int \frac{d\omega_\gamma}{2\pi} \int \frac{d\omega_\delta}{2\pi} \sum_{\alpha\beta\gamma\delta} \langle 1\beta | \mathcal{V}^{14}(\omega_1, \omega_\beta, \omega_\alpha, \omega_4) | \alpha 4 \rangle \\
&\times \langle \alpha\delta | K^0(\omega_\alpha, \omega_\delta, \omega_\gamma, \omega_\beta) | \gamma\beta \rangle \langle \gamma 2 | \Gamma^{4\text{-pt}}(\omega_\gamma, \omega_2, \omega_3, \omega_\delta) | 3\delta \rangle. \quad (4.3)
\end{aligned}$$

Combining the information in these three equations, we see that the diagrams of  $\Gamma^{4\text{-pt}}$  fall into four classes. One class of diagrams consists of diagrams that are simple in any of the three channels, that is, these diagrams cannot be cut

into two separate pieces by cutting any two lines. The lowest-order member of this class is the bare interaction, and the next is of fifth order in the bare interaction, shown in figure 4.4. We call this class  $I$ . In our calculations we will only include the first term in this series, that is,  $I = V$ .

Then there is the class of diagrams which are simple in the [12] channel, generated by repeated iterations of the type shown in equation (4.1). We call this class the  $L$  diagrams. The conventional ladder diagrams is a subset of this class. In terms of the  $\mathcal{V}^{12}$  interaction, we have that

$$\begin{aligned} \langle 12|L(\omega_1, \omega_\beta, \omega_3, \omega_4)|34\rangle = \\ \int \frac{d\omega_\alpha}{2\pi} \int \frac{d\omega_\beta}{2\pi} \int \frac{d\omega_\gamma}{2\pi} \int \frac{d\omega_\delta}{2\pi} \sum_{\alpha\beta\gamma\delta} \langle 12|\mathcal{V}^{12}(\omega_1, \omega_2, \omega_\alpha, \omega_\beta)|\alpha\beta\rangle \\ \times \langle \alpha\beta|K^0(\omega_\alpha, \omega_\beta, \omega_\gamma, \omega_\delta)|\gamma\delta\rangle \langle \gamma\delta|\Gamma^{4\text{-pt}}(\omega_\gamma, \omega_\delta, \omega_3, \omega_4)|34\rangle. \end{aligned} \quad (4.4)$$

Then there are the classes which are made from iterations of the types in

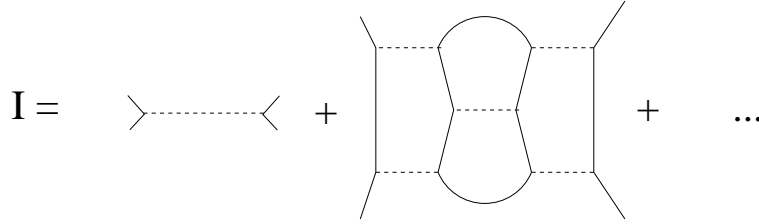


Figure 4.4: The diagram class I, class of diagrams simple in all three channels. The first diagram other than the bare interaction is of fifth order in the interaction. We have included only the first contribution (the bare interaction) in our calculations.

equations (4.2) and (4.3). It is fairly easy to show that each of the diagrams in the [14] channel class have an exchange counterpart in the [13] channel class. Working with antisymmetrized matrix elements in either channel will thus include all diagrams, and only one of the channels need be included in the calculation. We have chosen to work with the [13] channel class, and call this the  $R$  class. The diagrams summed in a standard RPA calculation result in a subset of this class. Expressing  $R$  in terms of  $\mathcal{V}^{13}$  gives

$$\begin{aligned} \langle 12|R(\omega_1, \omega_\beta, \omega_3, \omega_4)|34\rangle = \\ \int \frac{d\omega_\alpha}{2\pi} \int \frac{d\omega_\beta}{2\pi} \int \frac{d\omega_\gamma}{2\pi} \int \frac{d\omega_\delta}{2\pi} \sum_{\alpha\beta\gamma\delta} \langle 1\alpha|\mathcal{V}^{13}(\omega_1, \omega_2, \omega_\alpha, \omega_\beta)|3\beta\rangle \\ \times \langle \delta\alpha|K^0(\omega_\delta, \omega_\alpha, \omega_\gamma, \omega_\beta)|\gamma\beta\rangle \langle \gamma\beta|\Gamma^{4\text{-pt}}(\omega_\gamma, \omega_\beta, \omega_\delta, \omega_4)|\delta 4\rangle. \end{aligned} \quad (4.5)$$

With these definitions we see that the [12]-simple interaction  $\mathcal{V}^{12}$  can be written as the sum  $I + R$  and that the [13]-simple interaction  $\mathcal{V}^{13}$  is the sum  $I + L$ . The total interaction operator can be written as the sum of all three diagram classes:

$$\begin{aligned} \langle 12 | \Gamma^{4\text{-pt}}(\omega_1, \omega_2, \omega_3, \omega_4) | 34 \rangle &= \langle 12 | I(\omega_1, \omega_2, \omega_3, \omega_4) | 34 \rangle \\ &+ \langle 12 | L(\omega_1, \omega_2, \omega_3, \omega_4) | 34 \rangle + \langle 12 | R(\omega_1, \omega_2, \omega_3, \omega_4) | 34 \rangle \\ &\equiv \langle 12 | (I + L + R)(\omega_1, \omega_2, \omega_3, \omega_4) | 34 \rangle. \end{aligned} \quad (4.6)$$

Rewriting Eqs. (4.5) and (4.6) in terms of  $I$ ,  $L$  and  $R$  we obtain

$$\begin{aligned} \langle 12 | L(\omega_1, \omega_2, \omega_3, \omega_4) | 34 \rangle &= \\ &\int \frac{d\omega_\alpha}{2\pi} \int \frac{d\omega_\beta}{2\pi} \int \frac{d\omega_\gamma}{2\pi} \int \frac{d\omega_\delta}{2\pi} \sum_{\alpha\beta\gamma\delta} \langle 12 | (I + R)(\omega_1, \omega_2, \omega_\alpha, \omega_\beta) | \alpha\beta \rangle \\ &\times \langle \alpha\beta | K^0(\omega_\alpha, \omega_\beta, \omega_\gamma, \omega_\delta) | \gamma\delta \rangle \langle \gamma\delta | (I + L + R)(\omega_\gamma, \omega_\delta, \omega_3, \omega_4) | 34 \rangle. \end{aligned} \quad (4.7)$$

and

$$\begin{aligned} \langle 12 | R(\omega_1, \omega_2, \omega_3, \omega_4) | 34 \rangle &= \\ &\int \frac{d\omega_\alpha}{2\pi} \int \frac{d\omega_\beta}{2\pi} \int \frac{d\omega_\gamma}{2\pi} \int \frac{d\omega_\delta}{2\pi} \sum_{\alpha\beta\gamma\delta} \langle 1\alpha | (I + L)(\omega_1, \omega_2, \omega_\alpha, \omega_\beta) | 3\beta \rangle \\ &\times \langle \beta\gamma | K^0(\omega_\alpha, \omega_\beta, \omega_\gamma, \omega_\delta) | \alpha\delta \rangle \langle \delta 2 | (I + L + R)(\omega_\gamma, \omega_\delta, \omega_3, \omega_4) | \gamma 4 \rangle. \end{aligned} \quad (4.8)$$

The three equations (4.6), (4.7) and (4.8) together constitute the Parquet equations. In addition to these, some scheme for treating the self energy consistently has to be made. This is discussed in section 4.3. Furthermore, some simplifications with respect to the energy dependence is needed, as will be discussed below. However, before doing that, we need to introduce some additional notation.

#### 4.1.1 Angular momentum recoupling

To reduce the basis space, it is convenient to introduce an angular-momentum coupled basis, that is, a basis where two single particle states are coupled to total angular momentum  $J$ . Each channel naturally give rise to its own coupling scheme. When necessary we indicate the coupling in the matrix elements as  $\langle 12 | V | 34 \rangle_J$  to signify coupling between states 1 and 2 to total angular momentum  $J$  and  $M$  and so forth. In our harmonic oscillator single-particle basis, the two-particle basis states are independent of  $M$ , giving a huge



reduction in computational complexity. The conventional coupling order in the particle-hole channels is to couple incoming state to outgoing state. This is the same notation as in Ref. [96], see this work for an extensive discussion and examples.

The [12] coupling scheme is the standard coupling scheme. The antisymmetrized two-particle  $J_{[12]}$ -coupled state is given by

$$\begin{aligned} |\overline{12}\rangle &= |(n_1 j_1 l_1 s_1 t_{z1})(n_2 j_2 l_2 s_2 t_{z2})JM\rangle = \\ &= \frac{1}{\sqrt{2}}(1 - (-1)^{j_1+j_2-J}) \sum_{m_1 m_2} \sum_{m_{l1} m_{l2}} \sum_{m_{s1} m_{s2}} \langle j_1 m_1 j_2 m_2 | JM \rangle \langle l_1 m_{l1} s_1 m_{s1} | j_1 m_1 \rangle \\ &\quad \langle l_2 m_{l2} s_2 m_{s2} | j_2 m_2 \rangle |n_1 j_1 m_1 l_1 s_1 t_{z1}\rangle \otimes |n_2 j_2 m_2 l_2 s_2 t_{z2}\rangle, \end{aligned} \quad (4.9)$$

where the  $\langle l_1 m_{l1} s_1 m_{s1} | j_1 m_1 \rangle$  are Clebsch-Gordan coefficients.

Angular momentum algebra gives the following relations between matrix elements with different coupling schemes. [96]:

$$\langle \overline{12} | V | \overline{34} \rangle_J = \sum_{J'} (-1)^{j_1+j_4+J+J'} \hat{J}'^2 \left\{ \begin{matrix} j_3 & j_1 & J \\ j_2 & j_4 & J' \end{matrix} \right\} \langle \overline{12} | V | \overline{34} \rangle_{J'} \quad (4.10)$$

and

$$\langle \overline{12} | V | \overline{34} \rangle_J = \sum_{J'} (-1)^{j_1+j_4+J+J'} \hat{J}^2 \left\{ \begin{matrix} j_3 & j_1 & J \\ j_2 & j_4 & J' \end{matrix} \right\} \langle \overline{12} | V | \overline{34} \rangle_{J'}, \quad (4.11)$$

where  $\hat{J} = \sqrt{2J+1}$ . Similar relations hold between the [14] channel and the other two channels.

We have also found it useful to employ a matrix notation in the [13] channel that allows us to formulate the Parquet equations as matrix equations. We define the  $J_{[13]}$ -coupled matrix element as

$$\langle \widehat{13} | V | \widehat{24} \rangle_J \equiv \langle \overline{12} | V | \overline{34} \rangle_J \quad (4.12)$$

Employing the  $J_{[13]}$ -coupled matrix elements, the equations in the [13]-channel can be rewritten to a form close to matrix equations. The equation for  $R$ , see equation (4.8) becomes

$$\begin{aligned} \langle 12 | R(\omega_1, \omega_2, \omega_3, \omega_4) | 34 \rangle &= \langle \widehat{13} | R(\omega_1, \omega_2, \omega_3, \omega_4) | \widehat{24} \rangle = \\ &= \int \frac{d\omega_\alpha}{2\pi} \int \frac{d\omega_\beta}{2\pi} \int \frac{d\omega_\gamma}{2\pi} \int \frac{d\omega_\delta}{2\pi} \sum_{\alpha\beta\gamma\delta} (\langle \widehat{13} | (I + L)(\omega_1, \omega_2, \omega_\alpha, \omega_\beta) | \widehat{\beta\alpha} \rangle \\ &\quad \times \langle \widehat{\delta\gamma} | K^0(\omega_\delta, \omega_\alpha, \omega_\gamma, \omega_\beta) | \widehat{\alpha\beta} \rangle \langle \widehat{\gamma\delta} | (I + L + R)(\omega_\gamma, \omega_2, \omega_\delta, \omega_4) | \widehat{24} \rangle). \end{aligned} \quad (4.13)$$

This expression is easily transformed into a matrix equation by a suitable transformation of the  $K^0$  matrix. The expressions in the [12]-channel lend themselves to such a formulation immediately with  $J_{[12]}$ -coupled matrix elements.

## 4.2 Two-time propagators

The four-time four-point Green's function can be reduced to a two-time operator by either requiring the “upper” and “lower” times of the diagram be pairwise equal ( $t_3 = t_4$  and  $t_1 = t_2$ ), or by setting the “left-hand” times and the “right-hand” times of the diagram equal, that is,  $t_3 = t_1$  and  $t_4 = t_2$ . The first choice gives rise to the ladder reduction, while the second is the basis for the RPA approach, and we call it the ring (or chain) reduction.

The reduction from the four-point Green's function to different two-time operators corresponds to the reductions of the Bethe-Salpeter equation for relativistic spinors to different non-relativistic equations as the Lippmann-Schwinger-equation [97] or the Blankenbecler-Sugar equation [98].

### 4.2.1 The ladder propagator

The ladder two-time reduction of the four-point Green's function is defined by

$$\begin{aligned}
\langle 12 | \mathcal{G}^{pphh}(t - t') | 34 \rangle &\equiv \lim_{t_2 \rightarrow t} \lim_{t_4 \rightarrow t'} \langle 12 | K(t, t_2, t', t_4) | 34 \rangle \\
&= \lim_{t_2 \rightarrow t} \lim_{t_4 \rightarrow t'} -i \langle \Psi_0^N | \mathcal{T} [c_{2H}(t_2) c_{1H}(t) c_{3H}^\dagger(t') c_{4H}^\dagger(t_4)] | \Psi_0^N \rangle \\
&= i [g_{13}(t - t') g_{24}(t - t') - g_{14}(t - t') g_{23}(t - t')] \\
&\quad - \sum_{\alpha\beta\gamma\delta} \int dt_\alpha \int dt_\beta \int dt_\gamma \int dt_\delta g_{1\alpha}(t - t_\alpha) g_{2\beta}(t - t_\beta) \\
&\quad \times \langle \alpha\beta | \Gamma^{4\text{pt}}(t_\alpha, t_\beta, t_\gamma, t_\delta) | \gamma\delta \rangle g_{\gamma 3}(t_\gamma - t') g_{\delta 4}(t_\delta - t'). \quad (4.14)
\end{aligned}$$

The two-time reductions imply the propagation of either two particles (if  $t > t'$ , giving an intermediate state  $\Psi^{N+2}$ ), or two holes (if  $t < t'$ , the intermediate state then being  $\Psi^{N-2}$ ). For the moment we concentrate on the free part of the propagator, that is, the propagation of two non-interacting particles (as seen from the equations (4.6), (4.7) and (4.8), only this is needed to calculate the Parquet equations). we Fourier transform the first terms of this expression to obtain the free ladder propagator  $\mathcal{G}_0^{pphh}$ . It can be found by

inserting the inverse of the Fourier transform of the four-point Green's function (equation (3.18)) into the expression for the Fourier transform and taking the appropriate limit. Since  $\mathcal{G}_0^{pphh}$  is a function of one time difference only, we expect the Fourier transform to be a function of one energy only. As we will see below, the relevant total energy is the sum of the energy of state 1 and state 2, making coupling in the [12] channel the natural choice for this operator.

$$\begin{aligned}
\langle 12 | \mathcal{G}_0^{pphh}(\Omega) | 34 \rangle &= \int d(t_1 - t_3) e^{i\Omega(t_1 - t_3)} \langle 12 | \mathcal{G}_0^{pphh}(t_1 - t_3) | 34 \rangle = \\
&= \int d(t_1 - t_3) e^{i\Omega(t_1 - t_3)} \lim_{t_2 \rightarrow t_1} \lim_{t_4 \rightarrow t_3} \langle 12 | K_0(t_1, t_2, t_3, t_4) | 34 \rangle \\
&= \int d(t_1 - t_3) e^{i\Omega(t_1 - t_3)} e^{-i(\omega_1 + \omega_2)t_1} e^{i(\omega_3 + \omega_4)t_3} \int \frac{d\omega_1}{2\pi} \int \frac{d\omega_2}{2\pi} \int \frac{d\omega_3}{2\pi} \int \frac{d\omega_4}{2\pi} \\
&2\pi\delta(\omega_1 + \omega_2 - \omega_3 - \omega_4)(i) \left[ 2\pi\delta(\omega_1 - \omega_3)g_{13}(\omega_1)g_{24}(\omega_2) - 2\pi\delta(\omega_1 - \omega_4)g_{14}(\omega_1)g_{23}(\omega_2) \right].
\end{aligned} \tag{4.15}$$

Changing variables in equation 4.15 to  $\Omega = \omega_1 + \omega_2, \omega = \omega_1 - \frac{\omega_1 + \omega_2}{2}, \omega' = \omega_3 - \frac{\omega_1 + \omega_2}{2}$ , we obtain

$$\begin{aligned}
\langle 12 | \mathcal{G}_0^{pphh}(\Omega) | 34 \rangle &= \\
&i \int \frac{d\omega}{2\pi} [g_{13}(\Omega/2 + \omega)g_{24}(\Omega/2 - \omega) - g_{14}(\Omega/2 - \omega)g_{23}(\omega/2 - \omega)]. \quad (4.16)
\end{aligned}$$

To proceed, we insert the expression in equation (3.2) for the one-particle propagator. To ease readability, we use the abbreviation  $z_{\alpha\beta}^{n+}$  for the overlaps  $\langle \Psi_0^N | c_\alpha | \Psi_n^{N+1} \rangle \langle \Psi_n^{N+1} | c_\beta^\dagger | \Psi_0^N \rangle$  and so on. The integrals are simple contour integrals. Of the four terms, two have poles on the same side of the imaginary axis, and we close these on the opposite half plane so that they do not contribute to the integral, leaving two contributions evaluated by using the Residue theorem. Thus we obtain the following expression for the free ladder propagator

$\mathcal{G}_0^{pphh}(\Omega)$ :

$$\begin{aligned}
\langle 12 | \mathcal{G}_0^{pphh}(\Omega) | 34 \rangle &= i \int \frac{d\omega}{2\pi} \\
&\left[ \left( \sum_n \frac{z_{13}^{n+}}{\Omega/2 + \omega - \epsilon_n^+ + i\eta} + \sum_k \frac{z_{13}^{k-}}{\Omega/2 + \omega - \epsilon_k^- - i\eta} \right) \right. \\
&\times \left( \sum_m \frac{z_{24}^{m+}}{\Omega/2 - \omega - \epsilon_m^+ + i\eta} + \sum_l \frac{z_{24}^{l-}}{\Omega/2 - \omega - \epsilon_l^- - i\eta} \right) \Big] \\
&- \left[ \left( \sum_n \frac{z_{14}^{n+}}{\Omega/2 + \omega - \epsilon_n^+ + i\eta} + \sum_k \frac{z_{14}^{k-}}{\Omega/2 + \omega - \epsilon_k^- - i\eta} \right) \right. \\
&\times \left. \left( \sum_m \frac{z_{23}^{m+}}{\Omega/2 - \omega - \epsilon_m^+ + i\eta} + \sum_l \frac{z_{23}^{l-}}{\Omega/2 - \omega - \epsilon_l^- - i\eta} \right) \right] \Big] \\
&= \sum_{nm} \frac{z_{13}^{n+} z_{24}^{m+}}{\Omega - \epsilon_n^+ - \epsilon_m^+ + i\eta'} - \sum_{kl} \frac{z_{13}^{k-} z_{24}^{l-}}{\Omega - \epsilon_k^- - \epsilon_l^- - i\eta'} \\
&\quad + \sum_{nm} \frac{z_{14}^{n+} z_{23}^{m+}}{\Omega - \epsilon_n^+ - \epsilon_m^+ + i\eta'} - \sum_{kl} \frac{z_{14}^{k-} z_{23}^{l-}}{\Omega - \epsilon_k^- - \epsilon_l^- - i\eta'}. \quad (4.17)
\end{aligned}$$

This is a rather involved expression due to the complexity of the single-particle propagator. If we assume that the single-particle propagator only has one pole, that is, it has the structure of the unperturbed propagator in equation (3.3), we obtain a much simpler expression

$$\begin{aligned}
\langle 12 | \mathcal{G}_0^{pphh}(\Omega) | 34 \rangle &= \frac{\delta_{13} \delta_{24} \theta(1-F) \theta(2-F)}{\Omega - \epsilon_1 - \epsilon_2 + i\eta'} - \frac{\delta_{13} \delta_{24} \theta(F-1) \theta(F-2)}{\Omega - \epsilon_1 - \epsilon_2 - i\eta'} \\
&+ \frac{\delta_{14} \delta_{23} \theta(1-F) \theta(2-F)}{\Omega - \epsilon_1 - \epsilon_2 + i\eta'} - \frac{\delta_{14} \delta_{23} \theta(F-1) \theta(F-2)}{\Omega - \epsilon_1 - \epsilon_2 - i\eta'}, \quad (4.18)
\end{aligned}$$

where  $F$  is the Fermi level. When this approximation is done, the effect is to force the system to retain the input single-particle basis structure, that is, no fragmentation occurs. The single-particle energies, however, are not necessarily the same as the energies of the unperturbed Hamiltonian.

### 4.2.2 The ring propagator

We define the particle-hole ring propagator  $\langle 12|\mathcal{G}^{ph}(t-t')|34\rangle$  as the reduction

$$\begin{aligned} \langle 12|\mathcal{G}^{ph}(t-t')|34\rangle &\equiv \lim_{t_4 \rightarrow t} \lim_{t_3 \rightarrow t'} [\langle 12|K(t, t'; t_3, t_4)|34\rangle \\ &\quad - \langle \Psi_0^N | c_4^\dagger(t_4) c_1(t) | \Psi_0^N \rangle \langle \Psi_0^N | c_3^\dagger(t_3) c_2(t') | \Psi_0^N \rangle ] \\ &= \lim_{t_4 \rightarrow t} \lim_{t_3 \rightarrow t'} [-i \langle \Psi_0^N | \mathcal{T}[c_{2H}(t') c_{1H}(t) c_{3H}^\dagger(t') c_{4H}^\dagger(t)] | \Psi_0^N \rangle \\ &\quad - \langle \Psi_0^N | c_4^\dagger(t) c_1(t) | \Psi_0^N \rangle \langle \Psi_0^N | c_3^\dagger(t') c_2(t') | \Psi_0^N \rangle]. \quad (4.19) \end{aligned}$$

The incoming and outgoing states could in principle be any states, as the operator sequence in the propagator ensures that only state combinations of a hole-particle or particle-hole type give a non-zero expectation value. This is perhaps easier seen in a notation closer to the particle-hole formulation. Let  $\bar{\alpha}$  signify the time-reversed state of  $\alpha$ , that is,

$$|\bar{\mathbf{p}}_\alpha, \bar{m}_s\rangle \equiv \mathcal{T}_{\text{time-reversal}} |\mathbf{p}_\alpha, m_s\rangle = (-1)^{\frac{1}{2}+m_s} |-\mathbf{p}_\alpha, -m_s\rangle. \quad (4.20)$$

The phase convention shown is that of Bohr and Mottelson [99] for a particle with momentum  $\mathbf{p}_\alpha$  and spin projection  $m_s$ . The operator sequence in the particle-hole propagator can be written as

$$\langle \Psi_0^N | \mathcal{T}[c_{2H}^\dagger(t_2) c_{1H}(t) c_{3H}^\dagger(t') c_{4H}(t_4)] | \Psi_0^N \rangle, \quad (4.21)$$

and from this it is easy to find the expression for  $\mathcal{G}^{ph}$  in the particle-hole formalism.

The last term in equation (4.19) results from the fact that the exchange part of the propagator closes the diagrams into unconnected ground state energy diagrams, involving the one-body density matrix elements. We do not want to include these in the interaction operator, hence the definition (which in the literature often is called the polarization propagator). The proper exchanges of the interaction operator diagrams are generated automatically when antisymmetrized matrix elements are employed.

If we insert equation (3.16) into the expression for  $\mathcal{G}^{ph}$  in equation (4.19), we obtain  $\mathcal{G}^{ph}$  in terms of the interaction operator  $\Gamma^{4\text{-pt}}$ :

$$\begin{aligned} \langle 12|\mathcal{G}^{ph}(t-t')|34\rangle &= i[g_{13}(t-t')g_{24}(t-t') - g_{14}(t-t')g_{23}(t-t')] \\ &\quad - \sum_{\alpha\beta\gamma\delta} \int dt_\alpha \int dt_\beta \int dt_\gamma \int dt_\delta g_{1\alpha}(t-t_\alpha) g_{2\beta}(t-t_\beta) \\ &\quad \times \langle \alpha\beta | \Gamma^{4\text{-pt}}(t_\alpha, t_\beta, t_\gamma, t_\delta) | \gamma\delta \rangle g_{\gamma 3}(t_\gamma-t') g_{\delta 4}(t_\delta-t'). \quad (4.22) \end{aligned}$$

Looking at the free part of the propagator for the moment, we find the expression for  $\mathcal{G}_0^{ph}$  as a function of energy in a similar manner as for the ladder propagator. This time we define  $\Omega = \omega_1 - \omega_3$ ,  $\omega = \omega_1 - \frac{\omega_1 - \omega_3}{2}$ ,  $\omega' = \omega_2 + \frac{\omega_1 - \omega_3}{2}$ . Then

$$\langle 12 | \mathcal{G}_0^{ph}(\Omega) | 34 \rangle = i \int \frac{d\omega}{2\pi} [g_{13}(\omega + \Omega/2) g_{24}(\omega - \Omega/2)]. \quad (4.23)$$

We then insert the expression for the single particle propagators from equation (3.2) into the above expression, with the same notation for the overlaps as for the  $\mathcal{G}^{pphh}$  calculation. Due to the sign of the energy variable, this time we obtain that the two particle-hole terms survive:

$$\begin{aligned} \langle 12 | \mathcal{G}_0^{ph}(\Omega) | 34 \rangle &= -i \int \frac{d\omega}{2\pi} \left[ \left( \sum_n \frac{z_{13}^{n+}}{\omega + \Omega/2 - \epsilon_n^+ + i\eta} + \sum_k \frac{z_{13}^{k-}}{\omega + \Omega/2 - \epsilon_k^- - i\eta} \right) \right. \\ &\quad \times \left. \left( \sum_m \frac{z_{24}^{m+}}{\omega - \Omega/2 - \epsilon_m^+ + i\eta} + \sum_l \frac{z_{24}^{l-}}{\omega - \Omega/2 - \epsilon_l^- - i\eta} \right) \right] \\ &= \sum_{km} \frac{z_{13}^{k-} z_{24}^{m+}}{\Omega - \epsilon_k^- + \epsilon_m^+ + i\eta'} - \sum_{nl} \frac{z_{13}^{n+} z_{24}^{l-}}{\Omega + \epsilon_l^- - \epsilon_n^+ + i\eta'}. \end{aligned} \quad (4.24)$$

Note the difference in the definition of  $\Omega$  between this expression and the expression for  $\mathcal{G}^{pphh}(\Omega)$ .

Making the approximation that the single-particle propagator has the same structure as the unperturbed propagator in equation (3.3) in the expression for the ring propagator yields

$$\langle 12 | \mathcal{G}_0^{ph}(\Omega) | 34 \rangle = \frac{\delta_{13} \delta_{24} \theta(F-1) \theta(2-F)}{\Omega + \epsilon_2 - \epsilon_1 + i\eta'} - \frac{\delta_{13} \delta_{24} \theta(1-F) \theta(F-2)}{\Omega + \epsilon_2 - \epsilon_1 - i\eta'}. \quad (4.25)$$

### 4.3 Self-consistent Parquet equations

We are now ready to write down the Parquet equations in a formulation suitable for implementations, in our case a formulation which depends only on one energy. In doing this, we make the approximation that the total energy  $\Omega$  is the same in the case of the ladder and ring propagators. The energy-dependence of the interaction can be seen as representing an average incoming energy.

Writing the equation for  $R$  in the [13]-coupled notation given in Equation (4.12), we see that the Parquet equation can be rewritten in a compact

matrix formulation as

$$\begin{aligned}\Gamma(\Omega) &= [I(\Omega)] + [L(\Omega)] + [R(\Omega)], \\ [L(\Omega)] &= [(I + R)(\Omega)] [\mathcal{G}_0^{pphh}(\Omega)] [(I + R + L)(\Omega)], \\ [R(\Omega)] &= [(I + L)(\Omega)] [\mathcal{G}_0^{ph}(\Omega)] [(I + L + R)(\Omega)].\end{aligned}\quad (4.26)$$

The equation for the self energy, given in equation (3.22), connects the self energy with the interaction operator:

$$\begin{aligned}\Sigma(1, 2; \omega) &= -i \int_{C\uparrow} \frac{d\omega_1}{2\pi} \sum_{\alpha\beta} \langle 1\alpha | V | 2\beta \rangle g_{\alpha\beta}(\omega_1) \\ &\quad + \frac{1}{2} \int \frac{d\omega_1}{2\pi} \int \frac{d\omega_2}{2\pi} \sum_{\alpha\beta\gamma\delta\mu\nu} \langle 1\alpha | V | \beta\gamma \rangle g_{\beta\delta}(\omega_1) g_{\gamma\mu}(\omega_2) \\ &\quad \times \langle \delta\mu | \Gamma^{4\text{-pt}}(\omega_1, \omega_2, \omega, \omega_1 + \omega_2 - \omega) | 2\nu \rangle g_{\nu\alpha}(\omega_1 + \omega_2 - \omega).\end{aligned}\quad (4.27)$$

When we approximate the full interaction operator  $\Gamma^{4\text{-pt}}$  in this equation by the Parquet interaction operator  $\Gamma = I + L + R$  given in equation (4.26), we need to check whether we do any double-counting or not. When  $I$  consists of only the bare interaction, Jackson *et al.* [36] have shown that only contributions having the bare interaction  $V$  as a top rung of a ladder term can be included. The other terms lead to double-counting either because they are simply equal to an already included term, or because the diagram is equal to an included term with some self-energy insertion, and therefore must be excluded. Thus the correct propagator is the  $\mathcal{G}_0^{pphh}$  propagator and the correct coupling order is the [12] coupling, resulting in the following equation for the self energy:

$$\begin{aligned}\Sigma(1, 2; \omega) &= -i \int_{C\uparrow} \frac{d\omega'}{2\pi} \sum_{\alpha\beta} \langle 1\alpha | V | 2\beta \rangle g_{\alpha,\beta}(\omega') \\ &\quad + \frac{1}{2} \int \frac{d\omega'}{2\pi} \sum_{\alpha\beta\gamma\delta\mu\nu} \langle 1\alpha | V | \beta\gamma \rangle \langle \beta\gamma | G_0^{pphh}(\omega + \omega') | \delta\mu \rangle \langle \delta\mu | \Gamma(\omega + \omega') | 2\nu \rangle g_{\nu\alpha}(\omega').\end{aligned}\quad (4.28)$$

The single-particle propagator is expressed by the self energy via the Dyson equation (3.20), repeated here for easy reference:

$$g_{\alpha\beta}(\omega) = g_{\alpha\beta}^0(\omega) + \sum_{\gamma\delta} g_{\alpha\gamma}^0(\omega) \Sigma(\gamma, \delta; \omega) g_{\delta\beta}(\omega). \quad (4.29)$$

The propagators  $\mathcal{G}_0^{pphh}$  and  $\mathcal{G}_0^{ph}$  in the Parquet equations 4.26 are expressed by the amplitudes  $z_{\alpha\beta}$  and excitation energies  $\epsilon$  in the single-particle propagator found from solving the Dyson equation, creating complex dependencies which have to be solved iteratively.

### 4.3.1 Diagrams to fourth order

Diagrammatically, all fourth order diagrams of the Parquet contributions to the self energy are shown in figure. 4.5. All diagrams to fourth order for the ladder term are shown in figure 4.6, and for the ring term in Fig. 4.7. The propagators are fully dressed propagators. Iteration by iteration, the diagrams are not generated order by order in the interaction, but rather staggered, all diagrams to fourth order being generated after three iterations.

We can compare the self energy diagrams to fourth order shown in figure 4.5 with the corresponding Goldstone diagrams by closing the diagram by a hole line. Then we find that all Goldstone diagrams to fourth order are generated, in addition to several higher-order contributions as well (we remind the reader that the propagators are dressed, that is, all self energy insertions are included). Thus the Parquet method include ground state energy diagrams to the same level of precision as a coupled-cluster calculation including excitation operators to the fourth order, a CCSDTQ calculation [108].



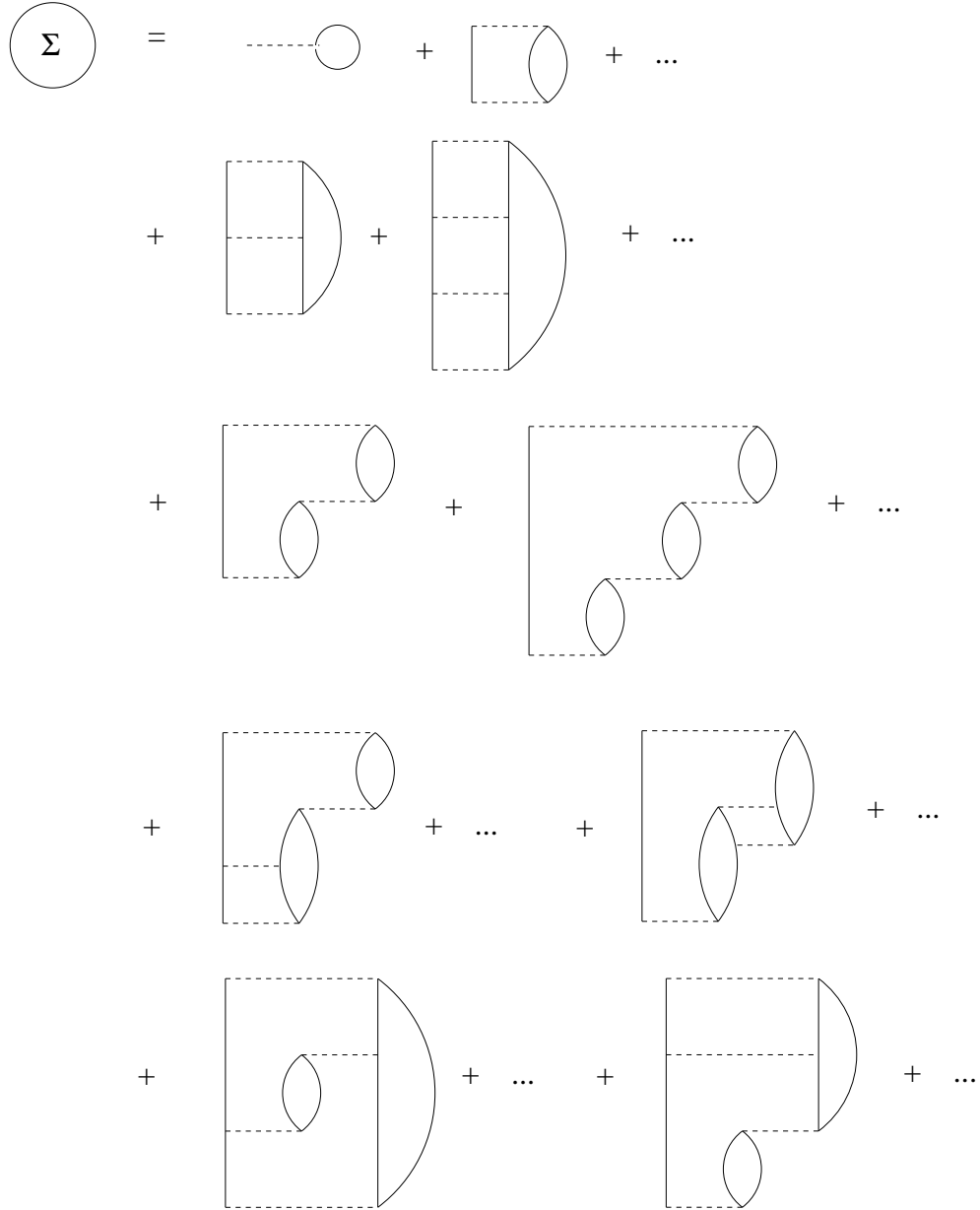


Figure 4.5: The self energy diagrams generated by the Parquet method. All contributions to the fourth order are explicitly drawn. The propagators are dressed propagators.

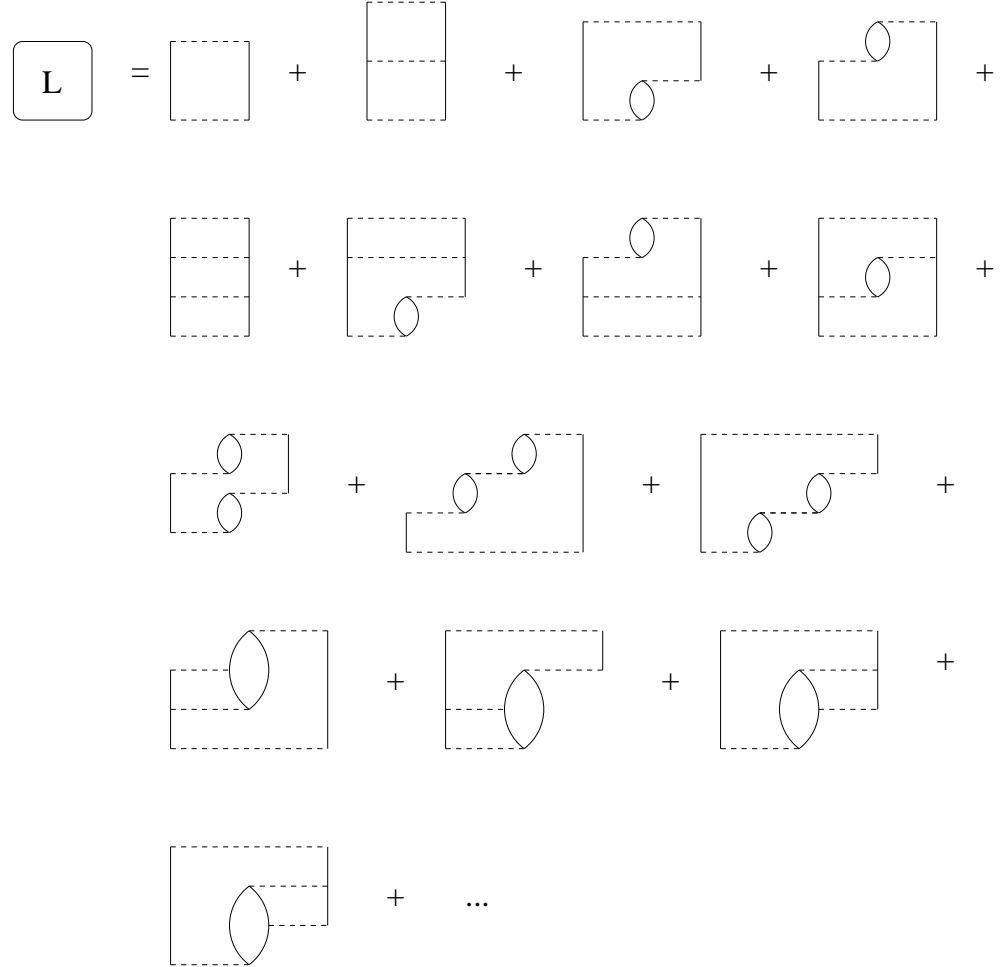


Figure 4.6: The ladder diagrams generated by the Parquet method. All contributions to fourth order are explicitly drawn. The propagators are dressed propagators.

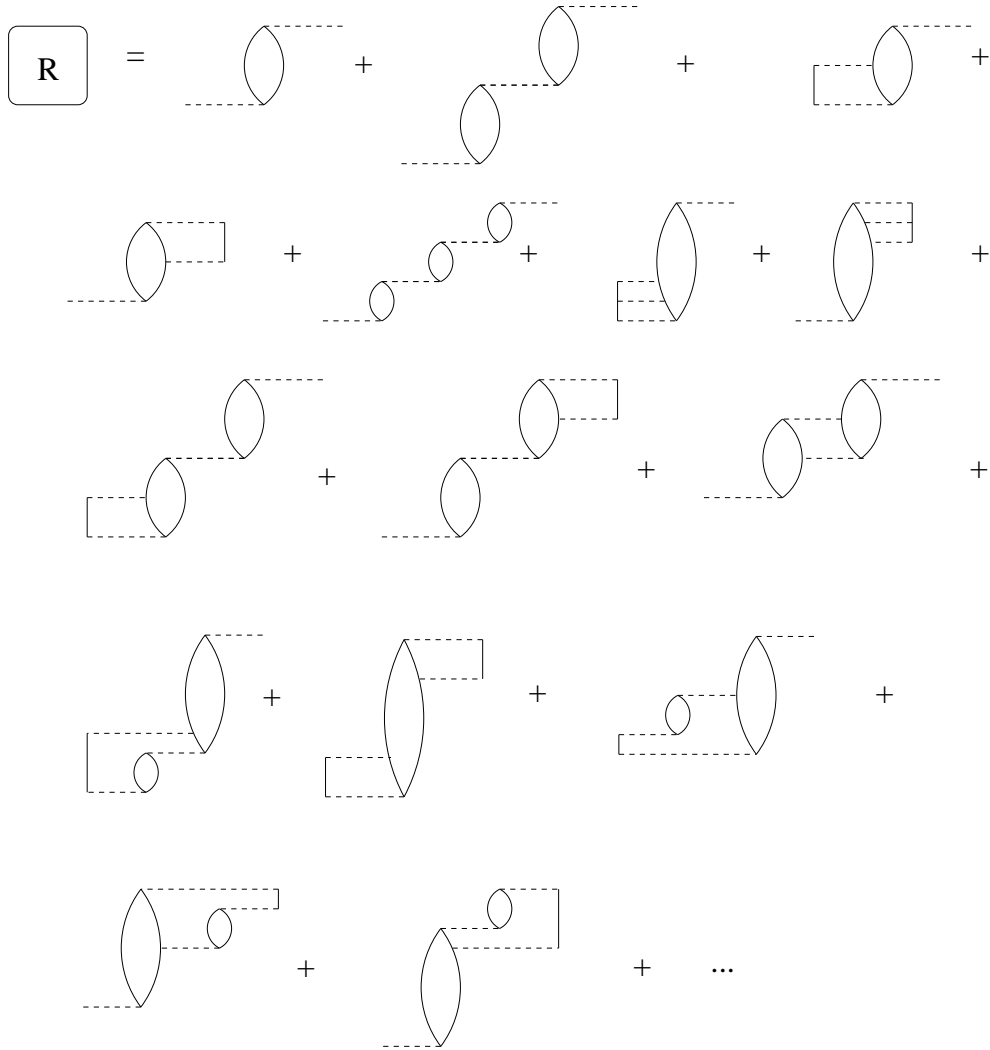


Figure 4.7: The ring diagrams generated by the Parquet method. All contributions to fourth order are explicitly drawn. The propagators are dressed propagators.

### 4.3.2 Matrix inversion method

The equations as described above have been implemented, but we have found severe limitations concerning the stability of the numerical solution, which will be discussed in detail in later chapters. These problems are mainly due to the poles of the propagators, which in turn generate poles in the interaction  $\Gamma$ . The interpolation to the correct input energies in the self energy equations sometimes becomes highly unreliable. To minimize the impact of these poles, we have investigated the following formulation of the Parquet equations employing approximate full propagators rather than the free propagators.

The two-particle propagators can be found by a matrix inversion procedure similar to the method used for the one-particle propagator described in section 3.4. Writing equations (4.14) and (4.22) in matrix form and inserting the resulting expression in equation (4.1) or equation (4.2) for the interaction operator we obtain a Dyson-like equation

$$[\mathcal{G}] = [\mathcal{G}_0] + [\mathcal{G}_0][\Gamma][\mathcal{G}_0] = [\mathcal{G}_0] + [\mathcal{G}_0](\mathcal{V} + [\mathcal{V}][\mathcal{G}_0][\Gamma])[\mathcal{G}_0] = [\mathcal{G}_0] + [\mathcal{G}_0][\mathcal{V}][\mathcal{G}]. \quad (4.30)$$

The interaction  $\mathcal{V}$  is here a generic abbreviation for either the  $\mathcal{V}^{12}$  or the  $\mathcal{V}^{13}$  interactions, simple in the given channel. Similarly,  $\mathcal{G}$  ( $\mathcal{G}_0$ ) is an abbreviation for either  $\mathcal{G}^{pphh}$  or  $\mathcal{G}^{ph}$  ( $\mathcal{G}_0^{pphh}$  or  $\mathcal{G}_0^{ph}$ ). Following the same procedure as for the one-particle case, we find an eigenvalue equation of the form:

$$([E] + [V(\Omega_\Lambda)])|\Lambda\rangle = \Omega_\Lambda|\Lambda\rangle. \quad (4.31)$$

To be able to obtain this eigenvalue equation, we have to assume that the free propagator  $\mathcal{G}^0$  is diagonal. The eigenvalues are seen from the Lehmann representations to be either the excitation energies of the  $N \pm 1$  system (ph case) or of the  $N \pm 2$  system (pphh case). Assuming simple poles, we can write the residue matrix as

$$[S_\Lambda] = \lim_{\Omega \rightarrow \Omega_\Lambda} (\Omega - \Omega_\Lambda)[\mathcal{G}(\Omega)] = \frac{1}{1 - \langle \tilde{\Lambda} | [\mathcal{V}'(\Omega_\Lambda)] | \Lambda \rangle} |\Lambda\rangle \langle \tilde{\Lambda}|, \quad (4.32)$$

and the propagator as

$$[\mathcal{G}(\Omega)] = \sum_{\Lambda} \frac{1}{1 - \langle \tilde{\Lambda} | [\mathcal{V}'(\Omega_\Lambda)] | \Lambda \rangle} \frac{|\Lambda\rangle \langle \tilde{\Lambda}|}{\Omega - \Omega_\Lambda \pm i\eta}. \quad (4.33)$$

In the implementation we make the approximation that the matrix elements of the interactions  $\mathcal{V}^{12}$  and  $\mathcal{V}^{13}$  vary slowly with the energy, so that the derivative in equation (4.32) is set to zero. This is not the case close to a pole, but as

the matrix elements have poles for different energies, the overall effects are hopefully not too large.

We also make an approximation to the eigenvalue equation similar to the single particle case, namely using a fixed energy to find the eigenvalues of equation (4.31), rather than solving the full problem. In the present implementation, this energy is fixed as the energy at which the propagator is to be calculated, the  $\Omega$  defined in equation (4.33). Combining the information in equation (4.30) with the Parquet equations in (4.26), we obtain a new formulation of the latter:

$$\begin{aligned} [\Gamma(\Omega)] &= [I(\Omega)] + [L(\Omega)] + [R(\Omega)], \\ [L(\Omega)] &= [(I + R)(\Omega)] [\mathcal{G}^{pphh}(\Omega)] [(I + R)(\Omega)], \\ [R(\Omega)] &= [(I + L)(\Omega)] [\mathcal{G}^{ph}(\Omega)] [(I + L)(\Omega)]. \end{aligned} \tag{4.34}$$

The main limitation on this approach is the underlying assumption on the free propagator  $\mathcal{G}_0$ . The free two-particle propagators are not necessarily diagonal in the correct solution.

#### 4.4 Approximate solution to the Dyson equation

The equation set (4.26) and (4.28) together with the Dyson equation (3.20) gives a solution to the one-body propagator if solved self-consistently. To find a viable implementation, we have to make some further simplifications, especially in the treatment of the energy variables.

As discussed above, in the exact solution, the standard Hartree-Fock quasi-particles and quasi-holes are no longer stable single-particle states. The energy of a single-particle state gets smeared out over a broad range of possible energies. While it is possible to find such multiple solution sets, see for example Ref. [100, 101, 102, 103], the ensuing complexity makes computations within our scheme far too demanding at present. We have therefore opted for an approximation where we keep only the solution closest to the first order energy  $\epsilon^{f.o.}$ . The first order energies are determined from the energy-independent first order contribution to  $\Sigma$  (which is the same as the Hartree-Fock self energy defined in equation 3.23):

$$\Sigma^{f.o.}(\alpha, \beta) = -i \int_{C^\uparrow} \frac{d\omega}{2\pi} \sum_{\gamma\delta} \langle \alpha\gamma | V | \beta\delta \rangle g_{\gamma,\delta}(\omega), \quad (4.35)$$

$$\epsilon_{\alpha\beta}^{f.o.} = e_{\alpha\beta}^0 + \Sigma^{f.o.}(\alpha\beta). \quad (4.36)$$

The energy of a given single-particle state is calculated from equation (3.25) with  $\Sigma$  calculated at the first order energy, that is, the energies are the eigenvalues of the equation

$$([e] + [\Sigma(\epsilon^{f.o.})])|\lambda\rangle = \omega_\lambda|\lambda\rangle, \quad (4.37)$$

which is now a simple, linear eigenvalue problem. The number of eigenvalues is then limited to  $N$ , the number of orbitals in the basis. As a consequence, the hole spectral function reduces to a series of at most  $N$  peaks, one for each energy state. Each energy has only one contribution, from a single, well-defined state, removing the need for the summation over states to obtain the spectroscopic factor for a given energy. The sum rule that the occupation and depletion numbers of a single basis state must sum to 1 reduces to the condition that the sum of the hole amplitude and particle amplitude for a given energy sums to 1, giving exactly complementary hole and particle spectral functions.

The integral over the energy of the single-particle propagator in equation (4.28) is solved by the Residue theorem. In the first order term the interaction is energy-independent, and so no complications occur. To perform the integration in the second term, we make the assumption that the

residues at the poles of the ladder propagator  $\mathcal{G}_0^{pphh}$  and the interaction  $\Gamma$  are small compared to the residue at the pole of the single-particle propagator. These residues will quickly be quenched by the denominator of the single-particle propagator as long as they are at other energies than the energies of the single-particle orbitals. Due to the approximate solution of the Dyson equation, the sums over  $n+$  and  $k-$  in the expression for the single particle propagator reduce to restricting the summations over orbitals to either over or under the Fermi level. Thus our expression for the self energy becomes

$$\begin{aligned}
\Sigma(1, 2; \omega) &= - \sum_{\alpha\beta} \langle 1\alpha | V | 2\beta \rangle \sum_k z_{\alpha\beta}^{k-} \\
&\quad + \frac{1}{2} \sum_{n+} \sum_{\alpha\beta\gamma\delta\mu\nu} \langle 1\alpha | V | \beta\gamma \rangle \langle \beta\gamma | G_0^{pphh}(\omega + \epsilon_{\nu\alpha}^{n+}) | \delta\mu \rangle \langle \delta\mu | \Gamma(\omega + \epsilon_{\nu\alpha}^{n+}) | 2\nu \rangle z_{\nu\alpha}^{n+} \\
&\quad + \frac{1}{2} \sum_{k-} \sum_{\alpha\beta\gamma\delta\mu\nu} \langle 1\alpha | V | \beta\gamma \rangle \langle \beta\gamma | G_0^{pphh}(\omega + \epsilon_{\nu\alpha}^{k-}) | \delta\mu \rangle \langle \delta\mu | \Gamma(\omega + \epsilon_{\nu\alpha}^{k-}) | 2\nu \rangle z_{\nu\alpha}^{k-} \\
&= - \sum_{\alpha\beta < F} \langle 1\alpha | V | 2\beta \rangle z_{\alpha\beta} \\
&\quad + \frac{1}{2} \sum_{\alpha\nu > F} \sum_{\beta\gamma\delta\mu} \langle 1\alpha | V | \beta\gamma \rangle \langle \beta\gamma | G_0^{pphh}(\omega + \epsilon_{\nu\alpha}^{f.o.}) | \delta\mu \rangle \langle \delta\mu | \Gamma(\omega + \epsilon_{\nu\alpha}^{f.o.}) | 2\nu \rangle z_{\nu\alpha} \\
&\quad + \frac{1}{2} \sum_{\alpha\nu < F} \sum_{\beta\gamma\delta\mu} \langle 1\alpha | V | \beta\gamma \rangle \langle \beta\gamma | G_0^{pphh}(\omega + \epsilon_{\nu\alpha}^{f.o.}) | \delta\mu \rangle \langle \delta\mu | \Gamma(\omega + \epsilon_{\nu\alpha}^{f.o.}) | 2\nu \rangle z_{\nu\alpha}.
\end{aligned} \tag{4.38}$$

Here  $z_{\nu\alpha}$  is the amplitude of the single-particle propagator at the first-order energy  $\epsilon_{\nu\alpha}^{f.o.}$ . We have chosen this solution method to incorporate the effect of the changes in the spectral function into the self energy while still conserving the total number of particles.

## 4.5 Summary of the different approximations

We have employed a number of approximations to the complete Parquet solution. The first is to truncate the infinite sum of diagrams in the class  $I$  of diagrams which are non-simple in all channels after the first term, keeping only the bare interaction. The effect of missing the corrections stemming from the missing diagrams of fifth order or higher is small compared to the effects of some of our other approximations.

We have also made an approximation on the energy dependence of our interaction  $\Gamma$ , namely that the energy parameter  $\Omega$  is the same in the calculation of  $L$  and  $R$ , even though it is defined differently relative to the energies of the incoming states in the two cases. The  $\Omega$  parameter thus represents an average incoming energy.

The most influential approximation is our approximate method for solving the Dyson equation described in section 4.4. Thus even our most complete solution is an approximation, and we have termed this the fixed-energy Dyson equation approximation (FED) in the discussion of our results. We have also employed an even cruder approximation termed the unperturbed propagator structure approximation (UPS). To facilitate later reference, we give a short summary of the ingredients and consequences of each approximation scheme below.

The small imaginary part  $i\eta$  in the propagator equations (4.18) and (4.25) is a mathematical necessity to ensure that the correct poles of the propagator is included when integrating over  $\omega$ , and the real physics occur in the limit of  $\eta \rightarrow 0$ . Ideally, this should be done before a numerical implementation, but we have found that the poles of the propagator give rise to serious convergence problems, and so the  $i\eta$  factor must be present also in the numerical implementation. The physical limit is then found as an extrapolation of results for different values of  $\eta$ . The effect of  $\eta$  is to move the poles away from the real axis. This reduces the severity of the poles and smooth the energy dependence of the real matrix elements in exchange for larger imaginary parts. Thus the overall effect is to reduce the effects of the interaction between the particles, making the results closer to a mean field result. This need for an extrapolation introduces an additional uncertainty to our results.

Our method for handling the poles and the Dyson equation is different from the implementation of the Green's functions approach employed by Barbieri *et.al.* [104, 6, 24]. They solve the Dyson equation numerically, and then use a small number of solutions close to the Fermi level, typically two or three. The remaining solutions are accounted for in an average manner. This simplifies the calculation considerably. In their approach, the interaction  $\Gamma$  is handled



in the Faddeev random phase approximation.

#### 4.5.1 The unperturbed propagator structure approximation - UPS

The unperturbed propagator structure approximation (UPS) employ the unperturbed structure of the propagator, as given in equation (3.3), repeated here for easy reference:

$$g_{\alpha\beta}^0(\omega) = \delta_{\alpha,\beta} \left( \frac{\theta(\alpha - F)}{\omega - e_{\alpha}^0 + i\eta} + \frac{\theta(F - \alpha)}{\omega - e_{\alpha}^0 - i\eta} \right), \quad (4.39)$$

This gives the expression for the two-time propagators given in equation (4.18) for  $\mathcal{G}^{pphh}$  and equation (4.25) for  $\mathcal{G}^{ph}$ . The total effect of performing this simplification in addition to the approximate Dyson equation solution method is that only the energies of the single particle states are changed during the self-consistency procedure. The single-particle energies are calculated self-consistently to ensure summation of the interaction diagrams to all orders. The spectral functions are just spikes with height 1 at the energy of the state, and 0 elsewhere. This approximation also ensures that the matrix inversion method described in section 4.3.2 can be applied to our case, as the non-interacting propagators then become diagonal. The energy sum rule (3.29) becomes particularly simple in this approximation, being a sum over the hole orbitals.

#### 4.5.2 The fixed-energy Dyson equation approximation - FED

The fixed-energy Dyson equation approximation employs the structure in equation (3.2) for the single-particle propagator. To ease the comparison to the UPS approximation, we state the main equation here as well:

$$g_{\alpha\beta}(\omega) = \sum_n \frac{z_{\alpha\beta}^{n+}}{\omega - \epsilon_n^+ + i\eta} + \sum_k \frac{z_{\alpha\beta}^{k-}}{\omega - \epsilon_k^- - i\eta}, \quad (4.40)$$

where  $z_{\alpha\beta}^{n+}$  is an abbreviation for  $\langle \Psi_0^N | c_{\alpha} | \Psi_n^{N+1} \rangle \langle \Psi_n^{N+1} | c_{\beta}^{\dagger} | \Psi_0^N \rangle$  and so on. Thus the two-time propagators have the forms given in equations (4.17) and (4.24). The approximated solution to the Dyson equation is still employed, ensuring that the total number of eigenstates is the same as the number of orbitals  $N$ . The number of possible terms in the sums over amplitudes in the expressions for the propagators is then limited to  $N$ . The definition of the hole spectral

function in equation (3.6), will, in our current notation be given by

$$S_h(\alpha, \omega) = \sum_k |z_{\alpha\alpha}^{k-}|^2 \delta(\omega - \epsilon_k^-). \quad (4.41)$$

The sum over  $k$  in this equation is limited to the number of orbitals, and the energies  $\epsilon_k^-$  are the orbital energies in the FED approximation. The spectroscopic factors in this approximation will be smaller than 1, as the coupling between states with different orbital numbers  $n$  will give hole spectral functions which have some probability of having a higher energy. As each energy can be identified with a definite orbital, the height of the spike at that energy gives the spectroscopic factor of that orbital.

The implication of this approximation is that while we loosen the restriction that the input basis states are 'good' states and allow the single-particles to become linear combinations of the chosen basis set, we still assume that the single-particle picture is valid, that is, the system can be described as a set of (quasi-)particles with a discrete energy spectrum.

### 4.5.3 Energy-dependence

In addition to the two different treatments of the single-particle propagator, we have also tried two different schemes for handling the energy dependence of the Parquet equations, giving a total of four possible schemes.

In the energy-independent scheme, a fixed starting energy  $E_{in}$  is chosen and used as the input  $\Omega$  in the equations for the two-time propagators. Typically,  $E_{in}$  has to have a value well removed from the poles of the propagators to obtain converged results. The generated interaction  $\Gamma(E_{in})$  is analogous to the interaction from a conventional  $G$ -matrix calculation, with some important differences. The ladder terms includes both particle-particle and hole-hole ladders, whereas the  $G$ -matrix only contains the particle-particle part. The starting energy could correspond to the energy of the incoming particles or to the energy difference between a particle-hole pair, depending on context. Like a conventional  $G$ -matrix, eventual use of the generated interaction would be hampered by the need to extrapolate for starting energies for which the poles of the propagator destabilize the solution (i.e. where the incoming particle energies correspond to a pole in the propagator). The inclusion of hole-hole terms imply that also negative starting energies will give this effect. In our approach this destabilization can be handled by increasing the  $i\eta$  parameter significantly, thus generating an interaction applicable to all energies.

In the energy-independent scheme, there are no differences between using the approximated full propagator as described in section 4.3.2 and the more

correct free propagator approach described in section 4.3, as expected from the fact that the approximation in the former approach concerns the derivative of the interaction with respect to the energy, which in the case of an energy-independent interaction is exactly 0.

In the energy-dependent scheme, a (real) energy grid is set up and the propagators and interactions are calculated at each value of the grid. The values of  $\Gamma(\Omega)$  used in the calculation of the self energy (equation 4.38) are then interpolated to the energy  $\Omega = \omega + \epsilon_{\nu\alpha}^{f.o.}$ . This scheme includes the poles in the generated interaction in a more correct manner than the energy-independent scheme, but the added number of poles gives additional convergence problems. In this scheme, the approximated full propagator as described in section 4.3.2 gives different results than the free propagator approach described in section 4.3.

#### 4.5.4 Schematic structure of the calculation

We provide a schematic overview of the structure of our implementation in figure 4.8. The self-consistency loop is continued unto convergence, that is, the single-particle energies and single-particle propagator do not change during the cycle.

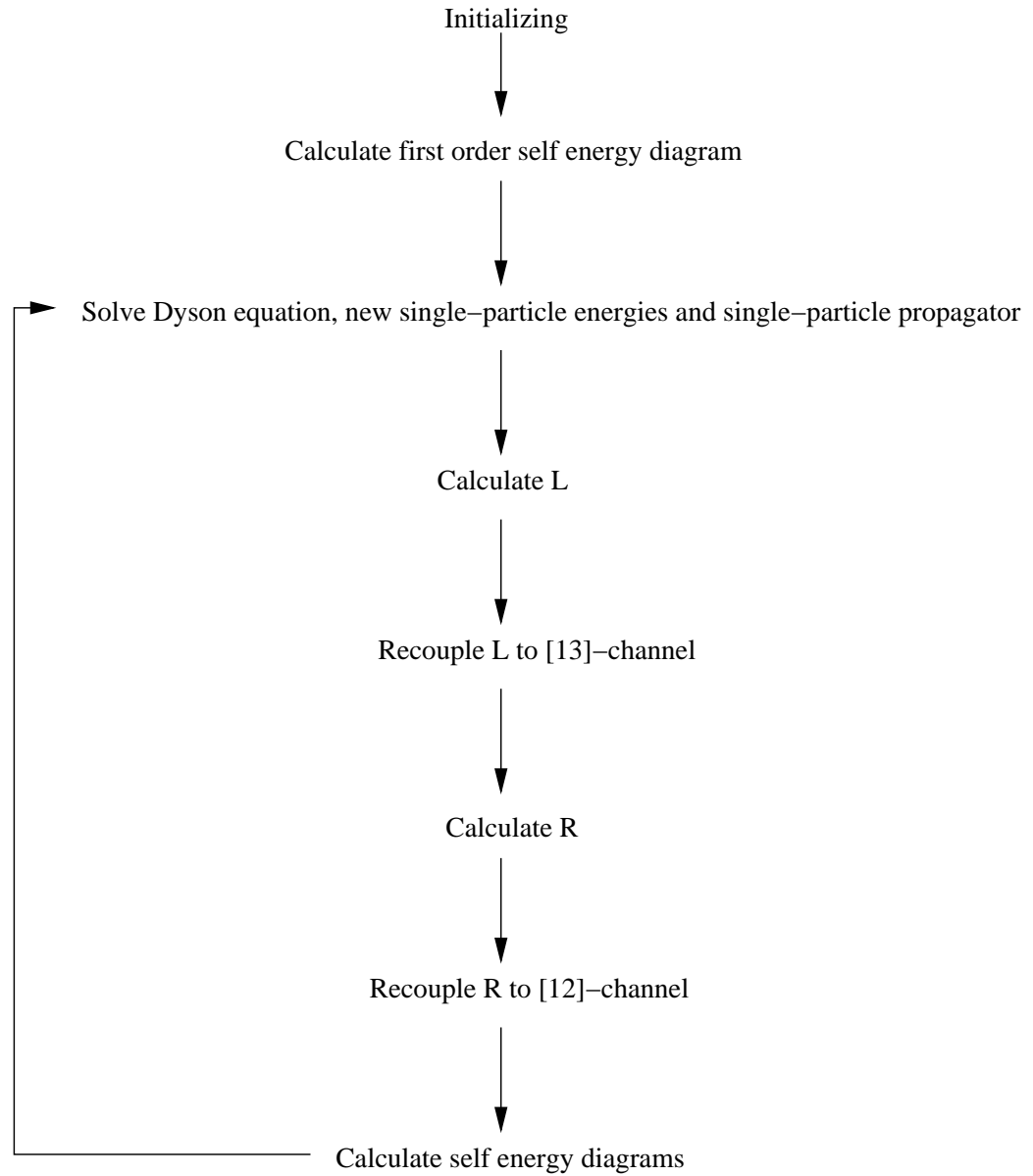


Figure 4.8: Schematic overview of the program structure. The loop is continued until the single-particle energies and single-particle propagator do not change during the cycle.

# 5 A simple model

As a first step, we discuss the performance of the Parquet method in a simple model, which capture some of the essential features of the interaction in nuclei. The structures seen in more realistic cases are here much simpler to analyze, making it possible to discern the origins of the observed features of the self energy and the spectral functions to a greater extent, including the relative effects of the pair-correlation and the particle-hole terms in the interaction. Thus the insights gained in this chapter are of relevance to the discussion of the more realistic case investigated in chapter In the first section, we describe the model as built around a three-term Hamiltonian. In section 5.2 we present the results of applying the Parquet method to the simplest version of the model in which only a pair-conserving part of the Hamiltonian is included. In section 5.3, we discuss the results of including a pair-breaking term. We give a brief summary of the main findings in section 5.5.

## 5.1 Description of the model

The model has  $N$  doubly-degenerate and equally spaced single-particle levels labelled by  $n = 0, \dots, N_{max}$  and spin  $\sigma = \pm 1$ . The Fermi level defines the boundary of the “closed core”, as shown in the first column of figure 5.1. We define a Hamiltonian of the system with three contributions, a one-body part  $H_0$  and a two-body interaction  $V$  consisting of two terms, as follows:

$$H = H_0 + V = \sum_{k\sigma} k c_{k\sigma}^\dagger c_{k\sigma} + \frac{1}{2}g \sum_{kj} c_{k+}^\dagger c_{k-}^\dagger c_{j-} c_{j+} + \frac{1}{2}f \sum_{jkl} (c_{k+}^\dagger c_{k-}^\dagger c_{j-} c_{l+} + c_{j+}^\dagger c_{l-}^\dagger c_{k-} c_{k+}) \quad (5.1)$$

The energy of the first level is set to 0, and the energy increases by a fixed amount for each level. We set this fixed level spacing to 1, and the coupling

constants  $g$  and  $f$  give the relative strengths between the level spacing and the interaction. The first term of the interaction has a pair structure, and can only excite two particles at a time, as shown in the second column of figure 5.1. The vacant positions are holes and are drawn as open circles. The second term in the interaction is a pair-breaking term, as it acts between pairs of opposite spin, creating excitations of the type shown in the third column of figure 5.1. This system can be solved exactly by diagonalization, enabling

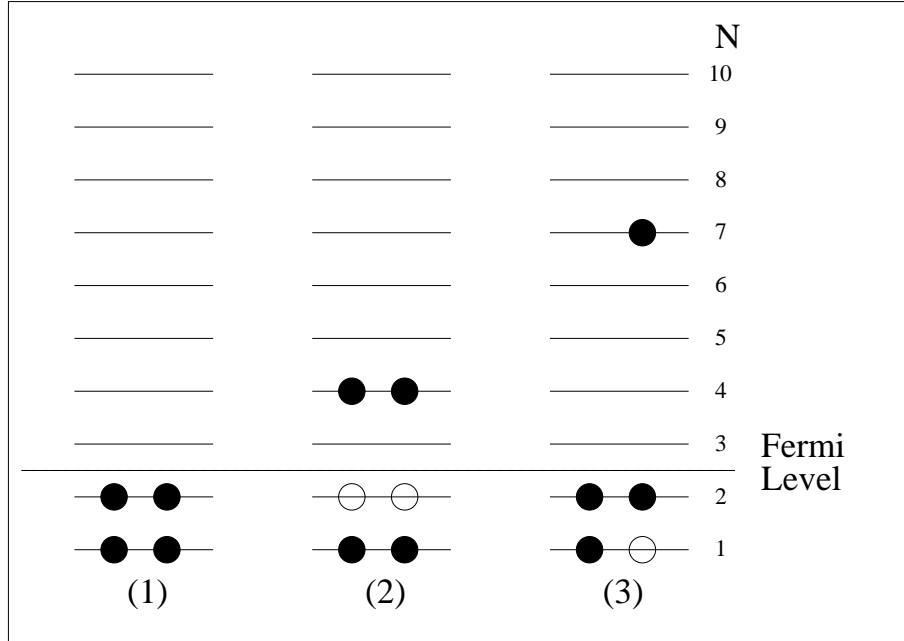


Figure 5.1: Sketch of the  $N = 10$ ,  $p = 4$  model in the ground state (1), an example pair excitation, the only type to occur when  $g \neq 0$ ,  $f = 0$  (2), and an example pair-breaking excitation which can occur when  $f \neq 0$  (3).

us to study the accuracy of the Parquet summation method. We pay especial attention to the effects of the relative strength between the level spacing and the interaction, and to the effects of increasing number of orbitals and particles. As our implementation of the Parquet method so far only includes two-body interactions, we can gain insights into the influence of many-body correlations beyond the two-body level. In nuclei, the pairing component of the interaction is known to be strong, as seen by the success of the seniority scheme models [105], and thus the pairing-only model is of interest in this context. We know that closed-core nuclei commonly have an interaction strength

of  $\sim 20 - 30\%$  of the level spacing [106, 107], so we will concentrate on the span  $[-1, 1]$  of interaction strengths.

We employ dimensionless variables in the discussion of this model.

## 5.2 Results for the pairing-only model

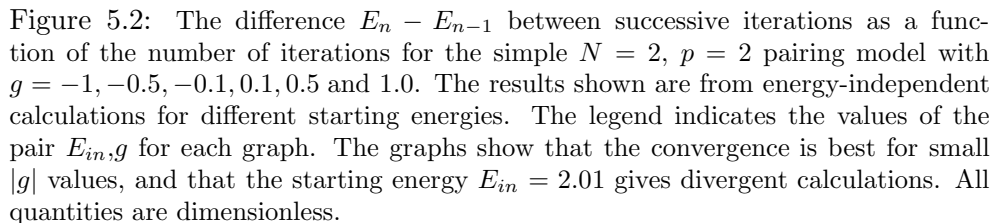
As a first step, we study the Parquet method applied to the simple pairing model, in which the particle-hole coupling constant is zero, i.e.  $f = 0$ . This implies that the self energy becomes diagonal, and thus the unperturbed propagator structure as given in equation (4.39) is conserved, and there is no difference between the two approximation schemes FED and UPS described in section 4.5.

### 5.2.1 Convergence with respect to $\eta$

Since our method is based on an iterative procedure, we need to investigate the stability of the solution and see if the results converge as the number of iterations increase. The  $\eta$  parameter in the two-time propagators (4.17) and (4.24) regulates the influence of the pole terms, determining the stability of the iterative procedure. Increasing values of  $\eta$  give calculations in which the effect of the poles are increasingly removed, increasing the imaginary parts of the results.

For the simplest case of  $N = 2$  and  $p = 2$ , the parameter  $\eta$  can be set to 0 in most cases for energy-independent calculations. The graphs in figure 5.2 show the difference in ground state energies between iteration  $n$  and the previous iteration,  $E_n - E_{n-1}$ , in a log-scale plot as a function of number of iterations. We show results for energy-independent calculations at different starting energies  $E_{in}$ . Most starting energies give convergence to machine precision within 10-15 iterations. The exception to this is starting energies exactly at the poles in the  $\mathcal{G}_0^{pphh}$  and  $\mathcal{G}_0^{ph}$  propagators used in the calculation of  $L$  and  $R$ , respectively. The starting energy  $E_{in} = 2.01$  is such an exception, as can be seen from the divergent patterns for this starting energy in figure 5.2. These poles lie around 0 in this system, with a larger number of poles at positive energies than negative. Negative values of  $E_{in}$  less than  $\sim -2$  always converge.

Comparing the graphs for different values of the interaction strength  $g$ , we see that the convergence properties for the  $\eta = 0$  calculations are less stable when the pairing constant  $|g|$  increases. Only for starting energies well away from zero can convergence be obtained. By setting  $\eta > 0$  all starting energies can be made to converge at all  $|g|$  values. At small values of  $|g|$ ,  $\eta$  values as small as  $5 \times 10^{-2}$  give convergence when  $E_{in}$  is equal to one of the poles of



Energy-dependent calculations have roughly the same convergence properties as the energy-independent case. Except for some unhappy cases where an exact pole in  $\Gamma$  is encountered, the results for all  $g$  values converge for  $\eta = 0$ . Setting  $\eta > 0$  gives faster convergence, as can be seen in figure 5.3, where we show results for calculations with an energy grid with 20 points for several  $g$  values both at  $\eta = 0$  and  $\eta = 1$ . The  $\eta > 0$  convergence pattern is not as regular as the  $\eta = 0$  case. Increasing the energy grid size (i.e. employing a more fine-grained grid) often gives less possibility for convergence, as the probability of hitting a pole in  $\Gamma$  increases. A more dense grid requires larger  $\eta$  values to obtain convergence.

Increasing the system size changes the convergence properties, as the num-



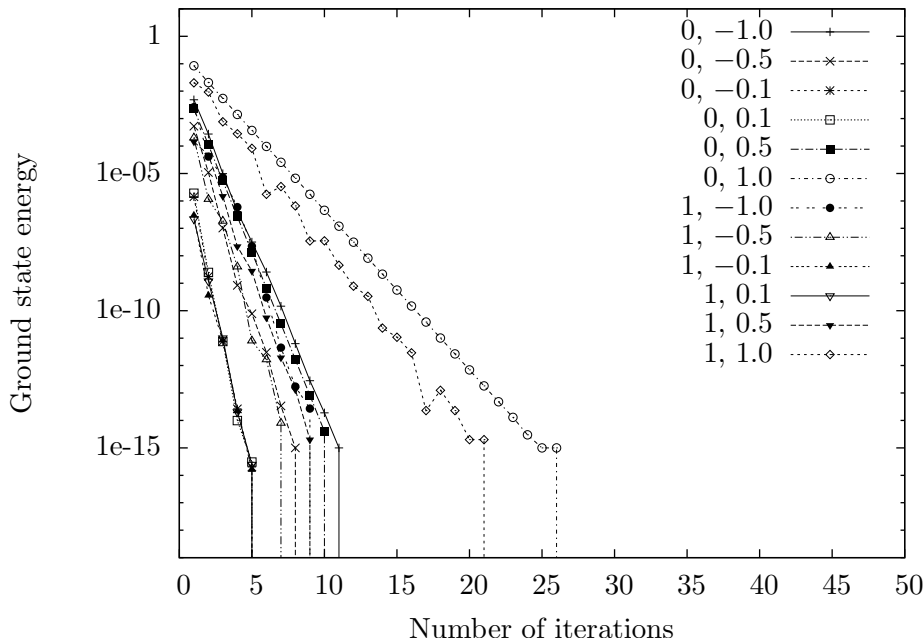


Figure 5.3: The difference  $E_n - E_{n-1}$  between successive iterations as a function of the number of iterations for the simple  $N = 2$ ,  $p = 2$  pairing model with  $g = -1, -0.5, -0.1, 0.1, 0.5$  and  $1.0$ . We show results for energy-dependent calculations for  $\eta = 0$  and  $\eta = 1$ . The legend consists of pairs of  $\eta, g$  values. All results are converged, also for larger  $|g|$  values. The convergence pattern is faster but more irregular when  $\eta = 1$ .

ber of poles increases. For the  $N = 10$ ,  $p = 4$  system energy-independent calculations converge to machine precision within 25 iterations for a starting energy of  $E_{in} = -20$ , but the energy-dependent calculations exhibit a slower convergence pattern compared with the  $N = 2$  case. This is seen in figure 5.4, where we see that for large values of  $|g|$  the  $\eta = 0$  calculations diverge. The  $\eta = 1$  calculations show slowly decreasing small oscillatory behaviour at these  $|g|$  values. The trend continues at least beyond 100 iterations, so it seems reasonable to conclude that the  $\eta = 1$  calculations eventually converge to machine precision. Smaller  $|g|$  values gives slow, exponential convergence for  $\eta = 0$ , and a much faster, more irregular convergence pattern for the  $\eta = 1$  calculations. Increasing the number of particles to 6 does not change the convergence properties substantially, implying that the number of levels is the factor with largest influence on the convergence properties of the calculations within the pair-conserving model.

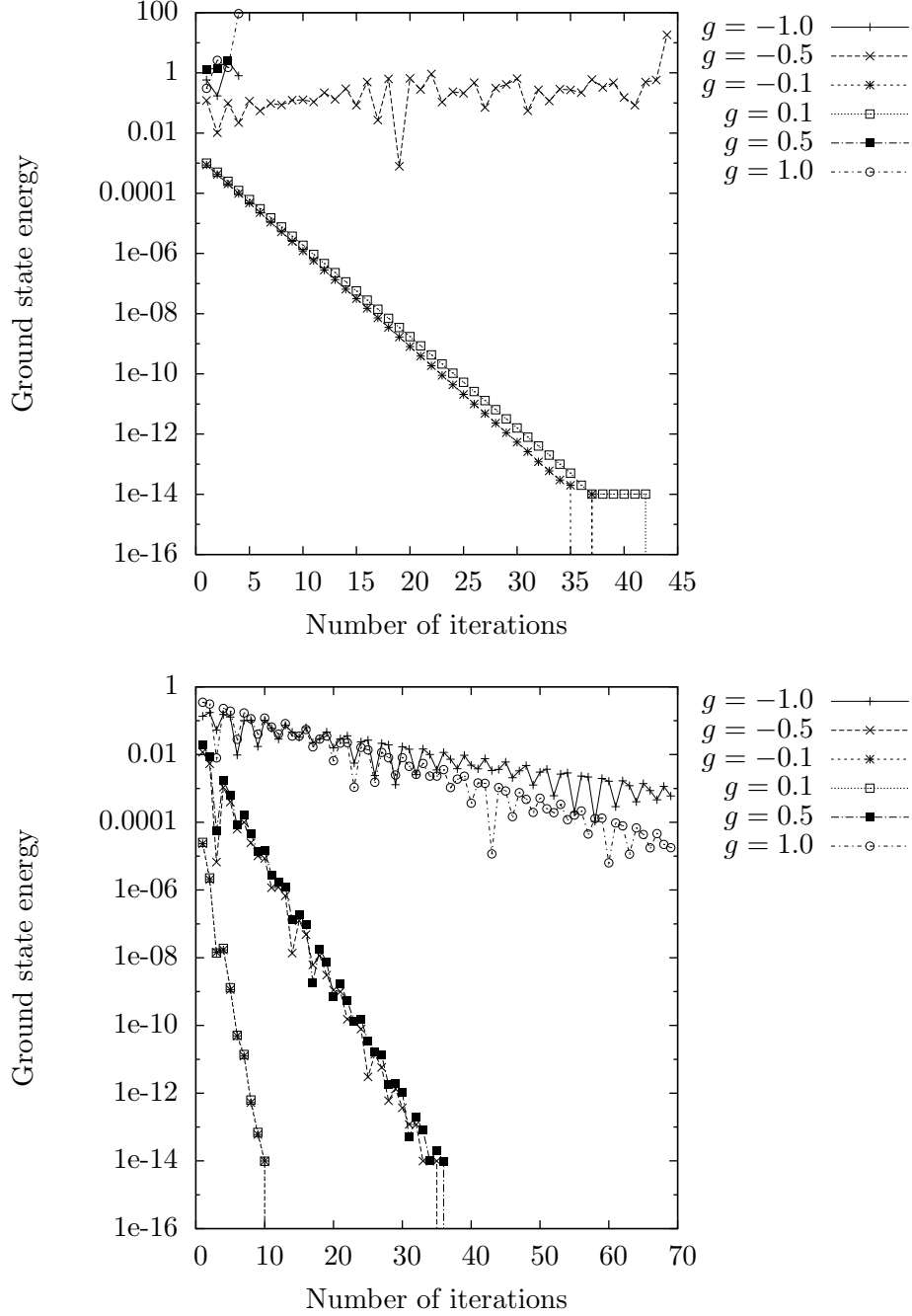


Figure 5.4: The difference  $E_n - E_{n-1}$  between successive iterations as a function of the number of iterations for energy-dependent calculations in the  $N = 10$   $p = 4$  pairing model with  $g = -1, -0.5, -0.1, 0.1, 0.5$ . In the upper panel we show results for  $\eta = 0$ , and in the lower panel  $\eta = 1$ . Only small values of  $|g|$  give convergent results in the  $\eta = 0$  case, while all values show convergent behaviour at  $\eta = 1$ .

### 5.2.2 Self energy

The pair model is ideal for studying the pole structure of the self energy, as it is easy to discern the effects of changing different parameters. The energy dependence of the self energy  $\Sigma$  can be investigated both for the energy independent and energy dependent cases. The first order term in equation (4.38) is energy-independent, giving the energies at which the self energy is calculated at each iteration. The energy-dependent term has poles stemming both from poles in the  $\mathcal{G}_0^{pphh}$  propagator and from the interaction  $\Gamma$ , giving a rich structure in an exact calculation. The pair-conserving interaction gives a diagonal self energy, and thus the energies of the single-particle orbitals are given by adding the self energy contribution at the first-order energy to the unperturbed energies directly.

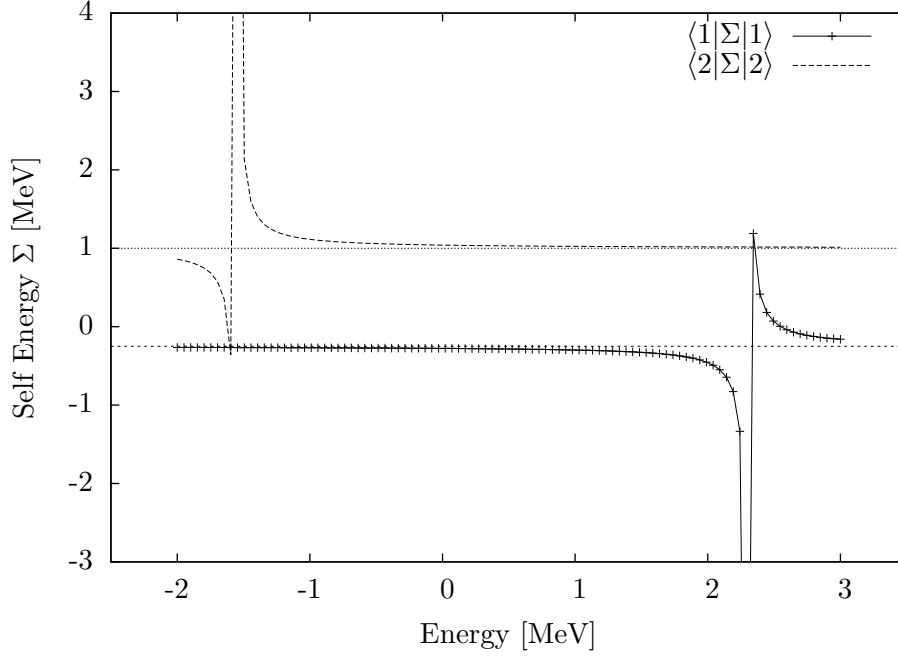


Figure 5.5: The energy dependence of the self energy for the two diagonal elements  $\langle 1|\Sigma|1\rangle$  and  $\langle 2|\Sigma|2\rangle$  of an  $N = 2$ ,  $p = 2$  calculation for an interaction strength  $g = -0.5$ . The first-order contributions are shown as straight lines, and we see that these determine the average values. The second-order terms contribute to the pole structure.

In the  $N = 2$ ,  $p = 2$  system however, the pole structure is considerably

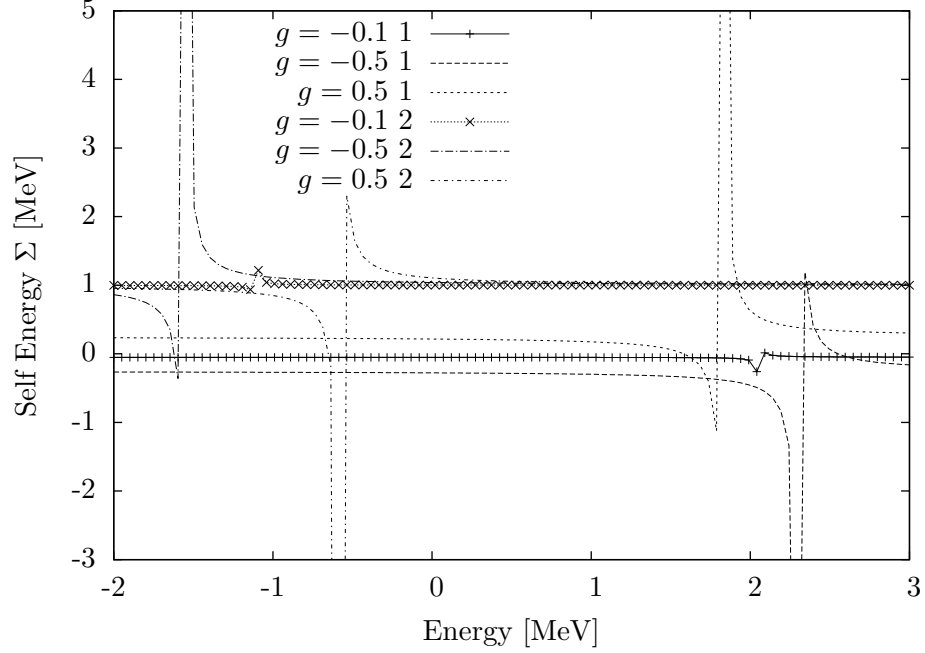


Figure 5.6: The energy dependence of the self energy for the two states of an  $N = 2$ ,  $p = 2$  calculation for interaction strengths  $g = -0.5, -0.1$  and  $0.5$ . The numbers 1 and 2 in the legend are abbreviations for  $\langle 1|\Sigma|1\rangle$  and  $\langle 2|\Sigma|2\rangle$ , respectively. The poles are much less pronounced for the  $g = -0.1$  case. The attractive  $g = -0.1$  and  $g = -0.5$  interactions push the lowest energy level down relative to the non-interacting level value at 0. In the repulsive  $g = 0.5$  case, the lowest level increases in energy relative to the non-interacting case.

simpler. The level scheme given in figure 5.1 reduces to two levels with energy 0 and 1, respectively. Thus the self energy has two matrix elements,  $\langle 1|\Sigma|1\rangle$  and  $\langle 2|\Sigma|2\rangle$ , the numbering of the states being according to the level number as shown in figure 5.1.

From analytical calculations on the two-level problem we would expect the two-hole-two-particle propagator  $\mathcal{G}^{pphh}$  based on first order energies as input to have poles at the first-order energies (see equation (4.36)) of two-hole-one-particle and two-particle-one-hole excitations. Choosing  $g = -0.5$ , the first-order energies of the two levels are -0.25 and 1.0, giving self energy poles occurring at the energies -1.5 (two-hole-one-particle) and 2.25 (two-particle-one-hole). The poles of the self energy in our calculations will occur at the energies found from solving the Dyson equation (by solving equation (4.37)) for the two particles (two holes) and at the first order energy of the hole

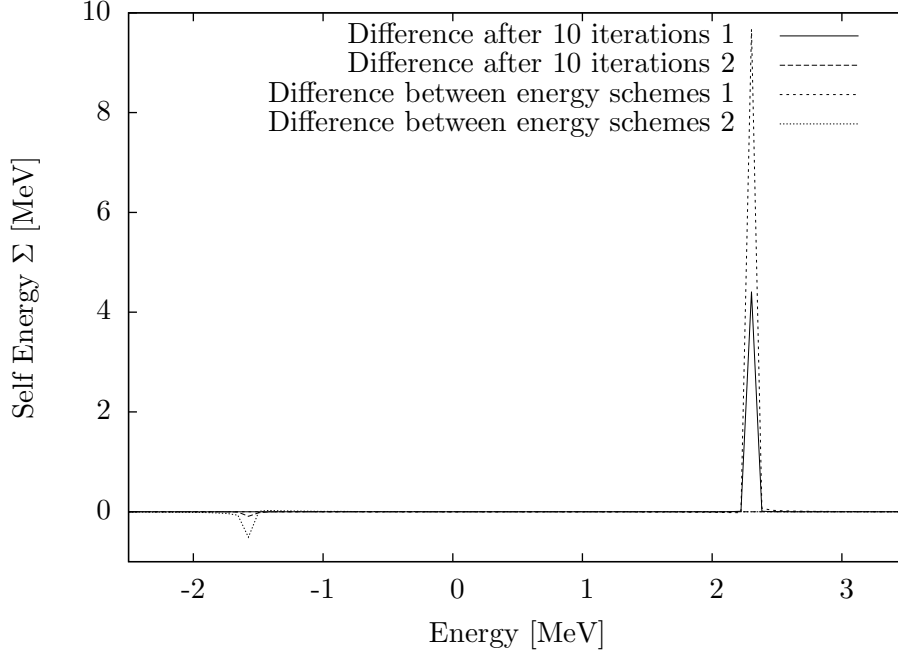


Figure 5.7: The differences between 1 and 10 iterations of an energy-independent calculation with  $E_{in} = -10$ , and between an energy-independent and an energy-dependent calculation in the  $N = 2$ ,  $p = 2$  system. The numbers 1 and 2 in the legend are abbreviations for  $\langle 1|\Sigma|1\rangle$  and  $\langle 2|\Sigma|2\rangle$ , respectively. Only energies close to the poles are affected in both cases.

(particle). At the energy scales involved and with our approximate solution of the Dyson equation, we do not expect the full energies to be very different from the first-order energies, and this is confirmed when we look at the poles of the self energy as shown in figure 5.5. This graph shows the diagonal elements  $\langle 1|\Sigma|1\rangle$  and  $\langle 2|\Sigma|2\rangle$  (the off-diagonal elements being zero in the pair model) as a function of energy. We have also included the first-order energies for reference. The self energy matrix elements shown are the result after the first iteration of a calculation without interactions, that is,  $L = R = 0$ . The poles have shifted from 2.25 to almost 2.3, and from -1.5 to -1.55. For reference, we also show the energy-independent first order contributions, and we see that the average value of the self energy is determined by the first-order term, the second-order term mainly contributing close to the poles. We also note that each matrix element of the self energy in the pair-conserving model only has contributions from either the pp or the hh part of  $\mathcal{G}_0^{pphh}$ , thus having only one pole each.

Reducing the absolute value of the interaction strength parameter  $g$  reduces the impact of the poles drastically, as seen from the set of graphs for  $g = -0.1$  in figure 5.6, explaining the very good convergence properties at the values of  $g$  close to 0. Furthermore, from comparing the  $g = -0.5$  with the input energies of the two levels, the main effect of an attractive force is to lower the average energy of the lowest-lying level and increasing the gap between the two levels. This lowers the ground state energy, as expected. The repulsive force reduces the gap by pushing the lowest level upwards in energy, as exemplified in the graphs for  $g = 0.5$  in figure 5.6.

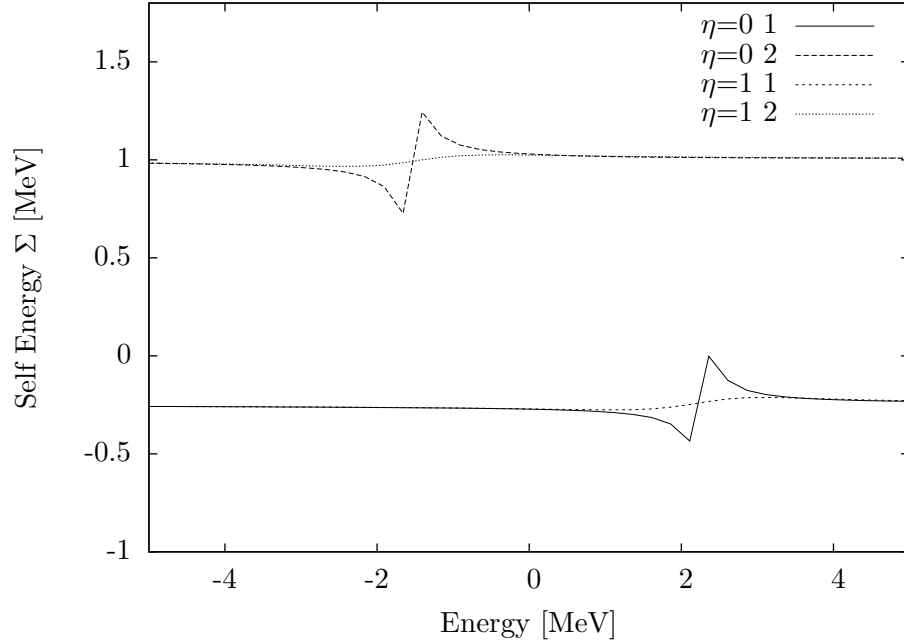


Figure 5.8: The energy dependence of the self energy for the two states of an  $N = 2$ ,  $p = 2$  system for a full Parquet energy-dependent calculation with  $\eta = 0$  and  $\eta = 1$ . The numbers 1 and 2 in the legend are abbreviations for  $\langle 1|\Sigma|1\rangle$  and  $\langle 2|\Sigma|2\rangle$ , respectively. The pole structure is almost completely quenched in the  $\eta = 1$  case.

Inclusion of an energy-independent  $\Gamma$  will give pole positions which depend on the starting energy, as the poles in the two-time propagators also have this dependence. The position of the poles in the self energy is further adjusted by the self-consistency procedure, but due to our approximate solution to the Dyson equation, the number of poles remain unchanged.

The dependence on the starting energy for the energy-independent cal-

culation is also minimal, although slightly increasing for increasing  $g$  values. The weak dependence reflects that the propagator in the  $\Gamma$  interaction has relatively little influence compared to the effect of the poles in the  $\mathcal{G}_0^{pphh}$  propagator when calculating the self energy.

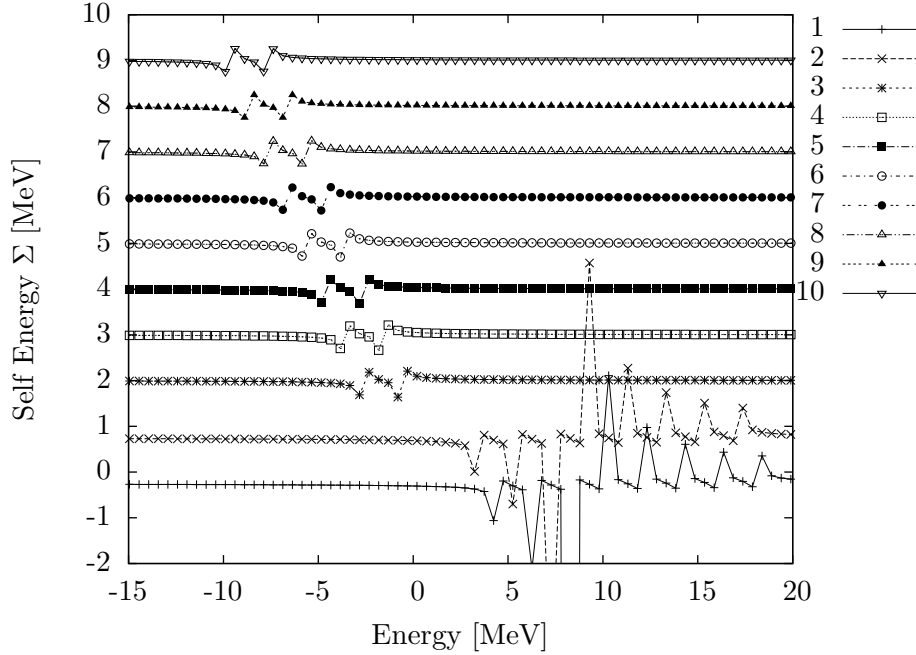


Figure 5.9: The energy dependence of the self energy for the 10 states of an  $N = 10$ ,  $p = 4$  system for an  $L = R = 0$  calculation. The numbers 1,2,...,10 in the legend are abbreviations for  $\langle 1|\Sigma|1 \rangle$  and so on. The number of poles reflect the number of possible two-hole-one-particle and two-particle-one-hole excitations, giving eighth poles in the self energy matrix elements corresponding to hole states and two in each of the self energy matrix elements corresponding to particle states.

The self-consistency procedure does not change the self energies notably, except at the poles, as can be seen from the graph in figure 5.7, where we have shown the difference between the self energy after 1 iteration and after 10 iterations for an energy-independent calculation at starting energy  $E_{in} = 10$ . This is representative for all calculations on this system, illustrating that the initial solution is already close to the self-consistent solution. The differences between the energy-independent and the energy-dependent calculations in this system are somewhat larger, as shown by the second graph in figure 5.7. Only energies close to the poles are affected in both cases.

Adding the imaginary component by setting  $\eta > 0$  in our calculations gives the expected smoothing out of the poles, as shown in figure 5.8, where we compare the self energy diagonal elements  $\langle 1|\Sigma|1\rangle$  and  $\langle 2|\Sigma|2\rangle$  for energy-dependent calculations with  $\eta = 0$  and  $\eta = 1$ . Thus setting a large  $\eta$  value results in an almost energy-independent self energy, that is, the calculation becomes similar to a mean-field calculations.

Increasing the number of particles and levels increase the number of possible two-hole-one-particle and two-particle-one-hole excitations, increasing the number of poles in the self energy. Thus we see eighth poles in each of the two self energy matrix elements corresponding to hole states and two poles each in the eighth self energy matrix elements corresponding to particle states for a calculation with  $N = 10$  and  $p = 4$ , shown in figure 5.9.



### 5.2.3 Comparison with exact diagonalization

We have compared the different approximation schemes discussed in section 4.5 with the exact ground state energies obtained from diagonalization. We compare the ground state energies as a function of the ratio of interaction strength  $g$  to the level spacing as the number of levels increase and as more particles are added.

For convergent starting energies in an energy-independent calculation, the different starting energies yield minimal differences. We have chosen to work mostly with a starting energy of -20, as this is convergent for all values of  $g$  we have studied. All convergent results for other starting energies have less than 3% deviation from the results shown.

In the upper panel of figure 5.10 we show results for the simplest case, with  $N = 2$  and  $p = 2$ , as a function of coupling strength. We compare the ground state energy found from an exact solution, a calculation where  $L = R = 0$ , an energy-independent calculation at different starting energies and extrapolated energy-dependent values. In the  $L = R = 0$  calculations we have performed a self-consistent calculation of the single-particle energies and binding energy based on the input interaction  $V$  alone.

We see that the agreement between our results and the exact is very good for small values of the coupling strength  $|g|$ , where the independent-particle properties are dominant. For stronger negative coupling relative to the level spacing, the Parquet calculations underbind, probably due to the error introduced in our approximate solution of the Dyson equation. The differences between full Parquet and the results for  $L = R = 0$  are very small, indicating that contributions to the ground state energy are provided by the first- and second-order self energy diagrams in the Parquet solution of this simple model. The results for the starting energies  $E_{in} = -10, -5, 5$  and  $10$  demonstrate that in the pair-conserving model the dependence on  $E_{in}$  is very small.

The energy-dependent results agree very well with the energy-independent data in the range of  $g$  values where the calculations converge. To improve the convergent range,  $\eta$  has to have a non-zero value, giving the graph in the upper panel of figure 5.10. A calculation based on several values of  $\eta$  and linearly interpolated to  $\eta = 0$  performs slightly better at large  $g$  values. The tendency to underbind at more negative  $g$  values persists, showing that the energy dependence alone is probably not enough to recover all of the missing binding.

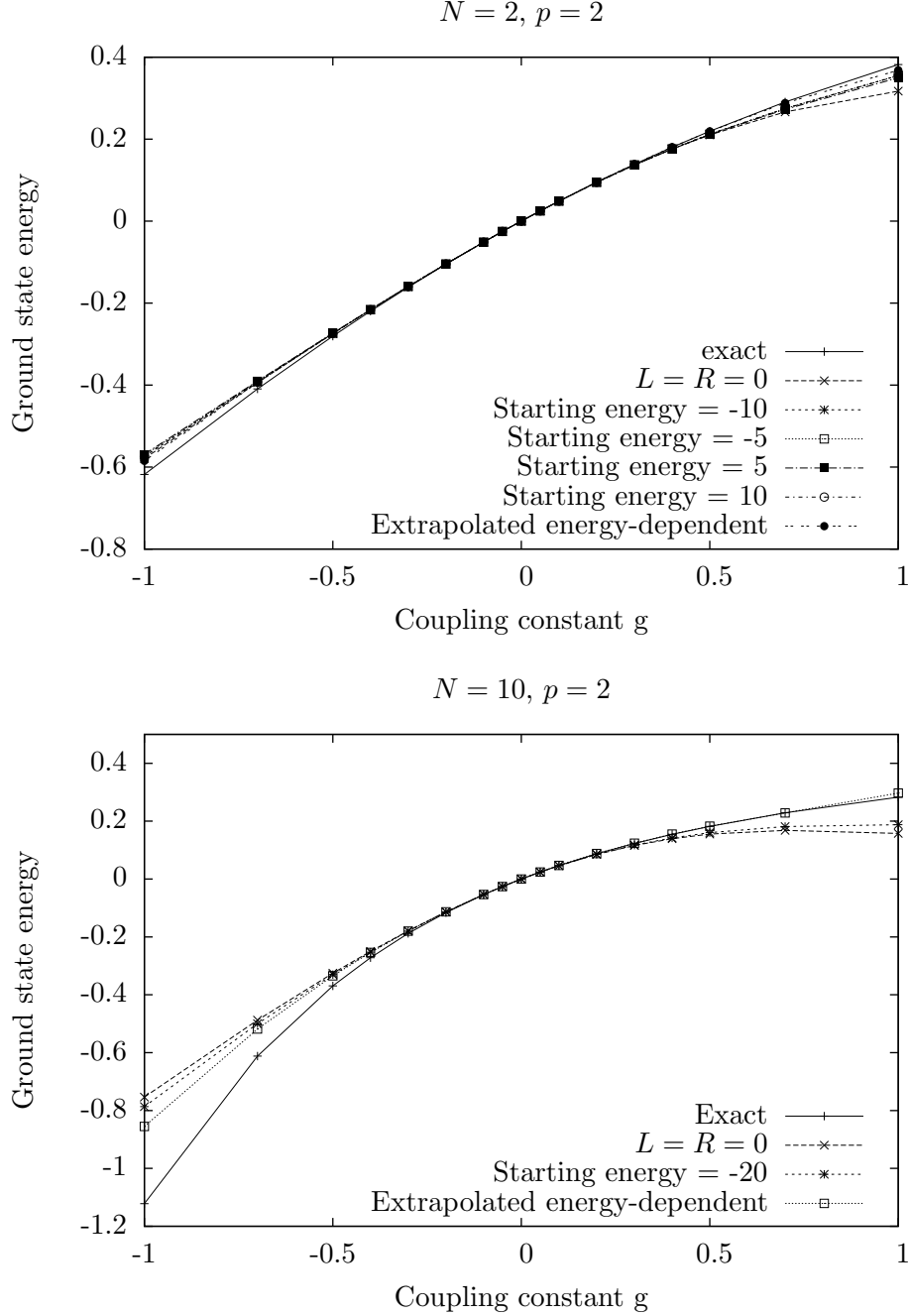


Figure 5.10: Comparison between the exact solution and the different Parquet solutions in the  $N = 2, p = 2$  model (upper panel) and in the  $N = 10, p = 2$  model (lower panel). The differences between the exact solution and the various Parquet solutions are much larger in the  $N = 10$  case. The energy-dependent results are slightly closer to the exact solution than the energy-independent results.

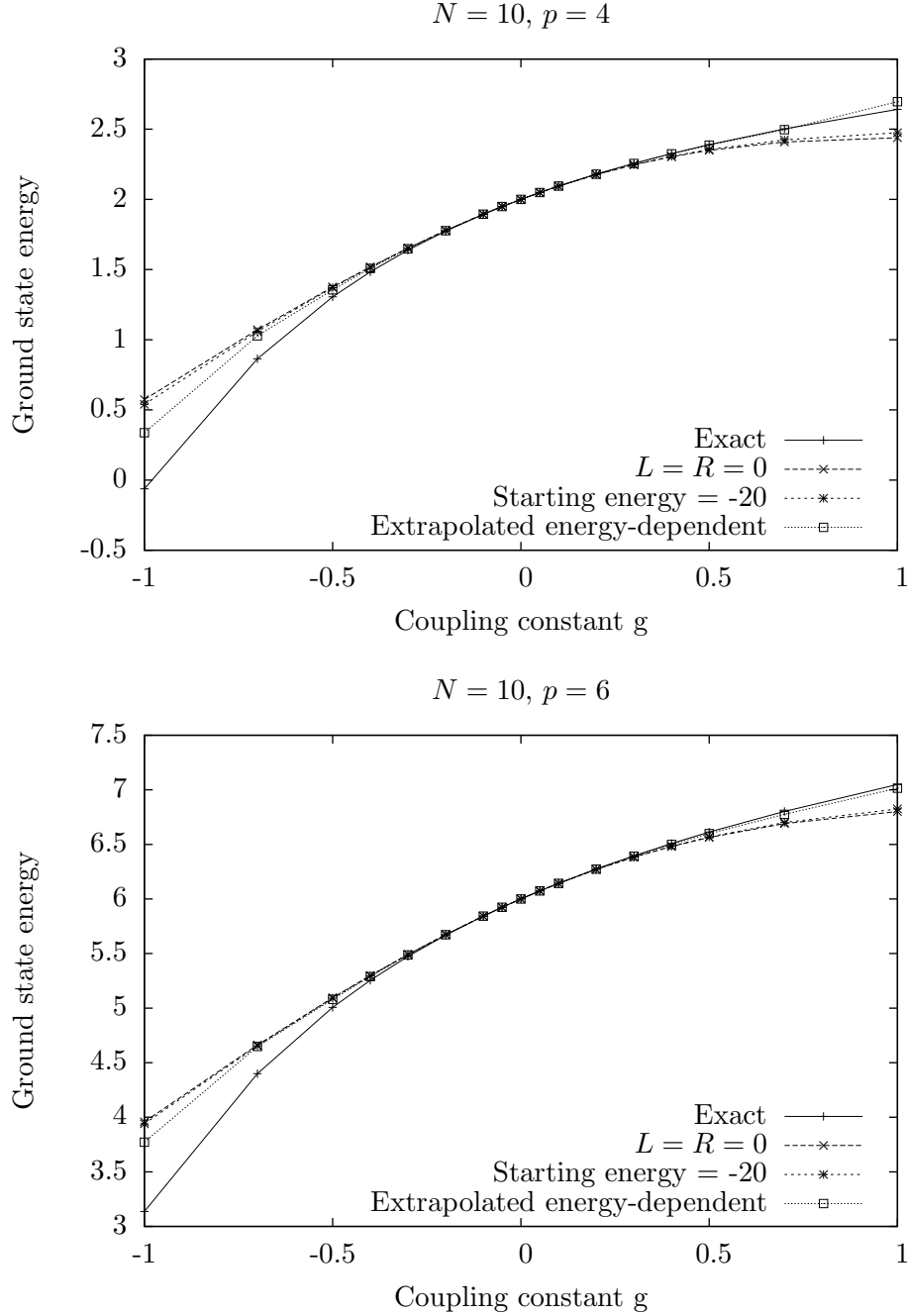


Figure 5.11: Comparison between the exact solution and the different Parquet solutions in the  $N = 10, p = 4$  model (upper panel) and in the  $N = 10, p = 6$  model (lower panel).

When we increase the number of levels to 10, while keeping the number of particles constant at two, we obtain the graphs in the lower panel of figure 5.10. We see increasing differences between the exact values and the Parquet calculated values at stronger negative coupling. The extrapolated values are still better than the energy-independent values which in turn are slightly better than the  $L = R = 0$  results. The dependence on  $E_{in}$  is still negligible, which is why only the  $E_{in} = -20$  graph is shown. Increasing the particle number to four (upper panel of figure 5.11) and then to six (lower panel of figure 5.11), we see the same behaviour.

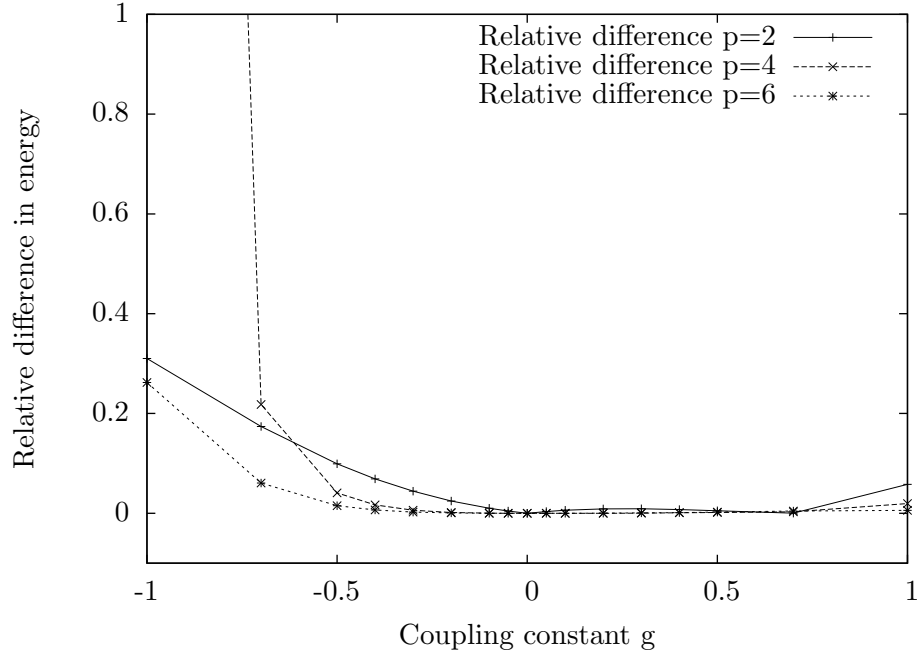


Figure 5.12: The relative difference in energy  $\varepsilon = |E^{\text{Parquet}} - E^{\text{Exact}}|/|E^{\text{Exact}}|$  for  $p = 2$ ,  $p = 4$  and  $p = 6$ .

To study the effects of increasing particle number, we show in figure 5.12 the absolute difference

$$\varepsilon = \frac{|E^{\text{Parquet}} - E^{\text{Exact}}|}{|E^{\text{Exact}}|}$$

between our energy-dependent results and the results from the exact diagonalization for the  $N = 10$  model with two, four and six particles. The odd data point at  $f = -1$  in the  $p = 4$  graph has a value close to 7. This rapid

increase is mainly due to the fact that the exact value at this point is close to 0, amplifying the difference at this point. We see that in general, the relative errors of our results reduce as the number of particles increase.

We have also investigated the changes in correlation energy as the number of particles change. We show in figure 5.13 a comparison between the energy-dependent results and exact diagonalization results. The two latter graphs are adjusted such that the ground state energies at  $g = 0$  are equal. Thus the graphs for  $p = 4$  and  $p = 6$  show the correlation energy  $E_C$  in the system due to the increased number of particles. As the number of particles increase, the correlation energy changes more rapidly with increasing interaction strength, as could be expected.

In the lower panel we show the relative difference in correlation energy

$$\varepsilon_C = \frac{|E_C^{\text{Parquet}} - E_C^{\text{Exact}}|}{|E_C^{\text{Exact}}|}$$

for the  $p = 4$  and  $p = 6$  cases relative to the  $p = 2$ . The errors have two distinct sources, namely the systematic errors introduced by the approximations employed in the solution, and the errors stemming from missing many-body correlations. If the error  $|E_C^{\text{Parquet}} - E_C^{\text{Exact}}|$  scales as the exact correlation energy with respect to the number of particles, the relative difference would be independent of particle number for four and six particles. In the lower panel of figure 5.13 we have plotted the relative difference. The graphs for four and six particles coincide in the range  $-0.7 < f < 0$ . The  $f > 0$  values show that the Parquet solution is very close to the exact, and the different behaviour might originate from the uncertainties in the extrapolation to  $\eta \rightarrow 0$ .

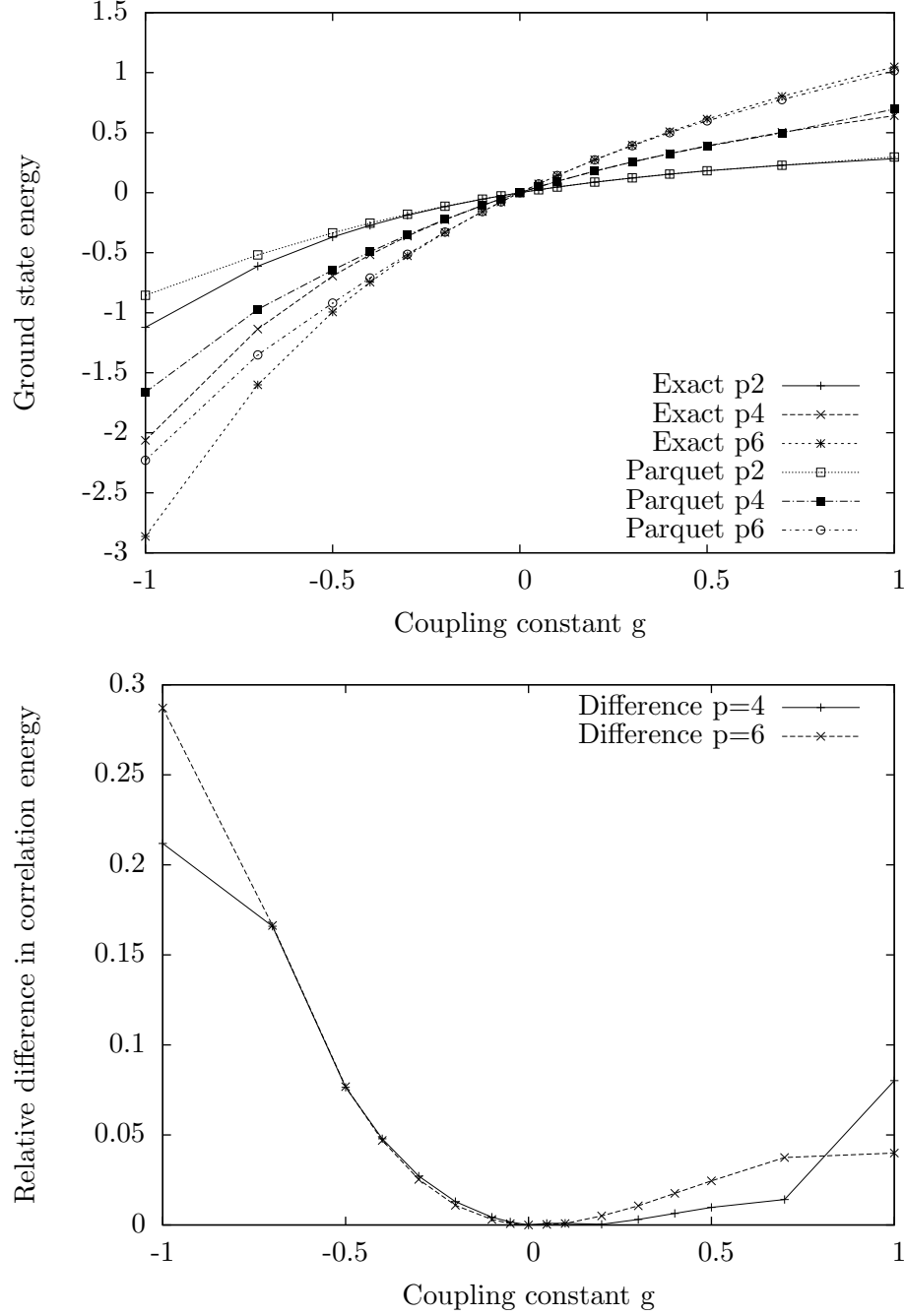


Figure 5.13: Comparison between the  $N = 10$ ,  $p = 2$  and adjusted  $p = 4$ ,  $p = 6$  exact and Parquet energy-dependent results are shown in the upper panel. The lower panel shows the relative difference in correlation energy  $\varepsilon_C = |E_C^{\text{Parquet}} - E_C^{\text{Exact}}|/|E_C^{\text{Exact}}|$  for  $p = 4$  and  $p = 6$ .

## 5.3 Pair-breaking interaction

Setting  $f \neq 0$  changes the interaction from a purely pair-conserving to a pair-breaking interaction. For simplicity, we set  $g = 0$  when discussing the impact of pair-breaking. This amounts to having a pair-breaking contribution equal in size to the pair-conserving contribution. The pair-breaking term introduces some new, interesting features to the model, most notably in the fact that the self-energy is no longer diagonal. Thus we can study the differences between the unperturbed-structure (UPS) approximation and the fixed-energy Dyson equation (FED) approximation discussed in section 4.5 in detail.

### 5.3.1 Convergence with respect to $\eta$

The convergence properties of the energy-independent UPS approximation for the  $f \neq 0$  interaction in the  $N = 2$ ,  $p = 2$  system are not quite as good as for the pairing only case, but generally similar. Most starting energies give convergence for  $f$  values close to zero, but only starting energies well away from zero give convergence for larger absolute values of  $f$ . None of the calculations converge at the value  $f = 1$ , where the first-order energies for the states 1 and 2 become equal. The results become unstable when this happens. In the upper panel of figure 5.14 we show the difference  $E_n - E_{n-1}$  between successive iterations for an energy-independent calculation with starting energy  $E_{in} = -20$  and  $E_{in} = -2$  for several  $f$  values for a  $N = 2$ ,  $p = 2$  system. All convergent points converge exponentially to machine precision within 60 iterations, most within 10 iterations. The most unstable combinations are small starting energies and large  $|f|$  values, reflected in the patterns seen for the combinations  $E_{in} = -20$ ,  $f = -1$  and  $E_{in} = -20$ ,  $f = 1$ .

For the energy-dependent unperturbed-structure (UPS) approximation calculations, convergence is good for energy mesh grids with 10-30 points. Increasing the number of points beyond that destabilizes the solution for some values of  $f$ , as then some of the mesh points hits the poles in  $\Gamma$  due to the two-time propagators. Increasing  $\eta$  remedies this, then an almost exact match between all grid sizes above 10 is observed. The exception is for  $f$  values close to 1, the breakdown point. The lower panel of figure 5.14 shows the convergence for different  $f$  values in an energy-dependent calculation for  $\eta = 0$  and  $\eta = 1$ . All points are convergent, although the oscillatory pattern for the  $f = 0.99$  case continues for at least 100 iterations. We observe that adding the imaginary component gives a more irregular convergence pattern, as in the pairing-only model.

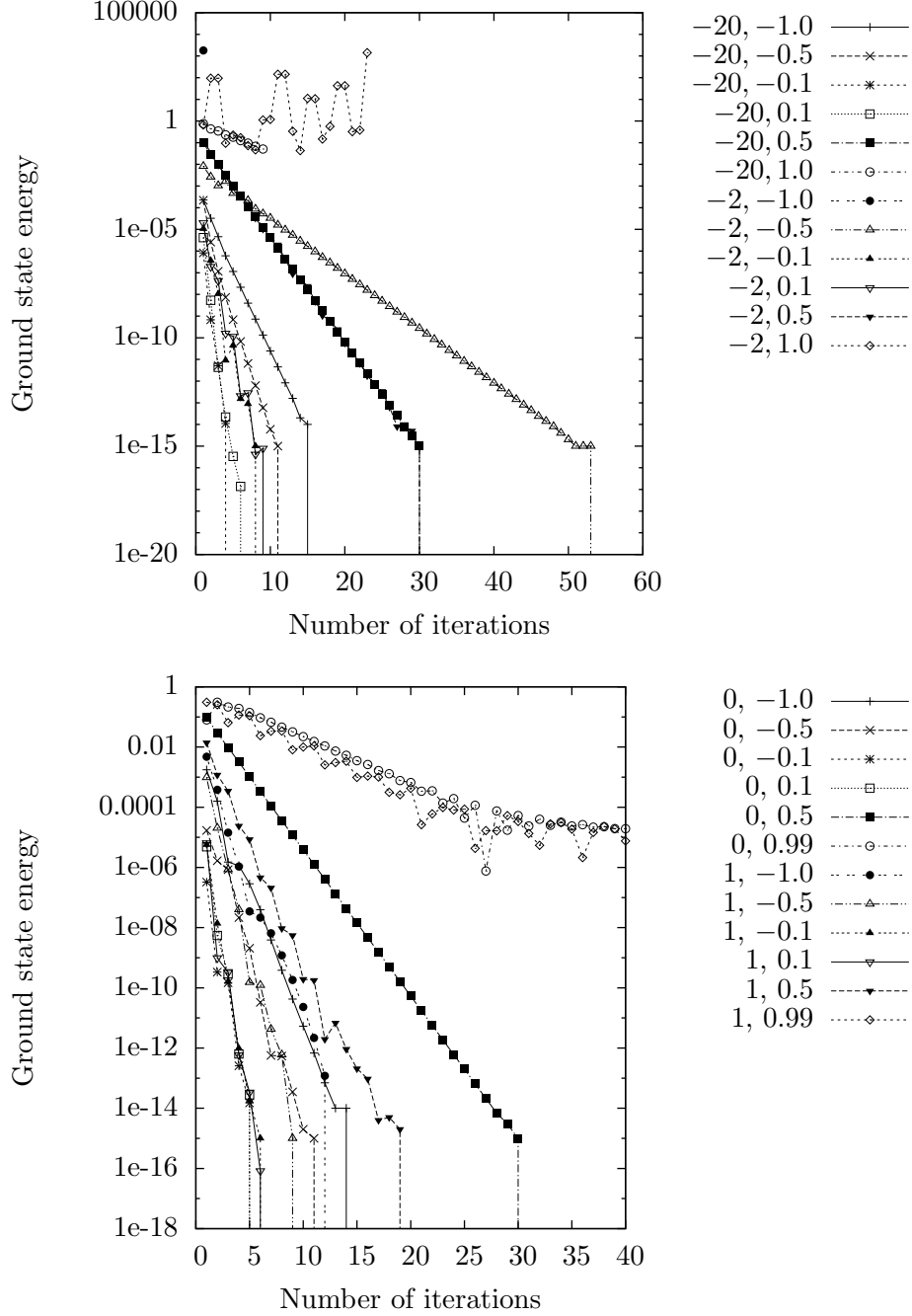


Figure 5.14: The difference  $E_n - E_{n-1}$  between successive iterations as a function of the number of iterations for the particle-hole  $N = 2$ ,  $p = 2$  model for several  $f$  values. The results in the upper panel are for energy-independent UPS calculations for starting energies  $E_{in} = -20$  and  $E_{in} = -2$ , as indicated in the pairs  $E_{in}, f$  values in the legends. In the lower panel we show results for energy-dependent UPS calculations for  $\eta = 0$  and  $\eta = 1$ , the legend being pairs of  $\eta, f$  values.



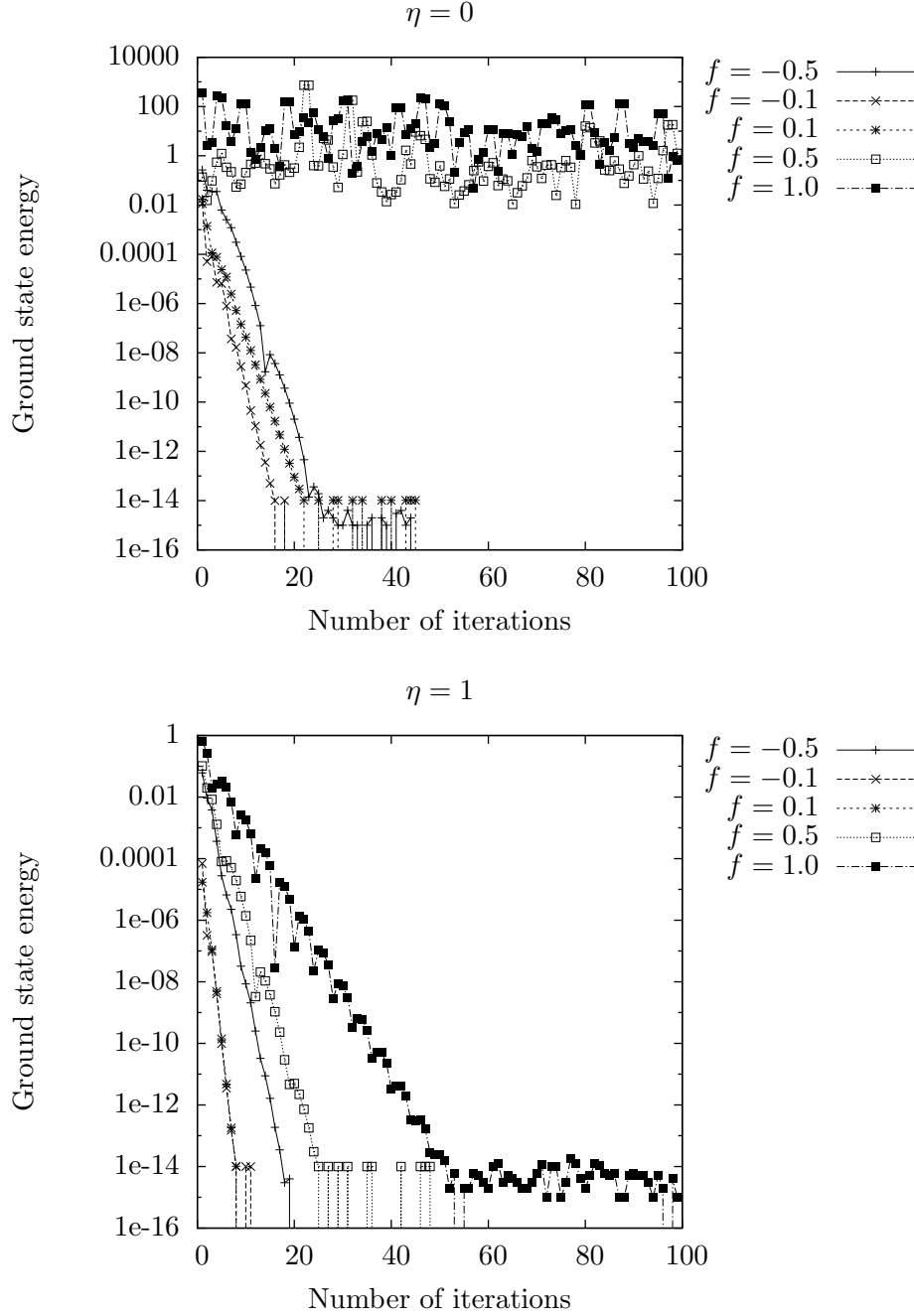


Figure 5.15: The difference  $E_n - E_{n-1}$  between successive iterations as a function of the number of iterations in the  $N = 10$ ,  $p = 4$  system. The calculations are energy-independent UPS calculations with  $E_{in} = -20$  for several  $f$  values with  $\eta = 0$  (upper panel) and  $\eta = 1$  (lower panel). Only small  $|f|$  values give convergent results for  $\eta = 0$ .

Extending to larger  $N$  and  $p$  values, obtaining convergent results for larger  $|f|$  values is increasingly hard, requiring  $\eta > 0$  even in the energy-independent case. In figure 5.15 we show the difference  $E_n - E_{n-1}$  between successive iterations for an energy-independent calculation with  $E_{in} = -20$  for several  $f$  values for a system with  $N = 10$  levels and  $p = 4$  particles. The upper panel shows results for  $\eta = 0$  and the lower panel for  $\eta = 1$ . Introducing  $\eta$  solves the convergence problems for large positive  $f$  values. The calculations for  $f = -1$  do not converge, but generally the convergence properties in this larger systems are better for smaller values of  $\eta$  than in the pair-conserving case, scaling better with increasing number of levels and particles.

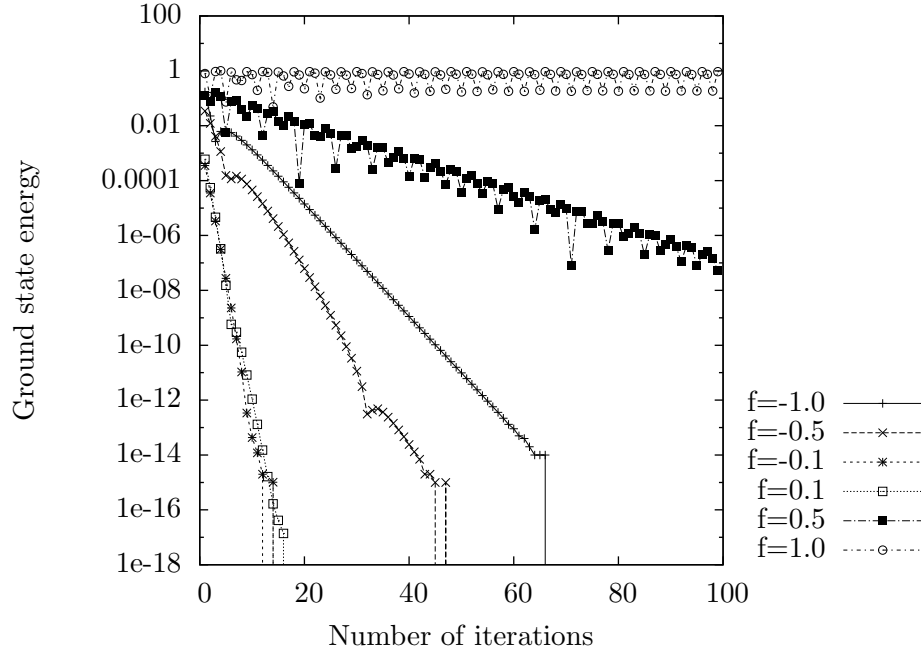


Figure 5.16: The difference  $E_n - E_{n-1}$  between successive iterations as a function of the number of iterations for energy-independent FED calculations with  $E_{in} = -20$  for several  $f$  values with  $\eta = 1$  in the  $N = 2$ ,  $p = 2$  model.

The off-diagonal elements of the self energy give off-diagonal elements of the single-particle propagator and consequently, the fixed-energy Dyson equation (FED) approximation employing the structure of equation (3.2) for the single-particle propagator gives different results from the UPS results.

For the energy-independent FED approximation, no convergent solutions can be found in the  $N = 2$ ,  $p = 2$  system for values of  $f > 0$  when  $\eta = 0$ .

Setting  $\eta > 0$  remedies this for values of  $f \lesssim 0.6$ , as illustrated in figure 5.16. Here we have shown the difference  $E_n - E_{n-1}$  for a calculation with  $\eta = 1$ . As seen from this figure, the slope of the graph for  $f = 0.5$  is rather moderate, and the  $f = 1$  graph oscillates without any decrease in amplitude.

Above  $f \sim 0.6$  the solutions start to oscillate for all  $\eta$ . Looking closer at the  $f$  values above 0.6, we see that there occurs a gradual transition from convergent to oscillatory behaviour. Fixing  $\eta = 10$ , the graphs in figure 5.17 shows that at  $f = 0.5$ , the convergence behaves nicely, while at  $f = 0.6$  oscillations starts to appear. A closer look confirms that the amplitudes diminish as the number of iterations increases. At  $f = 0.65$ , the maximum amplitude is not damped, and at  $f = 0.75$ , the solution oscillates between two values of the ground state energy.

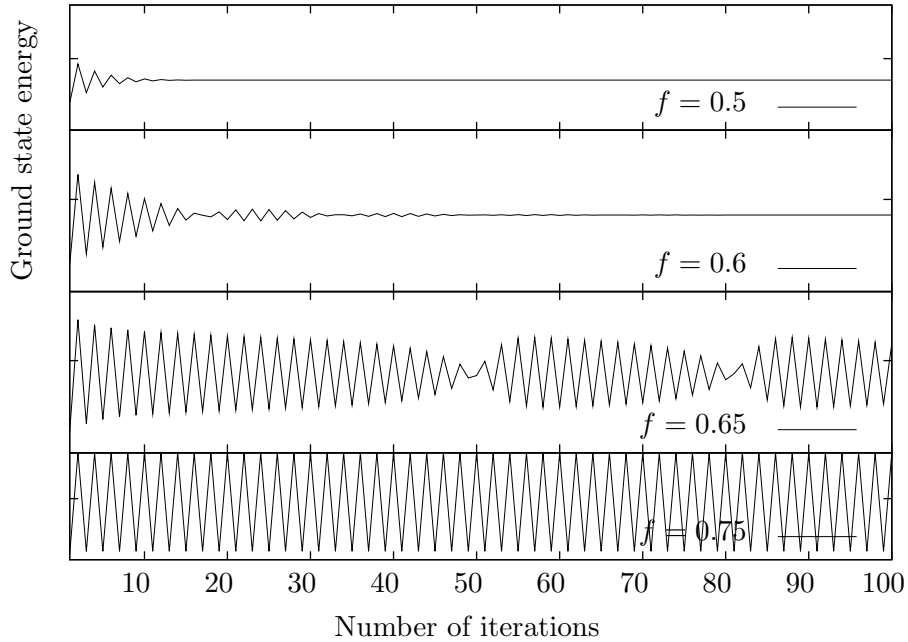


Figure 5.17: The ground state energy as a function of the number of iterations for FED calculations in the  $N = 2$ ,  $p = 2$  model with  $\eta = 10$  for  $f = 0.5, 0.6, 0.65$  and  $0.75$

The energy-dependent FED scheme performs in a similar manner as the UPS scheme with respect to number of mesh points in the energy grid, requiring larger  $\eta$  values for convergence for larger mesh sizes. The  $\eta = 0$  calculations do not converge, but the convergence is good for  $\eta > 0$  when  $f < 0.5$ , as in

the energy-independent case. For larger  $f$  values, the instabilities leads to in general poor convergence properties also in this approach. Increasing the number of levels to 10, negative values of  $f$  (attractive interaction) become unstable in the range values of  $f \sim -0.4$  to  $f \sim -0.6$ . An  $\eta$  value as large as 5 is needed before convergence is achieved. In figure 5.18 we show energy-independent calculations of the  $N = 10$ ,  $p = 2$  system for  $\eta = 1$  (upper panel) and  $\eta = 5$  (lower panel). On the other hand, the instability seen in the  $N = 2$  system at  $f > 0$  is not present any longer, that is, with higher  $\eta$  values we see convergent results for all positive  $f$  values up to 1.

The  $N = 10$ ,  $p = 4$  shows similar, but slightly less convergent patterns for positive  $f$  values, and there is no instability around  $f \sim -0.5$ . All negative  $f$  values are convergent at  $\eta = 1$ .

The energy-dependent calculations are more unstable in this approximation. For the  $N = 10$ ,  $p = 2$  system, convergence could not be obtained for any value of  $\eta$  when  $f \leq -0.7$ , and for the  $N = 10$ ,  $p = 4$  system, the limit for obtaining convergent results is  $f \leq -0.5$ .

Generally, the number of particles seems to have a larger impact on the convergence properties within the FED approximation scheme than within the UPS scheme.

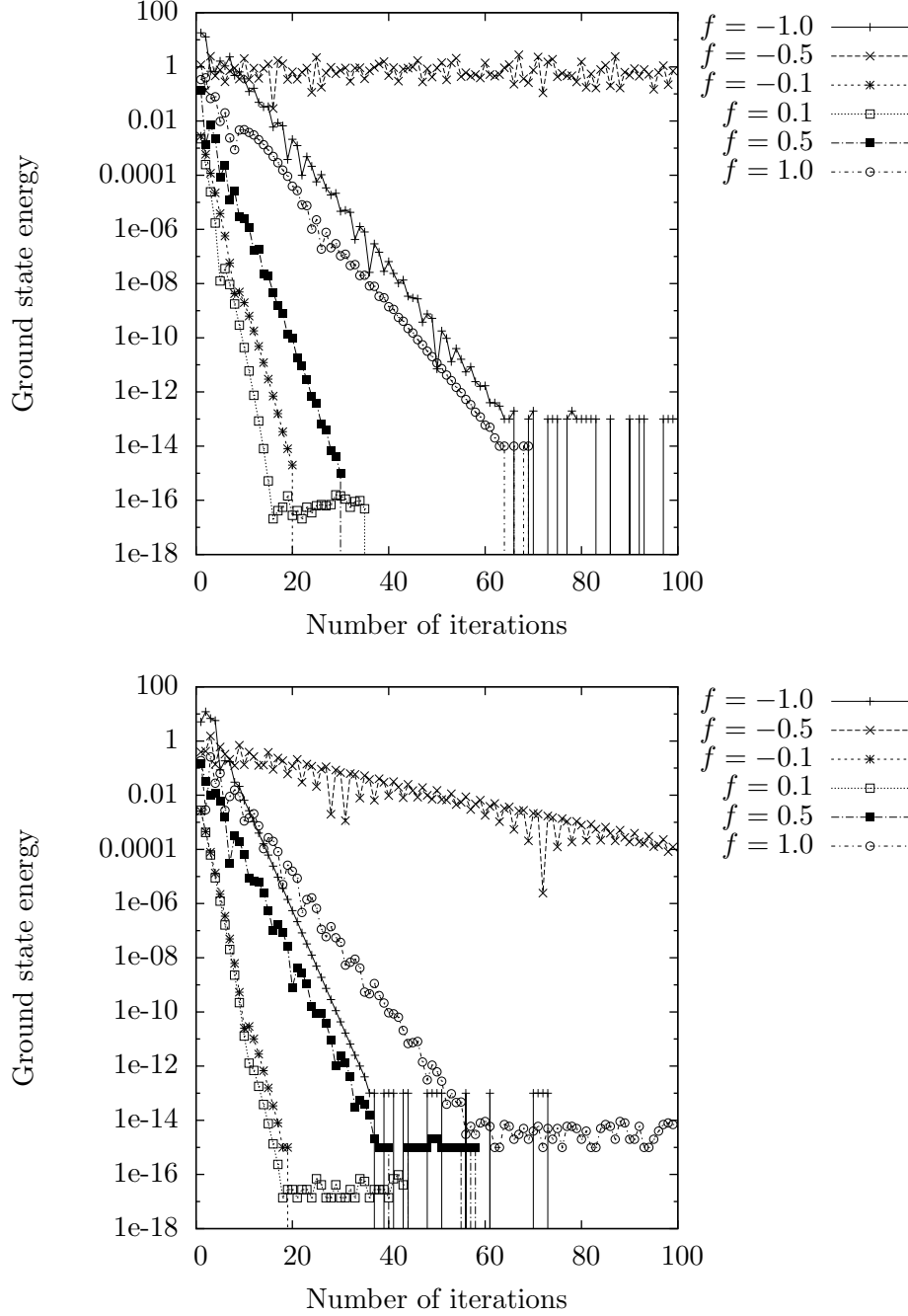


Figure 5.18: The difference  $E_n - E_{n-1}$  between successive iterations as a function of the number of iterations for energy-independent FED calculations with  $E_{in} = -20$  for several  $f$  values. with  $\eta = 1$  (upper panel) and  $\eta = 5$  (lower panel) in the  $N = 10$ ,  $p = 2$  model.

### 5.3.2 Self energy

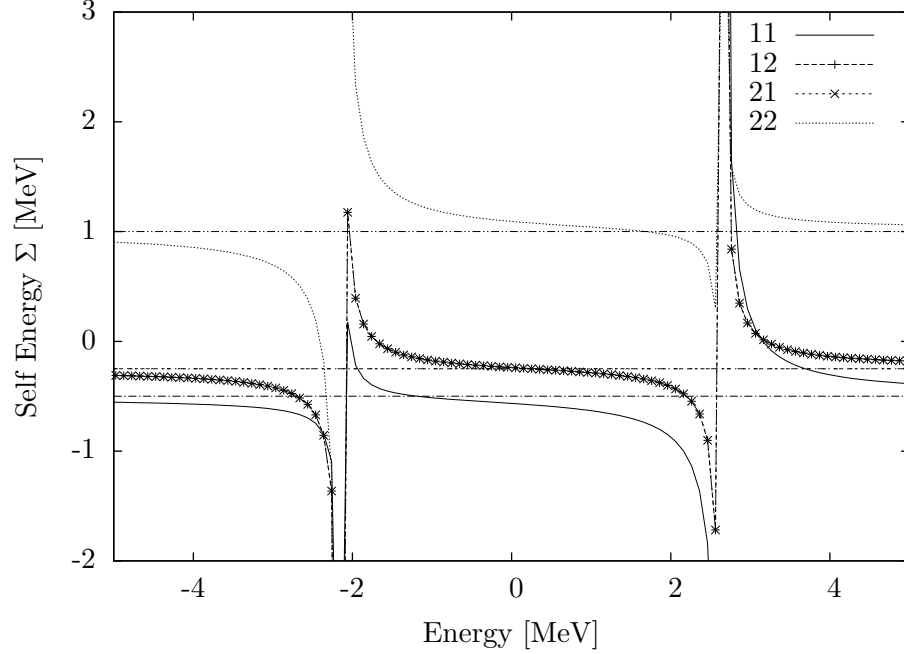


Figure 5.19: The energy dependence of the self energy for the states of an  $N = 2$ ,  $p = 2$  system with  $f = -0.5$  for an  $L = R = 0$  calculation with unperturbed propagator structure. The first-order contributions are also indicated by straight lines. The numbering of the states in the matrix elements is according to the level number as shown in figure 5.1.

The self energy exhibits some new features compared to the pairing-only model. The pair-breaking part of the interaction generates off-diagonal contributions to the first-order self energy, that is,  $\langle 1|\Sigma|2\rangle, \langle 2|\Sigma|1\rangle \neq 0$  in the  $N = 2$ ,  $p = 2$  model. This is illustrated in figure 5.19 showing the self energy matrix elements obtained by an energy-independent UPS calculation with  $L = R = 0$  and  $f = -0.5$ . The numbering of the states in the matrix elements is according to the level number as shown in figure 5.1.

Thus the solution to the Dyson equation gives single-particle energies that may differ considerably from the first-order energies  $\epsilon_{f.o.} = e_0 + \Sigma_{f.o.}$  (see equation (4.36) and the discussion in section 4.4). Looking at the self energy obtained by an energy-independent UPS calculation with  $L = R = 0$  and  $f = -0.5$  given in figure 5.19, due to the pair-breaking elements in the interaction,

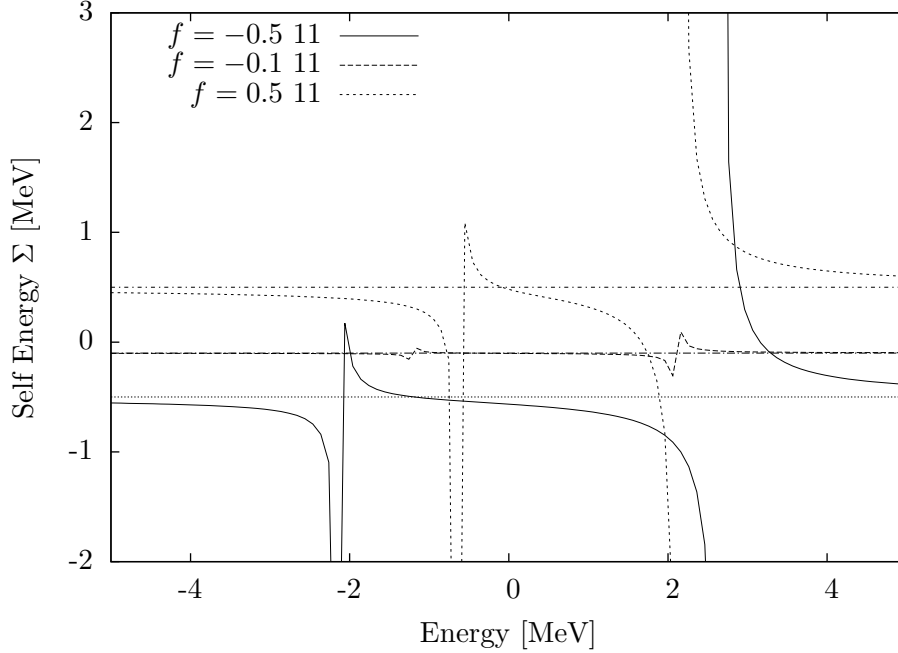


Figure 5.20: Comparison between the UPS self energy of the state  $\langle 1|\Sigma|1\rangle$  for  $f = -0.5, -0.1$  and  $0.5$ . The first-order energies are also shown as straight lines. The severity of the poles is considerably reduced for the  $f = -0.1$  case.

now each matrix element of  $\Sigma$  gets contributions from both the  $pp$  and the  $hh$  part of  $\mathcal{G}^{pphh}$ , resulting in each having two poles. This explains why the convergence properties of the  $N = 2, p = 2$  calculations are generally worse than in the pairing-only model.

As for the pairing only case, the differences when changing the starting energy, or including the full  $\Gamma$ , or changing the energy dependence scheme, or performing iterations are minimal.

Changing the interaction strength  $f$  produces similar reductions of the poles and shifts in the energy of the lowest level as varying  $g$ . Looking at the form of the interaction, we see that the matrix elements relevant for calculating the first-order energies are twice as large when  $f$  have the same numerical value as  $g$ . Comparing figure 5.20, where we have shown the lowest-lying state for  $f = -0.5, f = -0.1$  and  $f = 0.5$ , with the corresponding graph for  $g$  in figure 5.6, we find that the shift in either direction are doubled, as expected. This is why the instability due to the crossing of the first-order energies occur already at  $f = 1$ , while  $g = 1$  is fine.

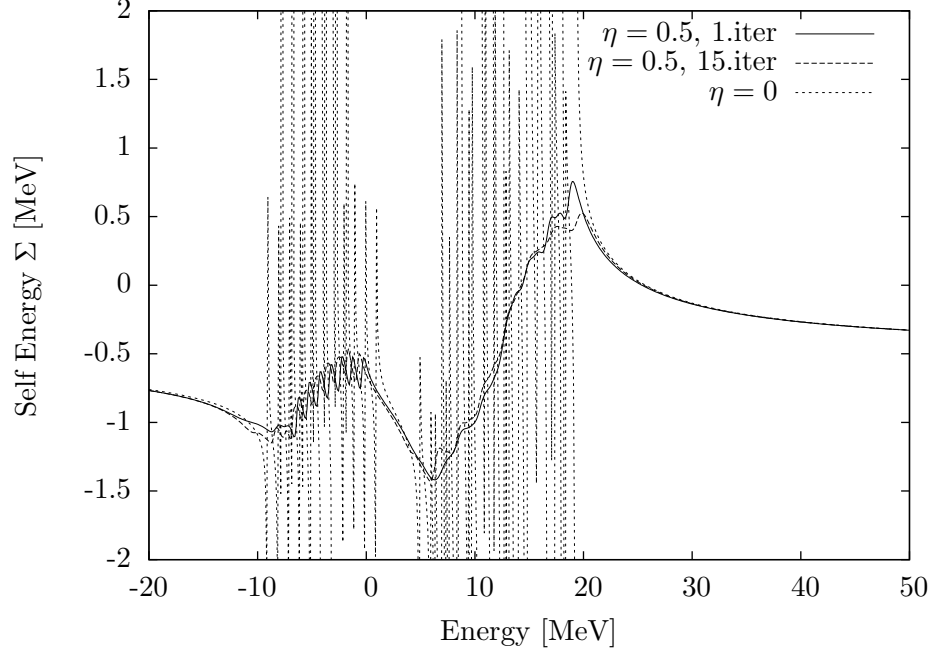


Figure 5.21:  $\langle 1|\Sigma|1\rangle$  for  $\eta = 0$  after the first iteration and for  $\eta = 0.5$  after the first iteration and after fifteen iterations in the  $N = 10$ ,  $p = 6$  system in a UPS energy-independent calculation. The number of poles in the  $\eta = 0$  case are smoothed to a continuous average for  $\eta = 0.5$ .

Increasing the number of particles give the expected increase in the number of poles, as seen in figure 5.21, where we have shown the self energy element  $\langle 1|\Sigma|1\rangle$  for a system with  $N = 10$  and  $p = 6$  at  $f = -0.5$ . The different graphs are for an  $\eta = 0$  calculation, an  $\eta = 0.5$  calculation after the first iteration and an  $\eta = 0.5$  calculation after 15 iterations. That the  $\eta = 0$  calculation does not converge comes as no surprise, given the number of poles to be handled. The density of poles is so high that the smoothening effect of  $\eta$  is to blur the pole structure for positive energies (due to two-particle-one-hole excitations) into resembling an average, while the pole structure at negative energies (due to two-hole-one-particle excitations) still can be discerned. The iterative procedure does not change the general features, but we observe that the remaining pole structure seems to shift somewhat to lower energies.

In figure 5.22 all diagonal matrix elements of  $\Sigma$  in the calculation with  $\eta = 0.5$  after 15 iterations are shown. The off-diagonal element  $\langle 1|\Sigma|2\rangle$  and  $\langle 2|\Sigma|1\rangle$  are representative for all the off-diagonal elements. They have values slightly



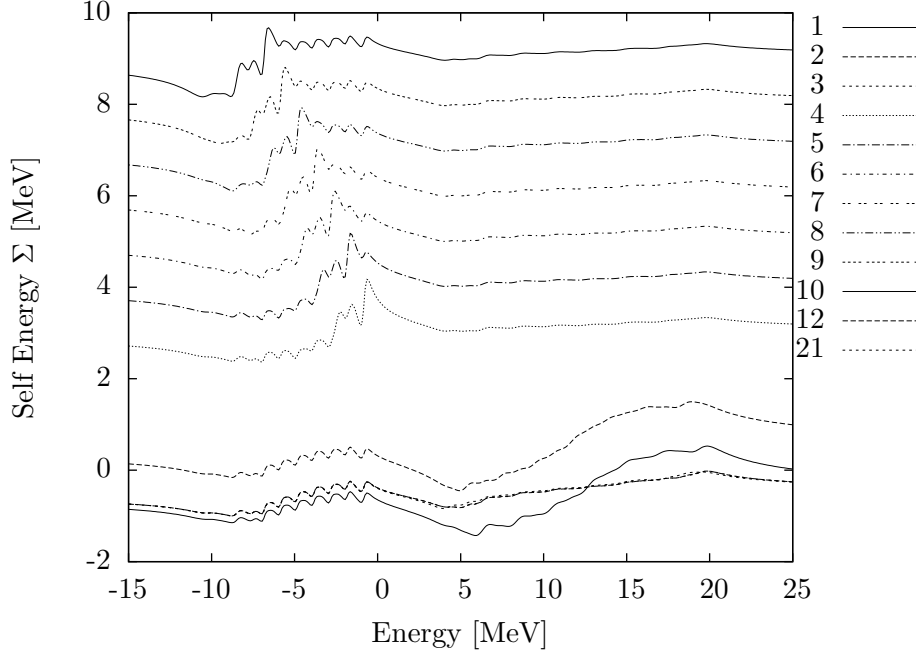


Figure 5.22: The diagonal matrix elements of  $\Sigma$  after fifteen iterations in the  $N = 10$ ,  $p = 6$  system in a UPS energy-independent calculation for  $\eta = 0.5$  at  $f = -0.5$ . In the legend, the number 1 is an abbreviation for the matrix element  $\langle 1|\Sigma|1\rangle$ , and so forth up to 10. The number 12 is an abbreviation for the off-diagonal element  $\langle 1|\Sigma|2\rangle$  and the number 21 an abbreviation for the element  $\langle 2|\Sigma|1\rangle$ . Only the hole states have remnants of the pole structure stemming from two-particle-one-hole propagation.

below 0, and the remnants of pole structure is most prominent at negative energies. Note that the two elements are equal, that is, the self energy matrix is symmetric. The diagonal elements have averages around the non-interacting level energies. Only the diagonal elements corresponding to hole states have a distinct shape stemming from two-particle-one-hole propagation. The pole structures of the hole diagonal elements and particle diagonal elements for the  $\eta = 0$  calculation have different averages (although both types show the characteristic two groups of poles seen in the  $\eta = 0$  graph of figure 5.21), and this is reflected in the different shapes of the  $\eta = 0.5$  graphs.

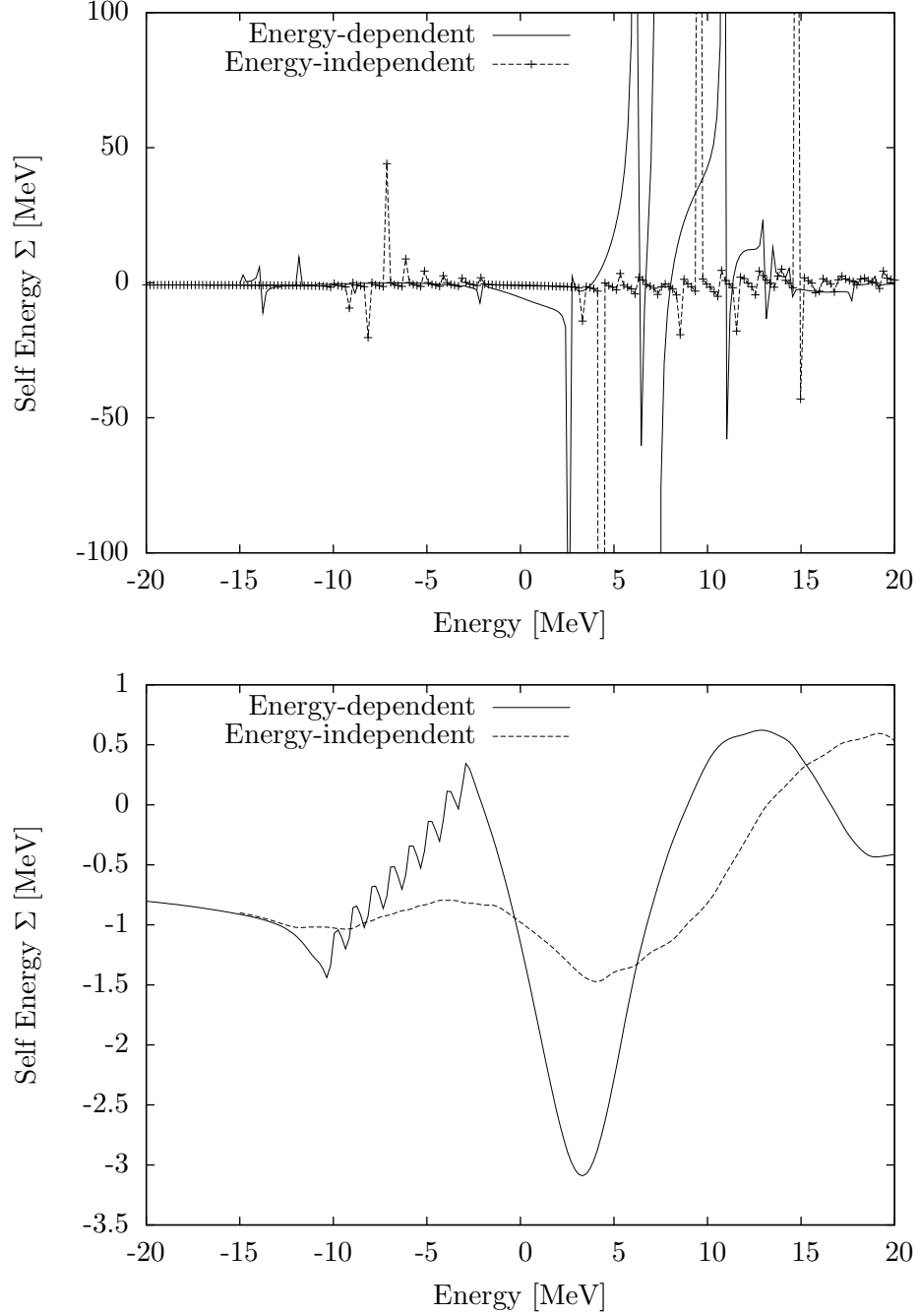


Figure 5.23: The difference between the matrix element  $\langle 1|\Sigma|1\rangle$  of the self energy of an energy-independent and an energy-dependent UPS calculation after 1 iteration in the  $N = 10$ ,  $p = 4$  system with  $\eta = 0$  in the upper panel and with  $\eta = 1$  in the lower panel.

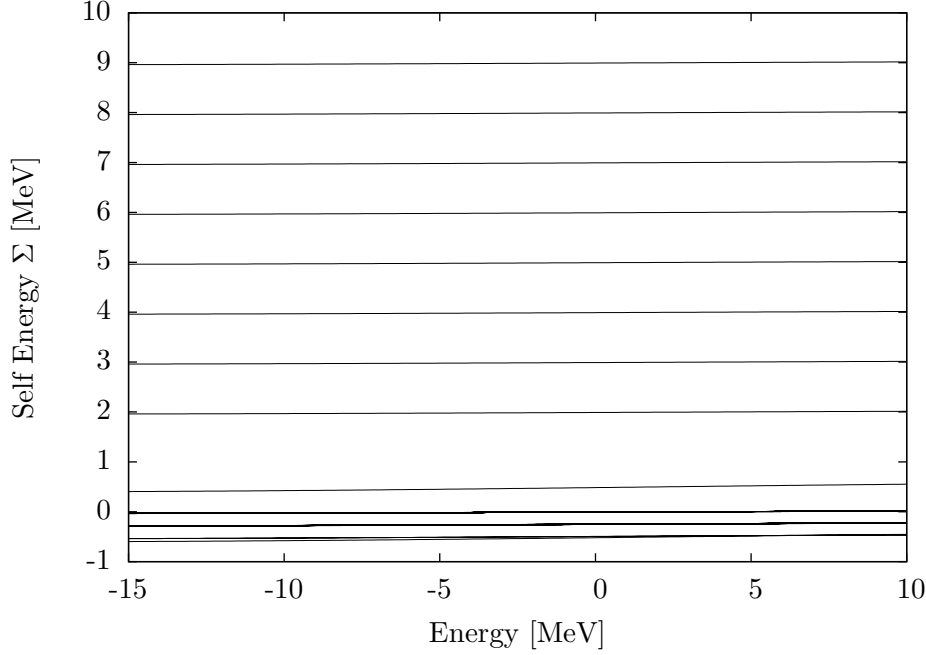


Figure 5.24: The matrix elements of the self energy after 10 iterations in the  $N = 10$ ,  $p = 4$  system in a UPS energy-dependent calculation with  $\eta = 30$ . The large  $\eta$  dampens all structure, making the self energy effectively energy-independent.

The  $\langle 1|\Sigma|1\rangle$  element in an energy-independent and an energy-dependent UPS calculation with  $\eta = 0$  is given in the upper panel of figure 5.23. The influence of the poles of the  $L$  and  $R$  contributions to  $\Gamma$  makes the energy-dependent self energy more irregular and the poles more prominent for positive energies than in the energy-independent case. We observe that the poles at negative energies are shifted to the left. In the lower panel we have shown the same two matrix elements after the first iteration when  $\eta = 1$  in both calculations. The simpler structure and generally smaller amplitudes in the energy-independent  $\eta = 0$  case give a faster damping with  $\eta$  than in the energy-dependent case, at least partly explaining the better convergence properties. The main contribution stemming from two-particle-one-hole propagation is shifted towards higher energies.

For very large  $\eta$ , the self energies become almost energy-independent, as seen from figure 5.24, where we have shown the self energies found after 10 iterations of an energy-dependent calculation in the  $N = 10$ ,  $p = 4$  system. The solution found is thus of a mean-field type, and increasing  $\eta$  further

changes very little. The solution is different from the first-order solution, however, as the self energies are complex, and there are a larger number of non-zero off-diagonal matrix elements. The self energy changes considerably when

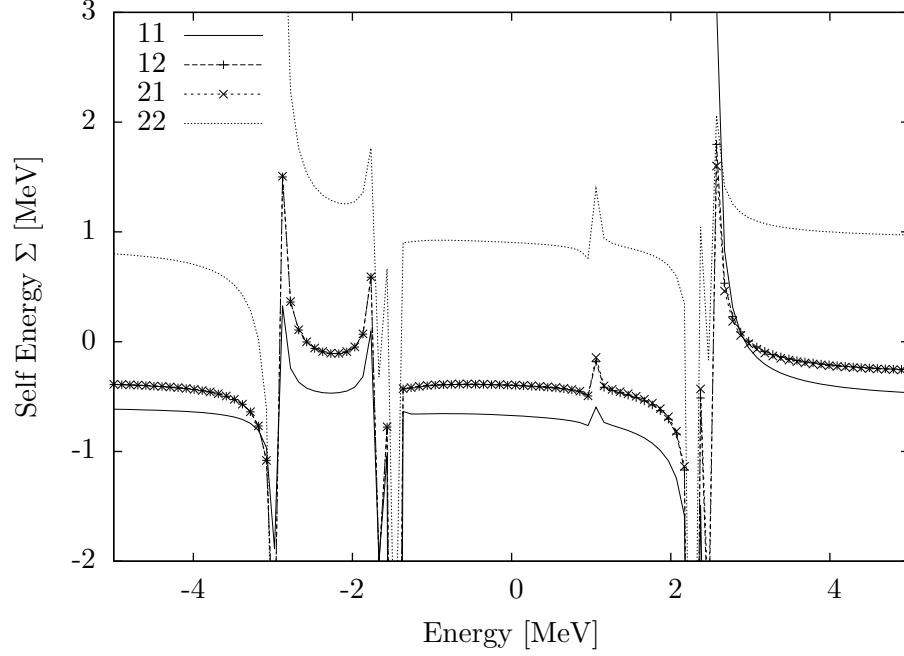


Figure 5.25: FED energy-independent  $\Sigma$  as a function of energy calculated for  $f = -0.5$  in the  $N = 2$ ,  $p = 2$  system. The legends shows the indices of  $\Sigma$ , that is,  $\langle 1|\Sigma|1 \rangle$  and so forth. The number of poles have increased compared to the self energy calculated in the UPS scheme of figure 5.19.

the FED approximation is employed. In figure 5.25 we show the self energy for a  $f = -0.5$  energy-independent calculation. Compared to the UPS self energy in figure 5.19, there are several more poles. The  $\mathcal{G}^{pphh}$  propagator has eight poles in this approximation (the Dyson equation solution gives only two energies in each sum in equation (3.2)), but some will probably be quenched by the small removal/addition amplitudes. The region around  $f = 0.5 - 0.7$  warrants closer inspection, as the convergence studies indicate that no convergent results can be found in the  $N = 2$ ,  $p = 2$  system. We see that as  $f$  increase the poles of the self energy based on first-order energies broaden significantly. At  $f = 1$  they merge, as shown in the graphs in the upper panel of figure 5.26. The second-order self energy contributions used in solving the Dyson equation in the first iteration are calculated from this self energy, and

the result of the broadening is seen in that the poles coming from the hole-hole-particle propagation moves fast towards larger energies as  $f$  increases. This is seen in the lower panel in figure 5.26, where the self energy after the first iteration for the different values of  $f$  is shown. The iterative self-consistency procedure is barely able to regain stability for  $f = 0.4$  at  $\eta = 0$ . When  $\eta$  becomes large, all structure is lost, and the solution found is a mean-field solution. The convergence failure at large  $f$  indicates that no such solution can be found within our scheme. Increasing  $N$  and  $p$ , we know that it is necessary to have  $\eta > 0$  to obtain convergence. As the number of poles in the larger systems quickly becomes quite large, the effect of  $\eta$  is to dampen the pole structure of the self energy to resemble an average self energy, in the same manner as in the UPS case. In the upper panel of figure 5.27 we have shown the matrix element  $\langle 1|\Sigma|1\rangle$  in the  $N = 10$ ,  $p = 4$  for calculations with  $\eta = 0$  and with  $\eta = 1$ . The self energy matrix elements in the  $\eta = 0$  case show the characteristic separation between the two groups of poles.

We have shown diagonal matrix elements  $\langle 1|\Sigma|1\rangle$  and  $\langle 3|\Sigma|3\rangle$  of the  $\eta = 1$  calculation in the lower panel of figure 5.27. These are representative for the self energy corresponding to holes ( $\langle 1|\Sigma|1\rangle$ ) and particles ( $\langle 3|\Sigma|3\rangle$ ). The general trends for all matrix elements are similar to the corresponding graphs for the UPS case given in figure 5.22. The average energies of the diagonal elements are determined by the input energy level, and the structure at negative energies shifting to the left with increasing level number.

The interesting feature to notice in the lower panel of figure 5.27 is the fact that the off-diagonal matrix elements are unequal, due to the off-diagonal elements of the single-particle propagator. Thus the self energy matrix in the Dyson equation is a non-symmetric matrix in the FED approximation.

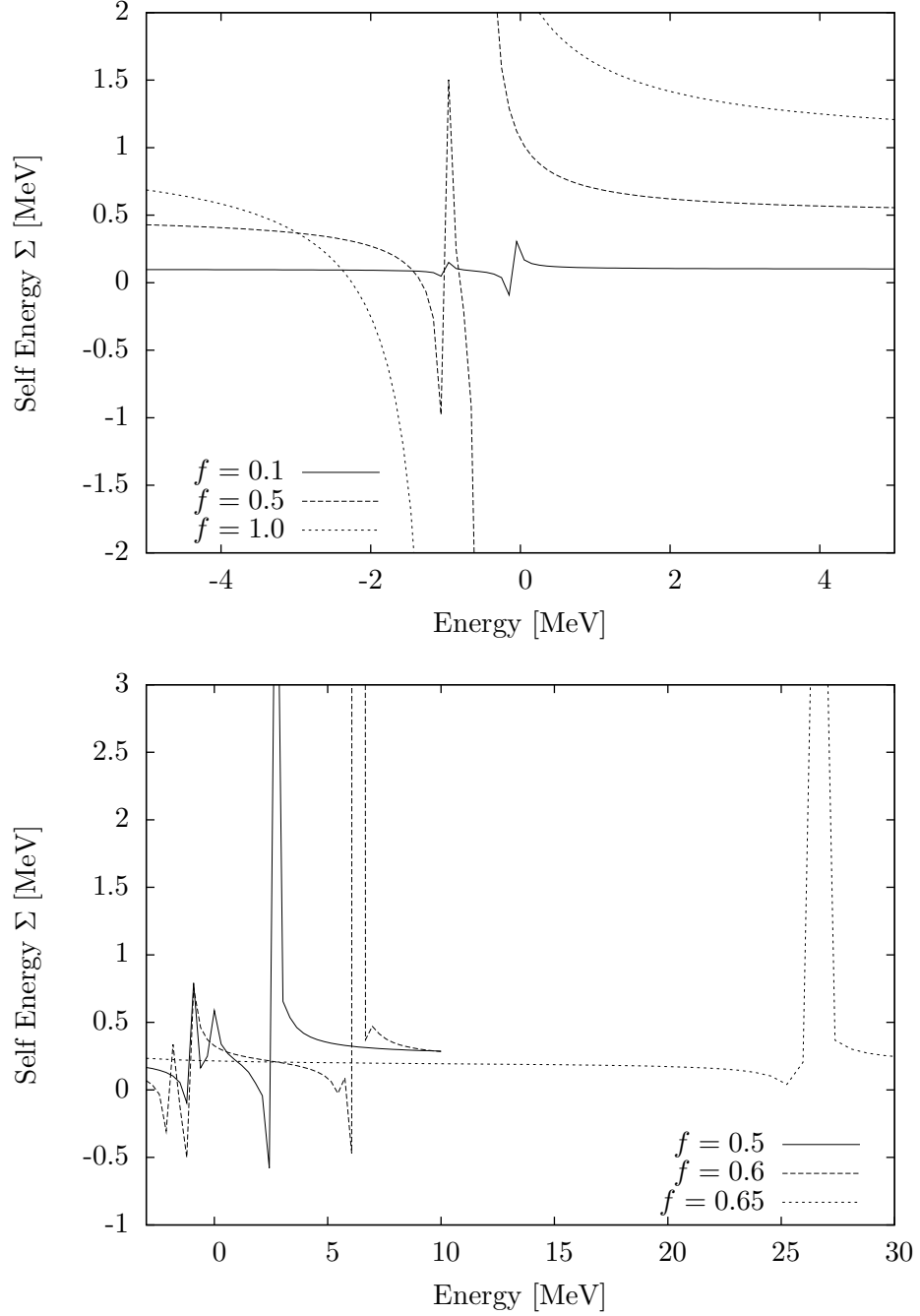


Figure 5.26: In the FED approximation scheme, we show  $\langle 1|\Sigma|1\rangle$  as calculated from the first order energies only for  $f = 0.1, 0.5$  and  $1$  in the upper panel,  $\langle 1|\Sigma|1\rangle$  calculated from energies including second-order contributions after the first iteration for  $f = 0.5, 0.6$  and  $0.65$  in the lower panel. We see how the merging of the poles occurring as  $f$  increase at the first-order level gives rise to 'runaway' poles in the full calculation.

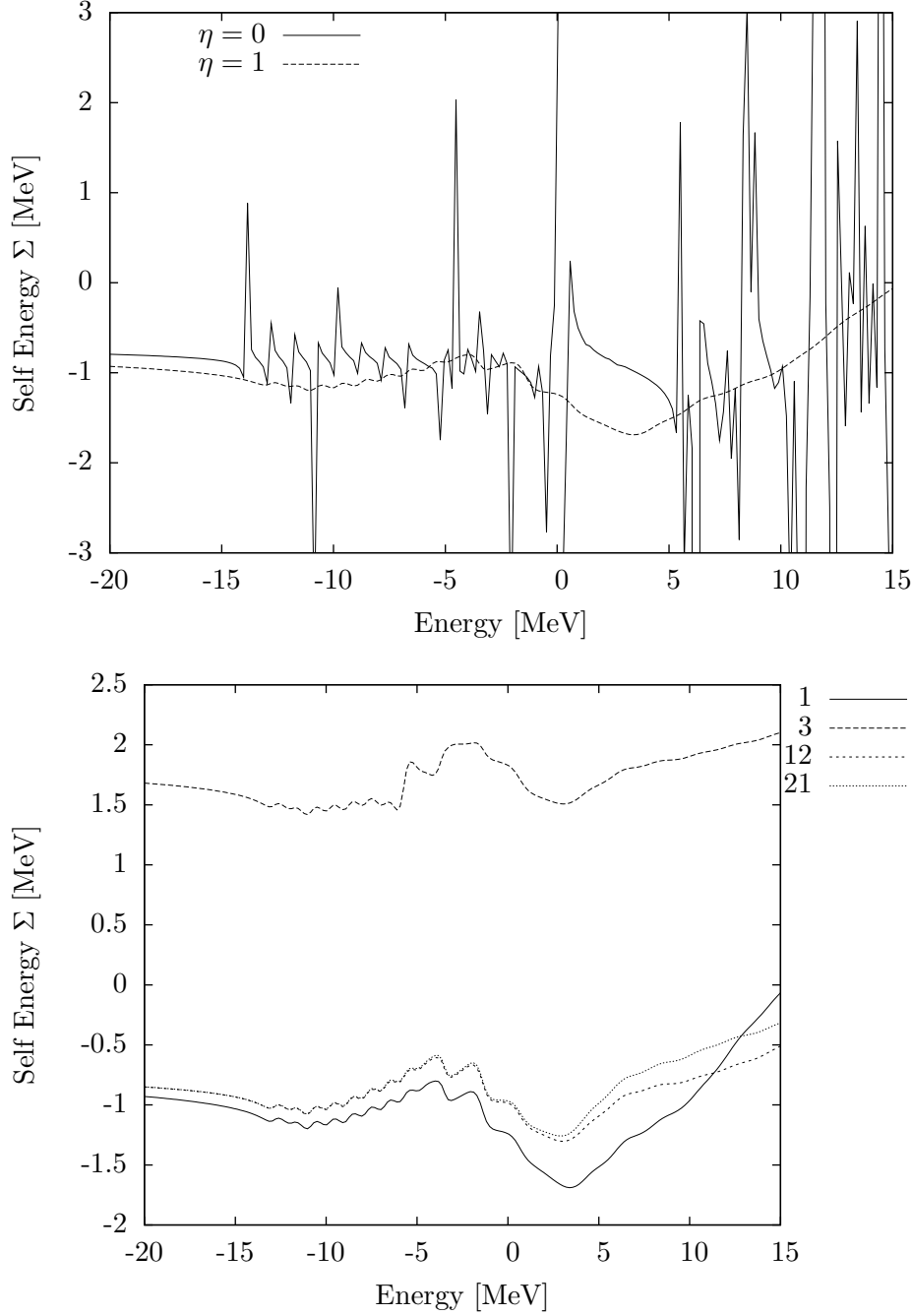


Figure 5.27: The upper panel shows the  $\langle 1|\Sigma|1\rangle$  matrix element in the  $N = 10$ ,  $p = 4$  system at  $f = -0.5$  for  $\eta = 0$  and for  $\eta = 1$  after the first iteration. The lower panel shows the diagonal matrix elements  $\langle 1|\Sigma|1\rangle$  (labelled 1) and  $\langle 3|\Sigma|3\rangle$  (labelled 3), and the off-diagonal elements  $\langle 1|\Sigma|2\rangle$  (labelled 12) and  $\langle 2|\Sigma|1\rangle$  (labelled 21). The off-diagonal elements are not equal.

### 5.3.3 Spectral functions

The spectral functions discussed in section 3.1 are not particularly interesting in the UPS approximation, as the form of the single-particle propagator forces all amplitudes to be exactly 1. In the FED approximation the single particle propagator has non-diagonal amplitudes, resulting in a discrete spectral function. As discussed in section 4.5.2, the coupling between states with different orbital numbers will give hole spectral functions which have some probability of having an higher energy. As each energy can be identified with a definite orbital, the height of the spike at that energy gives the spectroscopic factor of that orbital. When the interaction is 0, the particles are independent, and the

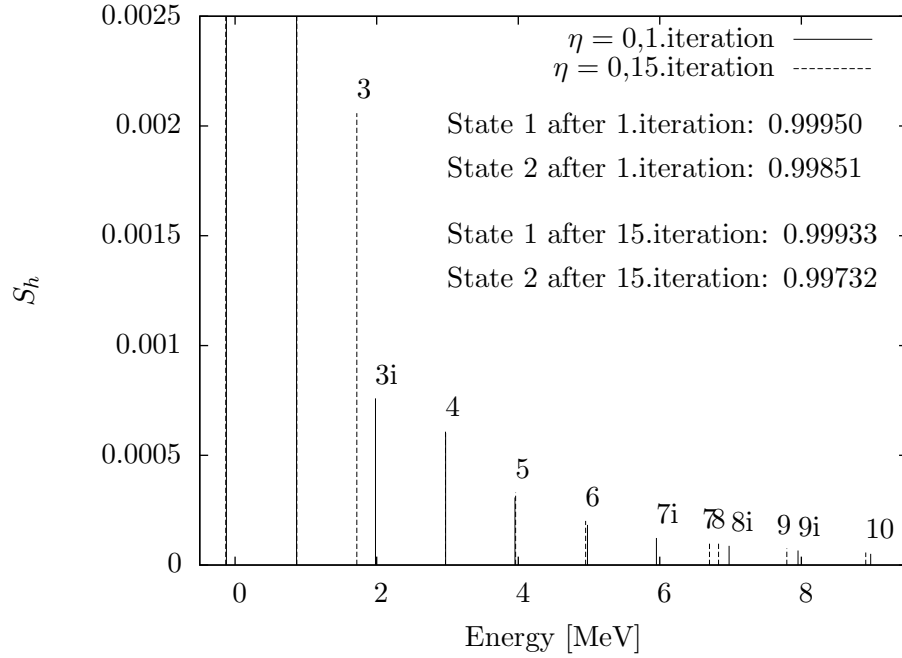


Figure 5.28: Spectral function in the  $N = 10$ ,  $p = 4$  system with  $f = -0.1$ , after 1 and after 15 iterations. The numbers above each bar is the level associated with that energy (due to the approximation of the Dyson equation, such a correspondence can be made), according to the numbers of figure 5.1. The duplicate numbers 3i and 3 and so forth indicate the spectral function after 1 iteration and after 15 iterations, respectively. Only a small amount of the hole strength is distributed to the particle states at this small  $|f|$  value.

spectral function will have one spike of height 1 at the energy of each basis state. The hole spectral function has thus 1 at the levels chosen to be holes,



and 0 at the levels chosen to be particles. The effect of changing the interaction strength  $f$  is to reduce the height of the most dominant spikes, giving small amplitudes also at the energies of the other basis states, as shown in figure 5.28 for a  $N = 10, p = 4$  system with  $f = -0.1$ . The state numbers are according to the level scheme in figure 5.1. Only a small amount of the hole strength is distributed to the particle states at this small  $|f|$  value. In the same figure we have also shown the hole spectral function obtained after 15 iterations, confirming that the process of self-consistency does not influence much on this function when the interaction strength is small. As explained in section 4.5.2 on the FED approximation scheme, the particle spectral function exactly mirrors the hole function.

Increasing the interaction strength to  $f = -0.5$  gives unstable results for  $\eta = 0$ . In the upper panel of figure 5.29 we compare the results for the hole spectral function in the  $N = 10, p = 4$  system at  $\eta = 0.5$  after the first iteration and after 15 iterations. The two lowest-energy (hole) states start out having a height close to 1, and there is very little strength on any of the higher-lying states. During the iteration procedure, the energy of the lowest state is considerably lowered, but the strength remains almost the same. The second hole state remains at almost the same energy, but the strength is reduced by around 30%, and the strength of the higher states increased accordingly. Especially the third state obtains a significant enhancement relative to the initial height, and also a reduction in energy. The energy shifts become smaller for the higher states, reflecting that the probability of excitations and the influence of the interaction is minimal at these energy scales. The effect of increasing  $\eta$  is illustrated in the lower panel of figure 5.29, where we have shown results after 15 iterations of calculations with  $\eta = 0.5, 1$  and  $7$  in the  $N = 10, p = 4$  system with  $f = -0.5$ . The  $\eta = 7$  results have a closer resemblance to a calculation with weaker interaction strength (lower absolute value of  $|f|$ ). The energy levels are more evenly spaced and more of the strength is conserved in the lowest levels, illustrating the general effect of  $\eta$  as a parameter which lessens the effect of the interaction and forces the solution closer to a mean-field pattern.

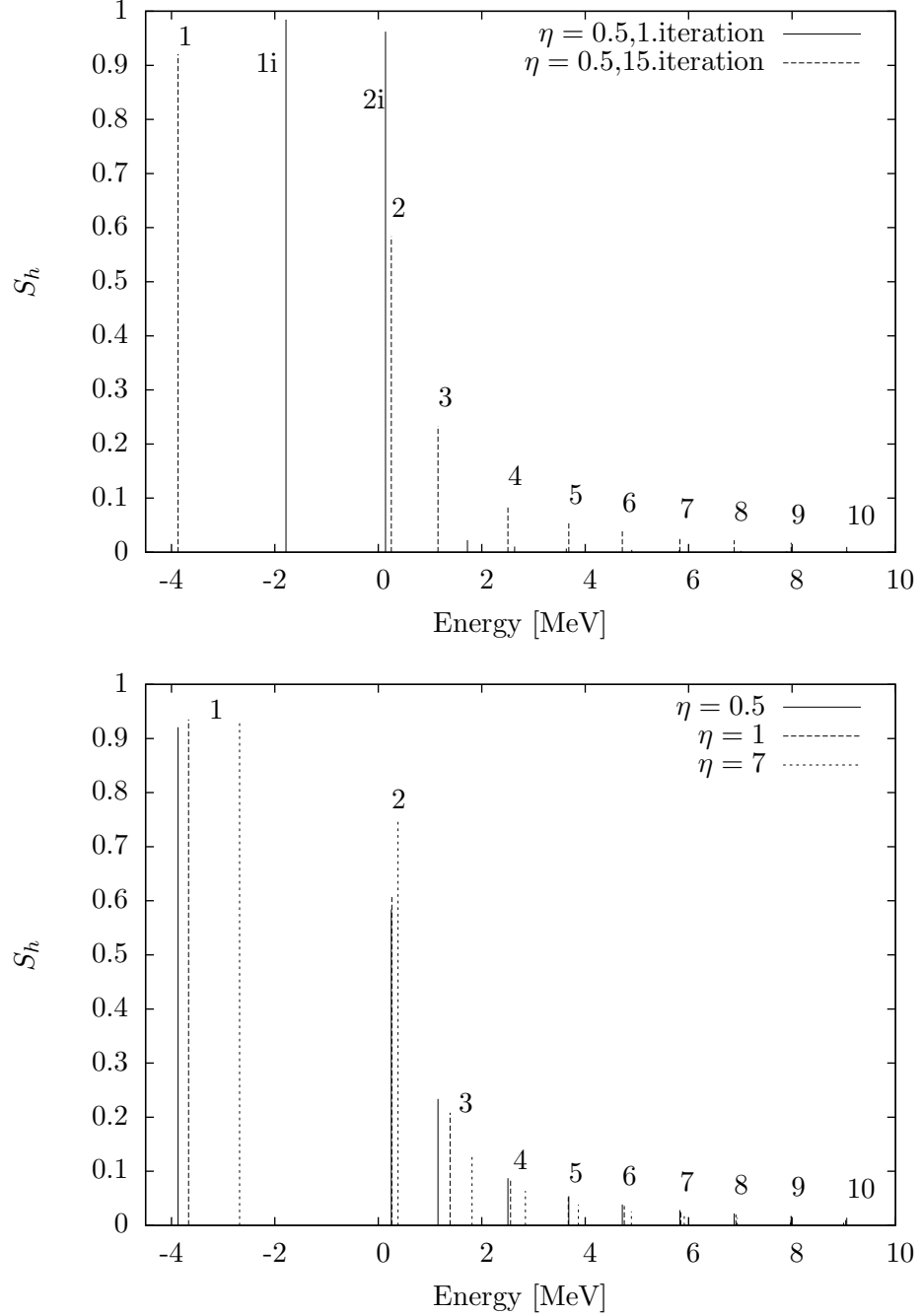


Figure 5.29: Spectral function in the  $N = 10$ ,  $p = 4$  system with  $f = -0.5$ . In the upper panel the differences between 1 and after 15 iterations is shown. The lower panel shows several  $\eta$  values after 15 iterations. The state numbers are according to the level scheme in figure 5.1. The duplicate numbers 1i and 1 and so forth indicate the spectral function after 1 iteration and after 15 iterations, respectively.

### 5.3.4 Comparison with exact diagonalization

The differences between different starting energies are minimal in the energy-independent UPS  $f \neq 0$  calculations, and thus we show results only for  $E_{in} = -50$ . However, based on the convergence results, we have done calculations for  $\eta = 1, 2, 3, 5$  and  $10$ , and used these results as a basis for a linear extrapolation to obtain the graphs in figure 5.30 and 5.31. For the energy-dependent calculations, only the  $N = 2, p = 2$  model has convergent results for small enough  $\eta$  values to make an extrapolation meaningful. Higher  $\eta$  values remove all pole structure from the self energy, creating an effectively energy-independent solution, and the differences between different  $\eta$  values are small. For the larger systems shown in figure 5.31 we show the results from calculations at  $\eta = 5$  (the lowest convergent value),  $30$  and  $60$ , to show the relatively minimal differences. In figure 5.30 we display results for the  $N = 2$ ,

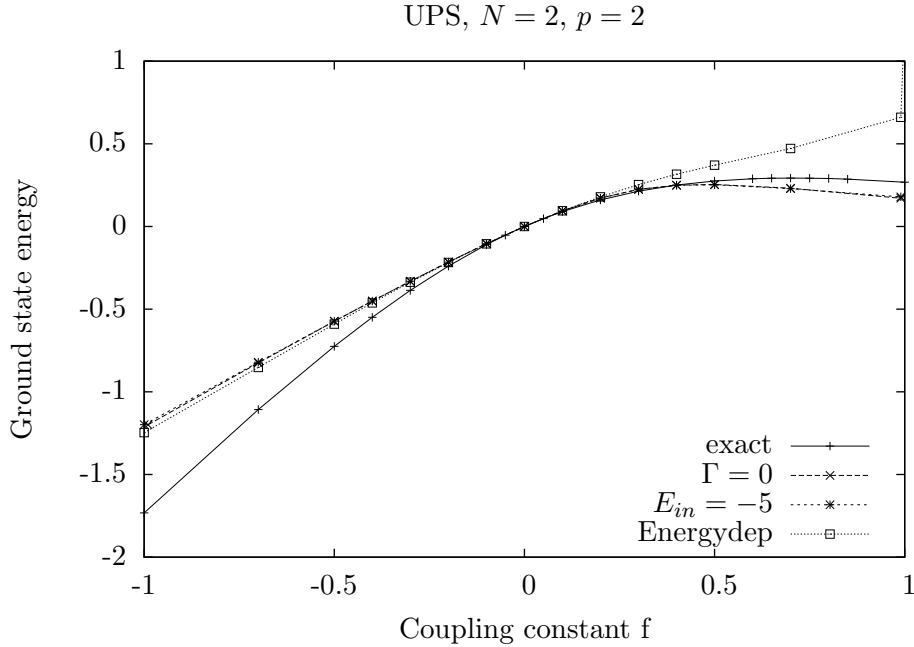


Figure 5.30: Ground state energy of UPS calculations compared with exact solution for the  $N = 2, p = 2$  model.

$p = 2$  system. We see how the differences between the energy-independent and energy-dependent calculations are small compared with the deviations from the exact solution for  $f < 0$ . The differences increase as  $|f|$  increase.

For  $f > 0$ , the energy-independent calculation does better than the energy-dependent version for the region where convergent results could be obtained.

The tendency for the energy-independent calculations to be closer to the exact results is seen also when the system size and particle number increase as in figure 5.31. The energy-independent calculations are able to follow the general curvature of the exact solution to a much higher degree than the energy-dependent results. This is mainly due to the poor convergence properties of the energy-dependent calculations. Closer inspection of the  $N = 10$ ,  $p = 4$  results in the lower panel shows that the  $\eta = 5$  curve (in the range of  $f$  values where convergent results could be obtained) has points more in keeping with the energy-independent results than the points from the calculations with larger  $\eta$  values.

The FED calculations for the simple  $N = 2$ ,  $p = 2$  system have a much closer correspondence to the exact calculation for  $f < 0$  values, as shown in figure 5.32. The differences between different starting energies are rather small in this approach as well. The upper panel of the figure shows graphs for  $E_{in} = -5$  and an extrapolation based on extrapolation from calculations with  $\eta = 1, 5$  and  $10$ . For  $f > 0$  the results destabilize around  $f = 0.3$ , as expected from the discussion on the convergence. The extrapolated results are not able to do any better than the  $\eta = 0$  results, and overbinds at  $f < 0$  in the same manner as the  $L = R = 0$  results. Energy-dependent calculations, as shown in the lower panel of figure 5.32, show in general the same behaviour as the energy-independent calculations. Results extrapolated from calculations with  $\eta = 1, 2, 3, 5$  and  $10$  manage to agree nicely with the exact solution up to  $f = 0.5$  before becoming too unstable.

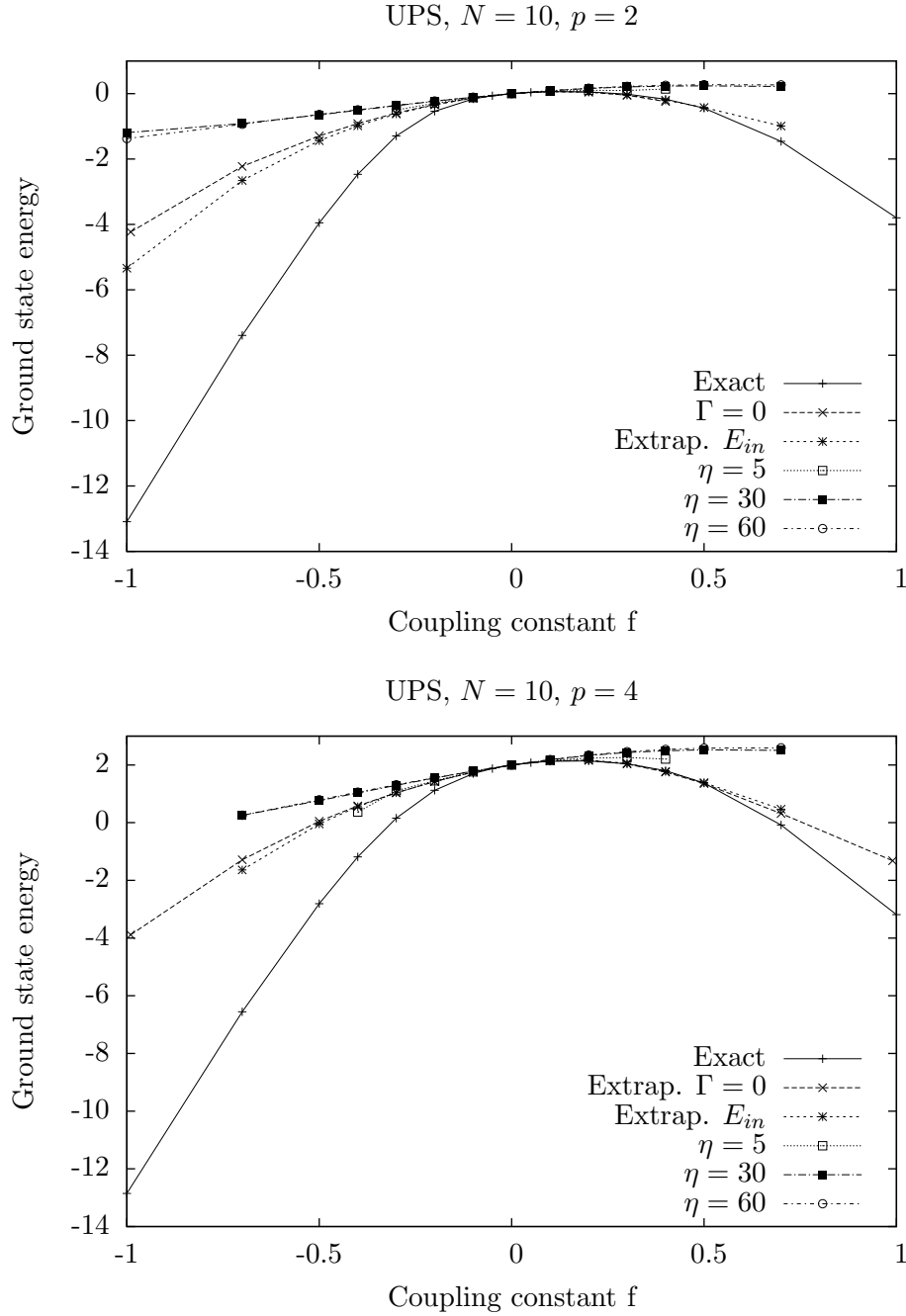


Figure 5.31: Ground state energy of UPS calculations compared with exact solution for the  $N = 10$ ,  $p = 2$  model (upper panel) and  $N = 10$ ,  $p = 4$  (lower panel). In general, the energy-independent calculations show best agreement with the exact solution, but the differences are large for  $f < -0.3$

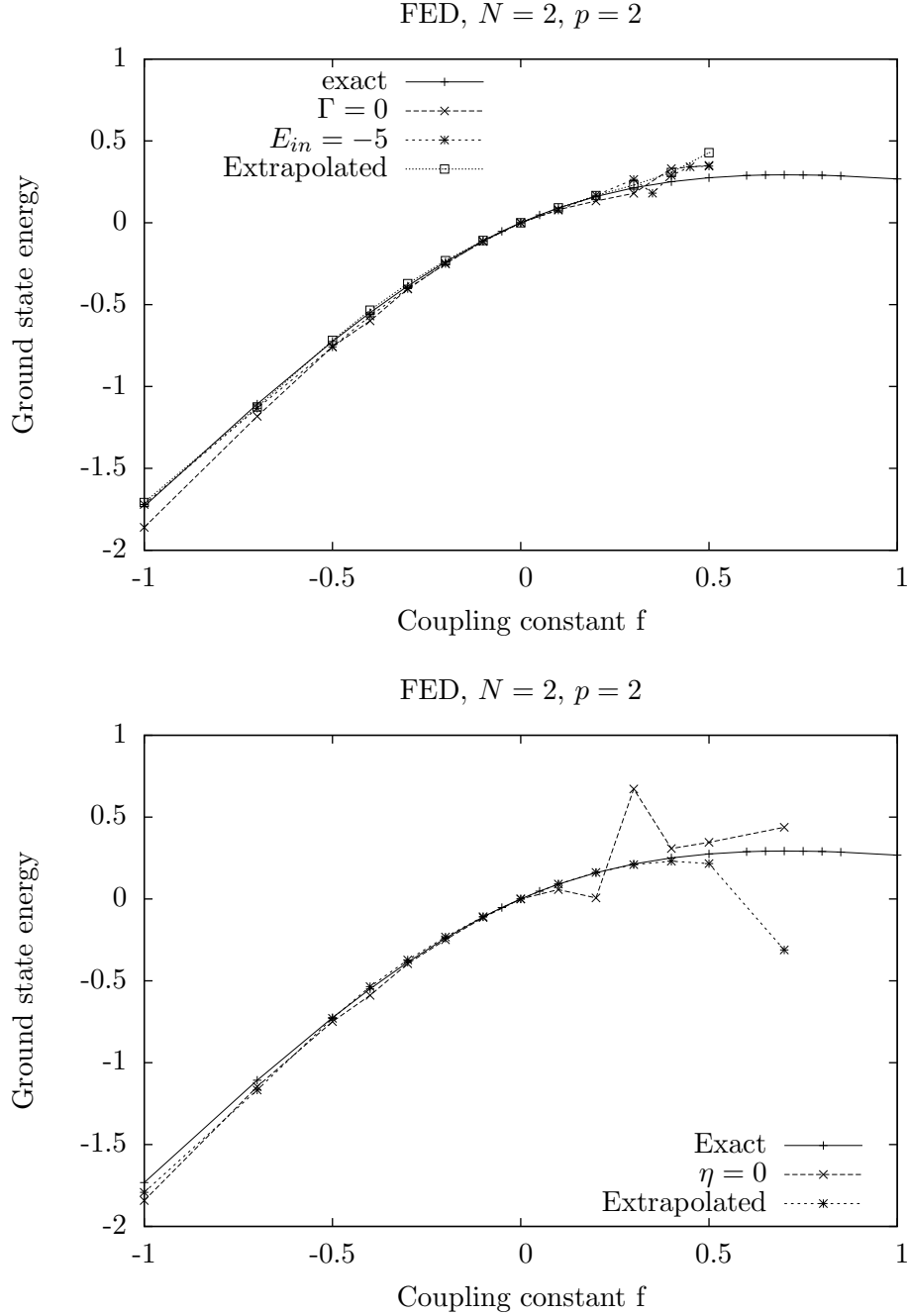


Figure 5.32: Ground state energy of FED calculations compared with exact solution for the  $N = 2, p = 2$  model. The results in the upper panel are for energy-independent calculations, while the lower panel shows energy-dependent results. For negative values of  $f$ , the agreement between the FED calculations and the exact solution is very good. The calculations become increasingly unstable for positive values of  $f$ .

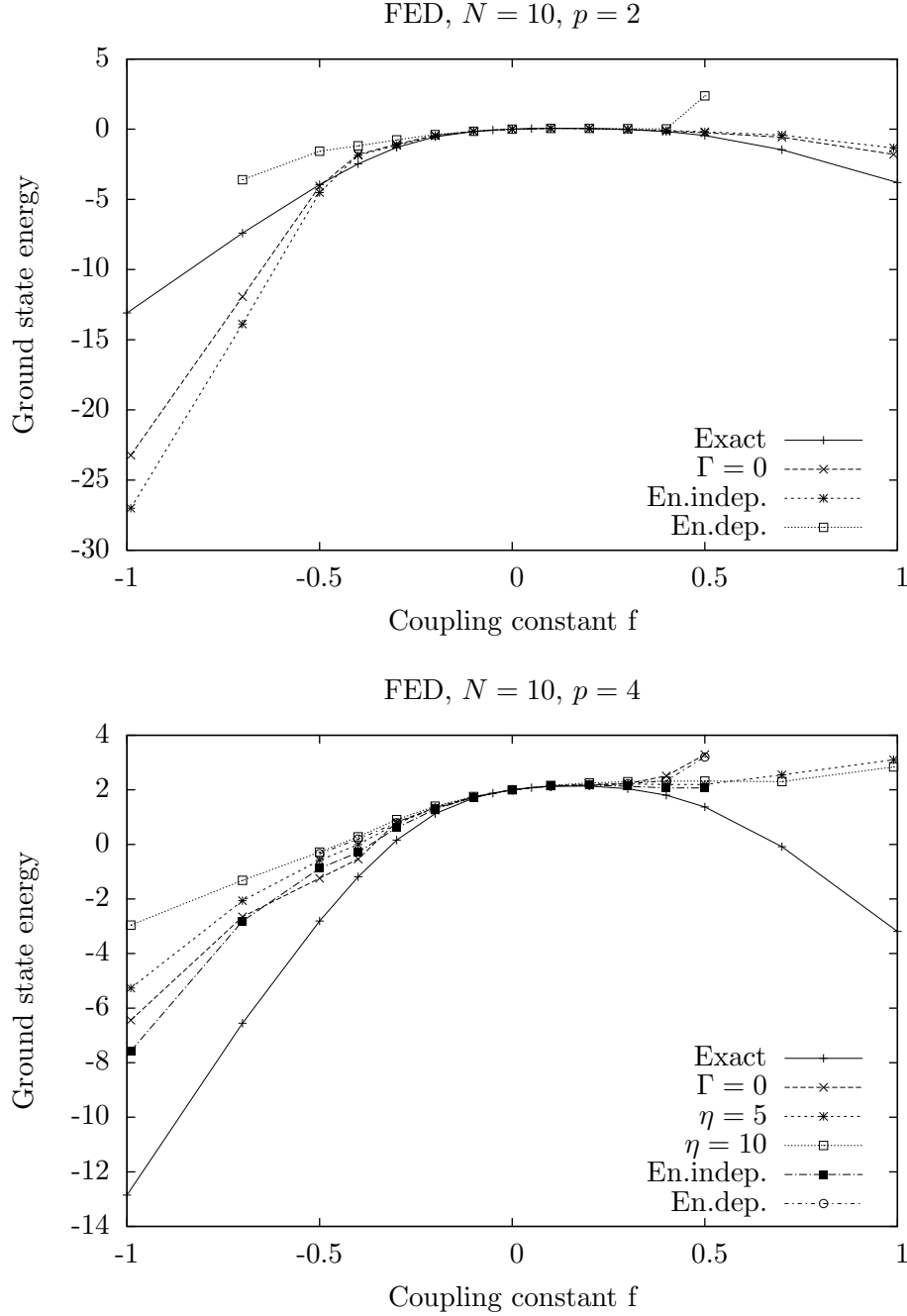


Figure 5.33: Ground state energy of FED calculations compared with exact solution for the  $N = 10$ ,  $p = 2$  model (upper panel) and  $N = 10$ ,  $p = 4$  (lower panel). The results shown are convergent, but unconverged results for lower  $\eta$  values indicate that the extrapolations probably do not reflect the correct  $\eta \rightarrow 0$  limit.

As stated in the section 5.3.1 on the convergence, all calculations become unstable at  $f = 1$ . It is possible to find convergent solutions for values of  $f > 1$ , but they are very far from the exact value. The exact ground state energy decreases, while the Parquet solutions increase. The failure is due to the reversal of the lowest-lying levels, violating our assumption that the input basis should not differ too radically from the expected solution.

The results for  $N = 10, p = 2$  and  $N = 10, p = 4$  are shown in figure 5.33, where we compare  $L = R = 0$ , energy-independent and energy-dependent calculation for calculations with the exact solution for both the  $N = 10, p = 2$  model (upper panel) and  $N = 10, p = 4$  (lower panel).

In the  $N = 10, p = 2$  model we see that the instability around  $f = -0.5$  seems to indicate a breakdown, as both the  $L = R = 0$  and the energy-independent calculations give far too negative ground state energies when  $f < -0.5$ . In the  $N = 10, p = 4$  model the energy-independent calculations and the energy-dependent calculations are rather close, and slightly closer to the exact solution than the  $L = R = 0$  calculations.

All values shown in figure 5.33 are converged, but the unconverged results at smaller  $\eta$  values show oscillations between a state with larger and a state with a much lower ground state energy than the exact value. The  $N = 10, p = 2$  results shown are consistent with the lowest energy, while the  $N = 10, p = 4$  results is more in line with the highest energy in these (large) fluctuations. This might indicate that the extrapolated results shown does not represent the ground state energy at  $\eta = 0$  properly in either system.

It must be remembered that all values are extrapolated and carry an uncertainty which roughly estimated is larger than the observed differences between the three approaches, and thus it is more prudent to look at the general trends rather than analyze the finer points in any great detail.

## 5.4 Selected combinations of $g$ and $f$

So far we have investigated the two extremes of only pair-conserving interaction and a pair-breaking term the size of the pair-conserving term. We know that the typical situation in a nucleus is to have a comparatively strong attractive pairing component in the interaction, being averagely about 0.5 in strength relative to the level spacing close to the Fermi gap in closed shells. The particle-hole part is considerably less, having 10%-20% of the pair strength. In our model the particle-hole interaction is modelled by the pair-breaking term. To get the most realistic approximation to a real nucleus within our model, we have therefore chosen to set  $g = -0.5$  and investigated the effect



of adding three different  $f$  values:  $f = -0.025 = 0.05g$ ,  $f = -0.005 = 0.1g$  and  $f = -0.25 = 0.5g$ .

We have investigated both the UPS and FED energy-independent approximations within a system with  $N = 10$  levels with 2,4, and 6 particles at  $E = -50$ . The convergence properties are generally good, for the UPS results only the combination of 6 particles and  $f = -0.25$  needs extrapolation, the other values converge at  $\eta = 0$ . The FED approximation results are unstable at  $f = -0.25$  for all particle numbers. All the extrapolated values shown use results for  $\eta = 1.0, 2.0, 3.0$  and  $5.0$  as basis. The results show that both ap-

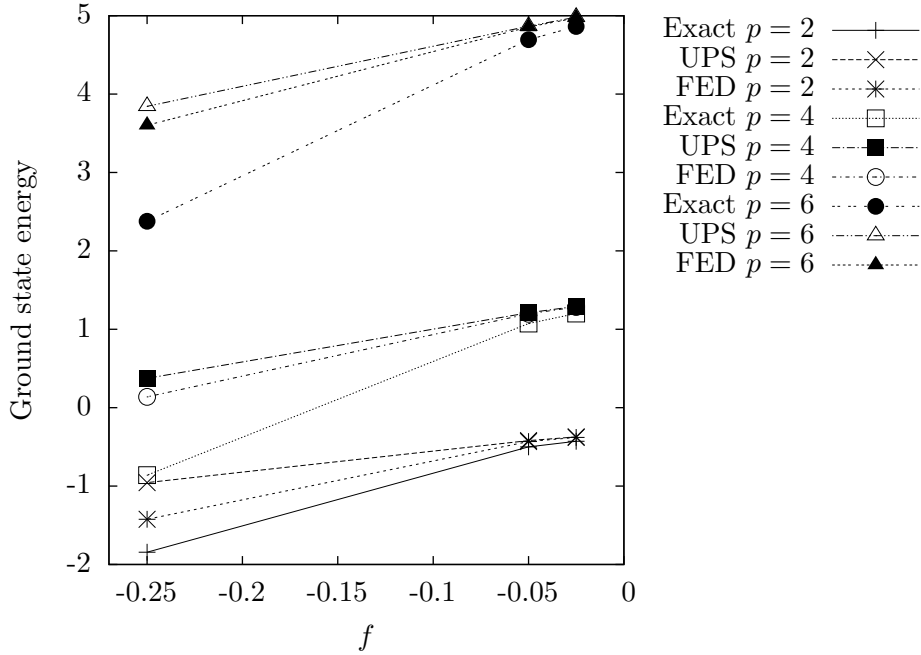


Figure 5.34: Ground state energy of UPS and FED calculations compared with exact solution in the  $N = 10$ ,  $p = 2, 4$  and  $6$  model for  $g = -0.5$  and  $f = -0.025 = 0.05g$ ,  $f = -0.005 = 0.1g$  and  $f = -0.25 = 0.5g$ .

proximation types underbinds as  $f$  increase, as could be expected. The FED approximation does consistently better, especially in the two-particle system.

## 5.5 Summary

We have found that the Parquet method performs generally well with the pair-conserving interaction. In this model there is no difference between the UPS and the FED approximations, as the system is diagonal in the self energy. The stability of our solutions depend on the parameter  $\eta$ , which regulates the influence of the pole structures in the propagators. The convergence properties with respect to  $\eta$  are normally quite good, with some notable exceptions when a pole in the generated interaction  $\Gamma$  is encountered. At small system sizes, the number of poles is sufficiently small so that no  $\eta$  is needed, but as the number of levels increases, a finite, but small  $\eta$  is needed. The number of particles have little impact on the convergence properties.

The energy-dependent scheme was found to perform slightly better than the energy-independent scheme when compared with the exact results. Over a range of interaction strengths between -0.5 and 0.5 of the level spacing both schemes show good agreement with the exact solution, also as the number of levels and particles in the model is increased. At larger interaction strengths, our solutions underbind the systems. In the pair-conserving model, the effect of increasing the number of available levels is rather large. It is difficult to ascertain the relative importance of the systematic errors stemming from the limitations imposed by our approximations when implementing the Parquet method versus the effect of missing many-body correlations. The study of the correlation energy with increasing particle number indicate that our solution method scale well with increasing particle number.

Introducing a pair-breaking force destabilizes the solutions in the region of strong repulsion ( $f \gtrsim 0.5$ ) in the smallest system with two levels and two particles, with a complete breakdown of the method when the first-order energies of the lowest levels become equal. Increasing the number of levels in the model gives larger differences between the exact solution and the Parquet solutions as the absolute value of the interaction strength increase. Increasing the number of particles gives increasingly larger discrepancies.

The energy-dependent calculation method is closer to the exact solution in the pair-conserving systems, but to obtain convergence in the pair-breaking systems,  $\eta$  has to be increased to such large values that the solution becomes a mean-field-type solution with an almost energy-independent self energy. The differences between results for different  $\eta$  values are small. Most of the correlations have been lost, and the energy-dependent results are rather far away from the exact solution.

The energy-independent calculation method gives results closer to the exact solution than the energy-dependent scheme. Within this simple model,

there is almost no dependence on the starting energy  $E_{in}$ , as long as this is chosen at values where the generated interaction  $\Gamma$  does not have any poles.

The general conclusion is that for the larger pair-breaking systems, the Parquet method as implemented is only in agreement with the exact solution for  $-0.3 \lesssim f \lesssim 0.2$ . The FED approximation performs better than the UPS approximation for  $f < 0$ , but is more unstable.

This model has many factors in common with realistic systems and many of the general conclusions and insights gained in this chapter can be carried over to the discussion of a real nucleus given in the next chapter.



## 6 Results for $^4\text{He}$

In this chapter we present the results of applying our implementation of the Parquet method to a real system, namely the  $^4\text{He}$  nucleus. This is the smallest doubly-closed nucleus. The  $^4\text{He}$  nucleus is well-studied, and there have been published numerous numerical studies with different approaches applied to this system. It is well-known that a correct treatment has to include three-body forces, but also that they are a correction to the two-body contribution. As a first test case it is therefore instructive to apply also our two-body based approach, and for this system we do not expect that too large model spaces are necessary to obtain meaningful results.

All results have been generated using a  $V_{lowk}$  potential (see section 2.3.2) with cutoff  $2.2\text{ fm}^{-1}$  based on the Argonne  $V_{18}$  (see section 2.2.1) potential as input interaction (we have no further terms in the expansion for  $I$  included, see section 4.5). The choice of the Argonne  $V_{18}$  input interaction is motivated by the number of other applications using this potential, most notably the benchmark result for  $^4\text{He}$  by the coupled-cluster method [9]. Our purpose is mainly to test the performance of the method, not the differences between the underlying interactions. Employing a  $V_{lowk}$  intermediate step ensures a faster convergence, thus reducing the model space needed. The calculations were performed in a harmonic oscillator basis, in model spaces including up to eight major harmonic oscillator shells. Most calculations are done in smaller spaces, due to huge memory costs.

We discuss results for  $^4\text{He}$  in the unperturbed-structure (UPS) approximation in section 6.1. After investigating the convergence in section 6.1.1, we discuss the self energy and the energy-dependence of the matrix elements of  $L$  and  $R$  within this scheme in sections 6.1.3 and 6.1.4. Then we present results for the ground state energy in the energy-independent scheme in section 6.1.5. Results for energy-dependent calculations are given in section 6.1.5, both within the standard scheme and within the matrix-inversion scheme for the two-time propagators as presented in section 4.3.2.

Results for  $^4\text{He}$  in the fixed-energy Dyson equation (FED) approximation

are presented in section 6.2. Based on the findings of chapter 5 and section 6.1, we focus on the energy-independent scheme. We discuss the convergence properties in section 6.2.1, the self energy in section 6.2.2 and the spectral functions in section 6.2.3. Finally, we present results for the ground state energy in section 6.2.4, followed by a short summary of the main findings of the chapter in section 6.3.

## 6.1 Results for unperturbed propagator structure (UPS) approximation

In this section we present results for the  ${}^4\text{He}$  ground state energy employing the unperturbed propagator structure (UPS approximation) described in section 4.5.1. In this approximation, we employ the unperturbed structure of the single-particle propagator (4.39). The harmonic oscillator orbitals are assumed to be a good basis set and only the energies are adjusted self-consistently. The propagators  $\mathcal{G}^{pphh}$  and  $\mathcal{G}^{ph}$  are solved by equations (4.18) and (4.25). For comparison, we present calculations for both the full Parquet and some for Parquet with only ladder terms included, i.e.  $R$  is set to zero in the calculations. This choice is a natural extension of the conventional  $G$ -matrix approaches, as only the ladder terms are summed to all orders.

We have chosen to discuss both the energy-independent and the energy-dependent solution schemes. In the energy-independent approximation we have removed the energy-dependence by choosing a fixed starting energy  $E_{in}$  in the calculation of the propagators in (4.18) and (4.25). In the energy-dependent scheme, an energy grid is set up and the propagators and interactions are calculated at each value of the grid. The interaction  $\Gamma(\Omega)$  is then interpolated in the calculation of the self energy. We saw in the previous chapter that in the case of a pairing-only interaction the energy-dependent scheme performed best, while the opposite was the case for the pair-breaking interaction.

### 6.1.1 Convergence properties

The stability of the UPS approximation results is generally good. We have investigated the convergence properties of the energy-independent approximation for different  $\eta$  and different starting energies  $E_{in}$ , as shown in figure 6.1.

The upper panel shows the difference  $E_n - E_{n-1}$  between the ground state energy of successive iterations for an energy-independent calculation at  $\hbar\Omega = 26$  MeV at  $\eta = 5$  for different starting energies. The smallest starting energies

$E_{in} < -100$  MeV follows the same general pattern. For  $E_{in} = -90$  MeV, the calculation still has a convergent behavior, while the outcome of the  $E_{in} = -75$  MeV calculation is more uncertain. The  $E_{in} = -50$  MeV calculation diverges, as do all higher starting energies at this  $\eta$  value.

In the lower panel figure 6.1, we show results for an energy-independent calculation at  $\hbar\Omega = 26$  MeV with a starting energy of -200 MeV. The differences  $E_n - E_{n-1}$  between the ground state energy of successive iterations are plotted in a log-scale plot as a function of number of iterations for different values of  $\eta$ . All the shown  $\eta$  values give converged results fast. This reflects that the impact of the poles are rather limited as long as the starting energy is well away from any poles of the propagator.

The energy-dependence is introduced by introducing a fixed energy grid and calculating the ladder and ring contributions for these energies and then interpolating to get the value at the energy in the self energy calculation. The poles of the propagators therefore play a larger role than in the energy-independent case. The rather poor convergence patterns with respect to  $\eta$  for the free propagator calculations are shown in the upper panel of figure 6.2 for calculations within six major harmonic oscillator shells. Only for  $\eta > \approx 65$  are the results converged, which makes any extrapolation rather uncertain. The convergence becomes slower with increasing  $\hbar\Omega$ , and even divergent for  $\eta=60$  at  $\hbar\Omega = 30$  MeV. The calculation shown has 30 points in the energy mesh, and increasing this number further does not improve on the convergence (in accord with the same observation seen in the simple model discussed in chapter 5).

To improve the convergence with respect to  $\eta$  we have tried the matrix inversion approach for calculating the two-particle propagators, as described in section 4.3.2. The main approximation relative to the free propagator approach is to assume that the derivative of the interaction in equation (4.32) is zero, an assumption that should be quite justifiable far from the poles, where the interaction changes little, but violated close to the poles. We also do not solve the eigenvalue equation (4.31) at the correct energy, but rather have chosen to use the value of  $\mathcal{V}$  at the input  $\Omega$ , to eliminate the need for an interpolation which would entail further uncertainties.

The convergence is as expected better in this approximation, as shown in the lower panel of figure 6.2, which show a calculation within six major harmonic oscillator shells. Compared to the results in figure 6.1 for the free propagator, we see that convergence occurs for values of  $\eta > \approx 30$ , half of the  $\eta$  value necessary for convergence in the free propagator calculations.

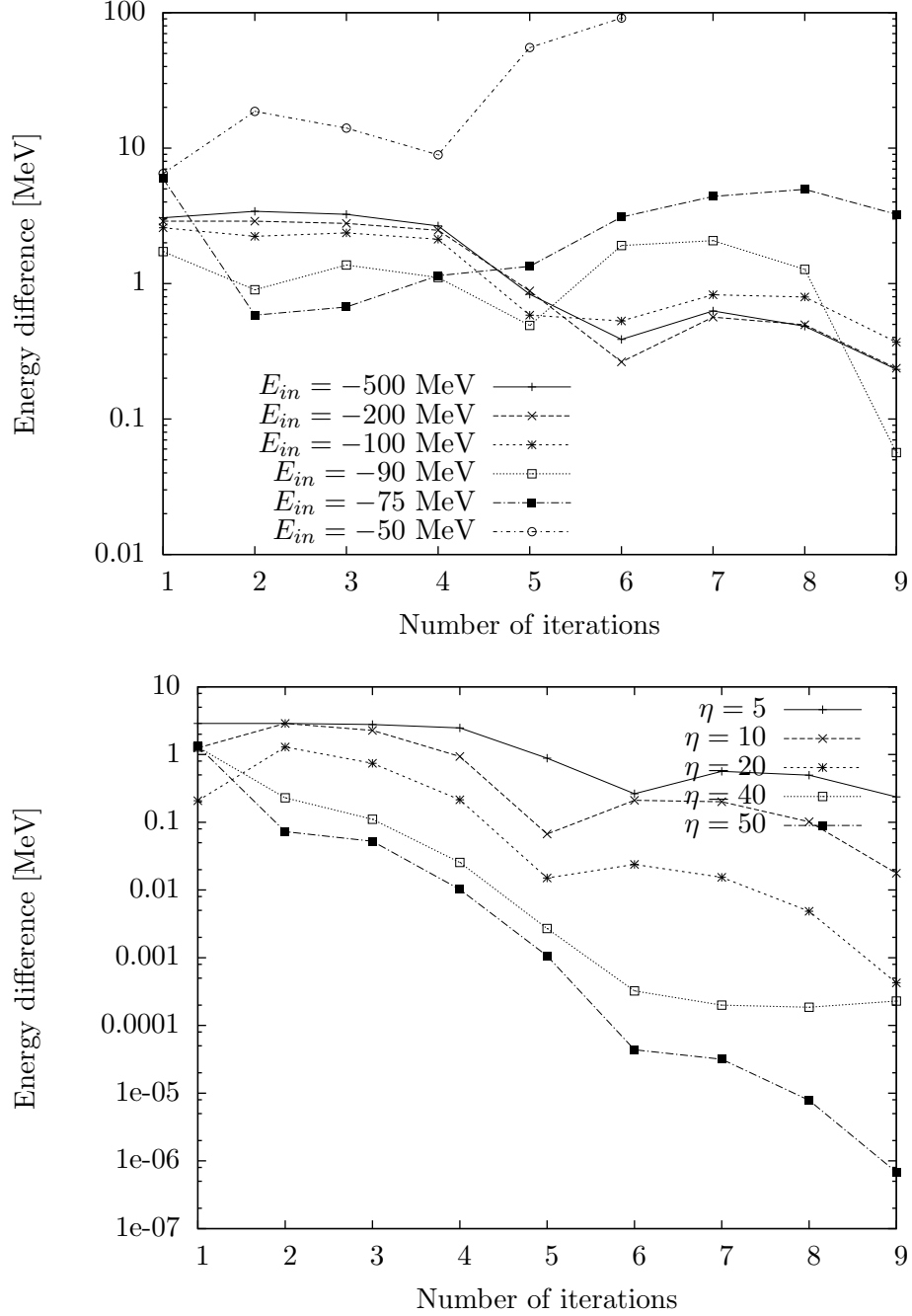


Figure 6.1: The differences  $E_n - E_{n-1}$  between successive iterations as a function of the number of iterations for energy-independent calculation within six major oscillator shells for  $\hbar\Omega = 26$  MeV at different starting energies at  $\eta = 5$  in the upper panel and at  $E_{in} = -200$  MeV with different values of  $\eta$  in the lower panel. Calculations with values of  $E_{in}$  higher than  $\sim 75$  MeV diverges, as do calculations with  $\eta < 5$ .



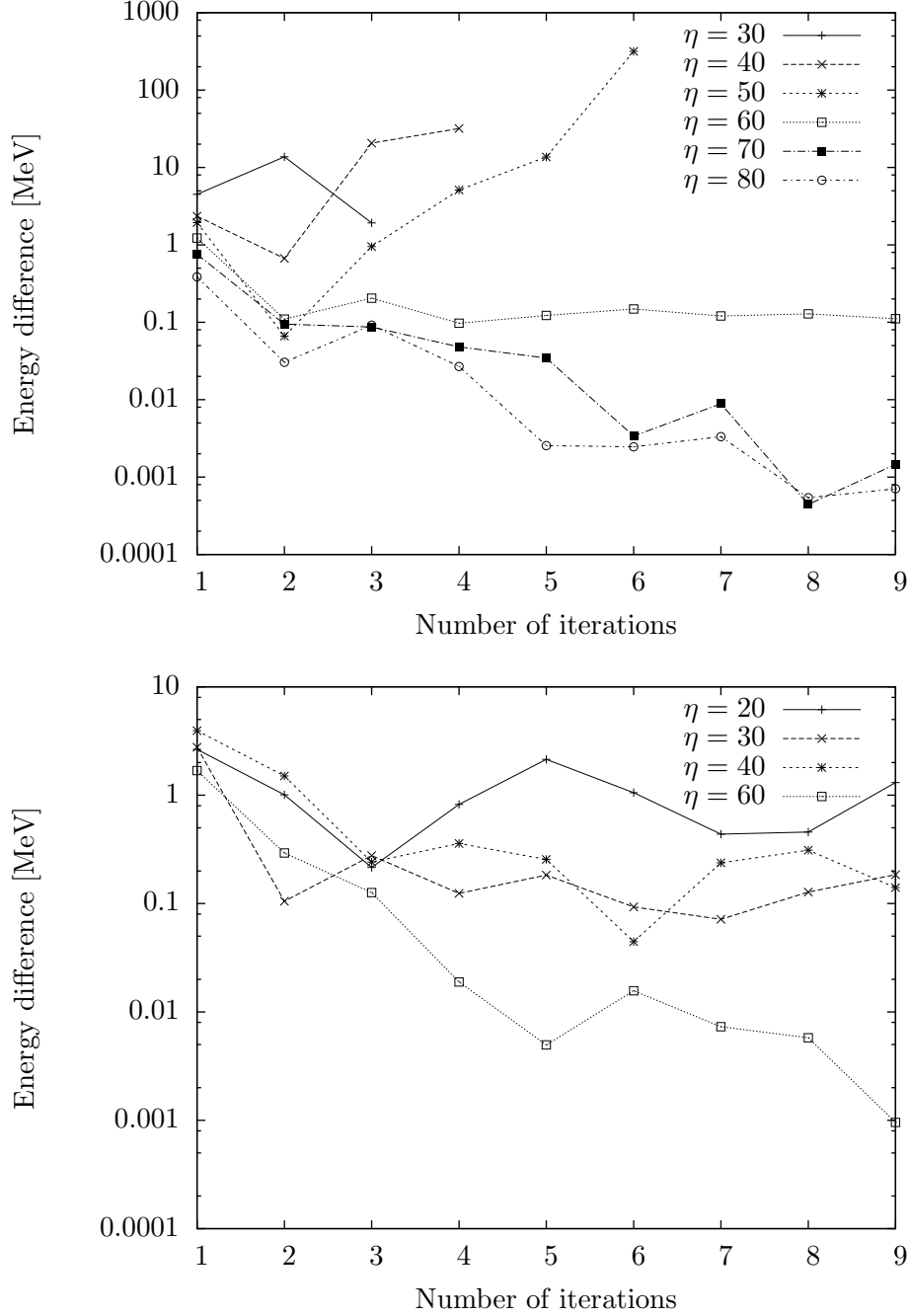


Figure 6.2: The differences  $E_n - E_{n-1}$  between successive iterations as a function of the number of iterations for energy-dependent calculation within six major oscillator shells for  $\hbar\Omega = 22$  MeV. In the upper panel we show results for free propagator scheme, and in the lower we have used the matrix inversion scheme described in section 4.3.2. The convergence is much improved by the inversion scheme.

### 6.1.2 Single-particle states in the first five major oscillator shells

In the following we will discuss several matrix quantities: the interaction matrix elements, the self energy and the spectral function, which all have the single particle basis as indices. For easy reference we give a table of the 30 orbitals included in the first five major oscillator shells in table 6.1. We have chosen to work with this model space when calculating the different matrix quantities in this presentation.

Number	$ nlj\rangle$	$n$	$l$	$2j$	$t_z$	$2n + l$
1	p $ 0s\frac{1}{2}\rangle$	0	0	1	-1	0
2	n $ 0s\frac{1}{2}\rangle$	0	0	1	1	0
3	p $ 0p\frac{3}{2}\rangle$	0	1	3	-1	1
4	n $ 0p\frac{3}{2}\rangle$	0	1	3	1	1
5	p $ 0p\frac{1}{2}\rangle$	0	1	1	-1	1
6	n $ 0p\frac{1}{2}\rangle$	0	1	1	1	1
7	p $ 0d\frac{5}{2}\rangle$	0	2	5	-1	2
8	n $ 0d\frac{5}{2}\rangle$	0	2	5	1	2
9	p $ 0d\frac{3}{2}\rangle$	0	2	3	-1	2
10	n $ 0d\frac{3}{2}\rangle$	0	2	3	1	2
11	p $ 1s\frac{1}{2}\rangle$	1	0	1	-1	2
12	n $ 1s\frac{1}{2}\rangle$	1	0	1	1	2
13	p $ 0f\frac{7}{2}\rangle$	0	3	7	-1	3
14	n $ 0f\frac{7}{2}\rangle$	0	3	7	1	3
15	p $ 0f\frac{5}{2}\rangle$	0	3	5	-1	3
16	n $ 0f\frac{5}{2}\rangle$	0	3	5	1	3
17	p $ 1p\frac{3}{2}\rangle$	1	1	3	-1	3
18	n $ 1p\frac{3}{2}\rangle$	1	1	3	1	3
19	p $ 1p\frac{1}{2}\rangle$	1	1	1	-1	3
20	n $ 1p\frac{1}{2}\rangle$	1	1	1	1	3
21	p $ 0g\frac{9}{2}\rangle$	0	4	9	-1	4
22	n $ 0g\frac{9}{2}\rangle$	0	4	9	1	4
23	p $ 0g\frac{7}{2}\rangle$	0	4	7	-1	4
24	n $ 0g\frac{7}{2}\rangle$	0	4	7	1	4
25	p $ 1d\frac{5}{2}\rangle$	1	2	5	-1	4
26	n $ 1d\frac{5}{2}\rangle$	1	2	5	1	4
27	p $ 1d\frac{3}{2}\rangle$	1	2	3	-1	4
28	n $ 1d\frac{3}{2}\rangle$	1	2	3	1	4
29	p $ 2s\frac{1}{2}\rangle$	2	0	1	-1	4
30	n $ 2s\frac{1}{2}\rangle$	2	0	1	1	4

Table 6.1: The quantum numbers of the 30 orbitals included in the first five major oscillator shells. In the state labels, p stands for proton and n for neutron.

### 6.1.3 L and R matrix elements

We have looked at some selected  $L$  and  $R$  matrix elements as function of energy for the energy-dependent calculations. We expect that the effect of increasing the parameter  $\eta$  is to quench the energy dependence, and making the poles less severe. This is also what we observe, as shown in figure 6.3. As representative cases, we have shown the real and imaginary terms of the proton matrix elements  $\langle 0s_{\frac{1}{2}} 0s_{\frac{1}{2}} | L | 0s_{\frac{1}{2}} 1s_{\frac{1}{2}} \rangle_0$  and  $\langle 0p_{\frac{3}{2}} 0p_{\frac{3}{2}} | L | 0p_{\frac{3}{2}} 0p_{\frac{3}{2}} \rangle_0$  generated by a free propagator calculation within five major oscillator shells at  $\hbar\Omega = 24.0$  MeV. The basis states are numbered according to table 6.1. We show calculations with  $\eta = 5.0$  and  $\eta = 70.0$  after the first iteration, and again for  $\eta = 70.0$  after 10 iterations (the  $\eta = 5.0$  calculation diverges after the first iteration). The same is shown for the  $R$  matrix elements  $\langle 0s_{\frac{1}{2}} 0s_{\frac{1}{2}} | r | 0s_{\frac{1}{2}} 1s_{\frac{1}{2}} \rangle_0$  and  $\langle 0p_{\frac{3}{2}} 0p_{\frac{3}{2}} | R | 0p_{\frac{3}{2}} 0p_{\frac{3}{2}} \rangle_0$  in figure 6.4. We see that for the values of  $\eta$  where we obtain convergence, very little of the structure of the interaction remains, especially for the  $R$  matrix elements, which exhibit strong variation with energy for the  $\eta = 5.0$  case.

We observe that the values at which the matrix elements start to deviate significantly from 0 is about  $-100$  MeV, consistent with the result observed in section 6.1.1 for the value at which the energy-independent calculations starts to diverge for small values of  $\eta$ . We also see that the effects of iterating to self-consistency are not very large, the matrix elements remain almost energy-independent.

Interaction matrix elements obtained by calculating the two-particle propagators using the matrix inversion approximation exhibit more interesting structures, as shown in figures 6.5 and 6.6 for the same  $L$  and  $R$  elements as above. This time they are calculated at  $\eta = 5.0$  and  $\eta = 30.0$  after the first iteration, and for  $\eta = 30.0$  after 10 iterations. We see that far more of the small- $\eta$  structure is conserved in the first iteration. After 10 iterations in the  $\eta = 30.0$  calculation, the structure is more complex and somewhat reminiscent of the structure at  $\eta = 5.0$ . As for the free propagator calculation, the damping is largest for the  $R$  matrix elements.

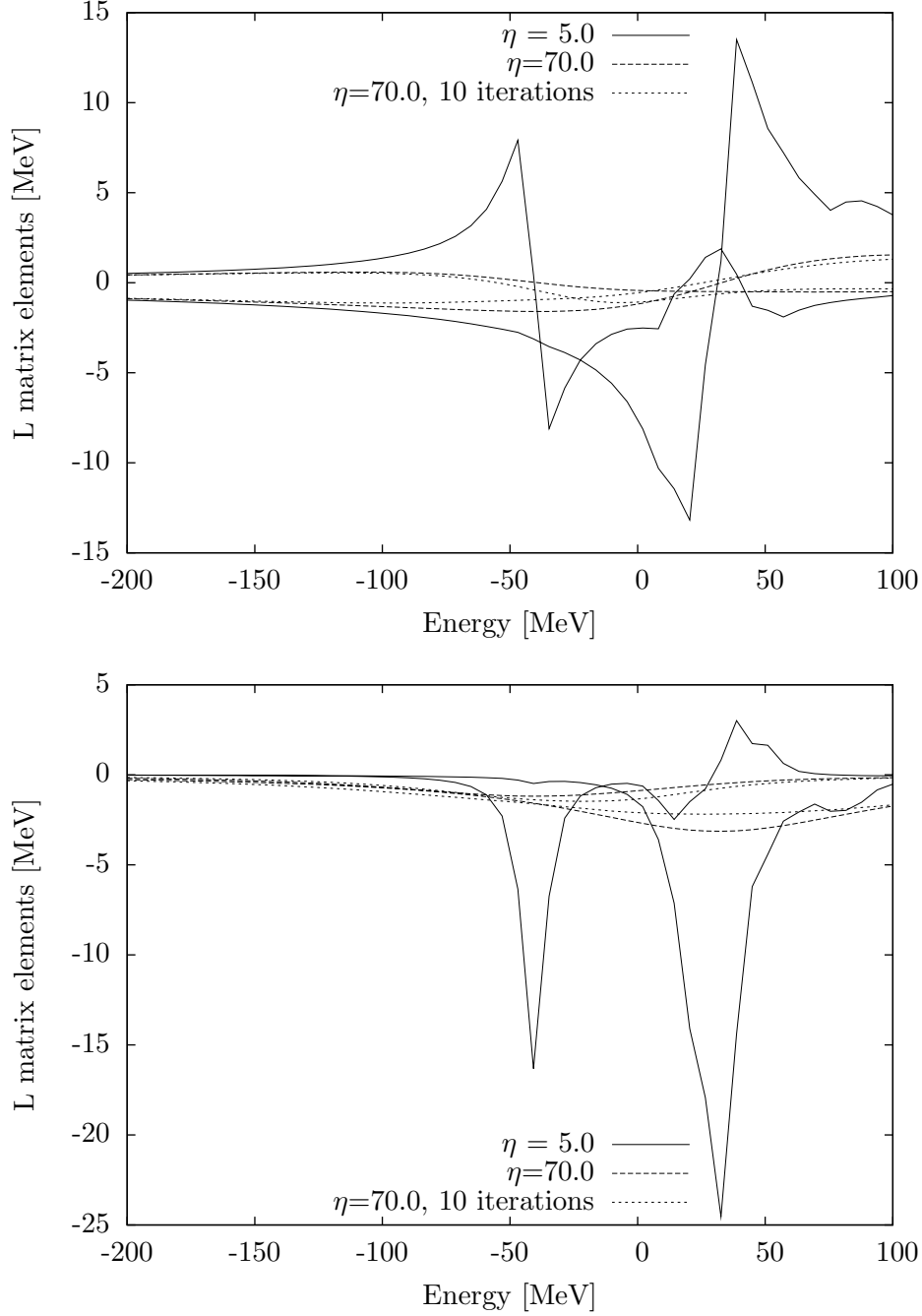


Figure 6.3: Real and imaginary parts of the matrix elements  $\langle 0s_{\frac{1}{2}}^{\frac{1}{2}} 0s_{\frac{1}{2}}^{\frac{1}{2}} | L | 0s_{\frac{1}{2}}^{\frac{1}{2}} 1s_{\frac{1}{2}}^{\frac{1}{2}} \rangle_0$  and  $\langle 0p_{\frac{3}{2}}^{\frac{3}{2}} 0p_{\frac{3}{2}}^{\frac{3}{2}} | L | 0p_{\frac{3}{2}}^{\frac{3}{2}} 0p_{\frac{3}{2}}^{\frac{3}{2}} \rangle_0$  generated by a free propagator calculation within five major oscillator shells at  $\hbar\Omega = 24.0$  MeV for the values  $\eta = 5.0$  and  $\eta = 70.0$ , after 1 and 10 iterations. The energy-dependence is severely reduced at  $\eta = 70.0$ .

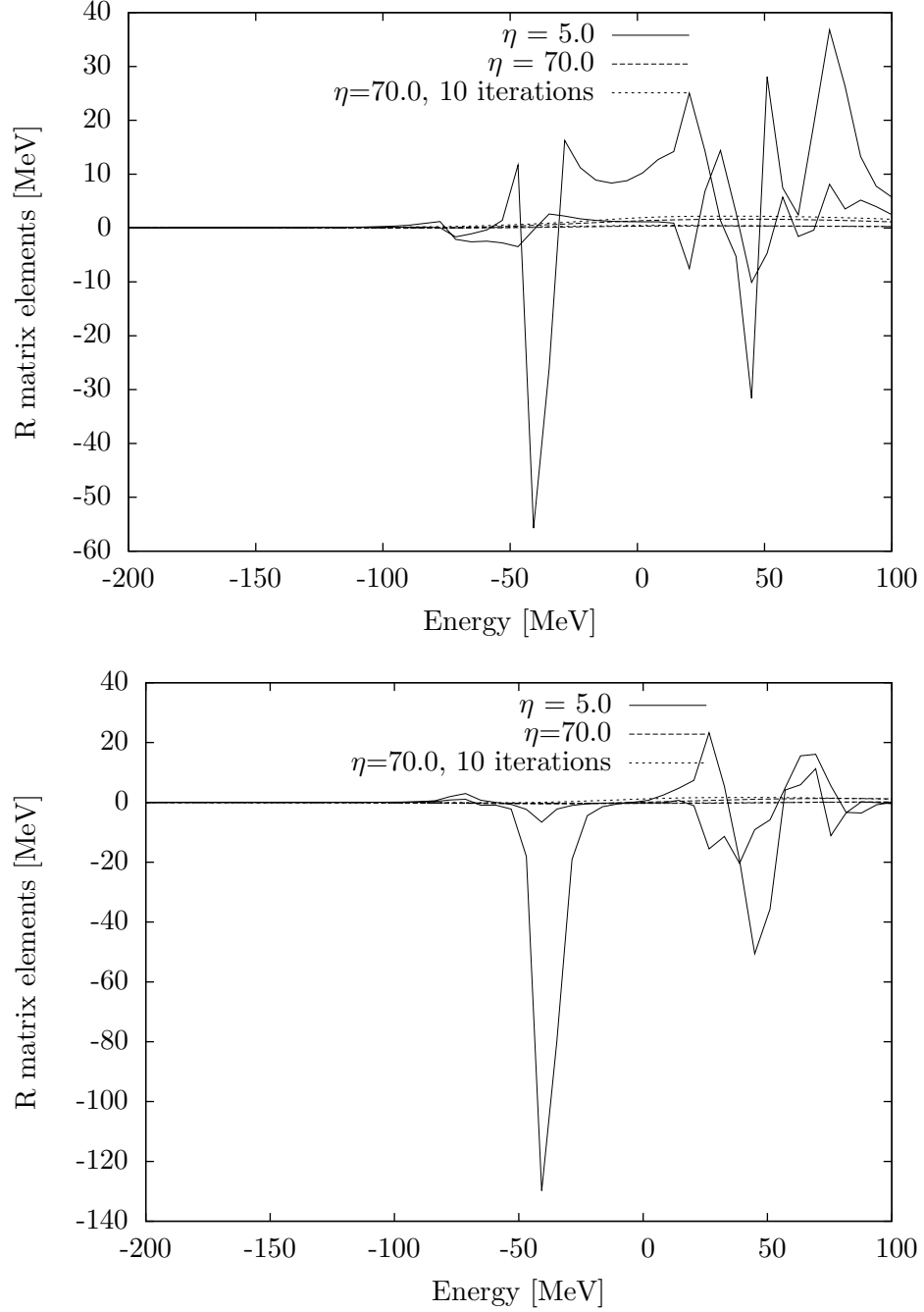


Figure 6.4: Real and imaginary parts of the matrix elements  $\langle 0s_{\frac{1}{2}}^{\frac{1}{2}} 0s_{\frac{1}{2}}^{\frac{1}{2}} | r | 0s_{\frac{1}{2}}^{\frac{1}{2}} 1s_{\frac{1}{2}}^{\frac{1}{2}} \rangle_0$  and  $\langle 0p_{\frac{3}{2}}^{\frac{3}{2}} 0p_{\frac{3}{2}}^{\frac{3}{2}} | R | 0p_{\frac{3}{2}}^{\frac{3}{2}} 0p_{\frac{3}{2}}^{\frac{3}{2}} \rangle_0$  generated by a free propagator calculation within five major oscillator shells at  $\hbar\Omega = 24.0$  MeV for the values  $\eta = 5.0$  and  $\eta = 70.0$ , after 1 and 10 iterations. The structures are quenched dramatically at  $\eta = 70.0$ , leaving almost energy-independent interaction matrix elements.

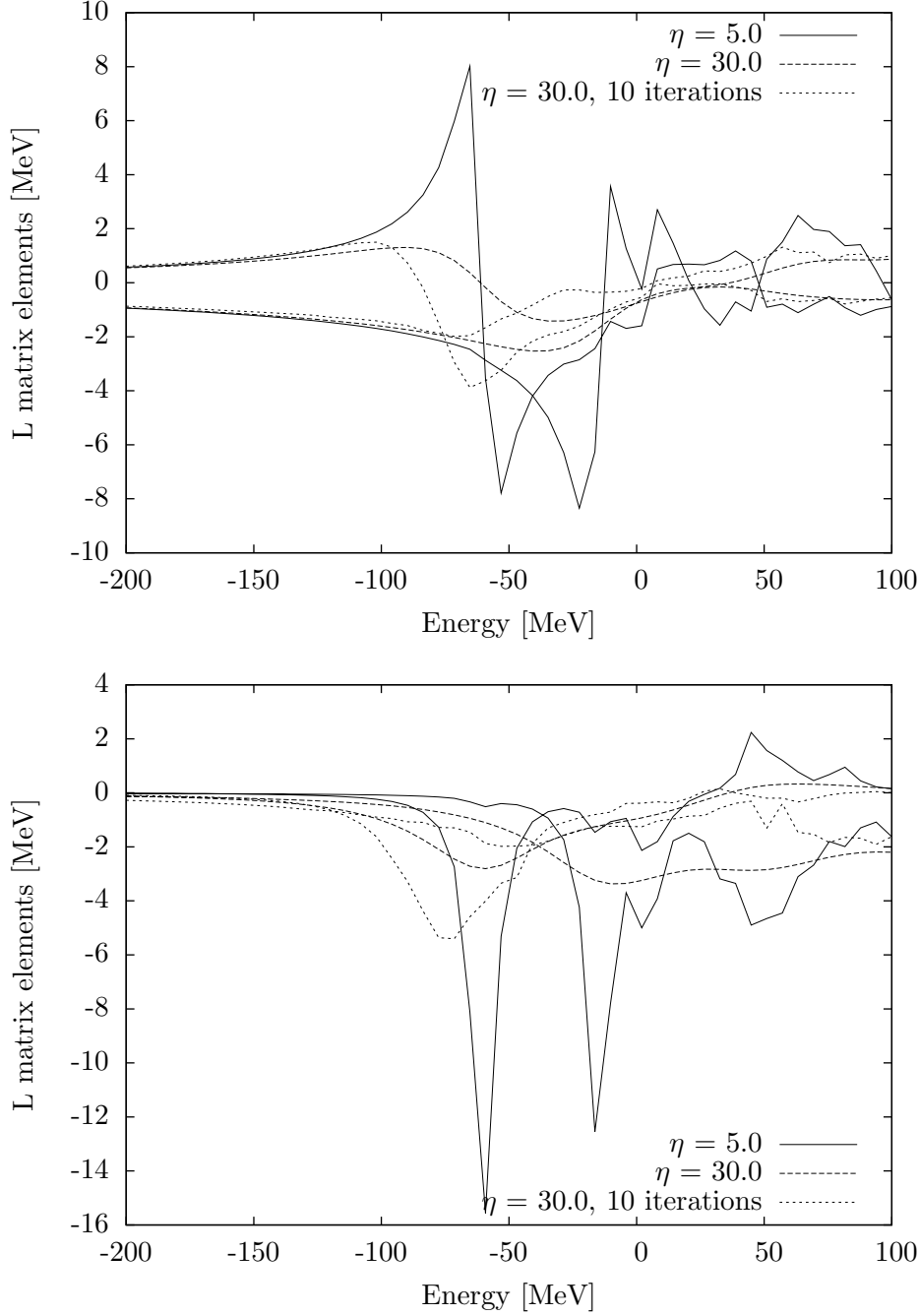


Figure 6.5: Real and imaginary parts of the matrix elements  $\langle \overbrace{0s_{\frac{1}{2}}^1 0s_{\frac{1}{2}}^1} | L | \overbrace{0s_{\frac{1}{2}}^1 1s_{\frac{1}{2}}^1} \rangle_0$  and  $\langle \overbrace{0p_{\frac{3}{2}}^3 0p_{\frac{3}{2}}^3} | L | \overbrace{0p_{\frac{3}{2}}^3 0p_{\frac{3}{2}}^3} \rangle_0$  generated by a matrix inversion approximation propagator calculation within five major oscillator shells at  $\hbar\Omega = 24.0$  MeV for the values  $\eta = 5.0$  and  $\eta = 30.0$ , after 1 and 10 iterations. The matrix inversion scheme retains far more of the energy-dependence than the free propagator scheme.

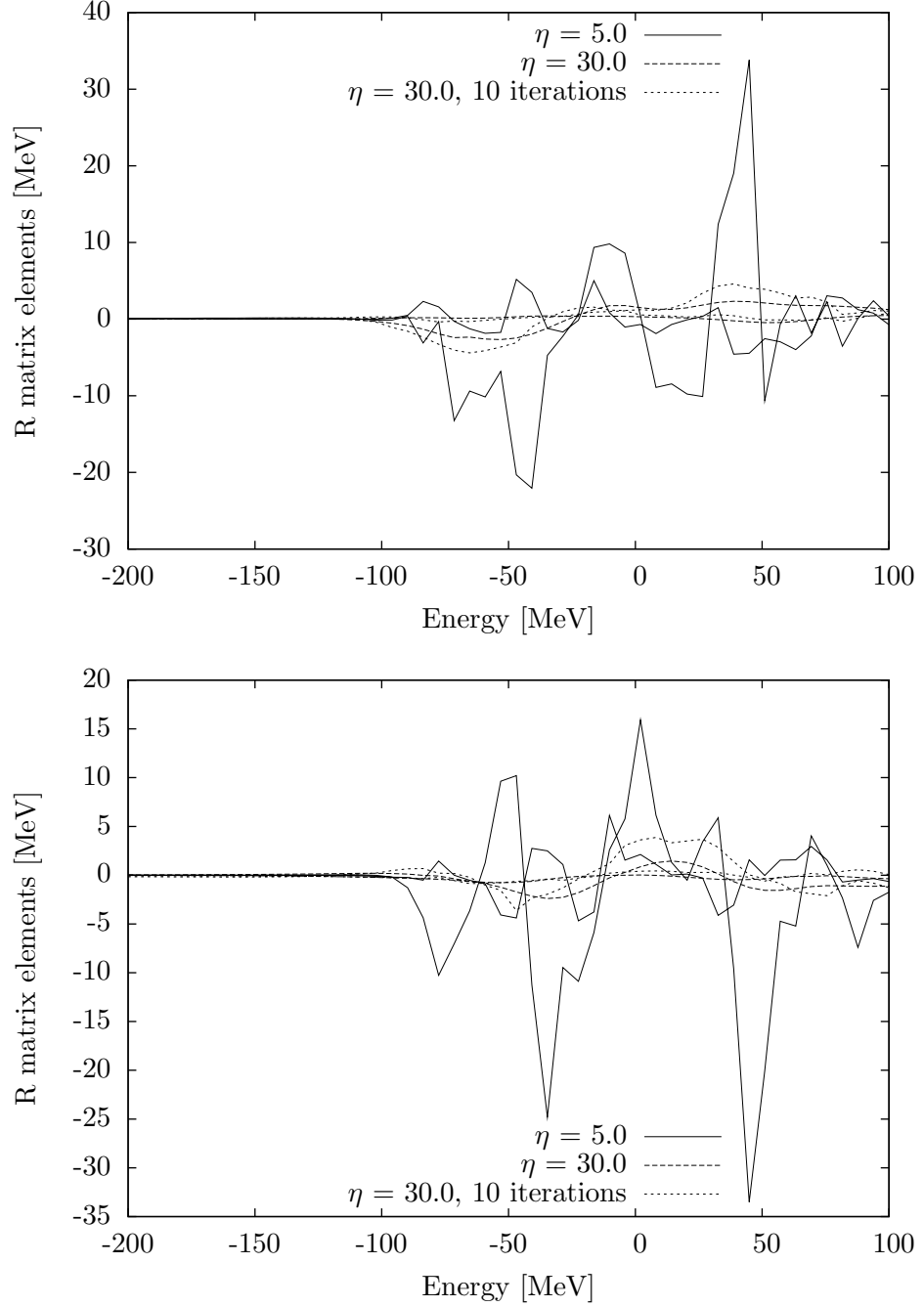


Figure 6.6: Real and imaginary parts of the matrix elements  $\langle \overbrace{0s_{\frac{1}{2}} 0s_{\frac{1}{2}}} | r | \overbrace{0s_{\frac{1}{2}} 1s_{\frac{1}{2}}} \rangle_0$  and  $\langle \overbrace{0p_{\frac{3}{2}} 0p_{\frac{3}{2}}} | R | \overbrace{0p_{\frac{3}{2}} 0p_{\frac{3}{2}}} \rangle_0$  generated by a matrix inversion approximation propagator calculation within five major oscillator shells at  $\hbar\Omega = 24.0$  MeV for the values  $\eta = 5.0$  and  $\eta = 30.0$ , after 1 and 10 iterations. The iterative procedure generates additional structure to the matrix elements.



### 6.1.4 Self energy

The pole structure of the self energy is considerably more complex in this realistic case compared to the self energies of the simple model of the previous chapter. We have chosen to mainly focus on the proton element  $\langle 0s_{\frac{1}{2}} | \Sigma | 0s_{\frac{1}{2}} \rangle$ . This is a hole state, and corresponds to a proton within the  ${}^4\text{He}$  nucleus.

In figure 6.7 we show  $\langle 0s_{\frac{1}{2}} | \Sigma | 0s_{\frac{1}{2}} \rangle$  after the first iteration of an energy-independent calculation within five major oscillator shells with the orbitals as numbered in table 6.1. The calculation shown is for  $\eta = 0.0$  at input energy -200 MeV with  $\hbar\Omega = 14$  MeV. The pole structure in this energy-independent case is exclusively given by the pole structure of the  $\mathcal{G}_0^{pphh}$  propagator in the second-order self energy, with the poles at negative energies stemming from the propagation of two holes and those at positive energies being the propagation of two particles. For reference, we have also shown the first order constant contribution as a straight line.

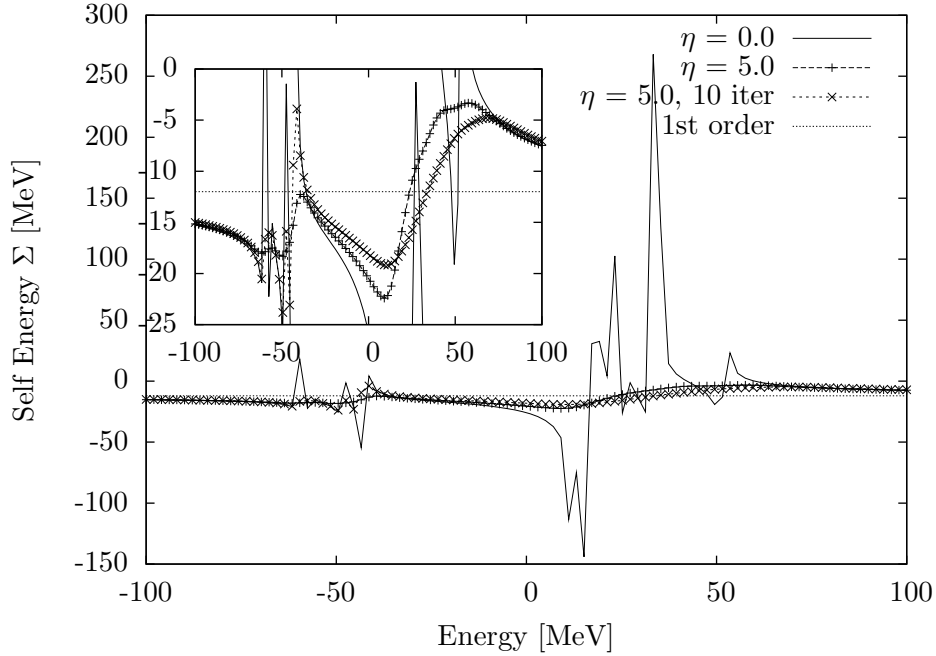


Figure 6.7:  $\langle 0s_{\frac{1}{2}} | \Sigma | 0s_{\frac{1}{2}} \rangle$  of an energy-independent calculation within five major oscillator shells and  $\hbar\Omega = 14$  MeV at input energy -200 MeV for  $\eta = 0.0$  after the first iteration and for  $\eta = 5.0$  after 1 and 10 iterations. The inset shows has a narrower  $y$  range, to show the structure of the  $\eta = 5.0$  calculation in more detail.

In this figure we have also included the effects of adding the imaginary component  $\eta$  in an energy-independent calculation, still after just one iteration. The quenching effect is rather large already at  $\eta = 5.0$ , the lowest values at which an energy-independent calculation converges. The last graph in figure 6.7 shows the result after 10 iterations of a full Parquet calculation. We see that additional structure has emerged, especially for negative energies. Further iterations do not change the graph perceptively on this scale.

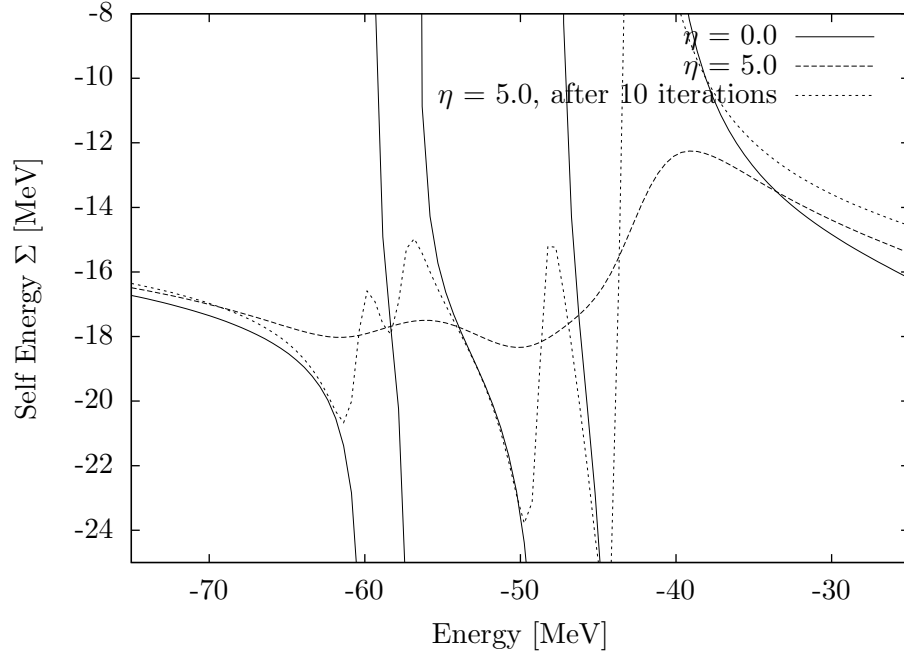


Figure 6.8:  $\langle 0s\frac{1}{2}|\Sigma|0s\frac{1}{2}\rangle$  of an energy-independent calculation within five major oscillator shells at input energy -200 MeV for  $\eta = 0.0$  after the first iteration and for  $\eta = 5.0$  after 1 and 10 iterations. This closeup shows how additional structure emerges during the iterative process.

A closeup on the energy region between -75 MeV and -25 MeV is shown in figure 6.8. The structure after 10 iterations more closely resembles the  $\eta = 0.0$  case than after one iteration only. This emergent structure indicates that the self-consistency procedure alleviates some of the effects of introducing the unphysical imaginary components. As shown in figure 6.9, the value of the imaginary part of  $\Sigma$  is of the same order as the real part. The deviations from zero are largest at the energies where the real part show signs of having poles, as expected.

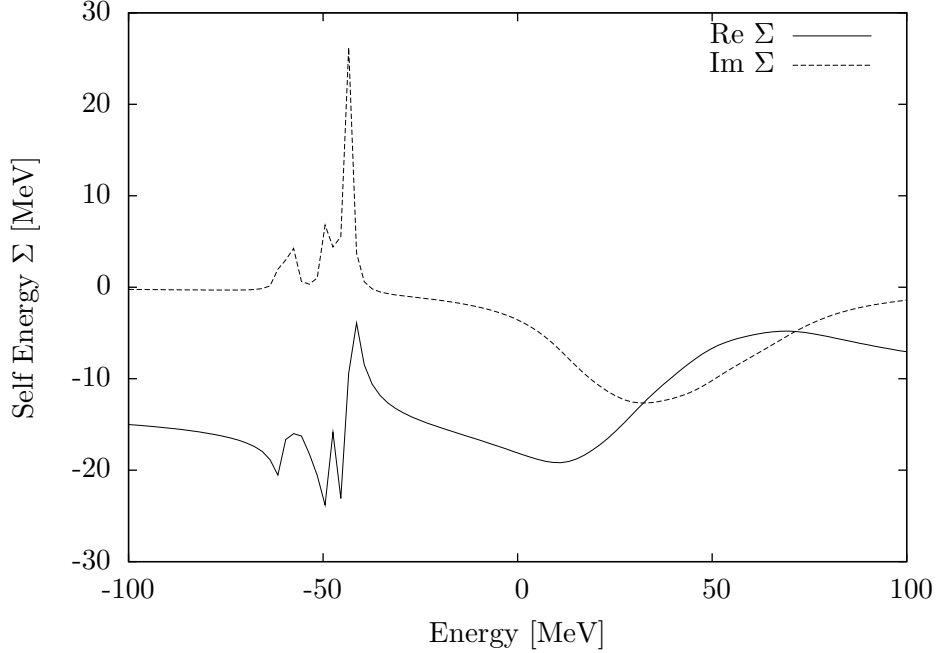


Figure 6.9: Real and imaginary components of  $\langle 0s_{\frac{1}{2}} | \Sigma | 0s_{\frac{1}{2}} \rangle$  of an energy-independent calculation within five major oscillator shells at input energy -200 MeV for  $\eta = 5.0$  after 10 iterations. The imaginary part mirrors the structure of the real part.

Selected matrix elements of  $\Sigma$  are shown in figure 6.10, for an energy-independent calculation with  $\eta = 5.0$  within five major oscillator shells at input energy  $E_{in} = -200$  MeV after 10 iterations. The first-order contributions are also shown. We see that the general structure of all the matrix elements are the same. This reflects that in the energy-independent scheme the poles are exclusively determined by the poles of the propagator. The overall position of the different elements is mainly determined by the first-order contribution. The off-diagonal elements  $\langle 0s_{\frac{1}{2}} | \Sigma | 1s_{\frac{1}{2}} \rangle$  and  $\langle 1s_{\frac{1}{2}} | \Sigma | 0s_{\frac{1}{2}} \rangle$  ( $\langle 1 | \Sigma | 11 \rangle$  and  $\langle 11 | \Sigma | 1 \rangle$  in the figure) are equal.

The differences between the graphs for different starting energies are minimal. In figure 6.11 we show the results from energy-independent calculations with  $\eta = 5.0$ , and  $\hbar\Omega = 24$  MeV within five major oscillator shells at starting energies  $E_{in} = -250$  MeV,  $-200$  MeV and  $-150$  MeV after 10 iterations. Comparing these graphs with the corresponding calculation at a starting energy  $-200$  MeV at  $\hbar\Omega = 14$  MeV in figure 6.7, we can also see the effect of varying the oscillator frequency  $\hbar\Omega$ . Larger frequency means larger spacing

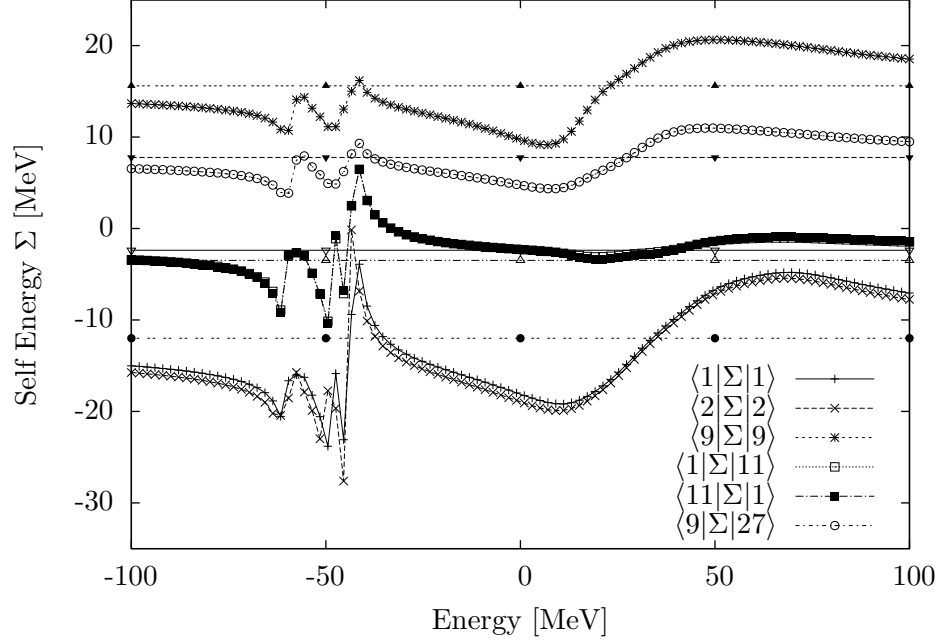


Figure 6.10: Several matrix elements of an energy-independent calculation within five major oscillator shells with the orbitals as numbered in table 6.1 at input energy -200 MeV for  $\eta = 5.0$  after 10 iterations. The first order contributions are drawn as straight lines. The overall position of the different elements are determined by the first order energies.

between the energy levels, and this moves the poles of two propagating holes or two propagating particles (and hence also the poles of  $\Sigma$ ) further away from each other.

The results for the energy-dependent calculations show that most of the structure of the self energy is unfortunately lost at the values of  $\eta$  necessary to achieve convergence. Figure 6.12 shows the results of energy-dependent calculations using free two-particle propagator after the first iteration for  $\eta = 5.0, 30.0$  and  $65.0$ . Comparing the  $\eta = 5.0$  calculation with the corresponding energy-independent calculation given in figure 6.7, we see that including pole terms stemming from the interaction  $\Gamma$  in addition to the existing structure changes the energy dependence of the self energy substantially, as could be expected. This is confirmed when looking at the first iteration of calculations for lower  $\eta$  (for which neither approximation converges, and thus no iterative results are available).

The two groups of structures stemming from the two-hole-one-particle and

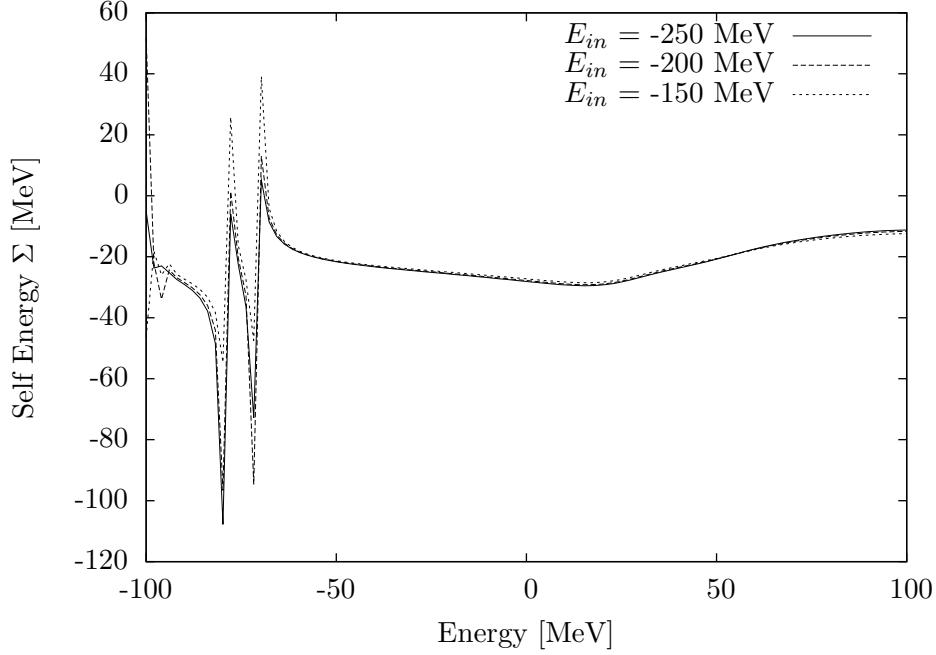


Figure 6.11:  $\langle 0s_{\frac{1}{2}} | \Sigma | 0s_{\frac{1}{2}} \rangle$  for calculations with starting energies -250 MeV, -200 MeV and -150 MeV, within five major oscillator shells at  $\hbar\Omega = 24$  MeV after 10 iterations. Note the different placement of the poles relative to the graph in figure 6.7.

two-particle-one-hole propagation are not seen very clearly. The observed energy dependence is reminiscent of the energy-dependent structure seen in the simple model discussed in chapter 5, figure 5.23. We observe that for  $\eta = 65.0$ , the value at which good converged results can be obtained for the free two-particle propagator case, there are no traces left of the pole structure. The graph is very smooth, and in the limit of very large  $\eta$  values,  $\Sigma(\Omega)$  approaches the energy-independent, first-order value as expected.

The matrix inversion approximation two-particle propagator calculations converge at about  $\eta = 30.0$ , and thus a comparison of the performance of the free two-particle propagator after the first iteration and the matrix inversion approximation two-particle propagator after 1 and 10 iterations at this value of  $\eta$  is provided in figure 6.13. The differences are not very large, showing the same smooth energy dependence with very little influence of the pole structure of either propagators or interaction.

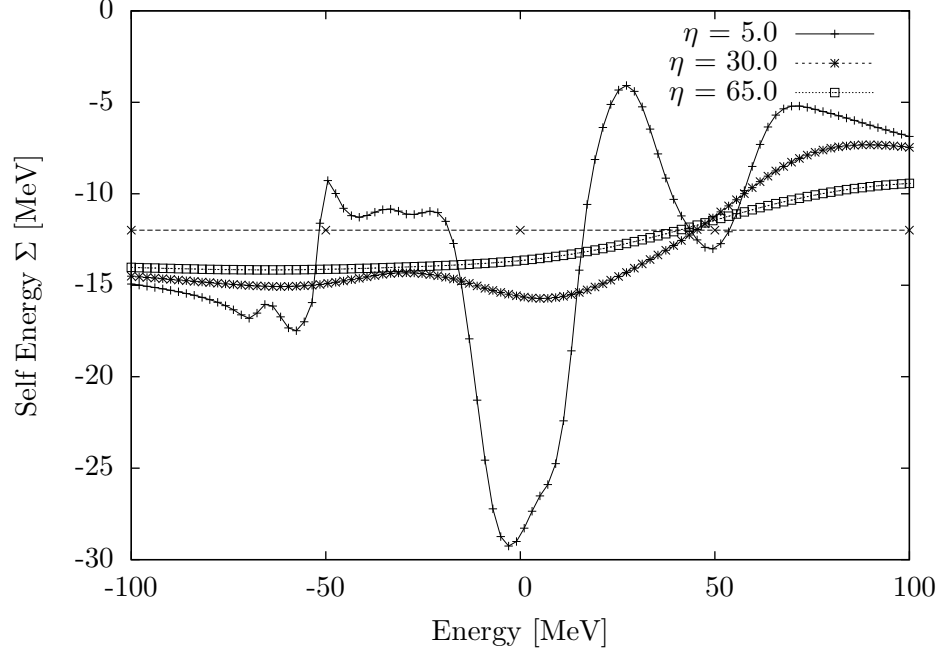


Figure 6.12:  $\langle 0s_{\frac{1}{2}} | \Sigma | 0s_{\frac{1}{2}} \rangle$  of an energy-dependent free propagator structure calculation within five major oscillator shells for  $\eta = 5.0, 30.0$  and  $65.0$  after the first iteration. At  $\eta = 65$ , where convergence is achieved, almost all structure is lost.

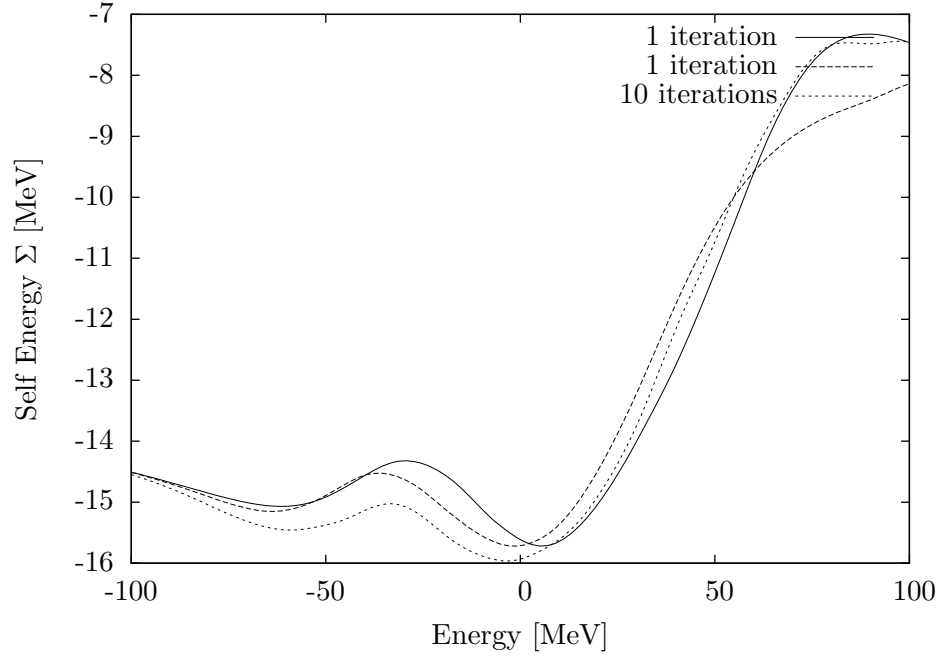


Figure 6.13:  $\langle 0s_{\frac{1}{2}} | \Sigma | 0s_{\frac{1}{2}} \rangle$  of an energy-dependent calculation within five major oscillator shells for  $\eta = 30.0$  for a free two-particle propagator calculation after the first iteration and for the matrix inversion approximation two-particle propagator calculations after 1 and 10 iterations. The differences are not substantial.

### 6.1.5 Ground state energy from energy-independent calculations

As discussed in the section on the two energy schemes, there are no difference between the free propagator approach and the matrix inversion scheme in the energy-independent calculations. All result shown in this section are generated according to the free propagator scheme.

In figure 6.14 we show both imaginary and real components for different  $\eta$  values as a function of oscillator frequency  $\hbar\Omega$  for a calculation within six major oscillator shells. As a result of introducing  $\eta$ , the ground state energy also has an (unphysical) imaginary component. Within the energy-independent scheme, the  $\eta$  dependence of the real part of the ground state energy is almost linear. The imaginary parts all have almost the same size, regardless of the  $\eta$  value. The variation with  $\hbar\Omega$  is not very large, with a minimal value around  $\hbar\Omega = 22$  MeV for all  $\eta$  values.

The dependence on the starting energy is shown in figure 6.15, for a calculation within six major harmonic oscillator shells, for  $\eta=5.0$  and  $\eta = 70.0$ . For starting energies above  $\sim -75$  MeV, the results are unreliable for the lowest value of  $\eta$ . As seen, a lower starting energy lowers the ground state energy. This can be understood if we compare with an  $L = R = 0$  calculation (no Parquet is performed), which has even lower energy. Starting energies further away from the real range of starting energies (the energy of two holes propagating would typically lie about  $-20$  MeV to  $-30$  MeV) show less impact of including the full interaction  $\Gamma$ .

For starting energies above  $\sim -75$  MeV, the value of  $\eta$  has to be increased to about 70-80 to get converged results. In the lower panel of figure 6.15 we see that the average position of the graphs decrease for  $E_{in} > -100$  MeV. The positive starting energies have rather low ground state energies. Thus it is not unlikely that the graph at realistic starting energies will lie somewhere in the middle between the two sets of graphs. Even if that is the case for  $\eta = 70$ , the situation might change in the physical limit  $\eta \rightarrow 0$ . Assuming a linear  $\eta$ -dependence, it is possible to extrapolate to  $\eta = 0.0$  in each case, but as these  $\eta$ -values are large there is no guarantee that the assumed dependence is correct.

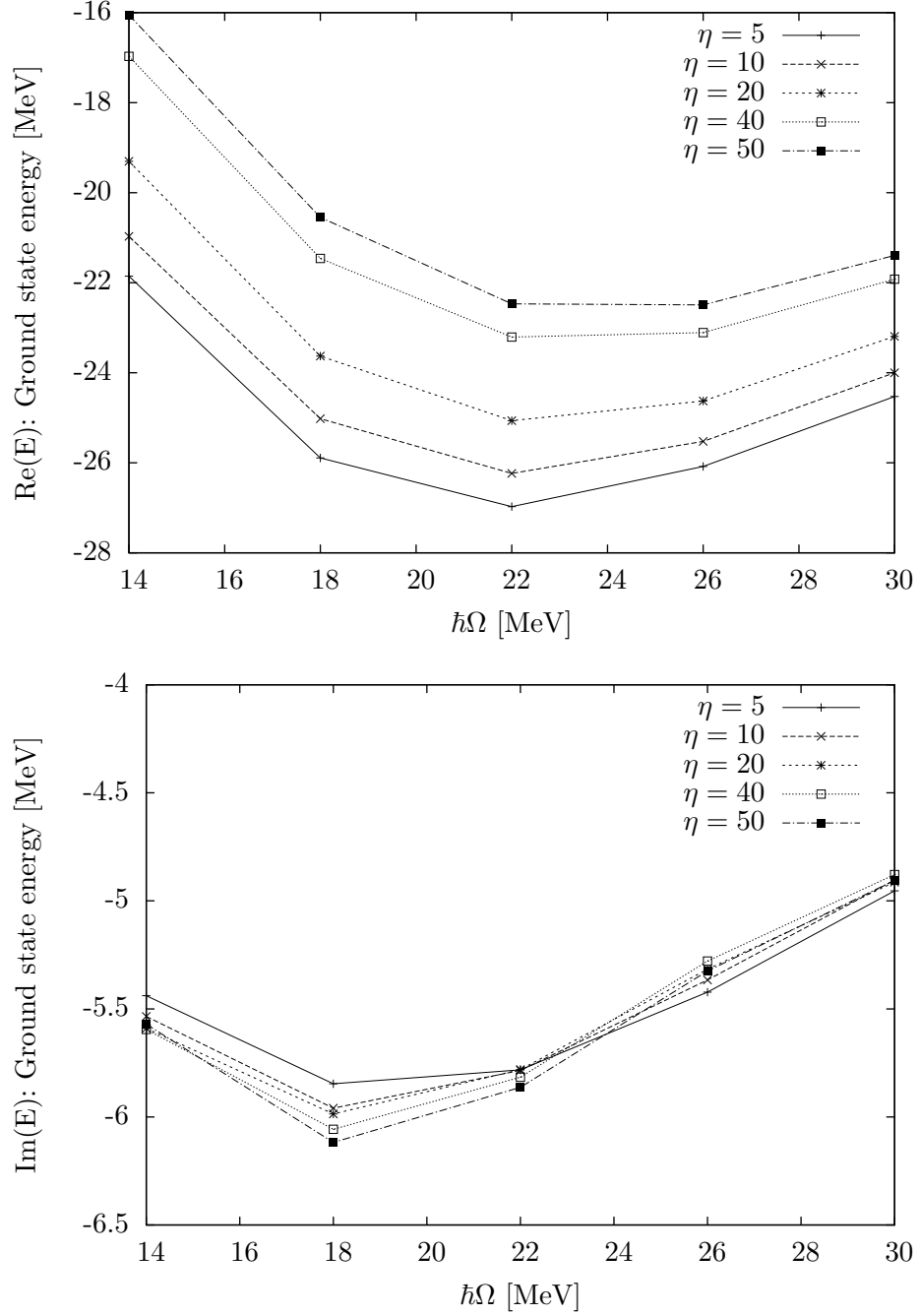


Figure 6.14: Real (upper panel) and imaginary (lower panel) parts of the energy for different  $\eta$  for a calculation within six major oscillator shells at starting energy of  $-200$  MeV. The  $\eta$  dependence is almost linear.



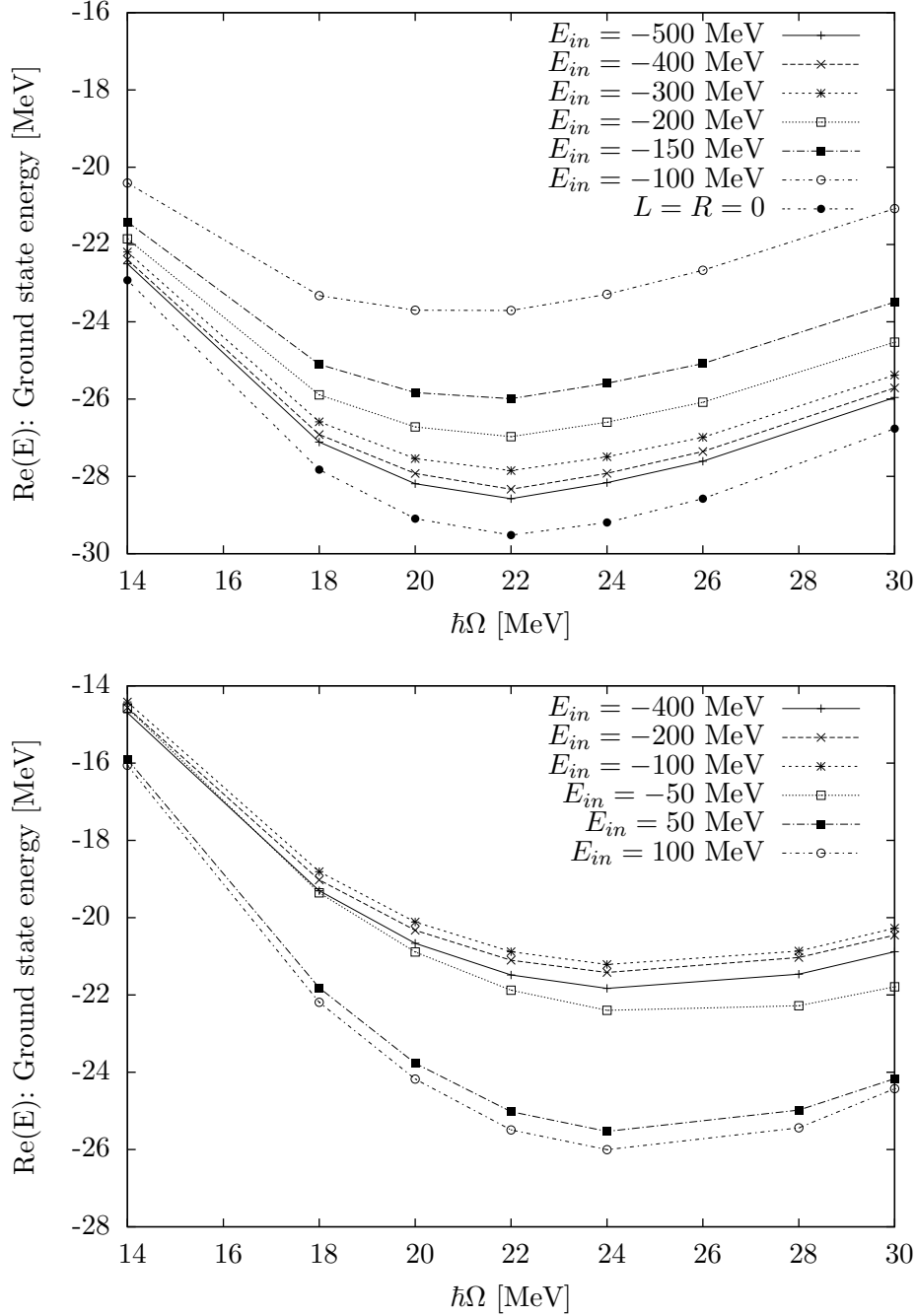


Figure 6.15: Dependence on the starting energy for an energy-independent Parquet calculation with fixed  $\eta = 5.0$  (upper panel) and  $\eta = 70.0$  (lower panel) within six major oscillator shells. In the upper panel, the lowest graph belongs to the  $L = R = 0$  calculation, while the ground state energy increases as the starting energy increases. In the lower panel, the negative starting energies give less ground state energy than the graphs for the positive starting energies.

We have also investigated the convergence of this approximation scheme with respect to the model space, as shown in figure 6.16. We have plotted extrapolated values within 5 – 8 major oscillator shells for calculations with  $E_{in} = -200$  MeV. The results show reasonable convergence, although there is still some dependence on the model space. There is also a certain dependence on  $\hbar\Omega$ , with a minimum which seems to be shifted towards smaller  $\hbar\Omega$  as the model space increases. The ground state energy found in this approximation scheme is probably lower than the experimental value of  $-28.3$  MeV, but larger model spaces are needed to ascertain any reliable value.

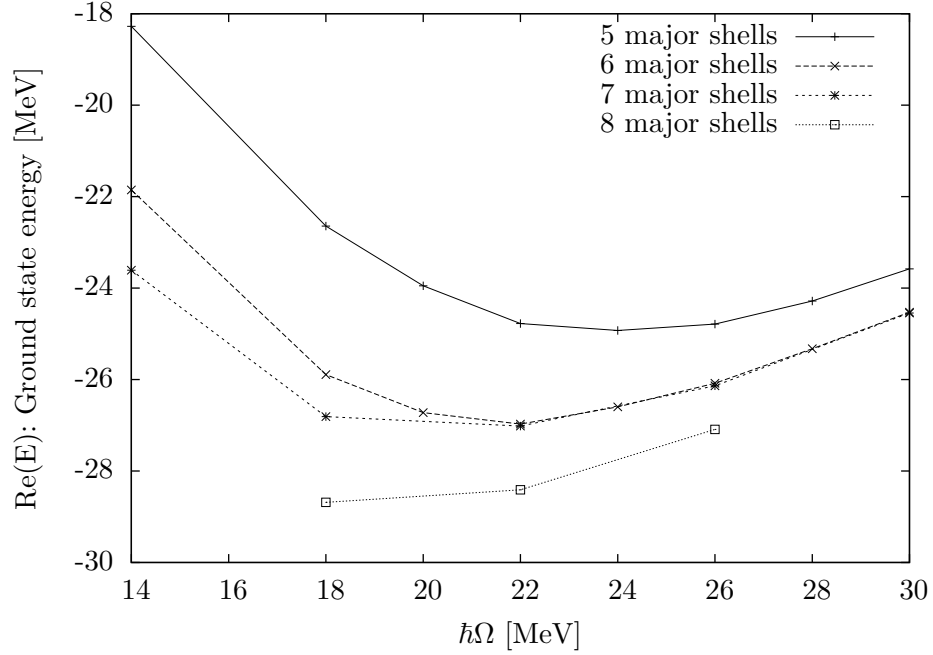


Figure 6.16: Results within 5,6,7 and 8 major oscillator shells at  $\eta = 5$  and  $E_{in} = -200$  MeV. There is still some dependence on the model space.

The differences between full Parquet calculations and Parquet with only ladder terms in this approach are small. The convergence properties of the ladder only approximation is somewhat better than the full Parquet, probably due to the reduced number of poles in  $\Gamma$ . The binding energy is somewhat smaller.

### 6.1.6 Ground state energy from energy-dependent calculations

#### Free propagator results

The convergence properties of the free propagator calculations were rather poor, as only calculations with values of  $\eta > 60$  converge. In figure 6.17 we show the real and imaginary parts of the ground state energy for a calculation within six major oscillator shells as a function of  $\hbar\Omega$  for several values of  $\eta$  above 70. The  $\eta$  dependence is generally as in the energy-independent case, reducing  $\eta$  gives a lower ground state energy. However, at larger  $\hbar\Omega$ , the graphs come very close. This indicates that the solutions found for the higher  $\hbar\Omega$  becomes increasingly closer to a mean-field type solution with energy-independent  $\Sigma$  due to the reduced resolution of the basis states when the spacing between levels is larger.

The imaginary part of the ground state energy in these calculations seems to be to a large extent independent of  $\eta$  and showing stronger dependence on the harmonic oscillator frequency than the energy-independent calculations. The imaginary part is shown in the lower panel of figure 6.17. We also see that the imaginary parts increase with increasing  $\hbar\Omega$ , consistent with the observation that the higher  $\hbar\Omega$  are more unstable and needs more iterations for convergence.

In the inset of the upper panel of figure 6.17 we compare the energy-dependent graph for  $\eta = 70$  with the corresponding graph from an energy-independent calculation with  $E_{in} = -200$  MeV. The differences are not very substantial, but the energy-dependent graph has a more pronounced curvature and the minimum lies at a slightly smaller  $\hbar\Omega$  value. The energy-independent graph is calculated at the standard starting energy  $E_{in} = -200$  MeV. Comparing with the graphs in the lower panel of figure 6.15, we see that the values for the ground state energy as found by the energy-dependent scheme falls well within the range of possible values found by the energy-independent calculations.

In figure 6.18 we show the ground state energy for calculations within 5-7 major oscillator shells as a function of the oscillator frequency  $\hbar\Omega$  for a fixed value of  $\eta=70$ . The results has the same features as in the energy-independent case, with the graphs for six and seven major shells very close and having a minimum at  $\hbar\Omega$  about 22 MeV. A calculation at eight major shells is needed to ascertain whether the differences between seven and eight shells are present also in this case.

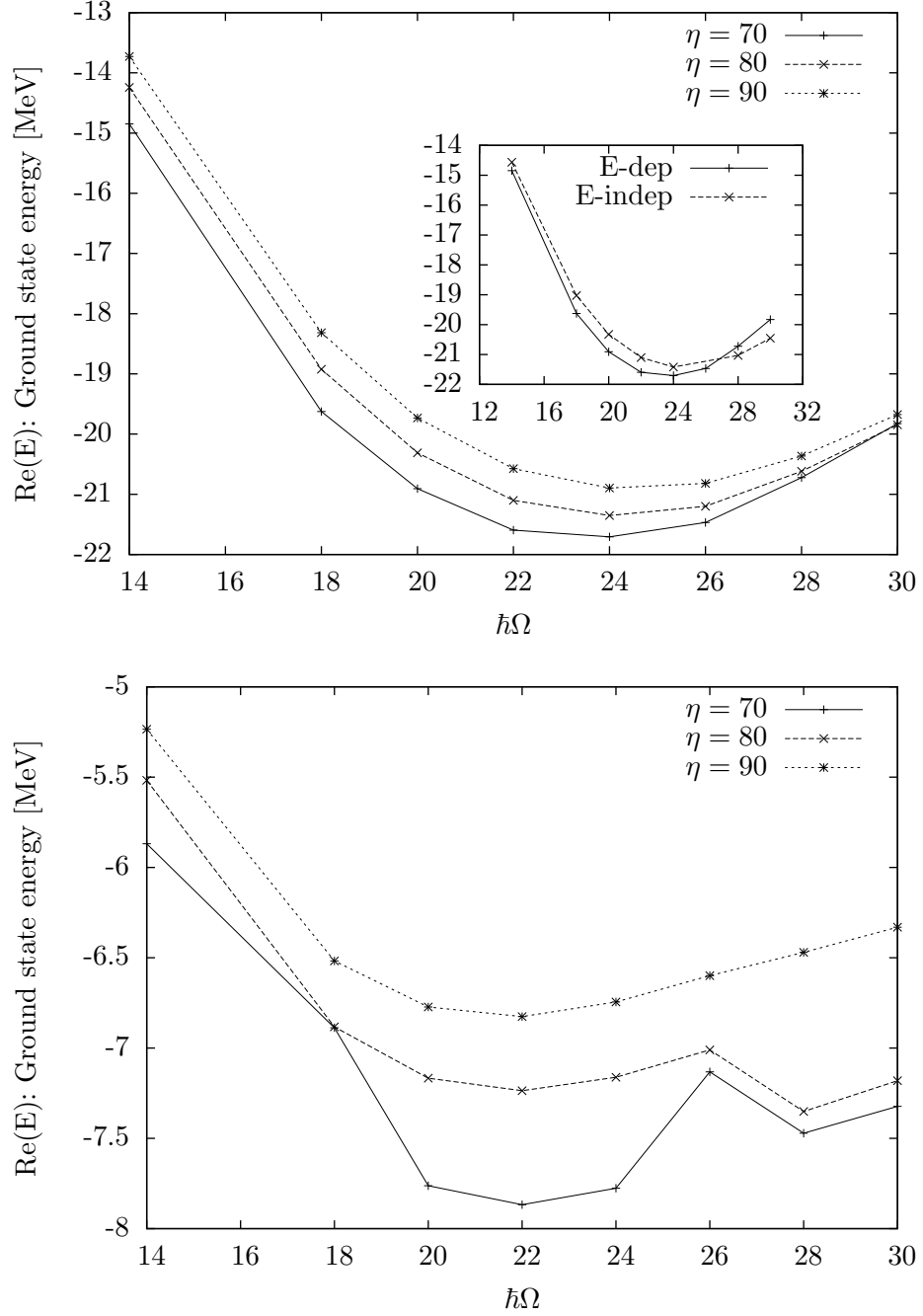


Figure 6.17: The real (upper panel) and imaginary (lower panel) parts of the ground state energy as function of  $\hbar\Omega$  for an energy-dependent calculation within six major shells following the free propagator scheme. The inset is a comparison between the energy-dependent and a corresponding energy-independent calculation.

Based on the evidence of figure 6.17, we can hardly assume a linear  $\eta$  dependence (at least not for large  $\hbar\Omega$ ), and it is difficult to perform an extrapolation with physical relevance based on the data sets. Based on the discussion on the performance of the UPS approximation in the simple model of chapter 5, we know that we probably cannot use the solutions found at large  $\eta$  to obtain meaningful results in the  $\eta \rightarrow 0$  limit.

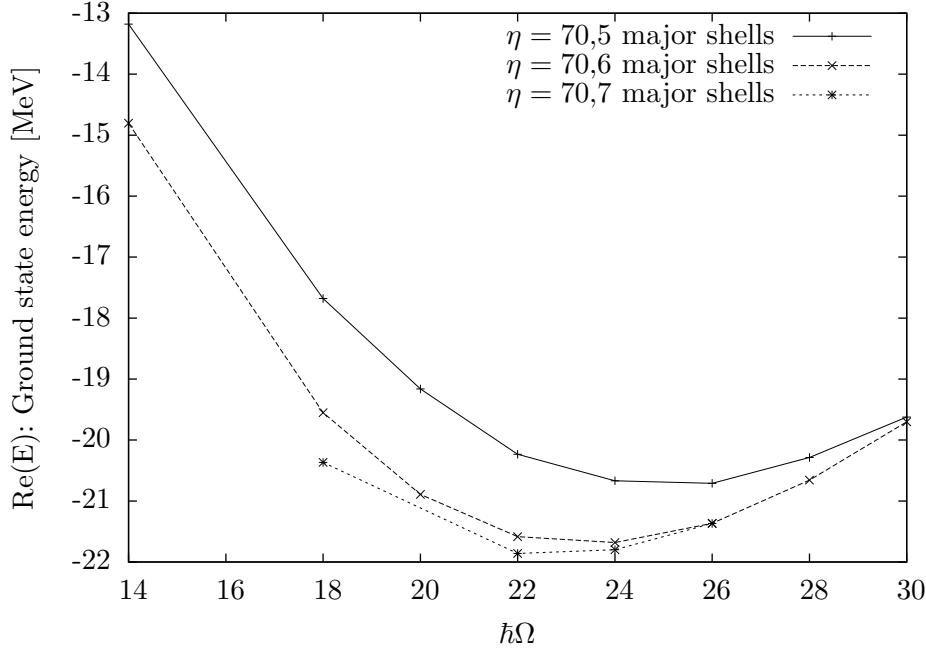


Figure 6.18: Calculation within five, six and seven major oscillator shells as a function of  $\hbar\Omega$  for  $\eta = 70$ . The differences between six and seven major shells are small.

Results for ladder calculations indicate that this approximation reduces the binding energy. In figure 6.19 we show results for a calculation within six major shells as a function of  $\hbar\Omega$  for several values of  $\eta$  above 60. Comparing with figure 6.17, the binding energy is reduced. Also, the minimum seems to be shifted slightly towards smaller  $\hbar\Omega$ . The convergence properties with respect to  $\eta$  are somewhat better, as could be expected since there are fewer poles involved.

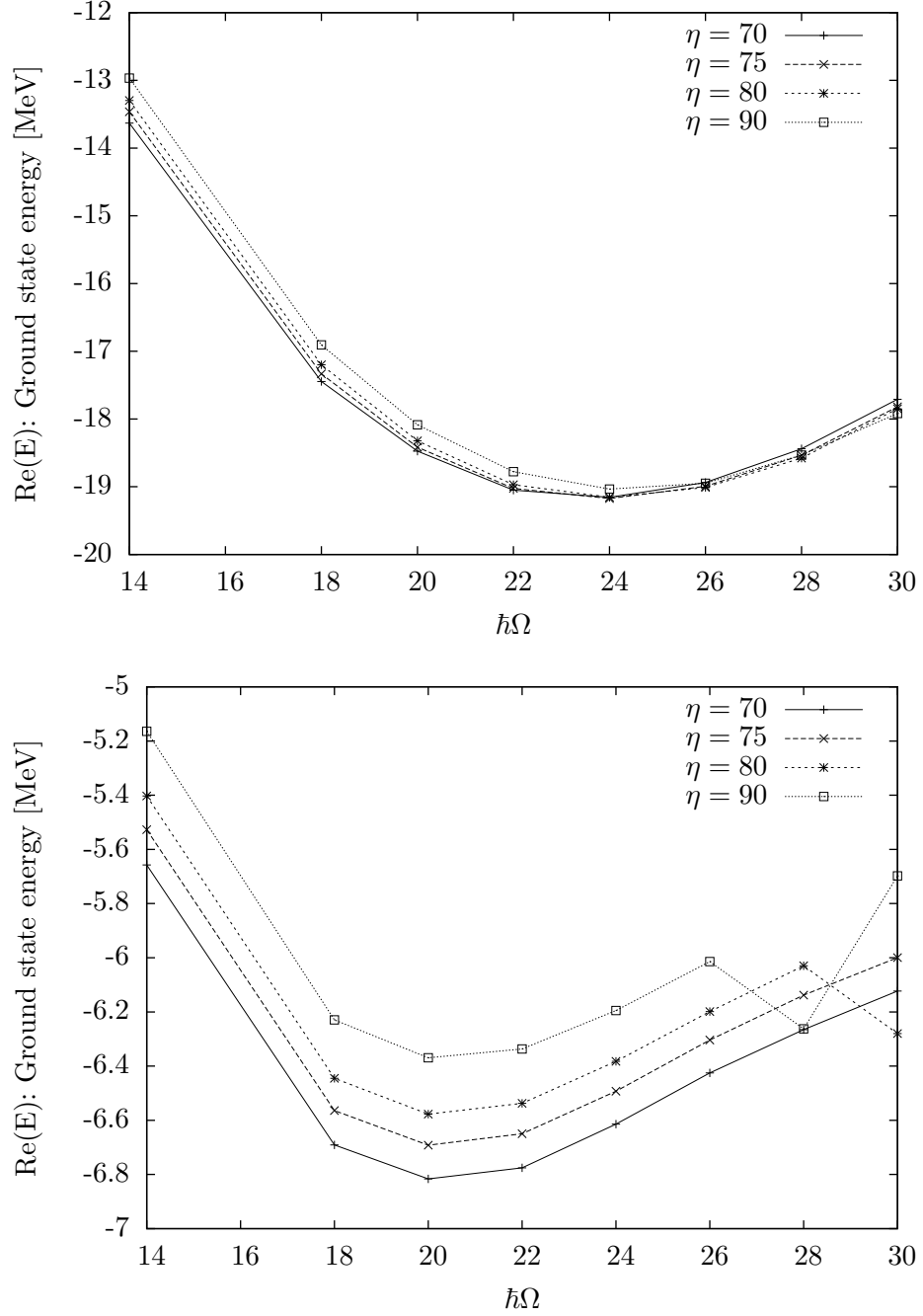


Figure 6.19: Calculation with only ladder terms included performed within six major shells for different values of  $\eta$ . The real part is shown in the upper panel and the imaginary in the lower panel. The differences between different  $\eta$  values are rather small. The ground state energy shows smaller binding energy than the corresponding full Parquet calculations given in figure 6.17.

The imaginary part of the ground state energy has a behaviour more similar to the energy-independent case, as shown in the lower panel of figure 6.19. Generally, the imaginary component increase for increasing values of  $\eta$ , but at larger  $\hbar\Omega$  this pattern is broken. The numerical values are of the same order as for the full Parquet calculations.

### 6.1.6.1 Result for Propagator found by Matrix Inversion Approximation

The results on the convergence properties, interaction matrix elements and the self energy found by applying the matrix inversion procedure indicates that this approach gives better convergence and better resolution with respect to the energy for the interaction matrix elements and the self energy. Unfortunately, this approximation gives severe overbinding. In figure 6.20 calculations for  $\eta = 30$  within 5,6 and 7 major oscillator shells are shown. The ground state energy in a fully converged model space and at  $\eta = 0$  would certainly lie below  $-33$  MeV.

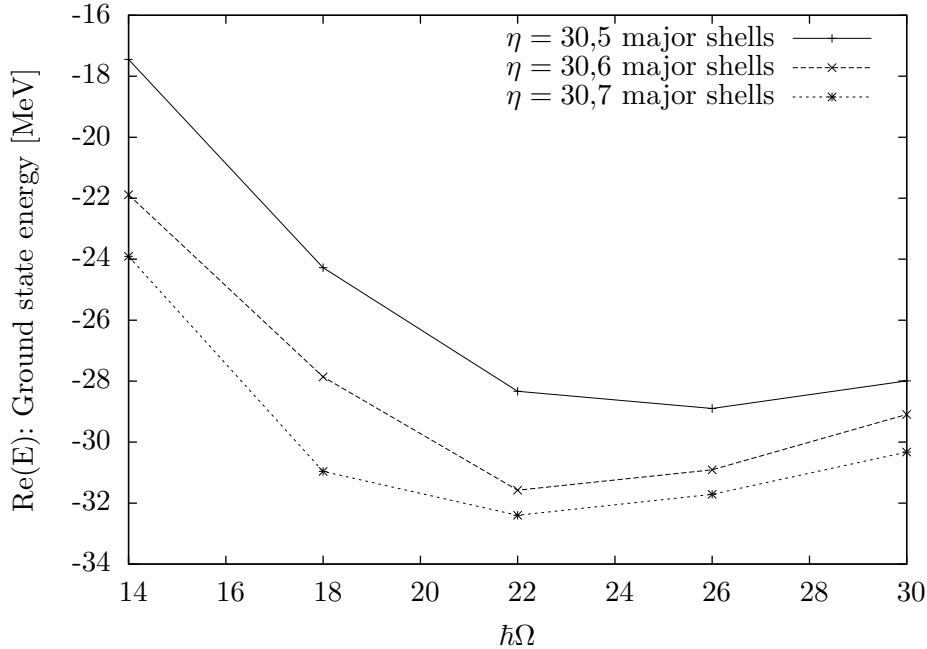


Figure 6.20: Results within five, six and seven major oscillator shells with propagator calculated according to the matrix inversion scheme, for calculations with  $\eta = 30$ . The binding energy found in this approximation scheme is too large.

## 6.2 Results for fixed-energy Dyson equation (FED) approximation

In this section we present results for the fixed-energy Dyson equation (FED) approximation discussed in section 4.5.2. This approximation assumes the form of the single-particle propagator given in equation (4.40). Thus the expressions for the free two-particle propagators are given by equation (4.17) for the particle-particle-hole-hole propagator  $\mathcal{G}_0^{pphh}$  and by equation (4.24) for the particle-hole propagator  $\mathcal{G}_0^{ph}$ . We still keep the approximation of solving the Dyson equation with a self-energy  $\Sigma$  calculated at a fixed energy, however, ensuring that the number of eigenvalues is the same as the total number of orbitals. First, we show results for the first-order approximation

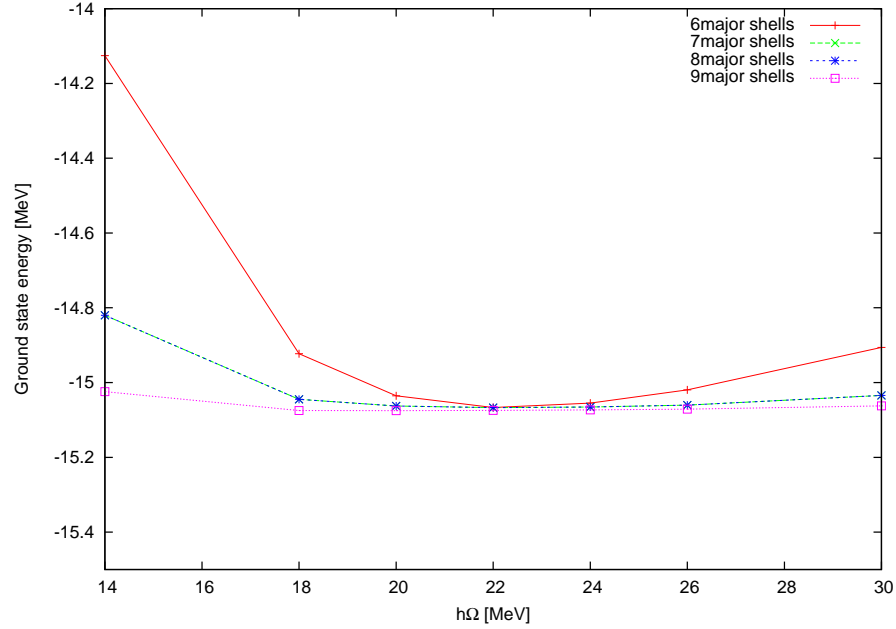


Figure 6.21: Standard Hartree-Fock calculation for increasing model spaces, from six to nine major oscillator shells. The convergence is very good, and with decreasing dependence on  $\hbar\Omega$  as the model space increases.

in figure 6.21. The self-consistency is performed using only the first-order, energy-independent term, as described in section 3.3.1. The self energy has the form

$$\Sigma(1,2)_{HF} = - \sum_{\alpha\beta < F} \langle 1\alpha | V | 2\beta \rangle z_{\alpha\beta}. \quad (6.1)$$



Here  $z_{\alpha\beta}$  is the amplitude of the single-particle propagator at the first-order energy  $\epsilon_{\alpha\beta}^{f.o.}$ . This is the conventional Hartree-Fock approximation, and the results agree with similar calculations performed within a variational scheme. The convergence is very good with respect to the model space, and as it is a first-order approximation without any two-time propagators,  $\eta$  is not needed. The ground state energy is calculated from the sum rule given in equation (3.29).

The FED calculations include an energy-dependent term to the self energy in addition to the above, giving the expression for the self energy given in equation 4.38, repeated here for easy reference:

$$\begin{aligned}
\Sigma(1, 2; \omega) = & - \sum_{\alpha\beta < F} \langle 1\alpha | V | 2\beta \rangle z_{\alpha,\beta} \\
& + \frac{1}{2} \sum_{\alpha\nu > F} \sum_{\beta\gamma\delta\mu} \langle 1\alpha | V | \beta\gamma \rangle \langle \beta\gamma | G_0^{pphh}(\omega + \epsilon_{\nu\alpha}^{f.o.}) | \delta\mu \rangle \langle \delta\mu | \Gamma(\omega + \epsilon_{\nu\alpha}^{f.o.}) | 2\nu \rangle z_{\nu\alpha} \\
& + \frac{1}{2} \sum_{\alpha\nu < F} \sum_{\beta\gamma\delta\mu} \langle 1\alpha | V | \beta\gamma \rangle \langle \beta\gamma | G_0^{pphh}(\omega + \epsilon_{\nu\alpha}^{f.o.}) | \delta\mu \rangle \langle \delta\mu | \Gamma(\omega + \epsilon_{\nu\alpha}^{f.o.}) | 2\nu \rangle z_{\nu\alpha}.
\end{aligned} \tag{6.2}$$

Based on the conclusions from the analysis of the simple model in chapter 5 and the unperturbed propagator structure (UPS) results above, we have concentrated on the energy-independent scheme for the FED results, as we expect this scheme to perform as least as good as or better than the more resource-consuming energy-dependent scheme.

### 6.2.1 Convergence with respect to $\eta$

For energy-independent calculations with fixed starting energy  $E_{in}$ , the FED approximation generally need smaller  $\eta$  values than the UPS approximation. Calculations within five major oscillator shells converge (very slowly) for  $\eta$ -values as small as 0.5 for  $\hbar\Omega$  values around 20-24 MeV. The calculations including six major shells converges for  $\eta$  values above 2, while  $\eta > 3 - 4$  is needed when seven major shells are included. All convergent solutions oscillate with decreasing amplitudes, and the convergence is faster for larger  $\eta$ . This is illustrated for the inclusion of six major shells case in figure 6.22, where the difference  $E_n - E_{n-1}$  between successive iterations is plotted in a log-scale plot as a function of number of iterations.

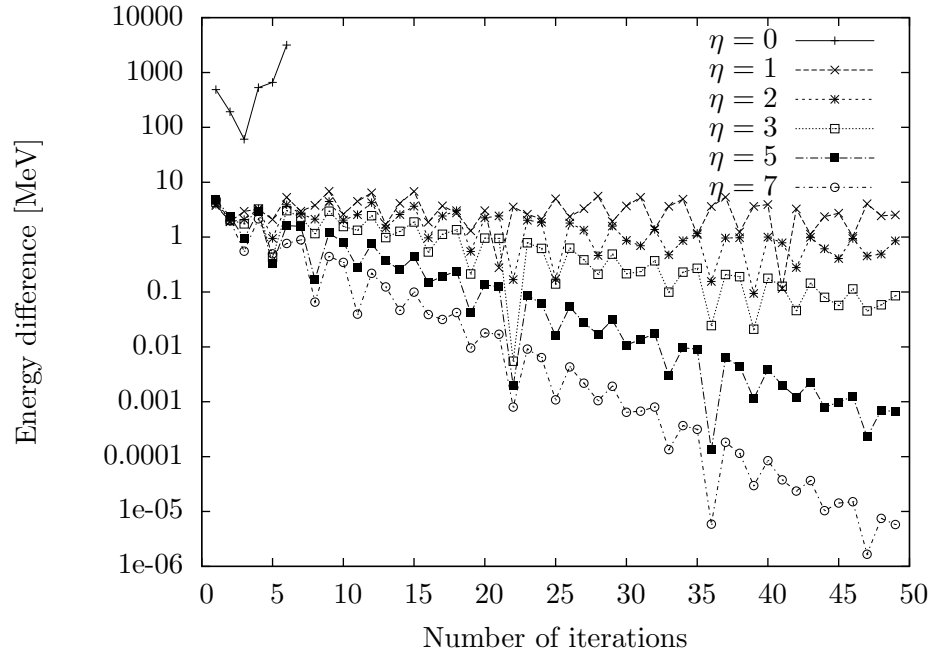


Figure 6.22: The difference  $E_n - E_{n-1}$  between successive iterations as a function of the number of iterations for an energy-independent calculation within six major shells for  $\hbar\Omega = 20$  MeV at  $E_{in} = -200$  MeV with different values of  $\eta$ . The convergence becomes gradually faster as  $\eta$  increases.

### 6.2.2 Self energy

In this section, we refer the reader to the state scheme of table 6.1 for an explanation of the state numbers.

From the discussion of the self energy in the simple model in chapter 5, we expect the self energy to have more poles in the FED approximation than in the UPS approximation. This is indeed the case, the pole structure of the  $\langle 0s_{\frac{1}{2}} | \Sigma | 0s_{\frac{1}{2}} \rangle$  element in the  $\eta = 0$  calculation shown in figure 6.23 have a very complex structure. Adding the  $\eta$ -factor quickly dampens the poles, as in the  $\eta = 1$  graph in figure 6.23. This is the reason why the FED results require smaller  $\eta$  values than the UPS results to converge.

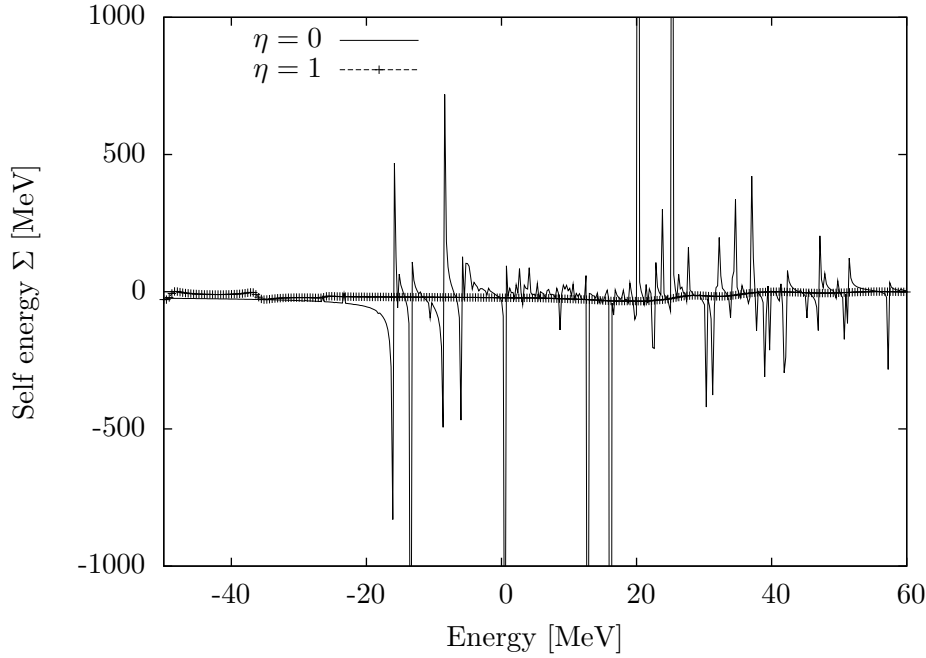


Figure 6.23: The matrix element  $\langle 0s_{\frac{1}{2}} | \Sigma | 0s_{\frac{1}{2}} \rangle$  after the first iteration for energy-independent calculations with  $\eta = 0$  and  $\eta = 1$  within six major shells for  $\hbar\Omega = 22$  MeV at  $E_{in} = -200$  MeV. The complex pole structure of the  $\eta = 0$  graph is quenched substantially by adding the imaginary component.

The effect of the self-consistency procedure is seen as a further quenching of most of the structure. However, the development patterns are not similar for all values of  $\eta$ , as can be seen in figure 6.25, where the upper panel show the self energy after 1 iteration, the lower after 30 iterations, in both cases for

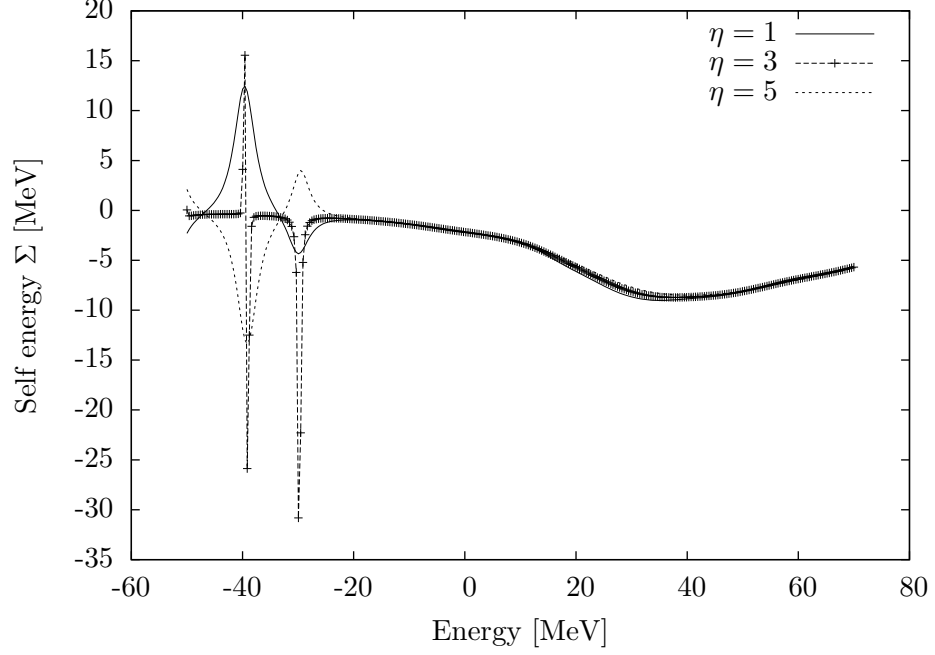


Figure 6.24: The imaginary component of the matrix element  $\langle 0s_{\frac{1}{2}} | \Sigma | 0s_{\frac{1}{2}} \rangle$  for energy-independent calculations with  $\eta = 1, 3$  and  $5$  within six major shells for  $\hbar\Omega = 22$  MeV at  $E_{in} = -200$  MeV after 30 iterations. The pole structure for the  $\eta = 3$  graph is clearly seen. The  $\eta = 1$  and  $\eta = 5$  graphs have reversed signs.

$\eta = 1, 3$  and  $5$ . We see that around  $\eta = 3$  the self energy of the lowest states has a pole structure for energies below  $-35$  MeV, while the graph for higher energies is smooth and not very different from the graphs of other  $\eta$  values. The imaginary part of the self energies shown in figure 6.24 reflect the pole structure seen in the real part of the matrix elements. The  $\eta = 1$  and  $\eta = 5$  graphs have reversed signs, and have wider, lower peaks than the  $\eta = 3$  graph.

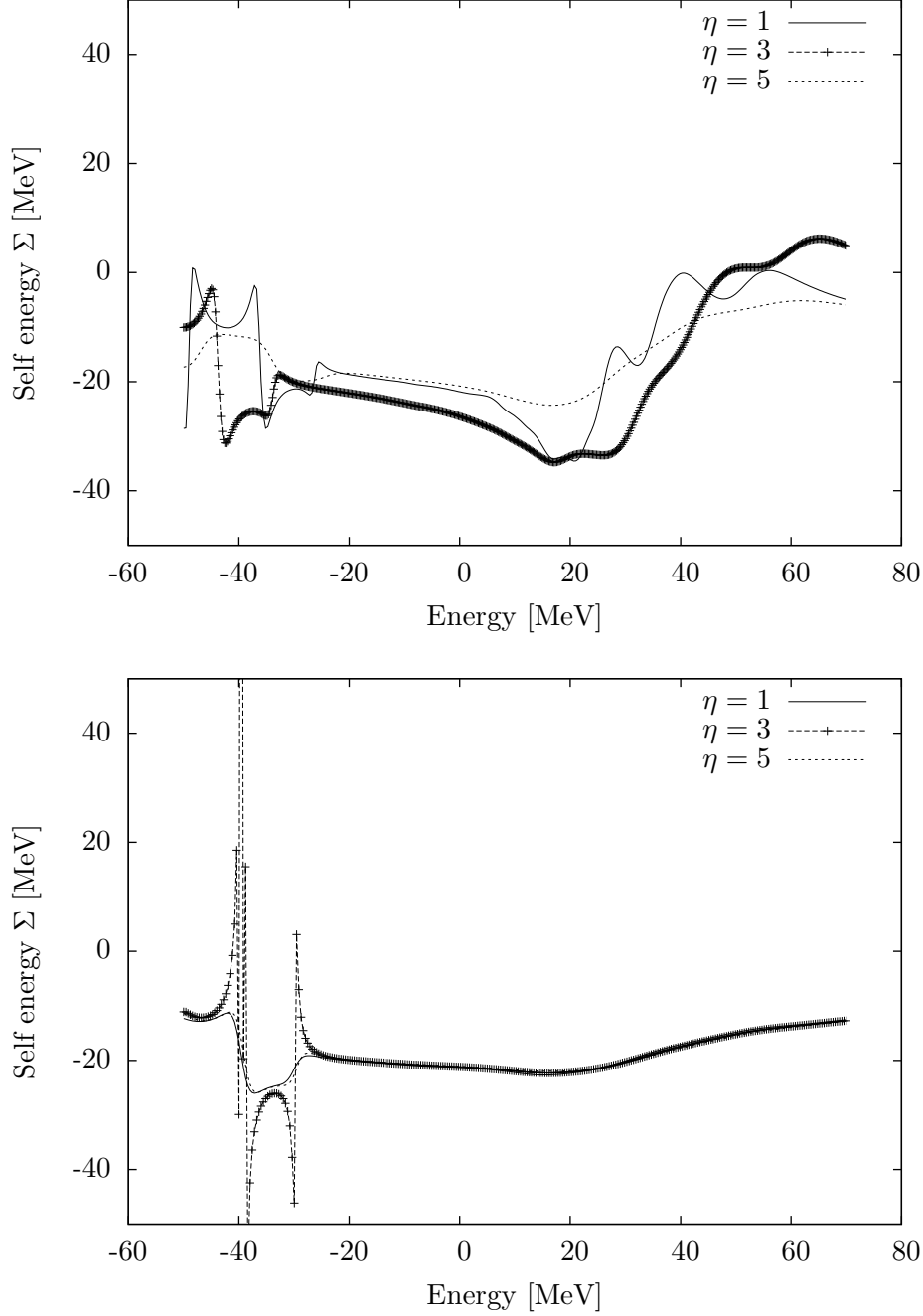


Figure 6.25: The matrix element  $\langle 0s_{\frac{1}{2}} | \Sigma | 0s_{\frac{1}{2}} \rangle$  for energy-independent calculations with  $\eta = 1, 3$  and  $5$  within six major shells for  $\hbar\Omega = 22$  MeV at  $E_{in} = -200$  MeV. The upper panel shows the self energies after the first iteration and the lower shows the self energies after 30 iterations. In the case of  $\eta = 3$ , a pole structure has emerged, but this is only weakly pronounced in the other two calculations.

Number	$ nlj\rangle$	$\eta = 1$	$\eta = 2$	$\eta = 3$	$\eta = 5$
1	p $ 0s\frac{1}{2}\rangle$	(-23.27,-1.684)	(-23.21,-1.640)	(-23.14,-1.600)	(-23.01,-1.529)
2	n $ 0s\frac{1}{2}\rangle$	(-24.14,-1.682)	(-24.08,-1.640)	(-24.02,-1.600)	(-23.89,-1.532)
3	p $ 0p\frac{3}{2}\rangle$	(2.027,-2.5422)	(2.077,-2.5041)	(2.132,-2.459)	(2.245,-2.369)
4	n $ 0p\frac{3}{2}\rangle$	(0.991,-2.5794)	(1.037,-2.5382)	(1.089,-2.490)	(1.197,-2.396)
5	p $ 0p\frac{1}{2}\rangle$	(5.280,-2.6070)	(5.333,-2.5298)	(5.390,-2.457)	(5.507,-2.333)
6	n $ 0p\frac{1}{2}\rangle$	(4.455,-2.6417)	(4.516,-3.8210)	(4.657,-3.695)	(4.870,-3.461)
7	p $ 0d\frac{5}{2}\rangle$	(7.904,-7.2897)	(8.208,-7.1628)	(8.489,-6.971)	(8.956,-6.517)
8	n $ 0d\frac{5}{2}\rangle$	(7.052,-7.4349)	(7.343,-7.2963)	(7.619,-7.095)	(8.088,-6.625)
9	p $ 0d\frac{3}{2}\rangle$	(11.06,-6.4667)	(11.18,-6.3308)	(11.33,-6.178)	(11.63,-5.871)
10	n $ 0d\frac{3}{2}\rangle$	(9.652,-8.4767)	(9.944,-8.0868)	(10.17,-7.697)	(10.49,-6.989)
11	p $ 1s\frac{1}{2}\rangle$	(4.349,-3.9416)	(4.514,-2.5636)	(4.575,-2.489)	(4.697,-2.361)
12	n $ 1s\frac{1}{2}\rangle$	(3.491,-3.8204)	(3.643,-3.7078)	(3.771,-3.589)	(3.967,-3.366)
13	p $ 0f\frac{7}{2}\rangle$	(16.22,-8.2392)	(16.33,-7.9549)	(16.44,-7.687)	(16.66,-7.217)
14	n $ 0f\frac{7}{2}\rangle$	(14.50,-11.406)	(14.81,-11.076)	(15.07,-10.74)	(15.51,-10.12)
15	p $ 0f\frac{5}{2}\rangle$	(21.23,-7.3497)	(21.22,-7.2405)	(21.22,-7.102)	(21.26,-6.805)
16	n $ 0f\frac{5}{2}\rangle$	(17.66,-7.8416)	(17.72,-7.6343)	(17.80,-7.434)	(18.00,-7.077)
17	p $ 1p\frac{3}{2}\rangle$	(10.17,-6.4793)	(10.29,-6.3229)	(10.43,-6.156)	(10.72,-5.831)
18	n $ 1p\frac{3}{2}\rangle$	(8.910,-8.5187)	(9.197,-8.1255)	(9.420,-7.731)	(9.728,-7.012)
19	p $ 1p\frac{1}{2}\rangle$	(15.53,-8.3050)	(15.62,-8.0211)	(15.72,-7.751)	(15.93,-7.273)
20	n $ 1p\frac{1}{2}\rangle$	(13.57,-11.365)	(13.87,-11.048)	(14.13,-10.72)	(14.55,-10.11)
21	p $ 0g\frac{9}{2}\rangle$	(24.74,-5.0822)	(24.80,-4.9318)	(24.87,-4.772)	(25.01,-4.464)
22	n $ 0g\frac{9}{2}\rangle$	(23.98,-5.1644)	(24.05,-5.0134)	(24.12,-4.853)	(24.26,-4.543)
23	p $ 0g\frac{7}{2}\rangle$	(26.98,-5.7629)	(27.05,-5.6003)	(27.10,-5.422)	(27.21,-5.071)
24	n $ 0g\frac{7}{2}\rangle$	(26.82,-9.2926)	(26.86,-9.1360)	(26.91,-8.963)	(27.05,-8.613)
25	p $ 1d\frac{5}{2}\rangle$	(22.18,-7.3909)	(22.18,-7.2723)	(22.19,-7.127)	(22.24,-6.821)
26	n $ 1d\frac{5}{2}\rangle$	(21.53,-6.4465)	(21.56,-6.2831)	(21.60,-6.109)	(21.71,-5.779)
27	p $ 1d\frac{3}{2}\rangle$	(26.18,-5.8580)	(26.24,-5.6929)	(26.30,-5.512)	(26.41,-5.155)
28	n $ 1d\frac{3}{2}\rangle$	(25.75,-9.2668)	(25.80,-9.1190)	(25.86,-8.954)	(26.00,-8.618)
29	p $ 2s\frac{1}{2}\rangle$	(20.57,-6.4353)	(20.58,-6.2791)	(20.62,-6.111)	(20.72,-5.787)
30	n $ 2s\frac{1}{2}\rangle$	(16.90,-7.8899)	(16.95,-7.6807)	(17.02,-7.478)	(17.20,-7.116)

Table 6.2: The energies of the 30 orbitals given in table 6.1 in energy-independent calculations within six major shells for  $\hbar\Omega = 22$  MeV at  $E_{in} = -200$  MeV for four different values of  $\eta$ . All numbers are in units of MeV. The labels p and n are abbreviations for proton and neutron, respectively. The differences are not very large.

Number	$ nlj\rangle$	5 shells	6 shells	7 shells
1	p $ 0s\frac{1}{2}\rangle$	(-23.01,-1.529)	(-26.05,-1.278)	(-26.21,-0.778)
2	n $ 0s\frac{1}{2}\rangle$	(-23.89,-1.532)	(-26.93,-1.281)	(-27.09,-0.780)
3	p $ 0p\frac{3}{2}\rangle$	(2.245,-2.369)	(0.272,-2.750)	(-0.1778,-2.20)
4	n $ 0p\frac{3}{2}\rangle$	(1.197,-2.396)	(-0.894,-2.698)	(-1.332,-2.157)
5	p $ 0p\frac{1}{2}\rangle$	(5.507,-2.333)	(4.811,-5.407)	(3.537,-7.747)
6	n $ 0p\frac{1}{2}\rangle$	(4.870,-3.461)	(3.774,-5.224)	(2.976,-4.229)
7	p $ 0d\frac{5}{2}\rangle$	(8.956,-6.517)	(9.667,-13.50)	(8.944,-14.64)
8	n $ 0d\frac{5}{2}\rangle$	(8.088,-6.625)	(8.498,-13.63)	(7.805,-14.89)
9	p $ 0d\frac{3}{2}\rangle$	(11.63,-5.871)	(15.24,-12.82)	(14.10,-12.11)
10	n $ 0d\frac{3}{2}\rangle$	(10.49,-6.989)	(14.41,-12.76)	(13.35,-12.01)

Table 6.3: The energies of the 10 first orbitals given in table 6.1 in energy-independent calculations within five six, and seven major shells for  $\hbar\Omega = 22$  MeV at  $E_{in} = -200$  MeV for  $\eta = 5$ . All numbers are in units of MeV.

Poles in the self energy primarily stem from poles in the  $\mathcal{G}_0^{pphh}$  propagator, and the poles of this propagator are determined by the energies of the single particle states. Looking at the orbital energies in the different calculations given in table 6.2, we see that the imaginary part is non-negligible and changes little as  $\eta$  increase. Thus the poles in the  $\mathcal{G}_0^{pphh}$  propagator do not lie on the real axis in our solutions, but have an imaginary component. The hole states have imaginary components around -1.6 MeV. These would give a pole for the two-hole-one-particle propagator with an imaginary part of around 3.2 MeV (due to the approximation in the Dyson equation solution, the particle energy in this calculation of the propagator is chosen to be the first order energy, which is purely real). The imaginary component of the pole energy may be surmised to be the reason why the  $\eta = 3$  calculations have the pole structure shown.

The pole structure at  $\eta = 3$  has little impact on the self-consistency procedure or the ground state energy, as the first-order energy of the lowest state at which  $\Sigma$  is calculated lies around -13 MeV. Such pronounced pole structures for higher  $\eta$  are unlikely as they must occur in the two-particle-one-hole regime of the self energy where the sum over possible states in the propagator is much larger. The development of the ten first orbitals with increasing model space is given in table 6.3. Generally, the orbital lower-energy orbital energies decrease with increasing model space. The higher-lying states like

the  $0d_{\frac{3}{2}}$  orbitals in the table show more fluctuations and less clear trends. The relevant experimental values for the lowest orbitals are the proton and neutron separation energies, the higher cannot be expected to correspond to definite physical states. From the Table of Isotopes we find that the proton separation energy for  ${}^4\text{He}$  is 19.81 MeV, corresponding to an orbital energy of  $-19.81$  MeV. Compared with the  $\sim -26$  MeV from our table 6.3, our method gives too strong binding. This overbinding trend is general for all lower orbitals. For example is the neutron  $0p_{\frac{3}{2}}$  orbital in  ${}^5\text{He}$  unbound (this nucleus is unstable), while we find a negative energy for this orbital, indicating a bound state.

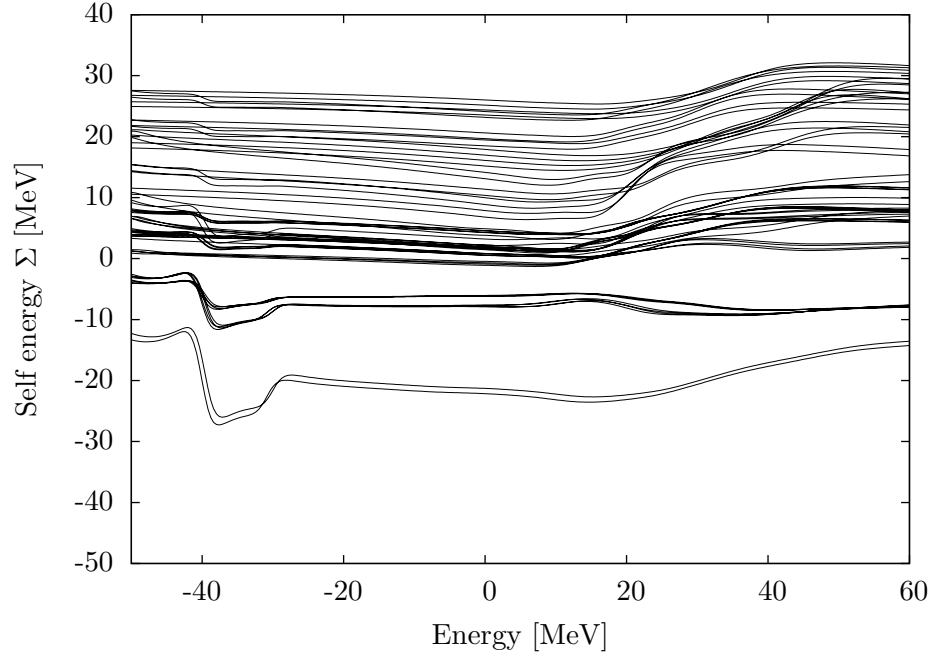


Figure 6.26: All 59 non-zero matrix elements of the self energy found after 30 iterations for an energy-independent calculation with  $\eta = 1$  within six major shells for  $\hbar\Omega = 22$  MeV at  $E_{in} = -200$  MeV. The two lowest self energy matrix elements correspond to the diagonal elements of the proton and neutron hole states  $0s_{\frac{1}{2}}$ . These are well separated from the rest of the matrix elements.

To give an impression of the general structure of all the matrix elements of the self energy, we have shown all 59 non-zero elements in figure 6.26. This is the self energy found after 30 iterations in an energy-independent calculation with  $\eta = 1$  within six major shells for  $\hbar\Omega = 22$  MeV at  $E_{in} =$



–200 MeV. The two lowest self energy matrix elements correspond to the diagonal elements of the proton and neutron hole states  $0s\frac{1}{2}$ . These are well separated from the rest of the matrix elements. The matrix elements with low self-energy values (corresponding to hole states and low-lying particle states) mainly show structure at negative energies, while the elements with higher self energy values are mostly featureless. All elements change in the range of 0-50 MeV input energy, most of them increase. The self energy matrix elements with values around 0 are the off-diagonal elements, while the elements at higher values are mostly diagonal elements. Some selected individual elements are displayed in figure 6.27, for an energy-independent calculation at  $\eta = 2$  within six major shells for  $\hbar\Omega = 22$  MeV at  $E_{in} = -200$  MeV. With this value of  $\eta$ , the pole structure is easily seen, but it does not dominate too much to obscure the details. Elements that couple to the lowest states, even those with comparatively high energy, as the proton state  $2s\frac{1}{2}$  (number 29 in the figure), shows the influence of the pole, as does lower-energy states with positive parity that do not couple directly, like the state  $0d\frac{3}{2}$  (number 9 in the figure). Higher-lying states with positive parity and all negative-parity states, like the proton states  $0g\frac{7}{2}$  (number 23 in the figure) and  $0p\frac{3}{2}$  (number 3 in the figure) show no traces of the poles. In the upper panel we see that the self energy matrix is not symmetric, the element  $\langle 0s\frac{1}{2}|\Sigma|1s\frac{1}{2}\rangle$  is not equal to the element  $\langle 1s\frac{1}{2}|\Sigma|0s\frac{1}{2}\rangle$ . We can also see that the pole is well-defined from the fact that the influence is clearly seen in the proton  $\langle 0s\frac{1}{2}|\Sigma|0s\frac{1}{2}\rangle$  orbital, but is less prominent in the corresponding neutron  $\langle 1s\frac{1}{2}|\Sigma|0s\frac{1}{2}\rangle$  element.

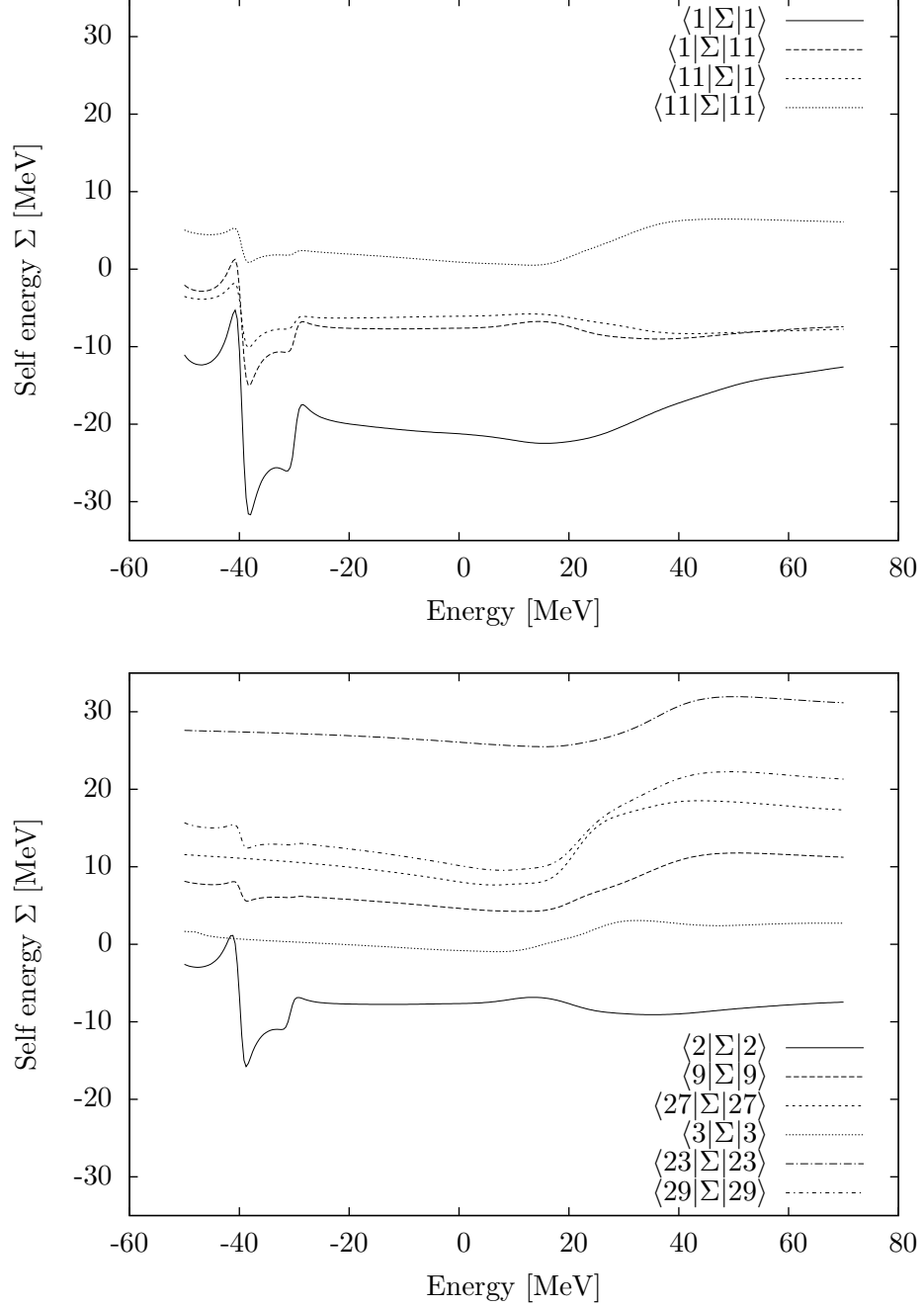


Figure 6.27: Some selected matrix elements for an energy-independent calculation at  $\eta = 2$  within six major shells for  $\hbar\Omega = 22$  MeV at  $E_{in} = -200$  MeV. The state labels are the orbital numbers according to table 6.2. The influence of the pole structure is only seen for states that couple directly to the hole states and positive parity states with comparatively low energy.

### 6.2.3 Spectral functions

The spectral functions in the FED approach results from the change of basis associated with solving the Dyson equation in our approximate manner. This shifts strength away from the pure single-particle orbitals and gives some strength to the states coupling to the hole orbitals. The equation for the hole spectral function was given in equation (4.41), repeated here for convenience:

$$S_h(\alpha, \omega) = \sum_k |z_{\alpha\alpha}^{k-}|^2 \delta(\omega - \epsilon_k^-). \quad (6.3)$$

The sum over  $k$  is, due to our approximation, limited to the number of orbitals. The energies  $\epsilon_k^-$  are then the orbital energies. Furthermore, only states coupled to hole states affects the hole spectral function. For calculations within five major oscillator shells, there are two such coupling states for each hole state. Thus we get a hole spectral function with three spikes, as in figure 6.28. This is generated from an energy-independent calculation with  $\eta = 1$  within five major shells for  $\hbar\Omega = 22$  MeV at  $E_{in} = -200$  MeV. As expected, most of the strength is still conserved in the hole states, even after 30 iterations, which shows a depletion of about 0.1. The energies of the states are shifted towards lower energies. This is an effect stemming from the tendency of the self-consistency procedure to enhances the interaction matrix elements coupling to the hole states. The effect makes the system more tightly bound and is well-known from standard Hartree-Fock calculations.

In the lower panel we show the four higher-lying orbitals in closer detail, and we see how the self-consistency procedure increase the energy and enhance the strength. This is also in accord with the expected damping of interaction matrix elements coupling to particle states.

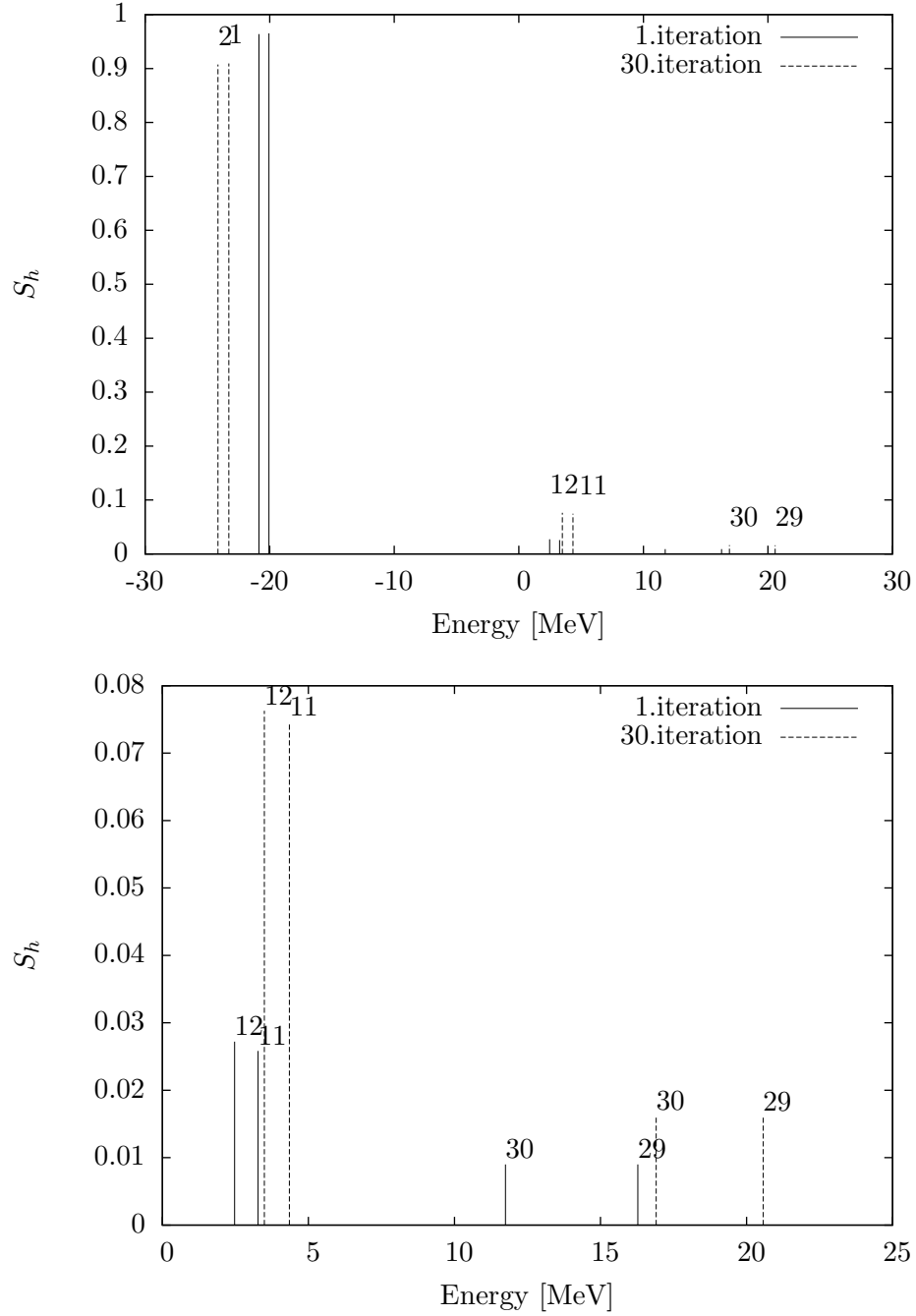


Figure 6.28: Spectral function for a calculation with  $\eta = 1$  after the first and after 30 iterations within five major oscillator shells. The lower panel shows a close-up on the higher-energy states. The numbers are according to table 6.2, with 1, 11 and 29 denoting proton  $0s_{\frac{1}{2}}, 1s_{\frac{1}{2}}$  and  $2s_{\frac{1}{2}}$  orbitals, respectively. The numbers 2, 12 and 30 are the corresponding neutron orbitals. The depletion of the hole states is about 0.1.

### 6.2.4 Ground state energy

The spread in values between different  $\eta$  values are much less than for the unperturbed propagator structure approximation. This is seen from figure 6.29, where we show real and imaginary components of the ground state energy for a calculation within six major oscillator shells with a starting energy of -200 MeV. Compared to the results for the unperturbed propagator structure (UPS) approximation, the curve as a function of  $\hbar\Omega$  is somewhat flatter, and the calculation gives considerably less binding energies, with a minimum at about  $\hbar\Omega = 18 - 20$  MeV.

The results are very close near the minimum of  $\hbar\Omega = 18 - 22$  MeV for small values of  $\eta$ . At  $\hbar\Omega = 20$  MeV the data points for  $\eta = 5$  and  $\eta = 7$  have exchanged their usual order,  $\eta = 7$  has a lower value than  $\eta = 5$ . Both points are well converged, as can be seen from the convergence graphs in figure 6.22. This closeness and occasional reversion of graphs for different  $\eta$  values is also seen for the calculations within seven major oscillator shells.

The imaginary parts of the ground state energy show a quite different behaviour than in the UPS approximation, not increasing regularly with  $\eta$ , and being larger at smaller  $\hbar\Omega$  values. Around  $\hbar\Omega = 20$  MeV we see that the imaginary part have a similar value for all  $\eta$  values. The dependence on the starting energy is shown in figure 6.30, and for comparison we include also the result of a calculation with  $L = R = 0$ . The general trends are the same as in the unperturbed approximation propagator scheme, with lower ground state energy for lower values of the starting energy, with the  $L = R = 0$  case as the limiting case. The same trend as for the UPS dependence is seen for positive  $E_{in}$ :  $\eta$  has to be substantially increased (to about 60 in the case of a calculation within five major shells), and the ground state energy found then is lower than the graphs for large negative values of  $E_{in}$ . The development as the model space increases from 5 to 7 major oscillator shells is shown in figure 6.31. The graph for 7 major shells contains some slightly unconverged values at  $\hbar\Omega = 14$  MeV and  $\hbar\Omega = 16$  MeV, but the remaining oscillations have amplitudes of less than 0.5 MeV. When 7 major shells are included, we see that the minimum is further shifted towards smaller  $\hbar\Omega$ . The graphs are not as close as for the UPS case, and we cannot conclude with any certainty that the calculations have converged with respect to model space.

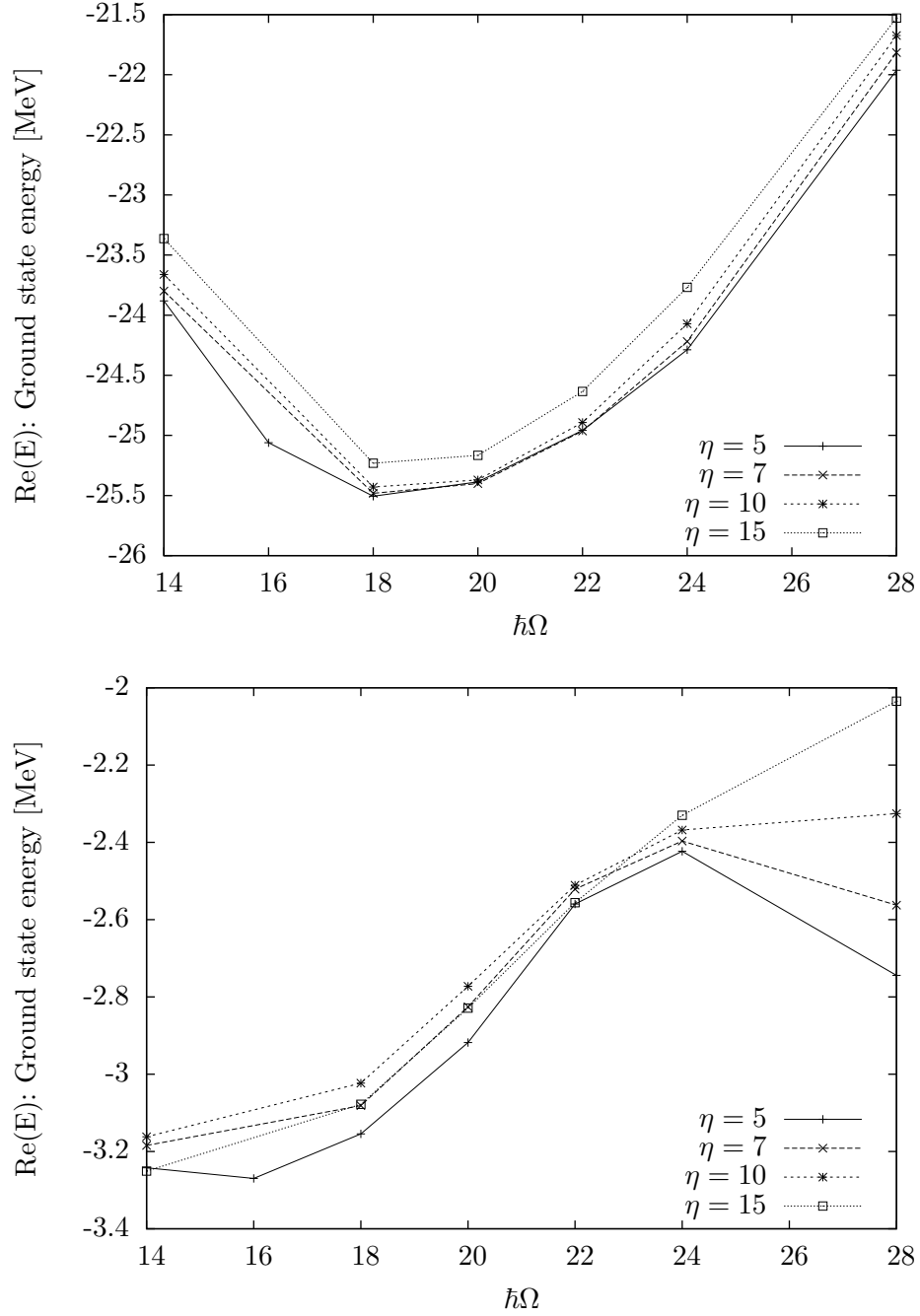


Figure 6.29: Real and imaginary parts of the energy for different  $\eta$  for a calculation within six major shells at starting energy -200 MeV. The graphs for different  $\eta$  are very close.

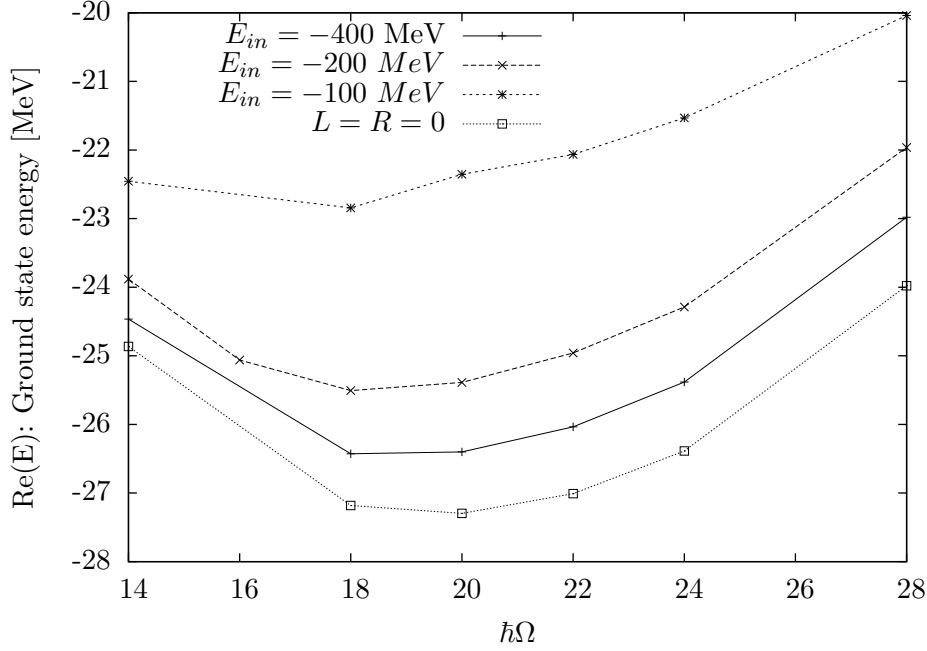


Figure 6.30: Calculations for different starting energies in a calculation with  $\eta = 5$  including six major oscillator shells. Results for  $L = R = 0$  are shown for comparison. The ground state energies becomes less as  $E_{in}$  increases.

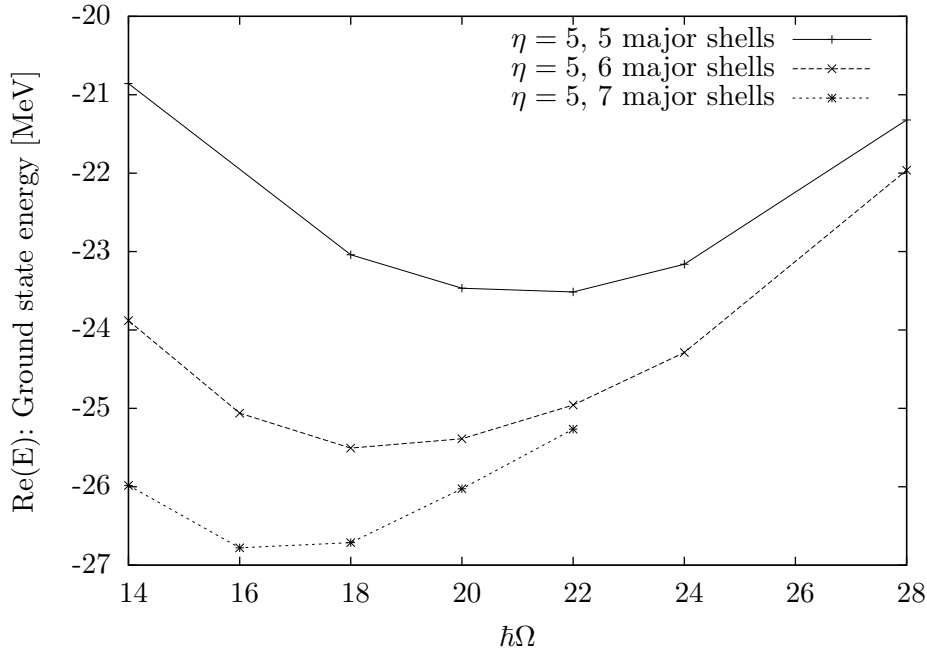


Figure 6.31: Calculations for 5,6 and 7 major oscillator shells with  $\eta = 5$  at starting energy -200 MeV. The ground state energy has not convincingly converged as the model space increases within the model spaces given here.

### 6.3 Summary of the ${}^4\text{He}$ results

Based on the results from the previous chapter, we investigated both the energy-independent and the energy-dependent scheme within the UPS approximation. We knew that the pairing component of the interaction in nuclei generally dominates, favouring the energy-dependent scheme, but also that the pair-breaking component is important. The results of section 6.1 clearly show that the number of poles generated by the  ${}^4\text{He}$  interaction is large enough to destabilize the energy-dependent scheme. Generally,  $\eta$  values as large as 70-80 are needed for convergence. The self energy in these calculations has lost almost all structure, as the graphs in figure 6.12 show.

We then tried to improve the convergence properties with respect to  $\eta$  by employing the matrix inversion scheme described in section 4.3.2. This was a success insofar as the convergence and the details of the self energy and interaction matrix element structure were concerned, but the ground state energy became far too low.

Thus we conclude that the most applicable scheme is the energy-independent scheme. This converges for calculations with  $\eta$  values small enough to preserve important parts of the self energy structure. The drawbacks of the scheme are primarily the dependence on the starting energy  $E_{in}$  and the knowledge that we lose the energy-dependence of the generated interaction  $\Gamma$ . The effect of missing the pole structure in  $\Gamma$  will certainly influence the final result, but any quantitative assessment is difficult.

The FED approximation scheme results are exclusively generated within the energy-independent scheme. The larger number of poles generated by this approach leads to a larger quenching of the pole structures for a given  $\eta$ , reflected in the fact that smaller  $\eta$  values are needed to obtain convergence than in the UPS scheme. The  $\eta$  dependence is less straight-forward. Rather than the almost linear dependence in the UPS case, the FED results for different  $\eta$  values yield very small differences in ground state energy at  $\hbar\Omega$  values close to the observed minimum. Also the self energies, the single-particle energies and the spectral functions generated for different  $\eta$  values show little variance with  $\eta$ . The reason for this behaviour is not entirely certain, but it might indicate that the solution we find is a stable minimum in the space of possible solutions to the iterative procedure. The closeness of this solution to the real solution is difficult to determine.

This solution has two well-defined hole states with complex energies. The effect is clearly seen in the self energy graphs, where a pole structure develops for negative energies around  $-35$  MeV for  $\eta$  values around 3, corresponding to the propagation of a two-hole-one-particle state. The spectral function for



these hole states has a strength around 0.9.

The self energy matrix elements found after the first iterations in calculations with  $\eta = 0$  vary fast with energy. This poses numerical difficulties for solving the Dyson equation, but the much more well-behaved self energy matrix elements obtained with  $\eta > 0$  ought to improve the stability and reliability considerably.



## 7 Conclusions and future work

The main motivation for the work presented in this thesis has been to investigate the stability and reliability of an actual implementation of the Parquet summation method and to establish the potential usefulness of this method as an *ab initio* method for nuclear structure calculations. The results so far are encouraging, albeit with some drawbacks concerning the limitations imposed by the numerical instabilities associated with the poles in the propagators.

The pole instabilities are handled by introducing an imaginary parameter  $i\eta$  into the calculation, which dampens out the divergences in the two-time propagators in exchange for an imaginary component of the calculated entities. To obtain physical results, it is necessary to extrapolate to  $\eta = 0$ . One of our main foci has been to study the impact of this  $\eta$  parameter on the ground state energy, the self energy and the spectral function, and to investigate into the stability of our solution as  $\eta$  is varied.

We have implemented four schemes of the Parquet self-consistency scheme, as summarized in section 4.5, with varying degrees of approximations. The largest impact is made by our approximate solution of the Dyson equation, which we have simplified from a non-linear eigenvalue equation to a normal linear eigenvalue equation by choosing the first-order energies as basis for the energy at which the self energy is calculated, rather than at the energy eigenvalue. The consequence is that the single-particle propagator has a fixed number of poles (equal to the number of orbitals).

The energy-dependence of the interaction operator  $\Gamma$  has been handled in two ways, one in which we choose a given so-called starting energy  $E_{in}$ , thereby introducing an extra energy dependence in our results, and one in which we have calculated  $\Gamma$  on a fixed, real grid of energies and interpolated in the calculation of the self energy.

We have investigated the differences between choosing an approximate single-particle propagator having the structure of the unperturbed propagator, giving what we have termed the unperturbed propagator structure (UPS) approximation, and the correct expression. However, as we still retain our ap-

proximate method of solving the Dyson equation, we have termed the scheme employing the correct expression the fixed-energy Dyson equation (FED) approximation.

The first part of our results, given in chapter 5, concerns a simplified model of the nucleus, a model with a constant spacing between single-particle levels and particles interacting via a constant interaction. We have looked at two schemes of the interaction, one in which only pair-excitations are allowed, and one with a pair-breaking term the same size as the pair-conserving term. In both cases we have investigated the stability with respect to  $\eta$  when varying different parameters, and compared the different approximation schemes to the exact solution found by matrix diagonalization.

The main conclusion of our study of the Parquet method applied to our simple model is that it is only applicable when the interaction strength is rather small compared to the level spacing. The fixed-energy Dyson equation (FED) approximation does consistently better compared with the UPS approximation, but both methods fail to find solutions close to the exact solution as the number of levels and particles increase. The energy-dependent scheme is closer to the exact solution for small systems where the number of poles are limited, but as the number of poles in both self energy and generated interaction  $\Gamma$  increase when the system size increases, this solution scheme needs large values of  $\eta$  to converge. Then too many details of the pole structure are lost, and the solutions found by this scheme are further removed from the exact solution than the energy-independent solution.

In chapter 6 we investigated the performance of our schemes of the Parquet self-consistency scheme in the more realistic case of the  ${}^4\text{He}$  nucleus. All results have been generated using a  $V_{lowk}$  potential with cutoff  $2.2 \text{ fm}^{-1}$  based on the Argonne  $V_{18}$  potential. The results confirm the findings from the simple model, establishing the energy-independent FED scheme as the currently overall best scheme. This retains the pole structure of the self energy to a larger degree than the other schemes, and have altogether best convergence properties with respect to  $\eta$ .

The ground state energy results are within a reasonable range of the experimental value of 28.3 MeV, but there are several reasons why a definite value as 'the' ground state energy can not be produced at present. Firstly, the calculations have not been performed in large enough model spaces to be certain of proper convergence. Secondly, the limit  $\eta \rightarrow 0$  must be found by extrapolation, which is difficult because the exact dependence on this parameter is unknown. Finally, the energy-independent approach has a dependence on the starting energy  $E_{in}$ , and as this does not correspond to a well-defined physical quantity there is no *a priori* natural choice of value for this energy.

However, the main conclusion is that the Parquet method can be implemented and give reasonable results which seems on the right track to becoming useful as an *ab initio* nuclear structure calculation method. It is easy to generate graphs for the self energy as a function of energy, and these can be used to determine the degree to which the solution incorporates correlations beyond a mean-field type solution. The spectral functions are easy to extract, as are spectroscopic factors. The FED solutions for small  $\eta$  values have very stable configurations changing little with  $\eta$ , perhaps an indication that the solutions are close to a stable minimum in the solution space, which may or may not be close to the solution when  $\eta \rightarrow 0$ . The numerical values for the ground state energy are in the vicinity of the experimental results. However, we are not yet at the level of precision needed to meet the current benchmark standard for *ab initio* calculations of  $^4\text{He}$  ground state energy. For a  $V_{lowk}$  potential with cutoff  $1.9 \text{ fm}^{-1}$  based on the Argonne  $V_{18}$  potential, a coupled-cluster calculation within 16 major oscillator shells gives a binding energy  $-29.18 \text{ MeV}$  for  $^4\text{He}$ , while a Fadeev-Yakubovsky calculation gives  $-29.19(5) \text{ MeV}$  [9].

The Parquet method certainly has the possibility for attaining a high level of accuracy. The angular-momentum coupling schemes allow for huge reductions in the model space, giving the possibility to perform much larger calculations. All Goldstone ground state energy diagrams to fourth order are included, a feat which in the coupled-cluster approach require inclusion of excitation operators to the fourth order (implying a CCSDTQ calculation) [108]. Recently, converged results for the ground state energy of  $^4\text{He}$  [109] within the self-consistent Green's function framework employed by Barbieri *et.al.* [104, 6, 24] have been presented. These results show that the required level of precision to meet the current standard is possible within implementations of Green's function based methods. The approach of Barbieri and co-workers does not include as many pphh correlations as the Parquet method, and is not as easy to improve systematically.

There are two primary directions for the immediate future work on the Parquet method. Firstly, the implementation needs to be made parallel and optimized to allow for larger model spaces. Due to the matrix multiplication scheme, large matrices have to be stored, and thus a memory distribution scheme must be developed. In addition, the FED approximation scheme requires a large number of sums which, when parallelized, can substantially reduce the computation time of each calculation. When these improvements have been implemented, we expect to be able to not only ascertain the convergence with respect to model space for the  $^4\text{He}$  case, but also to obtain converged results for larger nuclei like  $^{16}\text{O}$  and  $^{40}\text{Ca}$ . Our study of the simple model indicate that the errors of our results scale well with increasing particle

number. It should also be possible to perform calculations on smaller systems which are not doubly-magic.

The other concern is to solve the Dyson equation correctly. To do so on the basis of the self energy at  $\eta = 0$  is a numerically hazardous enterprise, given the number of poles. The  $\eta$  parameter quickly dampens the structure, giving a more well-behaved self energy, and the possibility of obtaining useful solutions to the Dyson equation increases. If we are able to obtain stable solutions, we will be able to find realistic spectral functions. Then we can study the fragmentation of single-particle strength observed in nuclei and extract spectroscopic factors to be compared both to experiment and to results obtained by other methods as e.g. the coupled-cluster method.

It is desirable to obtain a better precision level for the energy-dependent calculations, as the inclusion of the poles in the interaction  $\Gamma$  certainly will affect the results. In this respect, to implement a more correct approximation to the equation for the energy-dependent part of the self energy might serve as a starting point for a more thorough treatment of the poles in the interaction.

On a wider timescale, we want to develop the Parquet summation method to include higher-body corrections in a consistent, controllable manner. The basic framework for extending the Parquet equations to take three- and four-body correlations into account exists [39], but there still remains work, especially on the anti-symmetry conditions for fermions, before this set of equations are formulated in a way suited for implementation. However, there seems not at the present to be any fundamentally new problems to be overcome relative to the two-body case.

*Ab initio* approaches are in principle applicable to the whole nuclear chart, although calculations of unstable nuclei pose interesting problems, as both bound states, resonances and continuum states have important effects and very large basis sets are necessary to describe the combined effects of all three types. We want to study the performance of the Parquet method when applied to weakly bound systems, both comparing to available data and predicting new results where possible. Current phenomenological approaches are unreliable with respect to predictive power away from the nuclei they are tuned to reproduce, and comparing the relative merits of the different approaches will be interesting.

Another interesting extension of the Parquet method is to investigate its performance in nuclear matter calculations. Microscopic calculations in this field have traditionally included ladder-type interactions, and comparing these to calculations which also include particle-hole type of diagrams on an equal footing could yield useful information on the reliability and accuracy of such approaches. In a further perspective, the influence of medium effects on pair-

ing characteristics in microscopic superfluidity calculations constitutes an extremely difficult problem.

To obtain better theoretical foundations for calculations of heavier nuclei, it is crucial to develop an *Ab initio*-based Density Functional Theory. We would like to investigate the possibility of using Parquet and Green's functions formalism as a basis for such a functional, to attain a systematically improvable DFT theory, obtaining a self-consistent framework that goes beyond conventional mean-field approaches. Developing an energy density functional for use in nuclear matter in parallel to one applicable to finite nuclei seems instructional, as less symmetries are broken in infinite matter. This will be a natural extension of the work on nuclear matter, and is made easier by the similarities of nuclear matter and the electron gas, for which the DFT method was first developed.





# Bibliography

- [1] W.H. Dickhoff and C. Barbieri. Self-consistent green's function method for nuclei and nuclear matter. *Progress in Particle and Nuclear Physics*, 52:377–496, 2004.
- [2] W.H. Dickhoff and H. Mütter. Nucleon properties in the nuclear medium. *Reports on progress in physics*, 11:1947–2023, 1992.
- [3] A. Ramos, W.H. Dickhoff, and A. Polls. Binding energy and momentum distribution of nuclear matter using green's function methods. *Physical Review C*, 43:2239, 1991.
- [4] P. Bożek, D. J. Dean, and H. Mütter. Correlations and effective interactions in nuclear matter. *Physical Review C*, 74:014303, 2006.
- [5] A. Rios, A. Polls, and I. Vidaña. Hot neutron matter from a self-consistent green's-functions approach. *Physical Review C*, 79:025802, 2009. Arnau Rios and Artur Polls and Isaac Vidaña.
- [6] C. Barbieri. Single particle spectra based on modern effective interactions. *Physics Letters B*, 643:268 – 272, 2006.
- [7] Willem Hendrik Dickhoff and Dimitri Van Neck. *Many-body theory exposed!: propagator description of quantum mechanics in many-body systems*. World Scientific, Hackensack, NJ, 2005.
- [8] Maria Goeppert Mayer. On closed shells in nuclei. ii. *Phys. Rev.*, 75:1969–1970, Jun 1949.
- [9] G. Hagen, D. J. Dean, M. Hjorth-Jensen, T. Papenbrock, and A. Schwenk. Benchmark calculations for  $^3\text{h}$ ,  $^4\text{he}$ ,  $^{16}\text{o}$ , and  $^{40}\text{ca}$  with ab initio coupled-cluster theory. *Physical Review C*, 76:044305, 2007.
- [10] G. Hagen, T. Papenbrock, D. J. Dean, and M. Hjorth-Jensen. Medium-mass nuclei from chiral nucleon-nucleon interactions. *Physical Review Letters*, 101:092502, 2008.
- [11] Rodney J. Bartlett and Monika Musiał. Coupled-cluster theory in quantum chemistry. *Reviews of Modern Physics*, 79:291, 2007.

- [12] E. Caurier, G. Martínez-Pinedo, F. Nowacki, A. Poves, and A. P. Zuker. The shell model as a unified view of nuclear structure. *Rev. Mod. Phys.*, 77:427–488, Jun 2005.
- [13] D.J. Dean, T. Engeland, M. Hjorth-Jensen, M.P. Kartamyshev, and E. Osnes. Effective interactions and the nuclear shell model. *Progress in Particle and Nuclear Physics*, 53:419–500, 2004. Review.
- [14] S. Fujii, R. Okamoto, and K. Suzuki. Ground-state and single-particle energies of nuclei around  $^{16}\text{O}$ ,  $^{40}\text{Ca}$ , and  $^{56}\text{Ni}$  from realistic nucleon-nucleon forces. *arXiv:0908.3376v2 [nucl-th]*, 2009.
- [15] L. Coraggio, N. Itaco, A. Covello, A. Gargano, and T. T. S. Kuo. Ground-state properties of closed-shell nuclei with low-momentum realistic interactions. *Physical Review C*, 68:034320, Sep 2003.
- [16] L. Coraggio, A. Covello, A. Gargano, N. Itaco, T. T. S. Kuo, and R. Machleidt. Nuclear structure calculations and modern nucleon-nucleon potentials. *Physical Review C*, 71:014307, Jan 2005.
- [17] L. Coraggio, A. Covello, A. Gargano, N. Itaco, and T. T. S. Kuo. Nuclear structure calculations with low-momentum potentials in a model space truncation approach. *Physical Review C*, 73:014304, 2006.
- [18] Petr Navratil, Sofia Quaglioni, Ionel Stetcu, and Bruce R Barrett. Recent developments in no-core shell-model calculations. *Journal of Physics G: Nuclear and Particle Physics*, 36(8):083101 (54pp), 2009.
- [19] S. E. Koonin, D. J. Dean, and K. Langanke. Shell model monte carlo methods. *Physics Reports*, 278:1 – 77, 1997.
- [20] Takaharu Otsuka, Takahiro Mizusaki, and Michio Honma. Monte carlo shell-model calculations. *Journal of Physics G: Nuclear and Particle Physics*, 25:699–715, 1999.
- [21] S. Y. Lee and K. Suzuki. The effective interaction of two nucleons in the s-d shell. *Physics Letters B*, 91:173 – 176, 1980.
- [22] Kenji Suzuki and Shyh Yuan Lee. Convergent theory for effective interaction in nuclei. *Progress of Theoretical Physics*, 64:2091–2106, 1980.
- [23] Thomas T.S. Kuo and Eivind Osnes. *Folded-diagram theory of the effective interaction in nuclei, atoms, and molecules*, volume 364 of *Lecture notes in physics*. Springer-Verlag, 1990. ISBN 3540530231.
- [24] C. Barbieri and W. H. Dickhoff. Spectroscopic factors in  $^{16}\text{O}$  and nucleon asymmetry. *International Journal of Modern Physics A*, 24(11):2060, 2009.
- [25] C. Barbieri and M. Hjorth-Jensen. Quasiparticle and quasihole states of nuclei around  $^{56}\text{Ni}$ . *Physical Review C*, 79:064313, 2009.

- [26] L. Lapikás. Quasi-elastic electron scattering off nuclei. *Nuclear Physics A*, 553:297 – 308, 1993.
- [27] M. Leuschner, J. R. Calarco, F. W. Hersman, E. Jans, G. J. Kramer, L. Lapikás, G. van der Steenhoven, P. K. A. de Witt Huberts, H. P. Blok, N. Kalantar-Nayestanaki, and J. Friedrich. Quasielastic proton knockout from *o*16. *Physical Review C*, 49:955–967, Feb 1994.
- [28] R. Subedi, R. Shneor, P. Monaghan, B. D. Anderson, K. Aniol, J. Annand, J. Arrington, H. Benaoum, F. Benmokhtar, W. Boeglin, J.-P. Chen, Seonho Choi, E. Cisbani, B. Craver, S. Frullani, F. Garibaldi, S. Gilad, R. Gilman, O. Glamazdin, J.-O. Hansen, D. W. Higinbotham, T. Holmstrom, H. Ibrahim, R. Igarashi, C. W. de Jager, E. Jans, X. Jiang, L. J. Kaufman, A. Kelleher, A. Kolarkar, G. Kumbartzki, J. J. LeRose, R. Lindgren, N. Liyanage, D. J. Margaziotis, P. Markowitz, S. Marrone, M. Mazouz, D. Meekins, R. Michaels, B. Moffit, C. F. Perdrisat, E. Piasetzky, M. Potokar, V. Punjabi, Y. Qiang, J. Reinhold, G. Ron, G. Rosner, A. Saha, B. Sawatzky, A. Shahinyan, S. Sirca, K. Slifer, P. Solvignon, V. Sulkosky, G. M. Urciuoli, E. Voutier, J. W. Watson, L. B. Weinstein, B. Wojtsekhowski, S. Wood, X.-C. Zheng, and L. Zhu. Probing Cold Dense Nuclear Matter. *Science*, 320:1476–1478, 2008.
- [29] D. Rohe, C. S. Armstrong, R. Asaturyan, O. K. Baker, S. Bueltmann, C. Carasco, D. Day, R. Ent, H. C. Fenker, K. Garrow, A. Gasparian, P. Gueye, M. Hauger, A. Honegger, J. Jourdan, C. E. Keppel, G. Kubon, R. Lindgren, A. Lung, D. J. Mack, J. H. Mitchell, H. Mkrtchyan, D. Mocerj, K. Normand, T. Petitjean, O. Rondon, and E. Segbefia. Correlated strength in the nuclear spectral function. *Physical Review Letters*, 93:182501, Oct 2004.
- [30] C. Barbieri and L. Lapikás. Effects of rescattering in  $(e, e'p)$  reactions within a semiclassical model. *Physical Review C*, 70:054612, Nov 2004.
- [31] I.T. Diatlov, V.V. Sudakhov, and K.A. Ter-Martirosian. *JETP*, 5:631, 1957.
- [32] Anatoley T. Zheleznyak, Victor M. Yakovenko, and Igor E. Dzyaloshinskii. Parquet solution for a flat fermi surface. *Phys. Rev. B*, 55:3200–3215, Feb 1997.
- [33] V. Janis. Green functions in the renormalized many-body perturbation theory for correlated and disordered electrons. *Condensed Matter Physics*, 9:499–518, 2006.
- [34] N. E. Bickers and D. J. Scalapino. Critical behavior of electronic parquet solutions. *Phys. Rev. B*, 46:8050–8056, Oct 1992.
- [35] Joonhyun Yeo and M. A. Moore. Parquet-graph resummation method for vortex liquids. *Phys. Rev. B*, 54:4218–4231, Aug 1996.
- [36] A.D. Jackson, A. Lande, and R.A. Smith. Variational and perturbation theories made planar. *Physics Reports*, 86:55–111, 1982.

- [37] A. D. Jackson and T. Wettig. Necessary conditions for microscopic many-body theories. *Physics Reports*, 237:325 – 355, 1994.
- [38] A.D. Jackson, A. Lande, R.W. Guitink, and R.A. Smith. Application of parquet perturbation theory to ground states of boson systems. *Physical Review B*, 31:403, 1985.
- [39] Alexander Lande and Roger Alan Smith. Two-body and three-body parquet theory. *Physical Review A*, 45:913–921, Jan 1992.
- [40] K. Yasuda. Direct determination of the quantum-mechanical density matrix: Parquet theory. *Physical Review A*, 59:4133, 1999.
- [41] P.J. Ellis and E. Osnes. An introductory guide to effective operators in nuclei. *Reviews of Modern Physics*, 49:777, 1977. Folding, effective interactions.
- [42] Gordon Baym and Leo P. Kadanoff. Conservation laws and correlation functions. *Phys. Rev.*, 124:287–299, Oct 1961.
- [43] G. Baym. Self-consistent approximations in many-body systems. *Physical Review*, 127:1391–1401, Aug 1962.
- [44] A. Arriaga, V. R. Pandharipande, and R. B. Wiringa. Three-body correlations in few-body nuclei. *Physical Review C*, 52:2362–2368, Nov 1995.
- [45] P. Navrátil, V. G. Gueorguiev, J. P. Vary, W. E. Ormand, and A. Nogga. Structure of  $a = 10$ –13 nuclei with two- plus three-nucleon interactions from chiral effective field theory. *Physical Review Letters*, 99:042501, 2007.
- [46] E. Epelbaum, A. Nogga, W. Glöckle, H. Kamada, Ulf-G. Meißner, and H. Witała. Three-nucleon forces from chiral effective field theory. *Physical Review C*, 66:064001, Dec 2002.
- [47] J. Carlson, V. R. Pandharipande, and R. B. Wiringa. Three-nucleon interaction in 3-, 4- and [infinity]-body systems. *Nuclear Physics A*, 401:59 – 85, 1983.
- [48] Roger D. Woods and David S. Saxon. Diffuse surface optical model for nucleon-nuclei scattering. *Phys. Rev.*, 95:577–578, Jul 1954.
- [49] Steven Weinberg. Phenomenological lagrangians. *Physica A: Statistical and Theoretical Physics*, 96(:327 – 340, 1979.
- [50] V. G. J. Stoks, R. A. M. Klomp, C. P. F. Terheggen, and J. J. de Swart. Construction of high-quality nn potential models. *Physical Review C*, 49:2950–2962, Jun 1994.
- [51] R. B. Wiringa, V. G. J. Stoks, and R. Schiavilla. Accurate nucleon-nucleon potential with charge-independence breaking. *Physical Review C*, 51:38–51, Jan 1995.

- [52] R. Machleidt. High-precision, charge-dependent bonn nucleon-nucleon potential. *Physical Review C*, 63:024001, Jan 2001.
- [53] V. G. J. Stoks, R. A. M. Klomp, M. C. M. Rentmeester, and J. J. de Swart. Partial-wave analysis of all nucleon-nucleon scattering data below 350 mev. *Physical Review C*, 48:792–815, Aug 1993.
- [54] H. Heiselberg and M. Hjorth-Jensen. Phases of dense matter in neutron stars. 328:237, 2000.
- [55] L.-W. Siu, J. W. Holt, T. T. S. Kuo, and G. E. Brown. Low-momentum nn interactions and all-order summation of ring diagrams of symmetric nuclear matter. *Physical Review C*, 79:054004, 2009.
- [56] A. M. Shirokov, A. I. Mazur, S. A. Zaytsev, J. P. Vary, and T. A. Weber. Nucleon-nucleon interaction in the  $j$ -matrix inverse scattering approach and few-nucleon systems. *Physical Review C*, 70:044005, Oct 2004.
- [57] A.M. Shirokov, J.P. Vary, A.I. Mazur, S.A. Zaytsev, and T.A. Weber. Novel nn interaction and the spectroscopy of light nuclei. *Physics Letters B*, 621:96 – 101, 2005.
- [58] Evgeny Epelbaum. Few-nucleon forces and systems in chiral effective field theory. *Progress in Particle and Nuclear Physics*, 57:654 – 741, 2006.
- [59] D. R. Entem and R. Machleidt. Accurate charge-dependent nucleon-nucleon potential at fourth order of chiral perturbation theory. *Physical Review C*, 68:041001, Oct 2003.
- [60] K. A. Brueckner, C. A. Levinson, and H. M. Mahmoud. Two-body forces and nuclear saturation. i. central forces. *Phys. Rev.*, 95:217–228, Jul 1954.
- [61] K.A. Brueckner and J.L. Gammel. Properties of nuclear matter. *Physical Review*, 109:1023, 1958.
- [62] S.K. Bogner, T.T.S. Kuo, and A. Schwenk. Model-independent low momentum nucleon interaction from phase shift equivalence. *Physics Reports*, 368:1–27, 2003. RG, effective interaction.
- [63] S.K. Bogner, T.T.S. Kuo, A. Schwenk, D.R. Entem, and R. Machleidt. Towards a model-independent low momentum nucleon-nucleon interaction. *Physics Letters B*, 576:265–272, 2003. RG, effective interaction.
- [64] S. K. Bogner, R. J. Furnstahl, and R. J. Perry. Similarity renormalization group for nucleon-nucleon interactions. *Physical Review C*, 75:061001, 2007.
- [65] S.K. Bogner, R.J. Furnstahl, S. Ramanan, and A. Schwenk. Low-momentum interactions with smooth cutoffs. *Nuclear Physics A*, 784:79 – 103, 2007.

- [66] E. D. Jurgenson, P. Navrátil, and R. J. Furnstahl. Evolution of nuclear many-body forces with the similarity renormalization group. *Physical Review Letters*, 103:082501, 2009.
- [67] A. Nogga, H. Kamada, and W. Glöckle. Modern nuclear force predictions for the  $\alpha$  particle. *Physical Review Letters*, 85:944–947, Jul 2000.
- [68] A. Nogga, H. Kamada, W. Glöckle, and B. R. Barrett. The  $\alpha$  particle based on modern nuclear forces. *Physical Review C*, 65:054003, May 2002.
- [69] R.B. Wiringa and S.C. Pieper. Evolution of nuclear spectra with nuclear forces. *Physical Review Letters*, 89:182501, 2002.
- [70] A. Nogga, P. Navrátil, B. R. Barrett, and J. P. Vary. Spectra and binding energy predictions of chiral interactions for  ${}^7\text{Li}$ . *Physical Review C*, 73:064002, 2006.
- [71] G. Hagen, T. Papenbrock, D. J. Dean, M. Hjorth-Jensen, and B. Velamuri Asokan. Ab initio computation of neutron-rich oxygen isotopes. *Physical Review C*, 80:021306, 2009.
- [72] Takaharu Otsuka, Toshio Suzuki, Jason D. Holt, Achim Schwenk, and Yoshinori Akaishi. Three-body forces and the limit of oxygen isotopes. *arXiv:0908.2607v1 [nucl-th]*, 2009.
- [73] B. S. Pudliner, V. R. Pandharipande, J. Carlson, and R. B. Wiringa. Quantum monte carlo calculations of  $a \leq 6$  nuclei. *Physical Review Letters*, 74:4396–4399, May 1995.
- [74] Steven C. Pieper, V. R. Pandharipande, R. B. Wiringa, and J. Carlson. Realistic models of pion-exchange three-nucleon interactions. *Physical Review C*, 64:014001, Jun 2001.
- [75] R. Machleidt. The missing three-nucleon forces: Where are they? *arXiv:0909.2881v1 [nucl-th]*, Sep 2009.
- [76] B. S. Pudliner, V. R. Pandharipande, J. Carlson, Steven C. Pieper, and R. B. Wiringa. Quantum monte carlo calculations of nuclei with  $A < \sim 7$ . *Physical Review C*, 56:1720–1750, Oct 1997.
- [77] D. M. Ceperley. Path integrals in the theory of condensed helium. *Rev. Mod. Phys.*, 67:279–355, Apr 1995.
- [78] Doron Gazit, Sonia Bacca, Nir Barnea, Winfried Leidemann, and Giuseppina Orlandini. Photoabsorption on  ${}^4\text{He}$  with a realistic nuclear force. *Physical Review Letters*, 96:112301, 2006.
- [79] K. Varga and Y. Suzuki. Precise solution of few-body problems with the stochastic variational method on a correlated gaussian basis. *Physical Review C*, 52:2885–2905, Dec 1995.

- [80] M. Viviani, A. Kievsky, and S. Rosati. Calculation of the  $\alpha$ -particle ground state within the hyperspherical harmonic basis. *Physical Review C*, 71:024006, Feb 2005.
- [81] D. C. Zheng, B. R. Barrett, L. Jaqua, J. P. Vary, and R. J. McCarthy. Microscopic calculations of the spectra of light nuclei. *Physical Review C*, 48:1083–1091, 1993.
- [82] S.K. Bogner, R.J. Furnstahl, P. Maris, R.J. Perry, A. Schwenk, and J.P. Vary. Convergence in the no-core shell model with low-momentum two-nucleon interactions. *Nuclear Physics A*, 801:21 – 42, 2008.
- [83] P. Maris, J. P. Vary, and A. M. Shirokov. Ab initio no-core full configuration calculations of light nuclei. *Physical Review C*, 79:014308, 2009.
- [84] Alexander L. Fetter and John Dirk Walecka. *Quantum theory of many-particle systems*. McGraw-Hill, New York, 1971.
- [85] Richard D. Mattuck. *A Guide to Feynman Diagrams in the Many-Body Problem*. Dover Publications, Inc, 2 edition, 1976.
- [86] F. Coester and H. Kmmel. Short-range correlations in nuclear wave functions. *Nuclear Physics*, 17:477 – 485, 1960.
- [87] L. Coraggio, A. Covello, A. Gargano, N. Itaco, and T.T.S. Kuo. Shell-model calculations and realistic effective interactions. *Progress in Particle and Nuclear Physics*, 62:135 – 182, 2009.
- [88] L. Coraggio and N. Itaco. Self-consistent nuclear shell-model calculation starting from a realistic nn potential. *Physics Letters B*, 616:43 – 47, 2005.
- [89] Tore Berggren. On the use of resonant states in eigenfunction expansions of scattering and reaction amplitudes. *Nuclear Physics A*, 109:265 – 287, 1968.
- [90] Tore Berggren. On the treatment of resonant final states in direct reactions. *Nuclear Physics A*, 169:353 – 362, 1971.
- [91] N. Michel, W. Nazarewich, M. Ploszajczak, and J. Okolowicz. Gamow shell model description of weakly bound nuclei and unbound nuclear states. 2003.
- [92] S. K. Bogner, R. J. Furnstahl, and L. Platter. Density matrix expansion for low-momentum interactions. *The European physical journal A*, 39:219, 2009.
- [93] Jean-Paul Blaizot and Georges Ripka. *Quantum theory of finite systems*. MIT Press, Cambridge, Mass., 1986.
- [94] A.A. Abrikosov, Lev P. Gor’kov, and I.E. Dzhaloinskij. *Quantum field theoretical methods in statistical physics*. Pergamon Press, Oxford, 2nd ed. [rev. and enl.]. edition, 1965.

- [95] Paul C. Martin and Julian Schwinger. Theory of many-particle systems. i. *Phys. Rev.*, 115:1342–1373, Sep 1959.
- [96] T.T.S. Kuo, J. Shurpin, K.C. Tam, E. Osnes, and P.J. Ellis. A simple method for evaluating goldston diagrams in an angular momentum coupled representation. *Annals of Physics*, 132:237–276, 1981. shell model, diagrams, recoupling, effective interaction.
- [97] Jun John Sakurai. *Modern Quantum Mechanics; rev. ed.* Reading, MA, 1994.
- [98] R. Blankenbecler and R. Sugar. Linear integral equations for relativistic multichannel scattering. *Phys. Rev.*, 142:1051–1059, Feb 1966.
- [99] Aage Bohr and Ben R. Mottelson. *Nuclear structure [by] Aage Bohr [and] Ben R. Mottelson.* W. A. Benjamin, New York, 1969.
- [100] C. Barbieri. *Self-consistent Green's function study of low-energy correlations in  $^{16}\text{O}$ .* PhD thesis, Washington University, 2002.
- [101] C. Barbieri and W.H. Dickhoff. Faddeev description of two-hole-one-particle motion and the single-particle spectral function. *Physical Review C*, 63:34313, 2001.
- [102] C. Barbieri and W. Dickhoff. Faddeev treatment of long-range correlations and the one-hole spectral function of  $^{16}\text{O}$ . *Physical Review C*, 65:064313, 2002.
- [103] C. Barbieri and W. Dickhoff. Extension of the random phase approximation including the self-consistent coupling to two-phonon contributions. *Physical Review C*, 68:014311, 2003.
- [104] C. Barbieri, C. Giusti, F.D. Pacati, and W.H. Dickhoff. Effects of nuclear correlations on the  $^{16}\text{O}(\text{e},\text{e}^{\prime\prime},\text{pn})$  reactions to discrete final states. *Physical Review C*, 70:014606, 2004.
- [105] Igal Talmi. *Simple models of complex nuclei : the shell model and interacting boson model*, volume 7 of *Contemporary concepts in physics*. Harwood Academic Publishers, 1993.
- [106] D.J. Dean and M. Hjorth-Jensen. Pairing in nuclear systems: from neutron stars to finite nuclei. *Reviews of Modern Physics*, 75:607, 2003.
- [107] Morten Hjorth-Jensen. Private communication, 2009.
- [108] RJ Bartlett. Many-body perturbation-theory and coupled cluster theory for electron correlation in molecules. *Annual Review of Physical Chemistry*, 32:359–401, 1981.
- [109] Carlo Barbieri. Toward an ab-initio description of quasiparticle properties. *arXiv:0909.0336v2 [nucl-th]*, 2009.